One-dimensional Nanostructures of Hafnium Oxides: Fabrication with and without Ti/Fe Doping, and Magnetic Properties

by

Mahdi Beedel

A thesis
presented to the University of Waterloo
in fulfillment of the
thesis requirement for the degree of
Doctor of Philosophy
in
Chemistry (Nanotechnology)

Waterloo, Ontario, Canada, 2021

AUTHOR'S DECLARATION

I hereby declare that I am the sole author of this thesis. This is a true copy of the thesis, including any required final revisions, as accepted by my examiners.

I understand that my thesis may be made electronically available to the public.

Abstract

Since the discovery of giant magnetoresistance (GMR) in the late 1980s, which marked the emergence of spintronic technology, the integration of conventional semiconductor-based electronics with spintronics has always been of great interest due to important technological advantages. Dilute magnetic semiconductors (DMSs) have been developed as a viable solution for realizing this idea. The recent generation of DMSs are dilute magnetic semiconducting oxides (DMSOs) that promise real-life device applications due to their high Curie temperatures well above room temperature. Among all DMSOs, HfO_2 has received increased attention because of its technologically important properties such as high dielectric constant (κ~25), wide bandgap (~5.7 eV), high refractive index (n=2.9), and excellent thermal and chemical stabilities. More importantly, HfO_2 is the most CMOS-technology compatible metal oxide, and its ferromagnetic properties therefore promise easy integration of CMOS technology with spintronics. As the structural defects, particularly oxygen vacancies, are believed to play an important role in inducing ferromagnetism in DMSOs, nanostructures of HfO_2, especially one-dimensional (1D) nanostructures with high specific surface areas, are expected to exhibit enhanced ferromagnetic properties. Moreover, single-crystalline 1D nanostructures with their high crystal quality provide an excellent material system for studying the correlation between oxygen vacancy defects and ferromagnetism due to the minimal effects of other structural defects. However, the synthesis of single-crystalline HfO_2 1D nanostructures have hitherto been unsuccessful because of the extremely low vapor pressures and high melting points of Hf (2233 °C) and HfO_2 (2800 °C), and also of the suppression of vapor-liquid-solid (VLS) growth arising from pulsed laser ablation of oxide targets.

In the present work, we have synthesized undoped and doped HfO_2 nanostructures with different morphologies to investigate their novel magnetic properties. By precisely controlling the growth parameters in a catalyst-assisted pulsed laser deposition (PLD) system and by using different growth templates including chemically oxidized Si (Ox-Si), Ox-Si predeposited with gold nanoislands (GNI/Ox-Si) and with tin alloyed gold nanoislands (Sn-GNI/Ox-Si), we have been able to grow HfO_2 nano square pyramids and nano triangular pyramids on Ox-Si and GNI/Ox-Si, and nano-tetrahedrons, undoped 1D nanostructures [nanowires (NWs), nanospikes, nano-columns], Ti-doped and Fe-doped nanospikes, and Fe-doped distorted nanocubes on Sn-GNI/Ox-Si. The 1D nanostructures synthesized in this work are the first single-crystalline 1D HfO_2 nanostructures ever reported. In the first phase of the present work, we characterize the morphology, crystal structure and growth direction of the undoped HfO_2 nanostructures using scanning electron microscopy, glancing incidence X-ray

diffraction, and high resolution transmission electron microscopy, along with structural simulation by calculated atomic models. Our investigations reveal that Sn plays a crucial role in promoting the VLS growth of 1D nanostructures by alloying with GNIs to form Sn-GNI to increase both the VLS growth nucleation and growth rates. Furthermore, X-ray photoelectron spectroscopy shows that HfO_2 NWs are more oxygen-deficient than the HfO_2 nano square pyramids. Their room temperature ferromagnetic behavior compared to the weak paramagnetic behavior of HfO_2 nano square pyramids therefore confirms a strong correlation between high temperature ferromagnetism and the amount of oxygen vacancies in the lattice. Employing a modified bound magnetic polaron-hybridized band ferromagnetism model, we explain the role of oxygen vacancies in inducing high temperature ferromagnetism in HfO_2 NWs.

In an attempt to fabricate HfO_2 nanostructures with higher magnetic saturation, Ti-doped and Fe-doped HfO_2 nanostructures are also synthesized in this work. Morphological investigations reveal that Ti doping has a minor effect on the VLS growth mechanism producing $Hf_{1-x}Ti_xO_2$ 1D nanostructures (nanospikes) at different Ti atomic concentrations (x=0.01, 0.10, 0.25 and 0.50). On the other hand, doping with a magnetic material such as Fe is found to restrict VLS growth significantly, yielding nanospikes for 1 at. % Fe doping ($Hf_{0.99}Fe_{0.01}O_2$ nanospikes), but distorted nanocubes with stacked crystal flakes for 5 at. % ($Hf_{0.95}Fe_{0.05}O_2$), 10 at. % ($Hf_{0.90}Fe_{0.10}O_2$) and 20 at. % ($Hf_{0.80}Fe_{0.20}O_2$) Fe doping. Moreover, Ti doping up to 10 at. % is found to slightly increase the magnetic saturations of the HfO_2 nanostructures, while further doping (25 at. % and 50 at. %) reduces the magnetic saturation back to the same order of magnitude as that of the undoped HfO_2 NWs, which is attributed to the presence of the $HfTiO_4$ phase with a possible higher oxygen vacancy formation energy. In contrast, Fe doping has significantly increased magnetic saturations (e.g., up to two orders of magnitude higher than that of undoped HfO_2 nanostructures for 10 at. % doping) through F-center exchange interaction in the lattice. Further doping (20 at. %), however, is found to produce extrinsic properties due to possible atomic-scale magnetic ion clustering.

The present work offers valuable insights to the synthesis of other oxide nanostructures, especially 1D nanostructures of complex oxides. Indeed, the use of appropriate metal-alloy catalysts could provide the key to the PLD growth of other hitherto unobtainable 1D nanostructures of other metal oxides. Their magnetization measurements could further advance our understanding of defect-induced ferromagnetism in DMSO materials. The single-crystalline HfO_2 nanostructures introduced here could be an important stepping stone toward the integration of CMOS and spintronics technologies, given their high Curie temperatures and high material compatibility.

Acknowledgements

First and foremost, all praise belongs to Allah, the only true omniscient and creator.

I would like to express my utmost gratitude to my supervisor, Prof. Kam Tong Leung, for his patience, encouragement, and invaluable advice and suggestions to formulate this work. I gratefully thank him for providing me with the opportunity to join the Waterloo Advanced Technology Laboratory (WATLab), where I learned a lot from him about working with highly sophisticated instruments for materials analysis and characterization. I am deeply indebted to him for all the kind help and support he provided me during my study. He will always remain a true example of erudition, diligence and benevolence for me both in my academic career and personal life. I am also grateful to my advisory committee members, Prof. Vivek Maheshwari, Prof. Bo Cui and Prof. Daniel Thomas, for their helpful suggestions and feedback on this work, and I sincerely thank Prof. Fereidoon Razavi from Brock University for kindly accepting to be my external examiner.

In WATLab, I was very fortunate to work with highly talented scientists and amiable people. I would like to express my deep gratitude to all my current and former colleagues at WATLab, Dr. Joseph Palathinkal Thomas, Dr. Hanieh Farkhondeh, Dr. Nina Heinig, Dr. Lei Zhang, Dr. Marwa Abdellah, Dr. Nafiseh Moghimi, Dr. Seyedeh Fatemeh Rahnemaye Rahsepar, Dr. Md Anisur Rahman, Dr. Saurabh Srivastava, Dr. Jung-Soo Kang, Dr. Shantinarayan Rout, Dr. Donald McGillivray, Mr. Xiaoyi Guan, and Ms. Wenyu Gao for their continued support and sincere friendship. I am especially thankful to former WATLab member Dr. Samad Bazargan for his genuine friendship and constructive discussion on the catalyst-assisted PLD growth of HfO_2 1D nanostructures and their structural analysis. I also gratefully acknowledge all members of the University of Waterloo Chemistry Department, the skillful and knowledgeable engineers and technicians at the Science Machining and Electronics Shop, the Waterloo Institute for Nanotechnology (WIN), and, particularly, the Natural Sciences and Engineering Research Council of Canada (NSERC) for their generous funding of my research in Canada.

Last, but certainly not least, my most heartfelt gratitude goes to my much-loved family: My beloved parents, Masoud and Simin, whose unconditional and self-sacrificing love and continued prayers enabled me to finish this long journey, and my dear brothers, Javad and Majid, whose love and encouragement have always been true sources of motivation and inspiration in my life.

Dedication

To my dearly beloved parents, **Masoud and Simin**, whose endless love, self-sacrifice, and prayers have sustained me throughout my entire life.

Table of Contents

List of Figures

List of Tables

Chapter 1
Introduction

The present work focuses on the fabrication and $_m$agnetic properties of doped and undoped HfO_2 nanostructures as novel materials for spin-based applications. This chapter begins with a brief introduction to the history and basic concepts of spintronics and the significance of integration of this technology with conventional charge-based electronics. This will be followed by an overview of dilute magnetic semiconductors (DMSs), particularly dilute magnetic semiconducting oxides (DMSOs), as a promising class of materials for realizing the integration of spin-based and charge-based technologies. The main ferromagnetic mechanism in DMS and DMSO materials will also be discussed in this section. This chapter then continues with a short review of the properties and synthesis of HfO_2 nanostructures, particularly one-dimensional (1D) HfO_2 nanostructures, as novel DMSO nanomaterials. Next, a description of the pulsed laser deposition (PLD) method and superconducting quantum interference device (SQUID) magnetometry, along with the experimental details on PLD-assisted vapor-liquid-solid (VLS) growth of HfO_2 nanostructures and their magnetic characterization, will be provided. Finally, this chapter will conclude with the scope and structure of the thesis.

1.1 An Introduction to the Fundamentals of Spintronics

Charge and spin are two fundamental and intrinsic characteristics of the electron. Before the discovery of the giant magnetoresistance (GMR) effect in 1988 by the Nobel laureates Albert Fert and Peter Grünberg,[1,2] only the electron charge had been exploited in the design and development of electronic devices while the electron spin has always been overlooked. However, the discovery of GMR effect rapidly changed this picture, triggering intense research that led to the emergence of a new field in science and technology known today as spin-based electronics or spintronics. In spintronics, electron transport is controlled through the manipulation of electron spins.[3] For example, GMR arises from the magnetization effect of ferromagnetic layers on the electrical resistivity across a multilayer structure consisting of alternating ferromagnetic and nonmagnetic metals. Figure 1-1a,b depict the first observations of the GMR effect in a Fe/Cr multilayer and a Fe/Cr/Fe trilayer architectures.[4] In particular, neighboring ferromagnetic layers with antiparallel magnetization produce maximum resistivity (R_{ap}), while ferromagnetic layers with parallel magnetization produce minimum resistivity (R_p). The magnetoresistance (MR) can therefore be written as $MR=100\times[(R_{ap}-R_p)/R_p]$.[5] The concept of GMR effect can be explained by the two-current model proposed for the first time by Mott

in his work on the electrical conductivity of transition metals.[6] According to this model, spin-up and spin-down electrons can carry the electrical current in two independent channels. The resistivity in a ferromagnet arises from the scattering of electrons in the 4s bands (which are responsible for the electrical conduction) with the electrons in the 3d bands.[5] When the spins of the electrons are parallel to the magnetization of the ferromagnet (majority spin), the density of states (DOS) for the 3d bands at the Fermi energy (E_F) is small (Figure 1-1c). On the other hand, for the electrons with antiparallel spins to the magnetization of the ferromagnet (minority spin), the DOS of 3d bands becomes large. Since the probability of scattering is proportional to the DOS at the Fermi energy, the current channel with electrons of antiparallel spins to the ferromagnet magnetization exhibit higher resistivity due to the more scattering (Figure 1-1c). Therefore, in a sandwich structure of ferromagnet/nonmagnet/ferromagnet with parallel magnetic configuration of the ferromagnets, one of the electrical current channels could easily pass through both ferromagnetic layers creating a short circuit and low resistance. However, in the antiparallel magnetic configuration of the ferromagnetic layers, both spin-up and spin-down current channels experience some scattering in either of the ferromagnetic layers, which leads to higher overall resistivity (Figure 1-1d). The current in GMR can be measured either parallel to the interfaces [current in the plane (CIP)] or perpendicular to the interfaces [current perpendicular to the plane (CPP)] (Figure 1-2). The GMR effect was originally observed in a CIP measurement configuration, but the CPP measurement shows a stronger GMR effect.[7]

The discovery of GMR has revolutionized the data storage and recording technology. Hard-disk drives (HDDs) with GMR-based read heads are the most prominent devices fabricated based on GMR effect. The new read head technology originally introduced by IBM in 1997 could increase the recording density more than two orders of magnitude within 10 years leading to fabrication of HDDs with smaller sizes and much higher capacities (up to 1 terabyte).[3] Today, the capacity of available HDDs in the marketplace has already reached 20 TB and it is expected to grow up to 70-80 TB in near future.[8] Although the global market for HDDs has started to shrink since 2010,[9] due to the fast development of competing technologies such as solid state drives (SSDs), HDDs are still in high demand particularly for cloud and nearline storage.[10,11] Despite the disruptive impact of COVID-19 pandemic on the HDD supply market over the last two years, the global shipment of HHDs in 2021 is still projected to be over 200 million units,[12] with an expected petabyte shipments growth of 18.5 % per year between 2020 and 2025.[13]

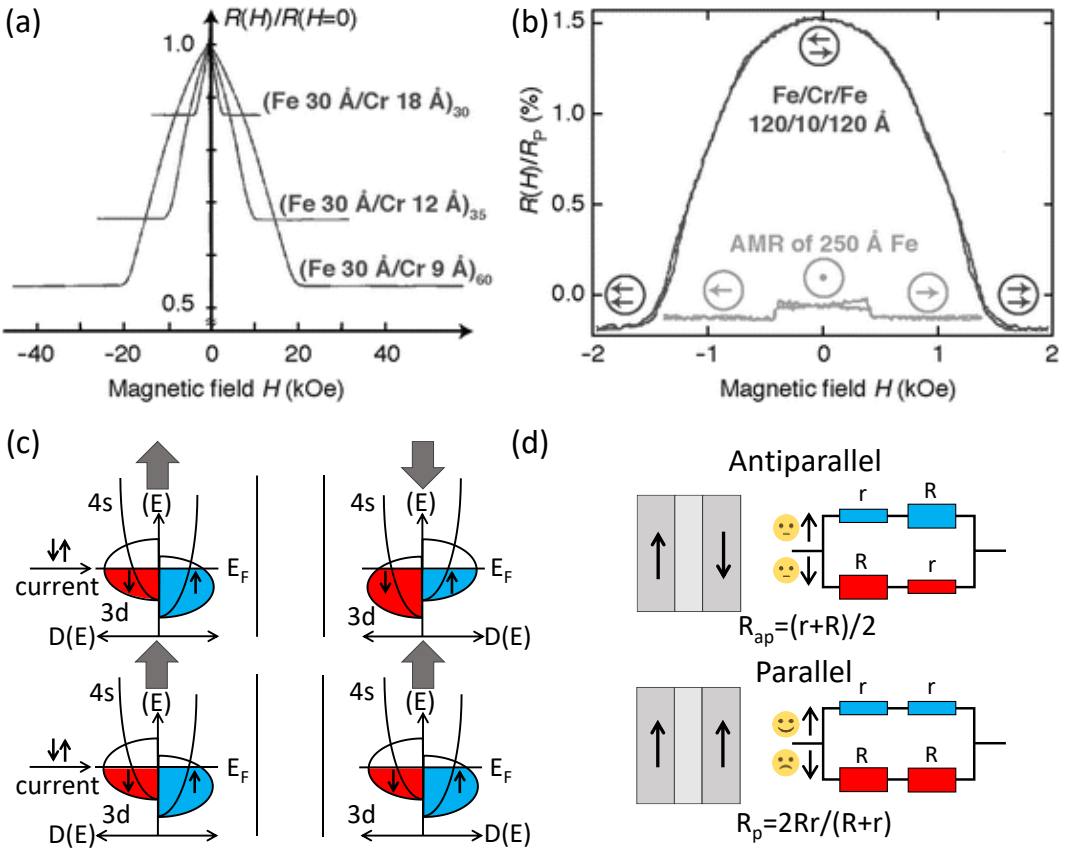

Figure 1-1. First observations of GMR showing magnetoresistance plots in (a) Fe/Cr multilayer and (b) Fe/Cr/Fe trilayer structures. R(H)/R(H=0) in (a) is the ratio of resistances in the presence and absence of the external field H, and $R(H)/R_p$ in (b) is the ratio of measured resistance to the resistance value when the magnetization of ferromagnetic layers is parallel to H. For comparison, the inset in (b) shows the anisotropic magnetoresistance (AMR) effect in a 250-Å-thick Fe film. Reprinted with permission from references [1] and [2]. Copyright (1988 and 1989) by American Physical Society. (c) Band structure of the ferromagnetic layers in the absence (H=0) and the presence (H≠0) of the external field, where D is the density of states and E_F is the Fermi energy. (d) Schematic diagram of the two-current model. r is the resistance of electrons with their spin parallel to the magnetization of ferromagnet and R is the resistance of electrons with their spin antiparallel to the magnetization of ferromagnet.

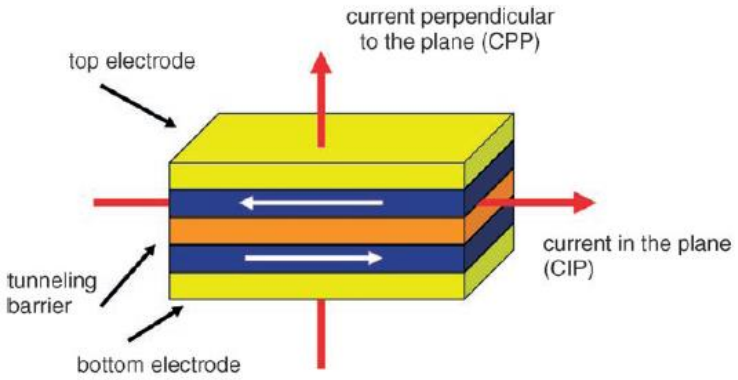

Figure 1-2. A typical GMR measurement configuration in a multilayer structure. The red arrows show the direction of the current in either current in the plane (CIP) or current perpendicular to the plane (CPP) configuration. The white arrows indicate the magnetization direction in the ferromagnetic layers. Reprinted with permission from reference [7]. Copyright (2007) by John Wiley and Sons.

Another key step in the development of spintronics was the study of tunneling magnetoresistance (TMR) in magnetic tunnel junctions (MTJs). The structure of a MTJ is very similar to a ferromagnet/nonmagnet/ferromagnet trilayer structure that exhibits GMR effect. Instead of a nonmagnetic middle layer, the ferromagnetic layers in a MTJ are separated by a thin insulating layer about 1 nm thick.[14] The spin polarized electrons tunnel through the barrier when the ferromagnetic layers have parallel magnetization and they are blocked when the ferromagnetic layers have antiparallel magnetization.[14,15] The schematic illustration of electron tunneling in a typical MTJ is depicted in Figure 1-3.[15]

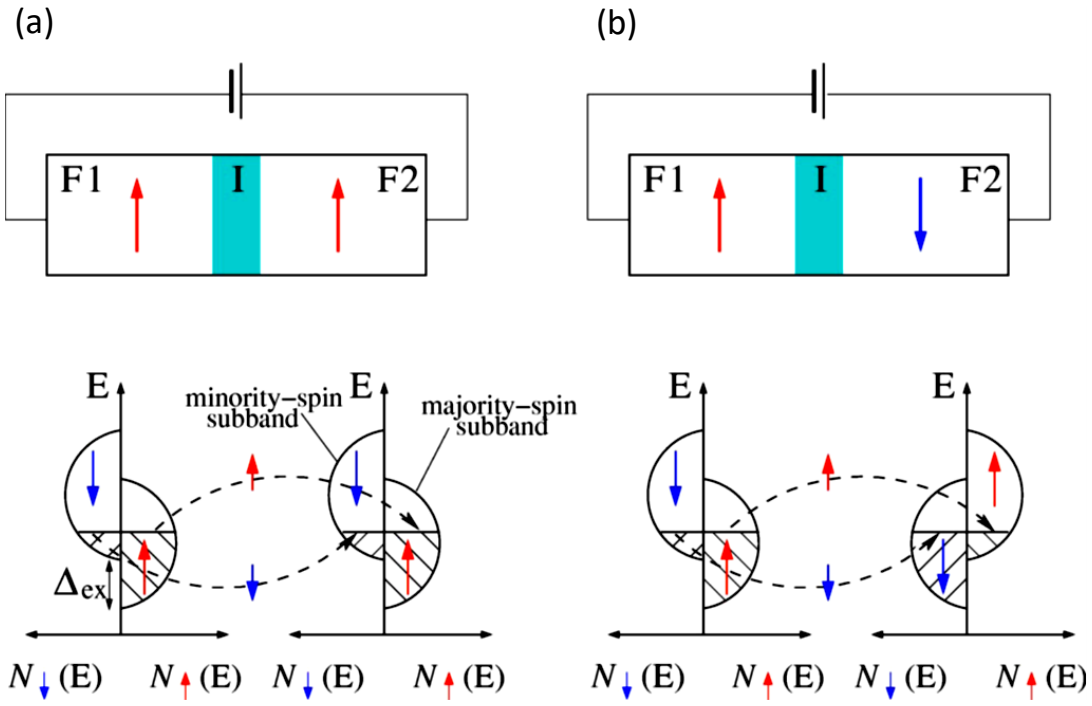

Figure 1-3. (Upper panels) Schematic circuit models of electron tunneling through an insulating barrier in a magnetic junction transistor with the ferromagnetic layers in (a) parallel and (b) antiparallel spin configurations. (Lower panels) Corresponding band diagrams show the spin-resolved densities of states for d electrons with spin splitting exchange Δ_{ex} as a result of magnetization of the ferromagnets. Dashed lines denote spin-conserved tunneling through the barrier. Reproduced with permission from reference [15]. Copyright (2004) by American Physical Society.

While the TMR effect was first observed in 1975[16] before the GMR effect, it did not attract much attention due to the small TMR ratio (14% at 4.2 K) and poor reproducibility.[3,14] The TMR ratio is defined as $(R_{AP}–R_p)/R_p$, where R_{AP} is the resistance across the tunnel barrier with the ferromagnets with antiparallel magnetization while R_p is the resistance across the tunnel barrier with the ferromagnets with parallel magnetization. Twenty years later, the first MTJs with a TMR ratio of ~20% and good reproducibility at room temperature were obtained by employing an amorphous alumina (Al_2O_3) thin layer as the tunnel barrier[17,18]. To date, the TMR ratios of MTJs have been significantly improved by using crystalline MgO (001) tunnel barriers,[5,14] reaching a record TMR of 604% at room temprature.[19] Recently, a new concept of magnetic memory called magnetic random access memory (MRAM) has been developed based on MTJs.[14] MRAMs are conceived to be a

promising candidate for a universal memory unit in computers as they can combine all the advantages of the existing memory technologies. This new technology has a great potential to produce memories with the fast read and write performance of static random access memory (SRAM), high density of dynamic random access memory (DRAM) and nonvolatility of the flash memories altogether.[14] Over the last thirty years, many spintronics phenomena with great potential for invention of novel devices have been found. Here, we have only discussed two of the most important spintronic effects to illustrate their potential for novel applications. The diagram shown in Figure 1-4 summarizes the recent developments in spintronic research and devices.[5,20]

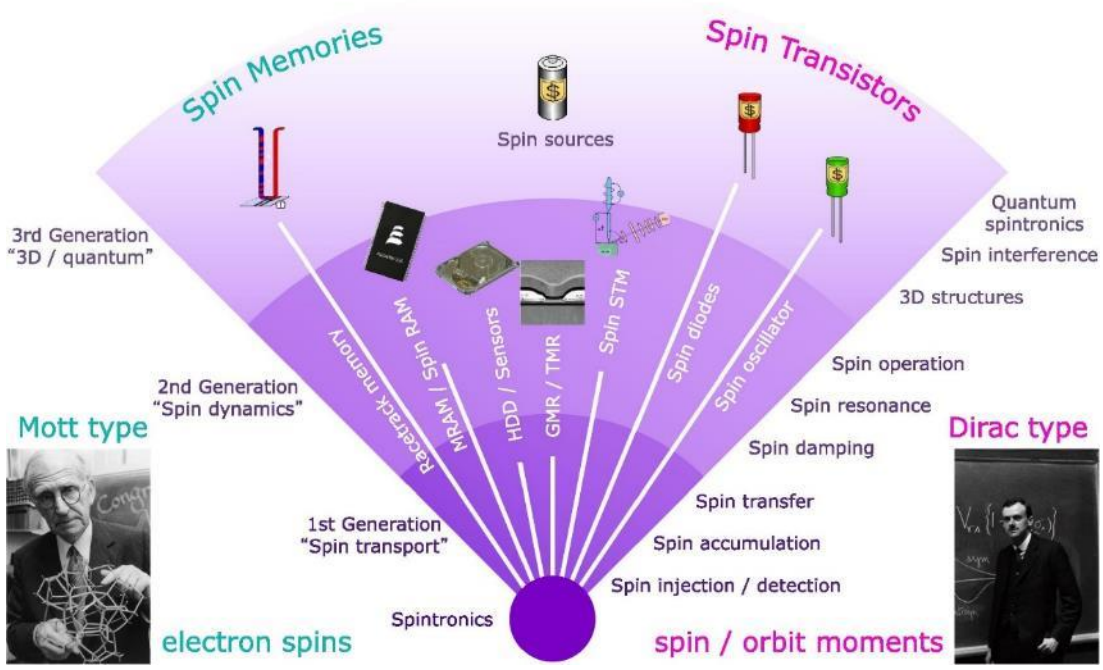

Figure 1-4. List of spintronic phenomena and devices. Reprinted with permission from reference [5]. Copyright (2014) by IOP Publishing, Ltd.

Manipulating the electrical current using the electron spin provides an extra degree of freedom in conventional charge-based semiconductor devices, thus increasing their capability and performance. The integration of spintronics and mainstream charge-based electronics could, therefore, produce devices with greater advantages such as nonvolatility, higher data processing speed and lower power consumption.[21] Moreover, the integration of these two technologies offers an excellent opportunity to combine all elements of data processing, i.e., storage, logic and communication, on a single chip.

Fabrication of electronic devices with more compact design could therefore be achieved using such type of multifunctional chips.[22] Designing a new material with both semiconducting and ferromagnetic properties is an important step toward realizing the integration of spintronics with mainstream charge-based electronics. For example, one of the main advantages of using a ferromagnetic semiconductor is the easier injection of spin-polarized current from a ferromagnetic semiconductor to a nonmagnetic semiconductor, when compared to the spin injection from a metallic ferromagnet to a nonmagnetic semiconductor, due to the absence of Schottky barriers.[7,15] Indeed, some ferromagnetic semiconductors such as europium chalcogenide[23] and ferrimagnetic or ferromagnetic spinels[24,25] have already been identified. However, these materials usually have a low Curie temperature (T_c) and they require difficult growth processes, and they are incompatible with substrates typically used in semiconductor-based electronics such as Si and GaAs. In this search for alternative ferromagnetic semiconductors, a new class of materials called the dilute magnetic semiconductors (DMSs) has been developed. The next section provides an introduction to the DMSs and the physics behind their magnetic properties.

1.2 Dilute Magnetic Semiconductors (DMSs)

1.2.1 History and Background

Dilute magnetic semiconductors are a recent class of advanced materials that are produced by dilute doping of a semiconductor with magnetic ions to generate magnetic ordering and spin functionality in the host material while preserving its semiconducting properties.26 The first generation of DMSs was developed in the 1980s and they were mainly based on II-VI compound semiconductors such as CdTe and ZnSe.27,28 The preparation of II-VI compounds with a large amount of magnetic dopants is relatively easy both in bulk form and epitaxial layers. This advantage originates from the fact that the valence of the cations in these compounds is identical to that of common magnetic dopants such as Mn, which leads to the formation of substitutional ternary alloys such as Zn1-xMnxSe ($0<x\leq0.57$) and Cd1-xMnxTe ($0<x\leq0.77$).27,28 However, the predominant antiferromagnetic exchange interaction between the magnetic ions in the II-VI DMSs results in spin-glass behavior and weak ferromagnetic response. Moreover, the n-type and p-type doping of these materials are found to be difficult, and their Curie temperature is too low (with $Tc\leq4$ K) making them unfavorable for practical applications.28,29 In the 1990s, the next generation of DMSs based on III-V semiconductors was introduced. The trivalent cations of the host lattice in the III-V DMSs are substituted by divalent magnetic ions (Mn+2) giving rise to a very low equilibrium solubility limit. However, as the result of

new development in crystal growth methods such as molecular beam epitaxy (MBE), it became possible to fabricate III-V semiconductors with magnetic ion content far beyond the equilibrium solubility limit.28 The first III-V DMS was (In,Mn)As30–32 that exhibited great magnetotransport properties, despite their very low Curie temperature (Tc<10 K). A breakthrough in this field was made with the growth of an innovative III-V DMS based on GaAs [(Ga,Mn)As], which exhibited a Curie temperature as high as 60 K33 and later up to 110 K with further improvement.28 To date, the (Ga,Mn)As DMSs have attracted the most attention among all DMS materials due to the prevalent application of GaAs in many electronic and optoelectronic devices such as high-speed transistors, light emitting diodes, and laser diodes.28,34–36 Owing to the continued improvements in post-growth annealing techniques, the Tc of (Ga,Mn)As has been steadily increased to 140 K,37 160 K,34 173 K,38 191 K39 and 200 K.40 Although the Tc record of 200 K has been an important achievement, it is still far below room temperature, making these DMS materials inappropriate for practical applications in actual devices.

In the search of DMSs with a Curie temperature above room temperature and high compatibility with the complementary metal oxide semiconductor (CMOS) technology, wide bandgap metal oxides have become the center of attention since the early 2000s. Pioneering work on this type of DMSs include the observations of room temperature ferromagnetism in Mn-doped ZnO[41] and Co-doped TiO_2,[42,43] which have triggered a new round of intense research in this field. A new class of DMSs generally categorized as dilute magnetic semiconducting oxides (DMSOs) has since been developed.[26] DMSOs have several important advantages over DMSs. The most important advantage of DMSOs is their high Curie temperature that could be well above room temperature (e.g., up to 850-930 K for Cr-doped indium oxide thin film[44]), making them promising candidates for realizable spintronic device applications. Moreover, the fundamental differences of oxide semiconductors from compound semiconductors, such as bonding characteristic, diversity and oxygen non-stoichiometry, could potentially provide more flexibility in controlling their properties.[26] However, achieving a uniform distribution of magnetic ions without any ion clustering or agglomeration throughout the host lattice in DMSOs is very difficult. Such uncertainty in the homogeneous doping of DMSOs has prevented any consensus on the origin of ferromagnetism in these materials.[26,45] Nonetheless, the magnetic ion distribution issue appears to be closely linked to the material growth conditions,[26,45] and it could be potentially resolved by using an appropriate growth technique. In the next section, we will briefly review some of the main magnetic interactions and ferromagnetic mechanisms that are commonly used to explain the origin of ferromagnetism in DMSs and DMSOs.

1.2.2 The Origin of Ferromagnetism in DMSs and DMSOs.

1.2.2.1 Direct exchange interaction

Exchange interaction is purely quantum mechanical in nature and it is the result of interaction between the wavefunctions of two identical particles such as electrons. If two electrons interact through exchange interaction directly and without any intermediary, the interaction is called direct exchange interaction. This interaction between two localized electrons can be described by the Heisenberg Hamiltonian as:[29,46]

$$\hat{H} = -\sum_{ij} J_{ij}\mathbf{S}_i.\mathbf{S}_j \qquad \textbf{Eq. 1-1}$$

where $\mathbf{S}_i$ and $\mathbf{S}_j$ are spin operators of the electrons and J_{ij} is the exchange coefficientt between the i^{th} and j^{th} spins. Depending on the sign of J_{ij}, the exchange interaction of the electrons can result in either parallel (or ferromagnetic, $J_{ij}>0$) or antiparallel (or antiferromagnetic $J_{ij}<0$) alignment of their spins. If the electrons belong to the same atom, J_{ij} is typically positive leading to parallel alignment of spins as reflected in Hund's first rule. However, if the interacting electrons are located at different neighboring atoms, the J_{ij} value is generally negative, giving rise to the antiferromagnetic alignment of the spins. The latter case typically occurs in a bonding molecular orbital when the atoms bond together.[29,46] Although direct exchange is an important interaction between two individual electrons, it does not play a prominent role in determining the magnetic behavior of ionic solids such as DMSs and DMSOs. Direct exchange interaction is a short-range interaction that arises when the orbitals of the neighboring ions overlap effectively. However, the separation between the magnetic ions in ionic solids is typically far beyond the effective range of direct exchange interaction. In solids, indirect exchange interactions that are mediated by a secondary factor would therefore be the more effective mechanism.[46]

1.2.2.2 Superexchange interaction

Superexchange interaction can be defined as the exchange interaction between the magnetic ions mediated by a nonmagnetic ion (e.g., oxygen in metal oxides). Hence, it is a type of indirect exchange interaction with a larger effective range than the direct exchange interaction. An antiferromagnetic superexchange, which is the most common exchange interaction in ionic solids and metal oxides, can be understood with reference to two transition metal ions separated by an oxygen ion shown in Figure 1-5. There is a kinetic energy advantage for the system if the two electrons in the p orbital of the

oxygen ion become delocalized by hopping to the empty states of the d orbitals in the neighboring transition metal ions. Two possible electron transitions are depicted in Figure 1-5a and b. As it is not energetically favorable for the system that the O 2p electrons flip their spins while hoping to the transition metal d orbitals, a certain alignment of the electron spins in the neighboring transition metal ion on one side would induce an antiferromagnetic alignment of electron spin in the transition metal ion on the other side.[46] Similar to the direct exchange interaction, superexchange interaction can be described by a Heisenberg Hamiltonian (Eq. 1-1).[29] The sign of J_{ij} in the superexchange interaction is usually negative and thus antiferromagnetic. However, it could also be ferromagnetic depending on the electron configuration of the d orbitals or the metal-oxygen-metal (M–O–M) bond angle.[29] These dependencies are discussed by Goodenough,[47,48] Kanamori[49] and Anderson,[50] today known as the Goodenough-Kanamori-Anderson (G-K-A) rules.

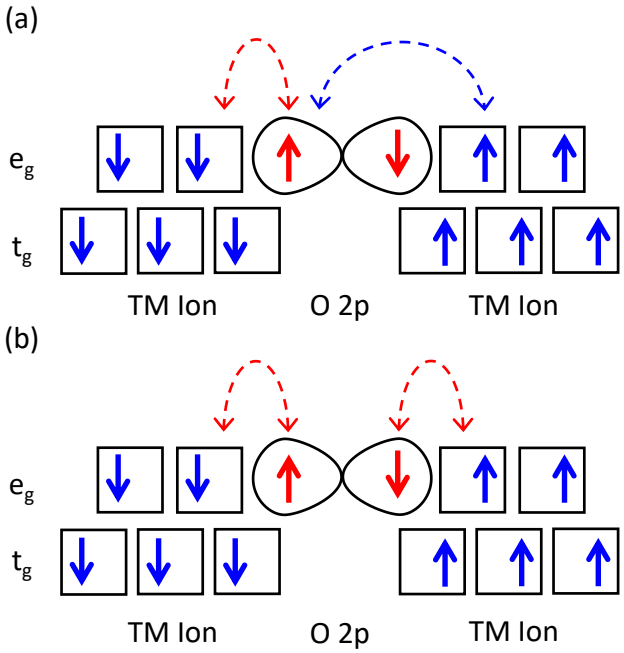

Figure 1-5. Schematic diagrams of an oxygen mediated superexchange interaction in a metal oxide for two possible electron delocalization schemes involving (a) one electron from O 2p orbital and one electron from d orbital of a neighboring transition metal (TM) ion becoming delocalized and hopping between p and d orbitals , and (b) both electrons of O 2p becoming delocalized and hopping between p and d orbitals. To prevent spin flipping while hopping, certain alignment of spins in the TM ion on one side induces an antiparallel alignment of spins in the TM ion on the other side.

1.2.2.3 Double exchange interaction

Double exchange interaction occurs in the systems with multivalent transition metal ions, i.e., those ions that can exist in different oxidation states such as Mn with the oxidation states of 3+ (Mn^{3+}) and 4+ (Mn^{4+}).[46] This type of interaction was first proposed to explain ferromagnetism in $La_{1-x}A_xMnO_3$ ($0<x<1$) oxides with a perovskite structure where A represents Ca, Sr, or Ba.[51] In these materials, the electrons in e_g orbitals of $Mn^{3+}(3d^4)$ ions tend to hop into the empty states of e_g orbitals of $Mn^{4+}(3d^3)$ ions to reduce the kinetic energy and therefore the total energy of the system. Since the electrons preserve their spin alignment while hopping, it is energetically favorable that the three electrons occupying the t_g orbitals in the receiving ion (Mn^{4+}) have the same spin as the hopping electron (Hund's first rule). This situation requires that both donating and receiving Mn ions have the same spin alignment (ferromagnetism). Therefore, double exchange interaction is a ferromagnetic interaction which generates metallic conduction in oxides, and it is also an indirect interaction because the hopping process is mediated by the oxygen ion located between the two magnetic metal ions.[29,46]

1.2.2.4 Carrier-mediated exchange

In some DMSs, the exchange interaction between magnetic ions can be mediated by charge carriers (electrons or holes). In this mechanism, a magnetic ion with a localized magnetic moment spin-polarizes the conduction electrons or holes, which in turn can couple to a neighboring magnetic ion located at the distance r from the first ion. Since the exchange interaction between the magnetic moments is mediated by the charge carriers, this corresponds to a type of indirect exchange interaction.[46] An earlier version of this interaction known as Zener carrier exchange interaction was first proposed by Zener to describe ferromagnetism in transition metals.[52] However, this model did not consider the oscillatory nature of spin polarization around a localized magnetic moment, which can induce not only ferromagnetic interaction but also antiferromagnetic interaction depending on the distance from that localized magnetic moment. A more accurate model was later developed by Ruderman, Kittel, Kasuya, and Yosida, known as the RKKY interaction, which included consideration of the oscillatory nature of the exchange interaction mediated by the carriers.[53] Based on this model, the sign of the exchange interaction, J_{RKKY}, oscillates with the distance (r) from a localized moment and can be described as:[29]

$$J_{RKKY}(r)=\frac{2\pi\, m^{*}k_F^4}{h}\, F\,(2k_F r) \qquad \textbf{Eq. 1-2}$$

where m^* is the effective mass and k_F is the Fermi wavevector of the electron gas, and h is the Planck's constant. The oscillatory function defined as $F(x)=(x\cos x-\sin x)/x^4$ is shown in Figure 1-6.

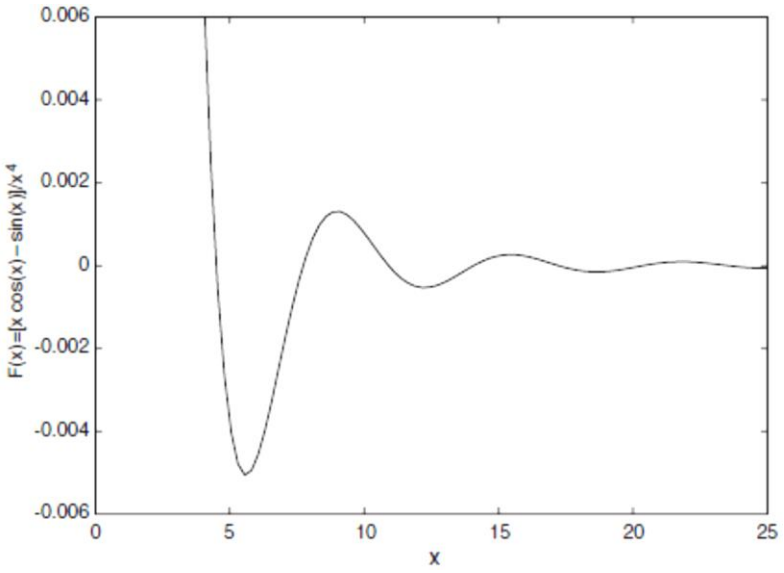

Figure 1-6. The oscillatory function in RKKY interaction, where x is proportional to k_Fr. Reproduced with permission from reference [29]. Copyright (2005) by IOP Publishing, Ltd.

RKKY exchange interaction is mainly used to explain ferromagnetic ordering in III-V DMS systems such as (Ga,Mn)As. The Mn ions doped into the III-V DMS lattice substitute the trivalent cations (Ga) and serve as the supplier for both local magnetic moment and the hole carrier. The electrons in the sp-d bonding states of the Mn-As bond spin-polarize the weakly bound holes in the antibonding states, which in turn couple with the electrons in the sp-d bonding states of the neighboring Mn-As bond.[54] The sign of RKKY interaction (j_{RKKY}) between the two Mn ions is, in effect, only ferromagnetic because the first zero of the oscillation, beyond which the interaction is antiferromagnetic, occurs at a distance far beyond the RKKY cut-off length (i.e. the charge carrier mean free path) due to the dilute hole concentration.[28,35,55]

1.2.2.5 Bound magnetic polarons (BMPs)

In the context of magnetic semiconductors, the bound magnetic polaron model was first employed to explain the insulator-metal transition in oxygen-deficient EuO.[56] Based on this model, an electron (hole) bound to the donor (acceptor) impurity is assumed to behave like a hydrogen atom with a

hydrogenic orbital that interacts with the neighboring magnetic ions lying within this orbital. As the result of such interaction, bound magnetic polarons (BMPs) are created, which in turn can interact with each other ferromagnetically. If the concentration of donor (acceptor) impurity and thus the number of BMPs exceeds the percolation threshold, the exchange interaction between BMPs leads to a long-range ferromagnetic ordering throughout the host lattice.[57,58] Although the BMP model is also applicable to III-V based DMSs such as (Ga,Mn)As,[59] it is mainly used to explain ferromagnetism in DMSO materials.[26,60] As DMSOs are typically wide-bandgap semiconductors or insulators with low density of itinerant carriers, carrier-mediated based models, e.g., RKKY exchange interaction, are not appropriate models to explain their ferromagnetic property,[61] unlike BMP based models that appear to provide a better explanation. Since structural defects such as oxygen vacancies can act as electron donors, the BMP model is particularly useful for explaining ferromagnetism in oxygen-deficient metal oxides.[62–65] However, despite a reasonable account of the long-range ferromagnetic ordering in DMSOs, the BMP model alone cannot reconcile their high Curie temperature (T_c). A more sophisticated model is required to provide a more accurate and complete picture.

1.2.2.6 Charge-transfer ferromagnetism

All the magnetic interaction models discussed so far are based on the Heisenberg approach, i.e., the direct or indirect exchange coupling between the localized magnetic moments. Charge-transfer ferromagnetism model, on the other hand, is based on the band ferromagnetism approach (also known as itinerant ferromagnetism) proposed for DMSOs doped with multivalent transition metals.[66] According to the band ferromagnetism theory, in transition metals, some electrons of the same spin state (e.g., down spin) in the conduction band and near the Fermi energy level can spin-flip and move to the sub-band with the opposite spin state (up spin) due to the exchange interaction with the internal molecular field. If the kinetic energy cost for the electrons transferring to the opposite spin sub-band is outweighed by the Coulomb energy reduction, spontaneous spin-up and spin-down splitting of the band occurs and leads to spontaneous ferromagnetism.[46] The balance between the energy cost and energy reduction in this process is determined by the Stoner criterion defined as $N(E_F) \geq 1/I$, where $N(E_F)$ is the density of states at the Fermi level and I is the Stoner parameter. The spontaneous spin splitting of the band occurs when the Stoner criterion is met. In DMSOs, the maximum of the narrow band associated with the defects does not coincide with the Fermi level. However, the multivalent transition ions doped into the lattice serve as charge reservoirs transferring electrons to the defect states, thus raising the Fermi level to the maximum of the density of states. As a result, the $N(E_F)$ becomes large and meets the Stoner criterion leading to the spontaneous spin splitting of the defect

band and, therefore, spontaneous ferromagnetism. A schematic representation of this mechanism is shown in Figure 1-7.[66,67] Although charge transfer ferromagnetism could successfully account for the high Curie temperature of DMSOs, it can only be used for the systems doped with the multivalent transition ions. We still need a model that can explain the ferromagnetic behavior of the undoped DMSOs or those systems doped with single-valent magnetic ions.

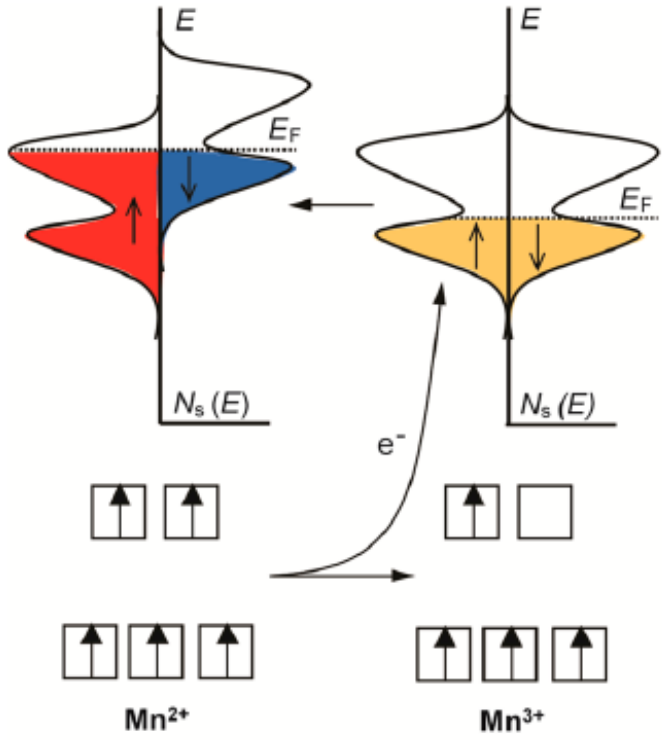

Figure 1-7. Schematic representation of charge-transfer ferromagnetism in defect-rich DMSOs. The electrons from Mn^{2+} transfer to the defect band (indicated with red and blue colors), increasing its Fermi level to the maximum of the band density of states where the Stoner condition is met, resulting in spontaneous band splitting. Reprinted with permission from reference [67]. Copyright (2014) by American Chemical Society.

1.2.2.7 Bound magnetic polaron-band ferromagnetism hybrid model

This model was first proposed by Coey et al. in 2005[68] in an attempt to explain both ferromagnetism and the high Curie temperature in DMSO materials by combining the BMP model with the band ferromagnetism formalism. According to this model, defects (such as oxygen vacancies) in the lattice

could act as donor impurity sites donating electrons to the lattice. As described in the BMP model, the exchange interaction between these bound electrons and their surrounding magnetic ions creates BMPs, which in turn interact ferromagnetically with one another and generate long-range ferromagnetic ordering.[29,68] The high Curie temperature could then be explained through hybridization of the impurity-derived band with the d states of magnetic ions leading to band spin splitting. From the band theory point of view, when the impurity donor site is formed in the lattice, it creates a narrow impurity band near the Fermi level of the magnetic ions. Due to the interaction between the electrons on the donor sites and the electrons in the d band of the magnetic ions, electrons could transfer from the impurity band to the empty states of the d band. The resulting hybridization of the impurity band with the d band causes spin splitting of the impurity band and produces high Curie temperature ferromagnetism.[68,69] The number of BMPs (δ) determined by the density of donor defects (e.g., oxygen vacancies) and the concentration of the magnetic ions in the host lattice (x) are two critical parameters in this model. The number of BMPs needs to be above the polaron percolation threshold δ_p (i.e., $\delta>\delta_p$) to create long-range ferromagnetic ordering, while the concentration of the magnetic ion dopants should be below the magnetic ion percolation threshold x_p (i.e., $x<x_p$), otherwise the antiferromagnetic interaction between the ions would dominate.[68] Figure 1-8 shows a schematic representation of impurity band splitting and hybridization with the 3d magnetic ions.

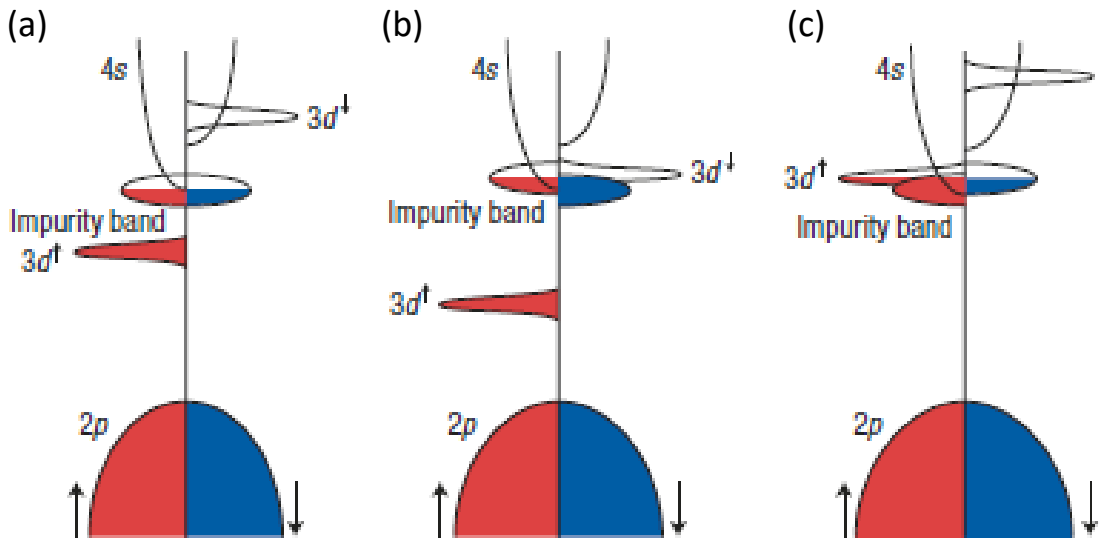

Figure 1-8. Schematic band structure of a DMSO with 3d ion dopants and donor impurities with (a) no band hybridization leading to low T_c, (b) band hybridization with $3d^n$ ions with $n \geq 5$ electron configuration, and (c) band hybridization with $3d^n$ ions with $n < 5$ electron configuration. Both (b) and (c) lead to high-T_c ferromagnetism. Reprinted with permission from reference [68]. Copyright (2005) by Springer Nature.

The BMP-band ferromagnetism hybrid model is particularly useful to explain high-T_c ferromagnetism in undoped DMSOs. A modified version of this model has been recently used to explain ferromagnetism in undoped defect-rich ZrO_2 nanostructures[63] and nanocrystals,[64] in which the transferred electrons from the oxygen vacancies to the empty d states of metallic ions could provide the required magnetic moment without any need for magnetic dopants. In the present work, we shall also explain the ferromagnetic behavior of the HfO_2 nanostructures using a modified version of this model. HfO_2 is a well-known material in the contemporary electronic industry with interesting properties. In the rest of this Chapter, we will briefly outline the significance of this material and its great potential to be used as a promising DMSO material. We will then briefly review various physical and chemical techniques used for the synthesis of HfO_2 nanostructures, and provide an introduction to pulse laser deposition for fabricating HfO_2 nanostructures and to SQUID magnetometry for magnetic property characterization.

1.3 Hafnium(IV) Oxide (HfO_2): A Promising Dilute Magnetic Semiconducting Oxide

Hafnium(IV) oxide or HfO_2, also commonly known as Hafnia, has received a lot of attention over the last two decades due to its technologically important properties such as high dielectric constant (κ~25), wide bandgap (~5.7 eV), high laser-induced damage threshold, high refractive index (n=2.9), and excellent thermal and chemical stability particularly in contact with Si substrates.[70–75] It also exhibits a rich variety of crystal structures that can be achieved by controlling the pressure, temperature, and other growth conditions as well as the dopant content.[76] Figure 1-9 shows the unit cells of these various crystal phase structures at different temperatures and pressures. The most stable crystal structure of HfO_2 at ambient condition is the monoclinic phase ($P2_1/c$, baddeleyite type, $T \leq 1020$ ℃), which transforms to the tetragonal phase ($P4_2nmc$, 1022 ℃<T<2422 ℃) and cubic phase (Fm3m, T>2422 ℃) with increasing temperature. At room temperature and with increasing pressure, the monoclinic phase undergoes a phase transformation to orthorhombic I (Pbcm) at 4-10 GPa and to orthorhombic II at P>29 GPa.[70,77–80] Owing to its many superior properties, HfO_2 has become an advanced material with great potential for a broad range of applications. For example, the high-pressure phase of HfO_2 (Figure 1-9c) can be quenched back to ambient condition[77–80] and used as a superhard ceramic oxide.[81] After the recent discovery of ferroelectricity in non-centrosymmetric orthorhombic phases of HfO_2,[82,83] it has also been subjected to numerous studies for ferroelectric field effect transistors (FeFET)[84,85] and ferroelectric random access memory (FRAM) applications.[86] Other applications include anti-reflective and protective optical coating,[87–90] memristors,[91–94] and gas sensors.[95]

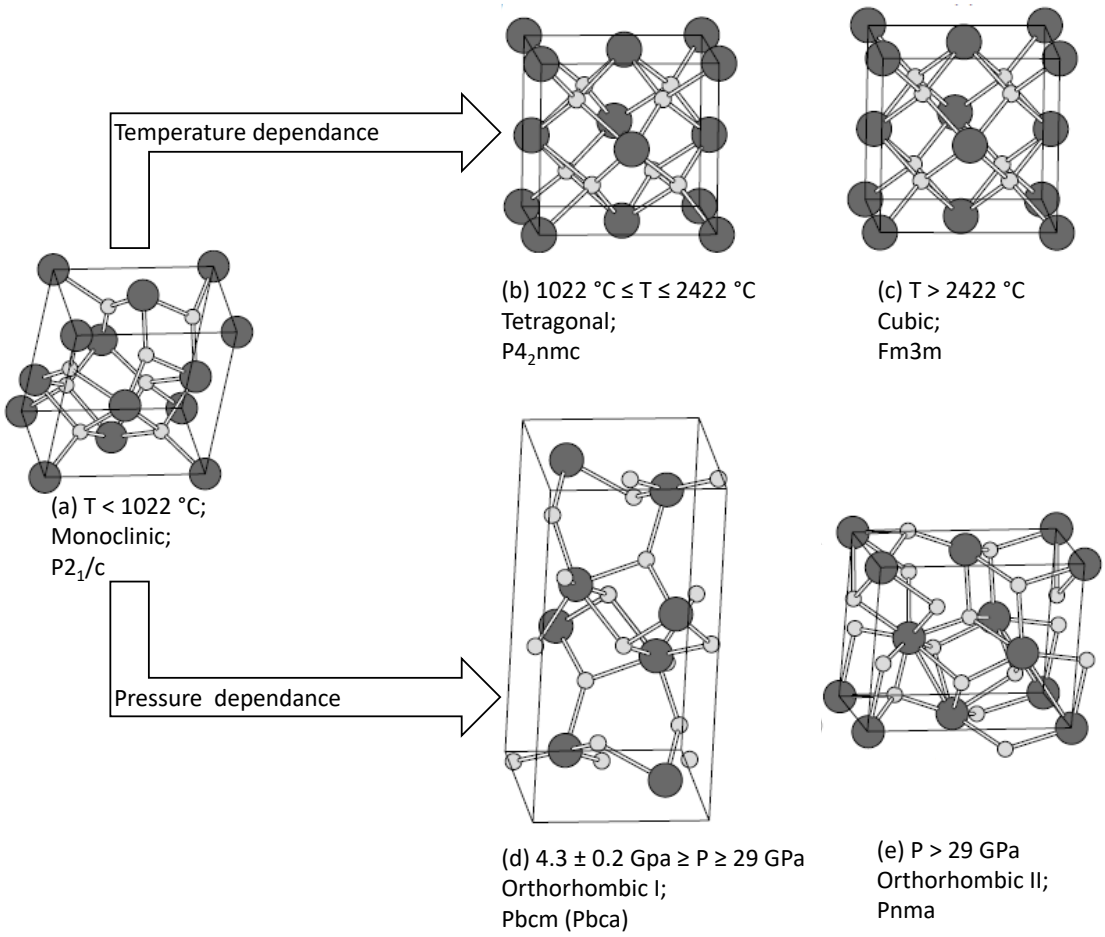

Figure 1-9. Unit cells of different HfO_2 polymorphs: (a) monoclinic; space group $P2_1/c$, (b) tetragonal; space group $P4_2nmc$, (c) cubic; space group Fm3m. (d) orthorhombic I; space group Pbcm, and (e) orthorhombic II, also called cotunnite; space group Pnma. Larger circles represent Hf atoms and smaller circles represent O atoms. Reproduced with permission from reference [70]. Copyright (2011) by Elsevier.

Among all potential applications, using HfO_2 as the gate dielectric of a metal-oxide-semiconductor field effect transistor (MOSFET) is the most established technological application of HfO_2. In general, a promising candidate for gate dielectric in MOSFETs should have a high dielectric constant (between 10 to 30), a large bandgap (above 5 eV), a high electrical breakdown field, and a large barrier height at interfaces with Si (above 1 eV) to minimize the current leakage. Moreover, the potential candidate should have high thermal and chemical stability in contact with the Si substrate. Among all the transition metal oxides, HfO_2 and other hafnium-based thin films have the most

optimum properties to fulfill the above requirements. Since MOSFETs with HfO_2 gate dielectrics can have a much more compact design due to the lower current leakage,[70] HfO_2 has recently found extensive application in modern electronic devices and it has become the metal oxide that is most compatible with CMOS technology. The discovery of ferromagnetism in undoped HfO_2 thin films in 2004[96] was therefore of great significance, because using an excellent CMOS compatible DMSO material with a Curie temperature well above room temperature in spintronic devices could be a major step forward in realizing the goal of integrating spintronics with conventional semiconductor-based electronics and CMOS technology.[97]

The observation of unexpected ferromagnetism in HfO_2 has also significantly improved our understanding of ferromagnetic mechanisms in DMSOs. As alluded to earlier, there has been no consensus about the origin of ferromagnetism in DMSO materials. While some researchers believe that the ferromagnetic property of DMSOs is intrinsic, originating from the structural defects in the lattice, others advocate that it is due to extrinsic effects such as magnetic ion cluster formation in the lattice after doping.[26] Undoped HfO_2 is a metal oxide with Hf^{+4} ions with a closed shell $[Xe]4f^{14}$ configuration and no unpaired electron or magnetic dopant.[96] The discovery of ferromagnetism in this material therefore has significantly strengthened the view that structural defects are the real source of ferromagnetism in DMSOs. Although the role of defects in generating ferromagnetism in DMSOs is generally accepted to date,[26,45,69,98] there is still ongoing discussion on the exact nature of these defects.[26,69] While a few studies[99,100] show cation vacancies are the source of ferromagnetism in DMSO materials, there is more solid evidence that oxygen vacancies are indeed the main source of ferromagnetism in both undoped and doped DMSOs.[62–64,97,98,101–103] Based on the role of structural defects, particularly oxygen vacancies, many models have been proposed thus far to explain the ferromagnetic behavior of DMSOs (Section 1.2.2). According to the BMP-band ferromagnetism hybrid model[68], which appears to be the most complete model, the amount of oxygen vacancies in the host lattice determines the number of BMPs (thus the total magnetic saturation value) and the degree of hybridization of the impurity band, which affects the Curie temperature. Compared to thin films, low-dimensional nanostructures, particularly 1D nanostructures such as nanowires (NWs) and nanospikes, have large specific surface areas that could potentially offer more surface defects and oxygen vacancies. They are therefore expected to exhibit enhanced ferromagnetic response, which has already been confirmed in recent reports of superior ferromagnetic properties in ZrO_2 1D nanostructures[63] and nanocrystals.[64] Considering the nearly identical chemistries and crystal structures of ZrO_2 and HfO_2,[76] similar improvements of magnetic properties in HfO_2 low-dimensional nanostructures, particularly HfO_2 nanowires and nanospikes, are expected. Moreover, 1D

semiconductor nanostructures exhibit novel electronic and optical properties due to high specific surface area, high crystalline quality, and size-dependent quantum confinement induced effects that could also affect their charge transport and magnetoresistance properties.[104–107] The synthesis of HfO_2 nanostructures, particularly 1D nanostructures, would therefore be of great interest to spintronic applications. In the next section, synthesis methods for fabricating HfO_2 nanostructures, especially 1D nanostructures, will be briefly reviewed.

1.4 Synthesis and Growth Methods of HfO_2 Nanostructures

To date, HfO_2 has been mainly used in the form of thin films in most applications. There are already numerous reports on the deposition of HfO_2 thin films using various deposition techniques, such as sol-gel, sputtering, pulsed laser deposition (PLD), (metal-organic) chemical vapor deposition [(MO)CVD], and atomic layer deposition (ALD). A detailed review of these methods can be found in reference [70]. There are, however, a limited number of reports in the literature about the synthesis of HfO_2 nanostructures, particularly 1D nanostructures. We briefly review some of these reports.

1.4.1 Synthesis of HfO_2 Nanoparticles

The most widely used methods for the synthesis of HfO_2 nanoparticles are chemical solution-based methods. In these methods, hafnium halide, typically hafnium tetrachloride ($HfCl_4$), is dissolved in water (for hydrothermal synthesis) or alcohol (for solvothermal synthesis). The pH of the resulting solution is then subsequently increased by gradually adding a strong base, such as KOH, NaOH and ammonia, which leads to precipitation of hafnium hydroxide [$Hf(OH)_4$]. In a simple precipitation method,[108,109] the $Hf(OH)_4$ precipitates are collected from the solution and calcinated at high temperature (500 °C) to obtain HfO_2 nanoparticles. In the hydrothermal[72,110,111] and solvothermal methods,[112,113] the $Hf(OH)_4$ suspension is used as a precursor solution and transferred to an autoclave reactor. The reactor is sealed and put in an oven at a selected temperature for an appropriate duration to produce HfO_2 nanoparticles. Hydrothermal treatment can also be assisted by ultrasonication or microwave radiation to increase the reaction rate, hence reducing the reaction time.[110,111] Although the solution-based methods are very simple and economical, they do not produce individual nanoparticles due to the strong tendency of the nanoparticles for agglomeration during the synthesis and calcination/drying process. An effective solution to deal with this problem is the addition of organic surfactants to the reaction system.[72,73] The organic surfactants serve as capping agents that can both reduce the agglomeration and control the shape and size of the nanoparticles.[73]

Reports on the synthesis of HfO_2 nanoparticles using physical methods are very limited. There are only a few reports on the synthesis of HfO_2 nanoparticles using pulsed laser ablation of solid targets in water[114,115] and air,[116] a standard technique that has often been used to synthesize various nanoparticles.[117] When the laser hits the target surface, a high-temperature and high-pressure metal plasma (the laser plume) is created by the laser shot. The as-generated laser plume rapidly cools down as a result of ultrasonic adiabatic expansion leading to the formation of metal clusters. These metal clusters subsequently react with the surrounding aqueous solution and form metal oxide nanoparticles.[117] The main advantages of this technique are that the size, crystal phase, and shape of the nanoparticles can be controlled by adjusting the laser pulse energy, wavelength, and repetition rate.[115] In addition, the agglomeration problem has been reported to be minor in the colloidal solutions produced by this method due to the repulsive surface charges resulting from partial surface oxidation of the nanoparticles.[114]

1.4.2 Synthesis of HfO_2 1D Nanostructures

To date, there have been only a few attempts to fabricate HfO_2 1D nanostructures, which mostly include the fabrication of HfO_2 nanotubes.[75,118–122] A widely used technique to synthesize HfO_2 nanotubes is the anodization of Hf foils in an electrochemical cell.[118–121] This method is basically used to fabricate porous oxide layers, the morphology and the inner diameter of the pores of which can be manipulated by adjusting the electrolyte composition and the applied potential to obtain arrayed nanotubes.[118–121] Another approach to the synthesis of HfO_2 nanotubes is the template-based method, in which the nanotubes are fabricated by the deposition of HfO_2 onto a template followed by removing the template after the deposition.[75,122] For example, well-arrayed HfO_2 nanotubes have been made by atomic layer deposition (ALD) of HfO_2 into the nanopores of an anodic aluminum oxide (AAO) template followed by chemically removing the templates in a basic solution.[122] In another attempt, HfO_2 superlong nanotubes (hollow nanofibers) are produced by ALD of HfO_2 thin film on electro-spun nylon nanofibers and subsequent removing the core polymeric nanofiber by calcination.[75] In these template-based methods, the thickness of the nanotubes can be precisely controlled by modifying the ALD parameters, but the resulting nanotubes are typically amorphous or polycrystalline. In addition to providing polymeric templates for the synthesis of HfO_2 nanotubes, electrospinning has also been used to directly fabricate HfO_2 nanobelts[123] and nanofibers.[124] In a typical electrospinning synthesis of HfO_2, a polymer solution of Hf is prepared and transferred to a glass syringe. Then a steady pressure is applied to the syringe plunger to gradually push the solution out while a high DC voltage (above 15 kV) is applied between the tip of the needle and a collector

plate. The collected nanofibers are then calcinated to remove the organic ingredients and obtain HfO_2 1D nanostructures. The calcination atmosphere and temperature can also be varied to modify the microstructure and structural defects in the as-fabricated nanofibers.[124]

All the aforementioned synthesis methods are based on wet chemistry, and they generally yield agglomerated products with a high possibility of cross-contamination of chemical impurities. As even a minute amount of contamination could produce erroneous results in magnetic property measurements, the products of these synthesis methods are not appropriate for magnetic property studies. More importantly, while single crystallinity and nearly perfect crystal quality of semiconducting NWs play a vital role in their superior physical properties, none of these methods are capable of producing high-quality single-crystalline 1D nanostructures. The most appropriate method to fabricate high-quality single-crystalline NWs is the vapor-liquid-solid (VLS) growth that could not only provide exceptional single crystallinity but also good control on the size and shape of the NWs with minimal risk of magnetic or chemical contamination.[125–127]

In a typical VLS growth process, the surface of a substrate is seeded with metal nanoparticles serving as both catalysts, particularly in a chemical vapour deposition (CVD) process, and nucleation sites.[125–127] The precursor of the desired semiconductor (or other material of interest) is introduced into the system in the vapor phase through the injection of gaseous reactants in CVD[128–131] (including MO-CVD[132]), or evaporation and sublimation of a solid source in a non-CVD process such as thermal evaporation,[133,134] electron beam evaporation,[135] molecular beam epitaxy (MBE),[136–138] or laser ablation.[139–141] In the presence of the semiconductor vapor, a (pseudo)binary alloy is formed between the metal nanoparticle catalysts and the semiconductor. When the substrate is annealed to a (growth) temperature higher than the eutectic point of the metal-semiconductor alloy, the metal catalyst melts and creates a liquid/vapor interface that incorporates more semiconductor material from the vapor phase into the liquid alloy.[104,125,127] In a CVD process, the initial decomposition of the reactants (e.g., SiH_4 or $SiCl_4$ in the case of Si NWs growth) occurs at the liquid/vapor interface and the products of the chemical reaction subsequently dissolve into the liquid alloy.[104] Eventually, the liquid alloy becomes supersaturated with the semiconductor material and the solid phase of the semiconductor starts to precipitate from the catalyst particle creating a solid/liquid interface also known as the growth interface. The growth process proceeds with continuous feeding of the semiconductor material from the vapor phase into the liquid catalyst resulting in the axial growth of the NW.[104,125,127] A schematic diagram of the described VLS mechanism for the case of Si NWs is illustrated in Figure 1-10.

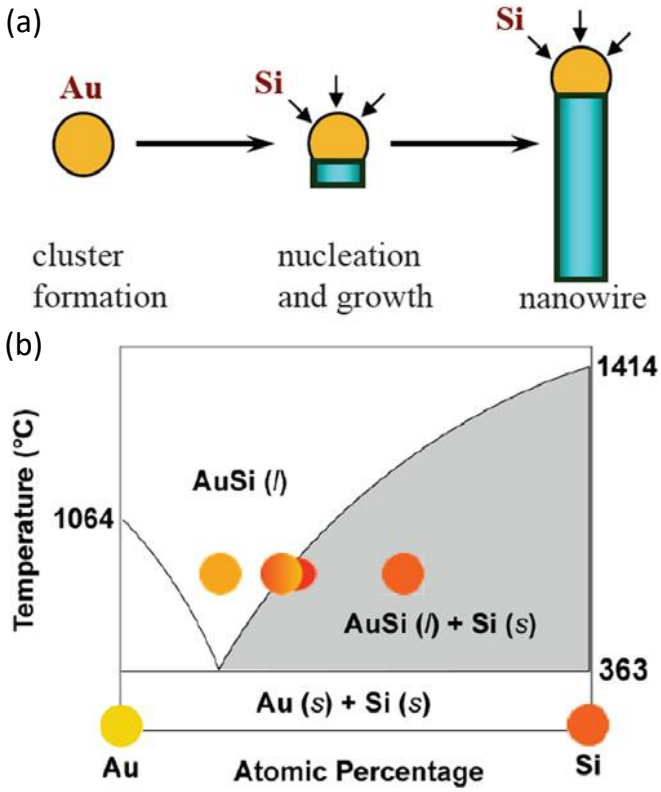

Figure 1-10. Schematic diagram of VLS growth of Si NWs. (a) A liquid alloy droplet of Au-Si is initially formed above the eutectic point of the Au-Si alloy system (363 °C). Continuous feeding of Si into the alloy droplet eventually supersaturates the droplet, resulting in precipitation of Si and axial growth of the Si NW. (b) Binary phase diagram of the Au-Si system showing the thermodynamics of VLS growth. Reprinted with permission from reference [104]. Copyright (2006) by IOP Publishing, Ltd.

To date, no successful VLS growth of HfO_2 1D nanostructures has been reported, which attests to the serious challenges in synthesizing HfO_2 low-dimensional nanostructures. Due to the extremely low vapor pressure and the high melting point of HfO_2, VLS growth of HfO_2 nanostructures using conventional CVD or physical vapor deposition methods is not feasible. Direct laser ablation of a solid target into the gas phase, therefore, appears to be the best approach to achieve VLS growth of this material. In the present work, we show that VLS growth of HfO_2 nanostructures is indeed attainable by the pulsed laser deposition method.

1.5 Pulsed Laser Deposition of HfO_2 Nanostructures

1.5.1 Background and Overview of PLD Growth

Pulsed laser deposition (PLD) started to develop as a thin film deposition technique in the 1960s, shortly after the first high-power ruby laser became available.[142] The first thin film deposition experiment that used laser ablation of materials was reported by Smith and Turner in 1965[143] when they used a ruby laser to deposit thin films on semiconductors, dielectrics, chalcogenides and organometallic materials. During the next thirty years, however, research activities in this field remained largely in a hibernation state with only a few publications per year.[142] The major breakthrough was achieved in 1987 when Venkatesan's group demonstrated that high-quality superconductor thin films with high T_c could be fabricated by pulsed laser ablation of a $YBa_2Cu_3O_{7-\delta}$ target, by taking the main advantage of the PLD technique in maintaining the stoichiometry of the target material.[144] This achievement triggered a new round of intense research that has led to many significant developments in this field.[142]

In a typical PLD process, an intense laser pulse is focused onto the surface of a target (solid or liquid) installed inside a vacuum chamber. Above a certain threshold power density, the interaction of the laser beam with the target surface results in significant material removal from the target in the form of a luminous plasma plume, which contains ionized atomic and molecular species. This plume then recondenses on a pre-heated substrate installed opposite the target, leading to the formation of a thin film of the material on the substrate.[145–147] The nature and quality of the PLD-grown thin films can be modified by many growth parameters such as material flux, growth (or substrate) temperature, nature of the substrate, nature of the ambient during growth, substrate-to-laser plume distance, and the laser source parameters (wavelength, energy fluence, pulse duration, and repetition rate).[145,147] For example, lasers with an ultrashort pulse duration (picosecond and femtosecond lasers) have been recently used for deposition of thin films with very different characteristics from those films deposited with conventional nanosecond pulsed lasers.[144,148,149] Additionally, it is possible to use different types of background gas (inert or reactive ambient) during the growth process that could affect the ablated species and the surface reactions and thus the chemical composition and properties of the deposited film.[146] Moreover, due to the high ablation rate of the targets, particularly advantageous in the case of high-melting-point materials, and high deposition rate, PLD has become a popular technique for the deposition of high-quality metal oxide thin films.[140,150] Indeed, the great advantage of PLD in preserving the stoichiometry of the target material has made this technique the most widely used method in fabricating DMSO thin films,[42–44,151,152] including HfO_2 ferromagnetic

thin films,[96,98,102,153] where the precise control of the magnetic dopants and oxygen vacancies is crucial.

These additional parameters provided by PLD are especially important in the VLS growth of 1D nanostructures by allowing the fabrication of NWs with various morphology and precisely controlled composition. Various oxide NWs have been synthesized recently using the PLD-based VLS growth method.[140,141,154,155] Of particular interest is the VLS growth of high-melting-point oxides,[63] which are difficult to produce by using other physical vapor deposition techniques. As HfO_2 is also an oxide material with a high melting point and low vapor pressure, a PLD-based approach appears to be the best approach to achieve VLS growth of HfO_2 1D nanostructures. To date, the synthesis of such nanostructures has been hitherto unattainable and the HfO_2 1D nanostructures remain elusive. The present work demonstrates, for the first time, the synthesis of high-quality, single-crystalline HfO_2 nanowires and other low-dimensional nanostructures by the PLD method.

In a typical PLD process, the vapor-solid (VS) mechanism is always competing with the VLS growth mechanism. VS growth corresponds to direct condensation of the solid material from the vapor phase, in contrast to VLS growth, in which the atomic species of the desired material first dissolves into a liquid catalyst from the vapor phase and then precipitates out as a solid phase from the supersaturated liquid phase.[140,156–158] In the case of a NW growth, the VLS growth is, therefore, responsible for the axial growth of the NWs, while the competing VS growth is responsible for the concurrent growth of the nanostructured film at the base of the NWs as well as the lateral growth of the NWs. The final products are NWs, provided that the VLS nucleation and growth rates are higher than those of the VS mechanism so that the VLS mechanism dominates over the VS mechanism. The nucleation and growth rates are proportional to the degree of supersaturation in the vapor phase, which in turn depends on the material supply flux and, for oxide NWs, the oxygen pressure inside the chamber.[156] In the case of a high material flux and a high oxygen pressure, the VLS growth is suppressed and the VS-grown film becomes the final product. For NWs, the material supply flux and the oxygen pressure, therefore, should stay within an optimum range.[156–158] If an oxide target is used to grow oxide NWs, the unintentional oxygen supply from the target can narrow the optimum material flux window so that the synthesis of oxide NWs becomes more challenging.[157] For the pulse laser deposition of HfO_2, an oxide target is typically used to provide better control over the stoichiometry of the final product. Therefore, the optimum material flux range may already be too narrow for the VLS growth of HfO_2 NWs. Moreover, HfO_2 is a hard material requiring a high energy laser pulse for ablation that could increase the material removal and hence the material supply flux.

Consequently, there is always a high likelihood of missing the already narrow optimum flux window, which makes the VLS growth of HfO_2 an extremely difficult task. In this work, we will use a novel technique to overcome these technical challenges. In the next section, we describe our experimental method and the details of the PLD instrumentation used in this study for HfO_2 nanostructure growth.

1.5.2 Experimental Details of PLD Method

Figure 1-11 shows the pulsed laser deposition system (NanoPLD, PVD Products) used in the present work to synthesize undoped and doped HfO_2 and other nanostructures. The system is comprised of a UV pulsed laser source, alignment optics, and a multiport deposition chamber. The laser source is an excimer KrF pulsed laser (Lambda Physik COMPex 205) operating with a wavelength of 248 nm, an energy of 100-600 mJ per pulse and a repetition rate of 5 Hz. During the deposition, the laser beam is aligned and partly focused by the appropriate lenses located between the laser source and the deposition chamber. A rastering mirror is used to direct the focused pulsed laser beam through a fused silica window at the entrance port of the chamber onto the surface of a target. Inside the deposition chamber, there is a six-target planetary carousel to accommodate target pellets, with each target holder rotating around the target axis at an adjustable rotation speed. The target rotation accompanied by rastering of the beam across the target diameter provides a unform ablation of the entire target surface. The substrate holder is used to secure the substrate facing down directly above the target and perpendicular to the laser plume expansion direction. The substrate holder consists of a windowed plate for positioning the substrate and a thermocouple connected to the holder to measure the deposition temperature. Substrates can be heated up to 900 ℃ through thermal radiation provided by an assembly of infrared lamps mounted at the back of the substrate holder. The distance between the target and the substate is adjustable by vertically moving the substrate holder with a linear motion manipulator. Before starting the deposition, the chamber is evacuated by a turbomolecular pump to achieve a base pressure lower than 1×10^{-6} Torr. The process gases (including inert gases such as Ar or N_2 or reactive gases such as O_2 and H_2) can be introduced into the chamber through a variable leak valve with a four-channel mass flow controller (MKS 247D).

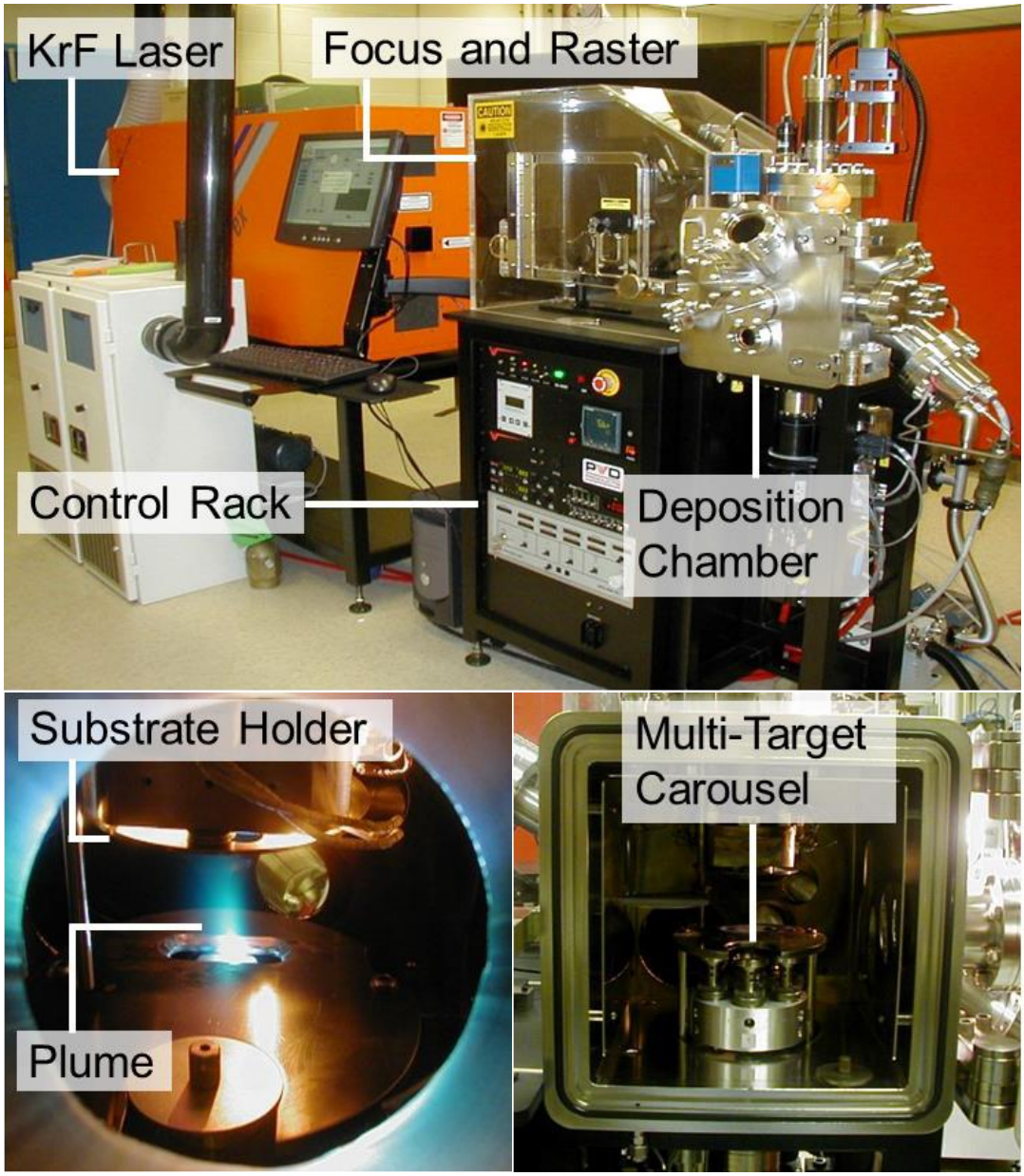

Figure 1-11. Photographs of the PLD system depicting (top) the pulsed KrF excimer laser with the laser gas storage cabinet, the alignment, focusing and rastering optics, the high-vacuum deposition chamber, and the control rack, which includes the electronics for controlling the pumping and substrate heating systems and the flow meter control switches; (bottom left) the ablation laser plume expanding from the target surface upward to the substrate surface secured by the substrate holder plate connected to a thermocouple, and (bottom right) the multi-target planetary carousel and substrate mount assembly inside the deposition chamber.

To investigate the effects of substrate templates on the nanostructural growth in the present work, we prepare three different growth templates. Chemically oxidized Si substates (denoted as Ox-Si), Ox-Si substrates seeded with gold nanoislands (denoted as GNI/Ox-Si), and Ox-Si substrates seeded with Sn-alloyed gold nanoislands (denoted as Sn-GNI/Ox-Si). The Ox-Si growth templates are prepared by RCA cleaning[159] of 10×10 mm^2 and 5×5 mm^2 Si wafers (525 μm thick, p-type, B-doped, with a resistivity of 1-5 Ω cm). The last HF treatment step is omitted in the cleaning procedure in order to maintain the chemically formed oxide layer on the Si surface. The GNI/Ox-Si templates are prepared by magnetron sputtering gold onto the Ox-Si substrates for 4-10 s followed by annealing in oxygen at 600 ℃ for 60 min in a tube oven. For Sn-GNI/Ox-Si templates, we adopt an in-situ technique that incorporates Sn into the GNIs from the vapor phase to obtain Sn-alloyed gold nanoislands (Sn-GNI) during deposition. First, Ox-Si substrates are seeded with GNIs in a similar way as described for GNI/Ox-Si templates. Then the as-prepared GNI/Ox-Si templates are mounted on the sample holder plate, which has been pre-sputter-coated with Sn. When the holder is heated up to the pre-selected temperature (generally above 500 ℃), Sn evaporates off the substrate holder and mixes with the GNIs on the substrate to obtain the Sn-GNI/Ox-Si templates.

HfO_2 and TiO_2 target pellets used for the deposition in the present work are prepared by cold pressing HfO_2 powder (Alfa Aesar, 99.9% purity) and rutile TiO_2 powder (Aldrich, 99.99% purity), respectively, with a pressure of 25-30 MPa followed by sintering at 900-1150 ℃ for 12-48 h in a muffle oven. The Ti-doped and Fe-doped HfO_2 targets are prepared similarly by grinding and mixing TiO_2 (Aldrich, 99.99% purity) and Fe powders (Aldrich, 60-80 nm particle size, ≥99% purity) with HfO_2 powder (Alfa Aesar, 99.9% purity) with the appropriate molar percent proportions determined by the desired doping concentrations. Finally, the doped/undoped HfO_2 and TiO_2 nanostructures are grown on the substrates, which are held at the growth temperature of 550-770 ℃ and a target-to-substrate distance of 25 mm, by ablating the appropriate as-prepared targets with a laser fluence of 350 mJ/pulse and repetition rate of 5 Hz for 60-90 min. More details of the target and substrate preparations can be found in the experimental sections of the relevant chapters, along with additional details about the morphological (SEM), structural (XRD, TEM) and chemical (XPS, AES) characterization of the as-grown nanostructures. Due to the importance of magnetic property measurement in the present work, we specially provide a more detailed discussion in the next section.

1.6 Characterization of Magnetic Properties of Nanostructured Materials

1.6.1 Background and Overview of SQUID Magnetometry

There are numerous experimental techniques with various sensing mechanisms to measure the magnetic fields and magnetic properties of materials. Some of these techniques include magneto-optical-based methods such as the magneto-optic Kerr effect (MOKE),[160] polarized neutron reflectometry (PNR),[161] and synchrotron-radiation-based methods such as X-ray magnetic linear dichroism (XMLD) and circular dichroism (XMCD).[162] Among all different magnetometric methods, superconducting quantum interference device (SQUID) magnetometers are the most accurate instruments for measuring the magnetic flux and SQUID magnetometry has become the most popular method to characterize and study the magnetic properties of low-moment samples including DMS materials.[163,164]

A SQUID sensor operates at cryogenic temperature and it typically consists of a superconducting loop interrupted by one (in an rf SQUID) or two (in a dc SQUID) insulating barriers known as Josephson junctions (Figure 1-12a). The operational principle of a SQUID sensor can be understood based on two quantum-mechanical effects: the Josephson effect and flux quantization in a superconducting loop.[165] The current flowing through a superconducting ring generates a magnetic field threading through the ring (Figure 1-12a). This magnetic field produces a magnetic flux that cannot take on any arbitrary value and its value must be an integer number of a quantity called the flux quantum (ϕ_0), which has an extremely small value ($\phi_0=2.068\times10^{-15}$ Wb).[163,165] Any increasing/decreasing external field applied to the superconducting ring can modify the flowing current leading to the periodic change of the voltage across the Josephson junctions. As the period of this oscillating voltage is equal to one quantum flux (Figure 1-12b), the SQUID can essentially act as a flux-to-voltage transducer, in which a tiny change in the flux signal originating from the sample can produce a corresponding voltage change measurable by conventional electronics.[165] To enhance the sensitivity of the sensor, the magnetic field of the sample is detected by the SQUID sensor indirectly through a flux transformer. As shown in Figure 1-12c, the magnetic field of the sample is inductively picked up by a second-order gradiometer connected to the input coil of the SQUID. The input coil is also inductively coupled into the SQUID loop, so that it delivers the pick-up field to the SQUID loop. The biasing current in the SQUID loop can be either ac (rf SQUID) or dc (dc SQUID). Nearly all commercial SQUIDs are dc SQUIDs due to their lower noise and hence higher sensitivity.[163,164]

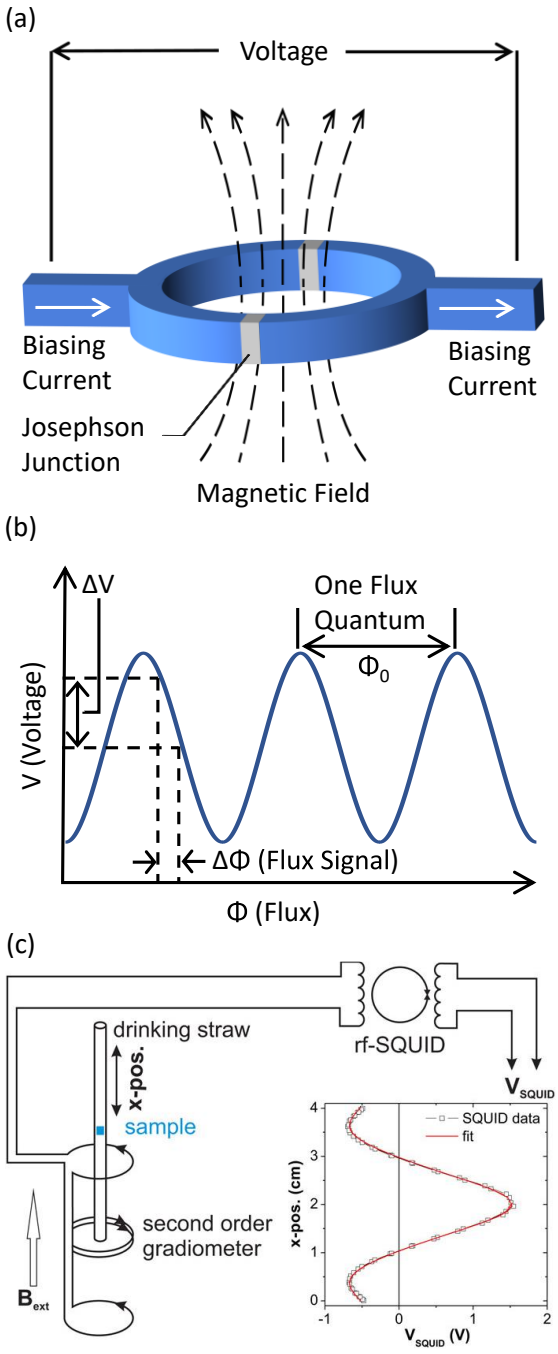

Figure 1-12. The operational principle of a SQUID magnetometer. (a) A SQUID loop with two Josephson junctions and the magnetic field passing through the loop induced by the bias current. (b) Oscillating response of the voltage as a function of the externally applied flux. (c) Schematic setup of a SQUID magnetometer showing the second-order gradiometer, input coil, and the SQUID voltage response vs. sample position (inset). Reproduced with permission from references [164]. Copyright (2018) by AIP Publishing.

1.6.2 Experimental Details of SQUID Magnetometry

The most widely used commercial SQUID magnetometers are manufactured by Quantum Design[166] and they offer excellent sensitivity with a high degree of automation. In the present work, a 7-Tesla Quantum Design Evercool Magnetic Property Measurement System (MPMS 3) equipped with a SQUID sensor is used to characterize the magnetic properties of doped and undoped HfO_2 and other nanostructures. The system can be used to measure the magnetic moments of the samples in a temperature range of 1.8-400 K with a sensitivity of 1×10^{-8} emu. The superconducting magnet and SQUID need to be maintained in cryogenic condition using liquid helium, which is provided by an integrated pulse-tube cryocooler-dewar system. Helium is also used to cool down the sample tube and to vent the tube when exchanging the sample. A sample must be smaller than 5×5 mm^2 in order to physically fit into the bore of the sample tube and it needs to be appropriately positioned so that it stays within the homogenous part of the magnetic field while being vibrated during measurement. A photograph of the MPMS 3 vibrating sample magnetometer (VSM) system used for magnetic characterization of the samples in this work is shown in Figure 1-13.

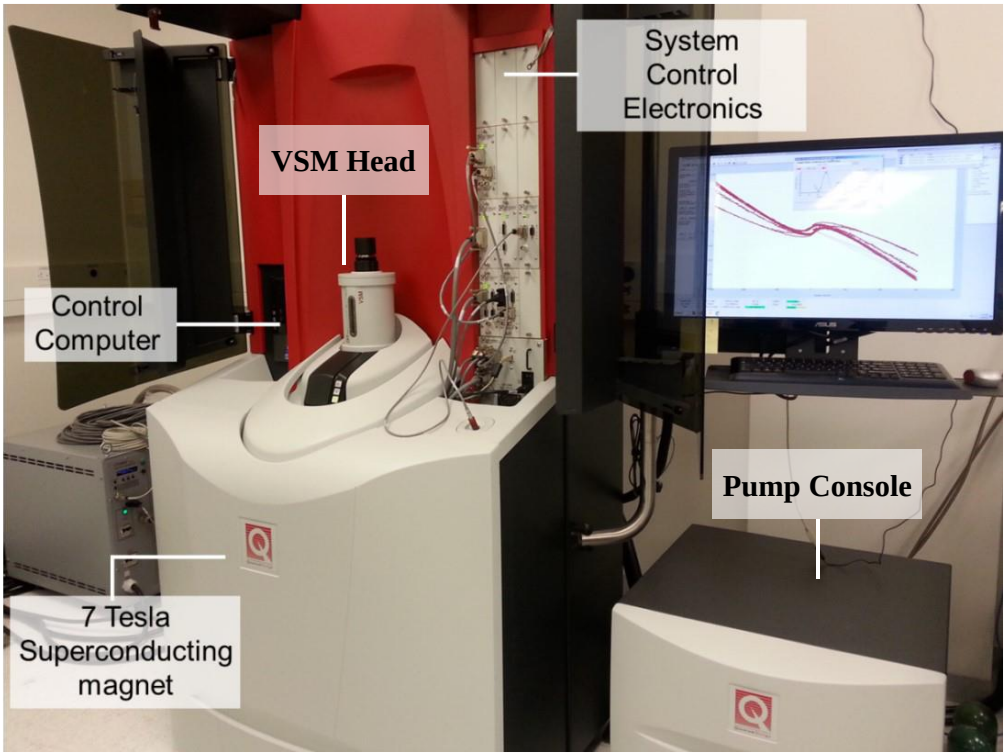

Figure 1-13 Photograph of the Quantum Design MPMS 3 SQUID Vibrating Sample Magnetometer with Evercool technology.

For magnetic measurements, nanostructures are grown appropriately on a 5×5 mm^2 substrate, which is mounted on a quartz paddle using a small drop of special glue. Great care is exercised in preparing and handling the sample, and only plastic tweezers are used to avoid any possible magnetic cross-contamination. Due to the much smaller mass of the as-grown nanostructures compared to that of the Si substate and the quartz sample holder, the magnetic signal of the nanostructures is masked by a massive diamagnetic signal. The diamagnetic background signal is therefore subtracted from the acquired signal to obtain the true magnetic response of the nanostructures. The as-obtained magnetic response is then normalized by the mass of the nanostructures. Assuming that the nanostructures form a densely packed film on the substrate, we estimate their mass by dividing the volume of the nanostructured film by the appropriate bulk densities of HfO_2, $HfTiO_4$ and TiO_2. Sigmoid basis functions and hyperbolic functions are then employed to curve-fit the resulting data points to the hysteresis loops using Hystlab version 1.0.9 software, which is a MATLAB-based software for processing magnetic data based on the correction methods of Jackson et al. and Paterson et al.[167,168]

1.7 Scope of the Thesis

The discovery of spintronic effects in the late 1980s has hitherto led to the developments of many novel devices with great impact on our daily life, such as hard-disk drives read heads and magnetic random access memories.[3,20,22] The main characteristic of these spintronic-based devices that has led to their superb performance is their capability in controlling the electrical current using the electron spin.[3] Spin manipulation of electrical current, if properly exploited in conventional charge-based electronics, can also provide new opportunities in fabricating more compact electronic devices with greater capabilities and performance such as nonvolatility, higher data processing speed, and lower power consumption.[21] For this reason, the integration of spintronic devices with mainstream semiconductor-based electronics has continued to be of great interest. A key step in realizing this idea is the development of new ferromagnetic semiconductors with high compatibility with the mainstream semiconductor-based electronic industry. In the quest for these next-generation advanced materials, dilute magnetic semiconductors (DMSs) based on III-V semiconductors such as (Ga,Mn)As DMSs, have been developed since the 1990s. Despite an attainable record of 200 K,[40] the Curie temperature (T_c) of these III-V DMSs has never reached room temperature, making them unfavorable for real-life device applications. The other class of DMSs that offers greater promise for practical device applications are wide-bandgap oxides doped with magnetic ions known as dilute magnetic semiconducting oxides (DMSOs). These materials exhibit not only excellent ferromagnetic properties but also Curie temperatures well above room temperature (up to 850-930 K[44]). Among DMSOs, HfO_2 has the most compatibility with semiconductor-based electronics owing to its extensive application in CMOS technology as gate dielectrics of metal-oxide-semiconductor field-effect transistors.[70] Moreover, HfO_2 has found many other applications in electronics and optics due to its technologically important properties such as high dielectric constant (κ~25), wide bandgap (~5.7 eV), high refractive index (n=2.9), and excellent thermal and chemical stability. For these reasons, the fabrication of ferromagnetic HfO_2 nanostructural materials and the investigation of their magnetic properties are of particular interest and they promise to be the essential step toward the integration of spintronics with conventional semiconductor-based electronics. As discussed in 1.2.2, structural defects, in particular oxygen vacancies, are generally believed to be the origin of ferromagnetism in DMSOs, including HfO_2 thin films and nanoparticles. Compared to thin films, HfO_2 nanostructures, especially VLS-grown 1D nanostructures, are expected to exhibit enhanced ferromagnetic properties due to their high specific surface area, which could offer more surface defects and oxygen vacancies. Enhanced ferromagnetic properties as a result of high specific surface area have already been observed in ZrO_2 nanowires[63] and nanocrystals,[64] both with very similar

crystal structures and chemistries to HfO_2. Moreover, VLS-grown 1D HfO_2 nanostructures could potentially exhibit novel charge transport and magnetoresistance properties because of their high crystalline quality and size-dependent quantum confinement induced effect. In addition, the exact nature of the structural defects inducing ferromagnetism in HfO_2 is still under intense debate. Although many studies attribute the origin of ferromagnetism in HfO_2 to oxygen vacancies, there is no direct evidence, such as surface-sensitive depth profile studies, to support those claims. VLS-grown 1D HfO_2 nanostructures (nanowires, nanospikes) provide an ideal testbed for such oxygen vacancy-induced ferromagnetism studies, because the high crystalline quality of the VLS-grown 1D nanostructures could minimize the effect of other structural defects. To date, the synthesis of single-crystalline HfO_2 1D nanostructures is an extremely challenging task due to the inherent technical difficulties and has hitherto remained unattainable. In this work, we report the first successful growth of HfO_2 1D nanostructures using PLD-based VLS-growth with the aid of Sn-alloyed gold nanoisland (Sn-GNI) catalysts.

In the present work, we pursue three main objectives: (a) To develop a fundamental understanding of how growth parameters, including growth temperature, growth templates (Ox-Si, GNI/Ox-Si, and Sn-GNI/Ox-Si), and the concentration of the doping elements, can affect the morphological and structural properties of HfO_2 nanostructures through the interplay of the underlying growth mechanisms (vapor-liquid-solid versus vapor-solid mechanisms); (b) To develop a better understanding of the role of oxygen vacancies in generating room-temperature ferromagnetism in HfO_2 by investigating the magnetic properties of single-crystalline VLS-grown HfO_2 nanostructures; and (c) To enhance the ferromagnetic properties of HfO_2 nanostructured films appropriate for spintronic applications by synthesis of high-surface-area morphologies (1D nanostructures) and by doping with magnetic and nonmagnetic ions.

In the present chapter of this thesis (Chapter 1), we provide a brief introduction to dilute magnetic semiconductors and dilute magnetic semiconducting oxides as promising spintronic materials, particularly the key models used to explain their ferromagnetic properties. We also give a review of the HfO_2 nanostructures and the primary techniques used for their synthesis and characterization. Our results for undoped and doped HfO_2 nanostructures are given in two chapters. In Chapter 2, we report the growth of multiple HfO_2 nanostructures using a catalyst-assisted pulse laser deposition method. By precisely controlling the laser radiation parameters, background vacuum pressure, Ar flow and pressure during the deposition and the GNI size, and by manipulating the growth temperature and growth template (Ox-Si, GNI/Ox-Si, Sn-GNI/Ox-Si), we are able to obtain HfO_2 nano square

pyramids on Ox-Si (without any catalyst) and GNI/Ox-Si, nano triangular pyramids on GNI/Ox-Si, nano-tetrahedrons, nano-columns, nanospikes and nanowires, all on Sn-GNI/Ox-Si. The HfO_2 1D nanostructures produced in this study (nano-columns, nanospikes and nanowires) are found to be single-crystalline. This is a significant result because they represent the first single-crystalline HfO_2 1D nanostructures ever reported. Our results show that Sn plays a crucial role in the interplay between VLS and VS growth mechanisms, and no 1D nanostructure can be obtained without Sn. The as-grown HfO_2 1D nanostructures with high crystalline quality provide an ideal platform for oxygen vacancy-induced ferromagnetism studies. When comparing the magnetic properties of HfO_2 nanowires (NWs) and square nano pyramids, we observe room-temperature ferromagnetism in HfO_2 NWs, and very weak paramagnetism in HfO_2 square nano pyramids. Our XPS depth-profiling studies confirm that the origin of ferromagnetism in HfO_2 NWs is likely due to the higher amount of oxygen vacancies in NWs compared to the square nano pyramids.

According to theoretical studies,[169,170] oxygen vacancy formation energy is lower in Ti-doped HfO_2. In order to establish a direct correlation between the amount of oxygen vacancies and ferromagnetic properties of HfO_2 in the first study, we investigate the effect of doping of Ti (a non-magnetic element) on the morphological, structural and magnetic properties of HfO_2 nanostructures in Chapter 3. In the first part of our study on doped HfO_2 nanostructures, we report the synthesis of Ti-doped $Hf_{1-x}Ti_xO_2$ (x=0.01, 0.10, 0.25, 0.50) 1D nanostructures on the Sn-GNI/Ox-Si growth template for the first time, by using the same catalyst-assisted PLD method. Our results show that Ti-doping does not prevent VLS growth and it leads to 1D nanostructures (nanospikes) for all doping concentrations from lightly doped $Hf_{0.99}Ti_{0.01}O_2$ (x=0.01) nanospikes to bimetallic oxide $Hf_{0.50}Ti_{0.50}O_2$ (x=0.50) nanospikes. We observe an increase in room-temperature magnetic saturation of HfO_2 nanostructures up to 92% for the doping concentration of 10 at. % (x=0.10). However, at higher doping concentrations (x=0.25 and 0.50), the magnetic saturation values become smaller, and that for bimetallic oxide nanostructures (x=0.50) is even smaller than undoped HfO_2 NWs. In the second part of Chapter 3, we present the results from our study on the effect of doping of Fe (a magnetic element) on HfO_2 nanostructures. This study allows us to compare the effects of a magnetic dopant (Fe ion) to those of a nonmagnetic dopant (Ti ion) on the morphological, structural and magnetic properties of HfO_2 nanostructures. Unlike Ti-doping, Fe-doping is found to significantly suppress VLS growth of HfO_2 nanostructures, producing nanospikes for 1 at. % Fe doping ($Hf_{0.99}Fe_{0.01}O_2$ nanospikes) and distorted nanocubes with stacked flake structures for 5 at. % ($Hf_{0.95}Fe_{0.05}O_2$), 10 at. % ($Hf_{0.90}Fe_{0.10}O_2$), and 20 at. % ($Hf_{0.80}Fe_{0.20}O_2$) Fe doping. The abrupt diminution of VLS growth with Fe is attributed to the counter-effect of Fe on the VLS nucleation rate that could negate the positive effect of Sn in

promoting VLS growth. When doping a nonmagnetic material such as HfO_2 with magnetic ions, obtaining a uniform distribution of magnetic ions in the host lattice is challenging. A nonuniform doping results in magnetic ion clustering that could produce extrinsic magnetic properties. Our magnetic property measurements indicate that Fe-doped HfO_2 nanostructures exhibit an intrinsic ferromagnetic response for doping concentration up to 10 at. %. However, for HfO_2 nanostructures doped with 20 at. % Fe, the magnetic response is mainly dominated by an extrinsic component, despite the lack of any magnetic clusters found in the corresponding XRD result. Moreover, we find that HfO_2 nanostructures doped with 5 at. % and 10 at. % Fe show much higher (up to two orders of magnitude) magnetic saturation values than the undoped HfO_2 nanostructures. These high M_s values are attributed to the exchange interaction between ferromagnetic centers (F-centers) created by the oxygen vacancies induced by the magnetic ions throughout the lattice.

The present work seeks to provide new insights for the synthesis of ferromagnetic semiconductor NWs, particularly oxide NWs. For those oxide nanowire growth processes that require an oxide target in order to have precise control over the stoichiometry of the final products, the use of an alloy catalyst could counterbalance the adverse effect of oxygen in promoting the VS growth and significantly facilitate the VLS growth of the nanowires. The ferromagnetic HfO_2 nanostructures introduced in this work, especially $Hf_{0.95}Fe_{0.05}O_2$ and $Hf_{0.90}Fe_{0.10}O_2$ nanostructures with high magnetic saturation values, can be promising materials for spintronic applications such as magnetic tunneling junctions, spin transistors, and spin-based logic circuits. Their high Curie temperatures provide viable opportunities for real-life device application. More importantly, considering the CMOS compatibility of HfO_2, these nanostructures have great potential for application in integrated CMOS and spintronic technology. These and other perspectives, along with future work, will be discussed in Chapter 4.

Chapter 2
Synthesis of Novel Single-Crystalline HfO_2 Nanostructures and Their Magnetic Properties

2.1 Introduction

Over the last two decades, hafnium dioxide (HfO_2), also commonly known as Hafnia, has been subjected to numerous investigations owing to its technologically interesting properties such as large dielectric constant ($\kappa \approx 25$), wide bandgap (~5.7 eV), high refractive index (2.9), high laser-induced damage threshold, and excellent thermal and chemical stability.[70–75] These superior properties have made HfO_2 an excellent advanced material candidate for a broad range of applications. For instance, many studies have shown that HfO_2, due to its large dielectric constant, can be used as gate dielectric to greatly suppress current leakage in metal-oxide-semiconductor field effect transistors, providing a significant breakthrough in the miniaturization of modern devices.[70,171–173] Other applications include anti-reflective and protective optical coatings,[87–90] ferroelectric field effect transistors,[84,85]memristors and resistive random access memories[91–94], and gas sensors.[95] Furthermore, it has been found that oxygen-deficient HfO_2 thin films and nanostructures can also serve as dilute magnetic semiconductors exhibiting ferromagnetism above room temperature.[96,98,152,174,175] Considering the high compatibility of HfO_2 with CMOS technology, high temperature ferromagnetism in HfO_2 is indeed a significant discovery, which promises to further extend the application of HfO_2 to the field of spintronics.[27,97]

Numerous studies have demonstrated the novel properties of semiconductor nanowires (NWs) stemming from their nanoscale dimension, high surface area-to-volume ratio, and single-crystalline structures with highly crystalline facets.[126,127,140] These unique properties have made semiconductor NWs very promising candidates for various applications ranging from electronic and optoelectronic devices to spintronic and renewable energy applications.[127] For example, defect-rich NWs of ZrO_2, a material with a very similar crystal structure and physical properties to HfO_2, have shown super-efficient performance in photocatalytic water splitting[176] as well as remarkable dilute ferromagnetic semiconductor properties.[63] It is therefore expected that HfO_2 NWs could also exhibit similar novel properties, including photocatalytic and ferromagnetic properties, superior to their HfO_2 thin film counterparts. To date, there have, however, been very few attempts to synthesize HfO_2 one-dimensional (1D) nanostructures.[75,119,120,122–124] Some of these attempts are based on electrospinning to fabricate HfO_2 nanobelts,[123] nanofibers,[124] and hollow nanofibers.[75] In other reports, electrochemical

anodization of metallic Hf foils in basic solutions[119,120] and atomic layer deposition of HfO_2 into anodic aluminum oxide templates[122] are used to synthesize HfO_2 nanotubes. However, all these methods are based on wet chemistry that may introduce cross-contamination of chemical impurities and, in some cases, they yield agglomerated products. Moreover, the products of these synthesis methods if performed without any subsequent heat treatment are amorphous or polycrystalline. While the single-crystalline structure and the high level of crystallinity play pivotal roles in producing superior physical properties in semiconductor NWs, none of the aforementioned methods has yet to produce single-crystalline HfO_2 1D nanostructures. For synthesizing high-quality single-crystalline NWs, vapor-liquid-solid (VLS) growth is well-known to be a very advantageous method with good control on the size and shape of the NWs.[125–127] To date, VLS growth of single-crystalline HfO_2 NWs remains unattainable and a very challenging task indeed.

Chemical vapor deposition, thermal evaporation, and pulsed laser deposition (PLD) are three possible synthesis methods to grow HfO_2 nanowires through the VLS mechanism. However, due to the extremely low vapor pressure and the high melting point of hafnia, synthesis of HfO_2 NWs by conventional CVD or thermal evaporation methods is not feasible. The PLD method therefore appears to be the best approach to produce VLS-grown HfO_2 NWs. Nevertheless, the PLD growth of metal oxide NWs, particularly HfO_2, could pose great fundamental challenges. As discussed by Suzuki et al.,[156] VLS and vapor-solid (VS) growth can occur concurrently in PLD-growth systems. If the VLS nucleation and growth rates outpace the VS nucleation and growth rates in the system, NWs will become the final products. VLS and VS nucleation rates are reported to greatly depend on the equilibrium pressure of the atomic species, which is associated with the supply flux of atomic species ablated from the target and the partial pressure of oxygen in the system. Increasing the supply material flux and oxygen pressure in the system would significantly suppress the VLS nucleation rate, leading to the growth of simple films as the final product. Based on their model, they have later introduced a concept called “material flux window” that can provide a practically useful criterion to predict the growth process in those systems with concurrent VLS and VS growth.[157,158] A material flux window is defined as an optimum range of supply material flux density within which the VLS growth mechanism outruns the competing VS mechanism. When a material flux density is below the lower extreme of the material flux window, neither VLS nor VS growth could occur. On the other hand, a flux density higher than the upper extreme of the window would lead to a predominant VS mechanism. The width of this optimum material flux window varies with the growth temperature and the oxygen pressure in the system, and it becomes narrower when the temperature and the amount of oxygen increase. For PLD growth of HfO_2, a HfO_2 target is commonly used to provide better control

on the stoichiometry of the final products. As pointed out by Klamchuen et al.,[157] metal oxide targets could introduce unintentional oxygen into the system so that the oxygen pressure could become high enough to significantly suppress the VLS nucleation rate. In other words, for VLS growth of HfO_2 by PLD, the width of the optimum material flux window for VLS growth is inherently narrow due to the oxygen generated by the target during laser ablation. Furthermore, HfO_2 is a hard material requiring a relatively high laser power for ablation. This high laser energy could provide a large material supply flux into the system, thus increasing the likelihood of missing the already narrowed optimum material flux window for VLS growth. Accomplishing VLS growth of HfO_2 NWs by PLD has thus far been unsuccessful and it remains an incredibly difficult if not impossible task.

As there is not enough control to adjust the material supply flux and the amount of oxygen originating from the target for VLS growth of HfO_2 NWs, we devise a different approach to enhance VLS growth against VS growth in the system. Considering the crucial role of the metal catalyst in controlling the VLS growth of NWs, we employ with the strategy of enhancing the VLS growth kinetics by modifying the gold catalyst. Earlier studies have shown that bimetallic catalysts could further improve the VLS growth of NWs.[177–180] Alloying gold with another metallic component could therefore be an effective strategy to promote the VLS growth mechanism. Among the obvious options (e.g., Sn, Ag, Mo, Hg, Pt, Cd), Tin (Sn) appears to be an effective modifying component. According to the Au-Sn binary phase diagram, Sn can create an eutectic composition with gold and significantly lower the gold melting point.[181] Furthermore, other studies have reported that when Sn is alloyed with other metals, such as silver, copper, zinc and gold, it can substantially modify the surface energy of these metals.[182–185] In this work, single-crystalline HfO_2 nanowires are fabricated, for the first time, by using a catalyst-assisted pulsed laser deposition technique. Here, Au-Sn alloys are used as the catalyst to enhance the axial VLS growth of NWs in competition with VS growth of HfO_2 nanocrystals. In this chapter, we first present a study of the structural properties of the as-grown nanostructures, followed by a discussion on the role of Sn as a VLS growth promoter. Based on the information obtained from different materials characterization investigations, we propose a plausible growth mechanism for the HfO_2 NWs. Lastly, we discuss the observed novel ferromagnetic properties of the HfO_2 nanostructures grown under different growth conditions.

2.2 Experimental Details

HfO_2 nanostructures are synthesized by catalyst-assisted pulsed laser deposition using a NanoPLD system (PVD Products) with a base pressure of 1×10^{-6} Torr. The system is equipped with an excimer KrF laser (248 nm wavelength) operated with a laser fluence of 350 mJ/pulse at a repetition rate of 5

Hz to ablate a HfO_2 target. The HfO_2 target is prepared by cold pressing of HfO_2 powder (Alfa Aesar, 99.9% purity) with a pressure of 30 MPa followed by sintering at 1150 °C for 48 h. Prior to the deposition, precut Si(100) chips (10×10 mm^2 and 5×5 mm^2, 525 μm thick, p-type, B-doped, with a resistivity of 1-5 Ω cm) are cleaned and chemically oxidized by following the RCA method.[159] To maintain an oxygen buffer layer on Si, the last cleaning step, i.e. HF treatment, is not performed. Chemically oxidized Si substrates are denoted as Ox-Si in this work. Gold nanoislands (GNIs) on Si are created by magnetron sputtering of a thin layer of gold (<10 nm thick) on Si followed by post-annealing in oxygen at 600 °C for 1 h. After annealing, GNIs with a Gaussian size distribution of 4-10 nm are produced on the Ox-Si surface. This resulting template (denoted as GNI/Ox-Si) is mounted in the PLD chamber using a windowed substrate holder and is oriented perpendicular to the expansion direction of the laser plume. The substrate-to-target distance is set to 25 mm to allow the substrate to be in close proximity to the laser plume. Infrared heat lamps located at the backside of the sample holder provide radiative heating to achieve different growth temperatures (from 550 °C to 770 °C). After reaching the predetermined growth temperature, deposition is initiated, and it continues for 60 min in 200 mTorr of Ar with a flow rate of 10 sccm. To introduce Sn into the system, we sputter-coated the windowed substrate holder with Sn prior to mounting it in the deposition chamber. The Sn target used for sputter coating is cut out of a Sn sheet (99.9% purity, Fisher Scientific). When the substate holder is heated by the infrared lamps, Sn is expected to evaporate and mix with the gold nanoislands to create the Au-Sn alloy catalysts. The growth templates prepared with these Sn-alloyed GNI catalysts are denoted as Sn-GNI/Ox-Si.

The morphologies of the nanostructures are studied by scanning electron microscopy (SEM) in a Zeiss Ultra-plus field-emission scanning electron microscope. The corresponding crystal structures are determined by glancing-incidence X-ray diffraction (GIXRD) at an incident angle of ω=0.4° in a PANalytical MRD X'pert Pro diffractometer with a Cu Kα source (1.54 Å). The composition and crystallinity of the individual HfO_2 NWs are examined by transmission electron microscopy (TEM) in a Zeiss Libra 200MC transmission electron microscope equipped with energy dispersive X-ray spectroscopy (EDS) at an acceleration voltage of 200 kV. For TEM sample preparation, HfO_2 nanostructures are scraped off the substate and dispersed in HPLC-grade isopropyl alcohol by sonication for 10 min, and are transferred by drop-casting the resulting suspension onto a copper TEM grid.

Using the information from XRD and TEM analyses, we also obtain the corresponding optimized unit cell by performing first-principle calculations based on the Density Functional Theory (DFT).

This optimized unit cell is used to build schematic crystal models of HfO2 NWs. DFT calculations are carried out by using the Vienna Ab-initio Simulation Package (VASP, version 5.4) with the Materials Exploration and Design Analysis platform (MedeA, version 2.19, Materials Design, Inc.). In particular, the electron-ion interaction is described by using the projector augmented wave (PAW) method.[186,187] The exchange-correlation energy is approximated by the generalized gradient approximation (GGA) using the Perdew-Burke-Ernzerhof (PBE) functional.[188] The cutoff energy for the convergence of the plane wave expansion is set at 400 eV. The atom positions are relaxed until the forces on all of the atoms were less than 0.05 eV/Å, while the energy convergence of the self-consistent field is set to 1.0×10-5 eV. For Brillion zone sampling, the Γ point with a k-point spacing of 0.5 Å-1 is selected with a 3×3×3 mesh. The ionic geometry is optimized by using the conjugate-gradient algorithm. A unit cell containing four Hf atoms and eight O atoms with the monoclinic structure is used to model the HfO2 crystal structure. Finally, the optimized unit cell and crystal models of the NWs are visualized by using the 3D visualization program VESTA.

The chemical-state composition of the HfO_2 nanostructures is analyzed by X-ray photoelectron spectroscopy (XPS) performed in a Thermo-VG Scientific ESCALab 250 Microprobe with a monochromatic Al Kα X-ray source (1486.6 eV photon energy). For depth profiling, the sample surface is sputtered by an Ar^+ ion beam with a kinetic energy of 3 kV, while a low-energy electron flood gun operated at a filament current of 1.75 mA is used for charge compensation. To examine the chemical-state composition of individual HfO_2 NWs, we employ electron-induced Auger electron spectroscopy (AES), with a considerably higher spatial resolution than XPS (20 nm for AES vs. 3 μm for XPS), in a Thermo-VG Scientific Microlab 350 Microprobe equipped with a built-in field-emission electron source. An electron beam with an energy of 10 kV is focused with an estimated spot size of less than 10 nm on the individual nanowires, and the emitted Auger electrons are detected by a hemispherical energy analyzer. For AES-depth profiling, an Ar^+ ion beam with an energy of 3 kV is rastered over a 2×2 mm^2 area generating a sample current density of 1 $\mu A/mm^2$.

The magnetic property of the HfO_2 nanostructures is studied at different temperatures by using a superconducting quantum interference device (SQUID) magnetometer (Quantum Design MPMS SQUID-VSM). The magnetic field used to induce magnetic moment in the samples is applied parallel to the sample surface. Only plastic tweezers and clean quartz paddles are used for sample preparation and measurement to eliminate any possible ferromagnetic cross-contamination. The magnetic data are corrected by subtracting the diamagnetic contribution from the bare substrate and quartz paddle. The recorded magnetic moments of the nanostructures are normalized by their mass, which is calculated

by assuming that the nanostructures are densely packed within the measured volume with a bulk density of 9.68 g/cm^3.[189] The ferromagnetic hysteresis loops are fitted to the data points by using sigmoid basis functions and hyperbolic functions in Hystlab version 1.0.9 software. Hystlab is a MATLAB-based software for processing magnetic data based on the correction methods of Jackson et al. and Paterson et al.[167,168]

2.3 Results and Discussion

2.3.1 SEM and XRD Studies

Figure 2-1a1-a4 shows the SEM images of a typical HfO_2 film deposited by PLD on Ox-Si without any GNI catalyst in 200 mTorr of Ar at different temperatures: 550 °C, 650 °C, 720 °C and 770 °C, respectively. At 550 °C (Figure 2-1a1), a nanostructured film consisting of distorted square pyramid shaped crystals with rough facets is observed. As the growth temperature increases to 770 °C and consequently causes greater diffusion of the atoms on the surface, the nanostructured film is found to consist of well-faceted square pyramid shaped crystallites with an average grain size of 40 nm (Figure 2-1a4). The growth of ordered crystals with similar shapes and crystal facets indicates that there is a preferential growth crystallographic orientation for HfO_2 even without any catalyst or initial seed layer on the Ox-Si surface. When the deposition is performed on GNI/Ox-Si (Figure 2-1b1-b4), the grain size of the nanostructures becomes discernibly larger. This trend is more notable for those nanostructures grown at 650 °C and 720 °C. As reported in an earlier study,[140] formation of the coarser nanostructures on the GNI-seeded substrate can be attributed to the GNIs providing more favorable nucleation sites. The initial nuclei appearing on the GNIs then start to grow through the vapor-solid (VS) mechanism in some preferential crystallographic directions. However, the most notable observation by comparing Figure 2-1a1-a4 with Figure 2-1b1-b4 is the very similar morphology of the as-formed nanostructures. This similarity suggests that the prominent growth mechanism of HfO_2 on Si substates both without and with GNIs (Ox-Si and GNI/Ox-Si) is VS growth with no evidence of any VLS growth. One possible reason for the lack of VLS growth could be the chemical bonding of GNIs to the Si surface as discussed in a previous study[140] on growth of tin oxide NWs on a hydrogen-terminated Si. The presence of this chemical bonding in effect deactivates the catalyst, preventing VLS growth of the nanostructures. However, the Ox-Si surface here includes a 6 nm thick oxygen layer, which serves as a buffer layer preventing chemical interaction between the GNIs and the Si surface. Therefore, the lack of VLS growth, in this case, could instead be attributed

to the much higher rate of nucleation and growth through the VS mechanism that overwhelmingly outpaces the VLS growth.

Figure 2-1c1-c4 shows the morphology of HfO_2 nanostructures grown at the same series of increasing temperature (550 °C, 650 °C, 720 °C and 770 °C) on Ox-Si substrates with tin-modified GNIs as the catalysts (Sn-GNI/Ox-Si). Evidently, at the lower growth temperature of 550 °C (Figure 3-1c1), considerably larger tetrahedral shaped crystals (nano-tetrahedrons with 300-500 nm edge lengths) are formed, along with fine crystallites similar to those found for the GNI/Ox-Si substrate. The formation of these large crystals might be caused by the emergence of concomitant VLS growth promoted in the presence of Sn-GNIs. During the initial stages of nucleation and growth, both VLS and VS mechanisms contribute to the growth process, giving rise to the coarser final crystals on GNI nucleation sites. This kind of crystal coarsening has also been observed in a previous study.[140] As the growth temperature increases, the morphology of the nanostructures changes significantly, from nano-tetrahedrons at 550 °C to nano-columns with a triangular cross section at 650 °C, and finally to long tapered nanowires at 770 °C. HfO_2 nanospikes and NWs grown at higher temperatures (Figure 2-1c3 and Figure 2-1c4) also appear to have a triangular cross section with an edge size of 100-150 nm near the base and about 20 nm near the tip. The NWs grown at 770 °C are evidently longer (with an average length of 2.5 μm) than the nanospikes grown at 720 °C (with an average length of 1.5 μm). Furthermore, the lateral faces of the NWs do not appear to be smooth but contain some fine features, which will be discussed in more detail in the TEM analysis section below. Gold nanoparticles at the tips of the NWs (marked with circles in Figure 2-1c3 and Figure 2-1c4) are typically found in catalyst-assisted PLD growth of 1D nanostructures,[63,140,141] and their presence clearly confirms the VLS growth mechanism of these HfO_2 1D nanostructures. Results from energy-dispersive X-ray spectroscopy collected in scanning TEM analysis and high-resolution TEM images (discussed below) show no evidence of catalyst consumption due to incorporation of the catalyst into the crystal structure of the NWs. The observed tapering of the NWs can be explained by the coexistence of both VS and VLS mechanisms. While the VLS mechanism controls the longitudinal growth of the NWs, the lateral growth of the NWs occurs due to the VS growth of the initial crystal planes already emerged out of the catalyst in the VLS mechanism. Since the base of a NW is exposed to the material vapor for a longer time, its cross section usually becomes larger than the cross section near the tip. Furthermore, nanocrystals similar to those nanostructures grown in the absence of Sn are still visible among the 1D nanostructures (Figure 2-1c2-c4). This observation further supports that the VLS growth and VS growth occur concurrently in our system.

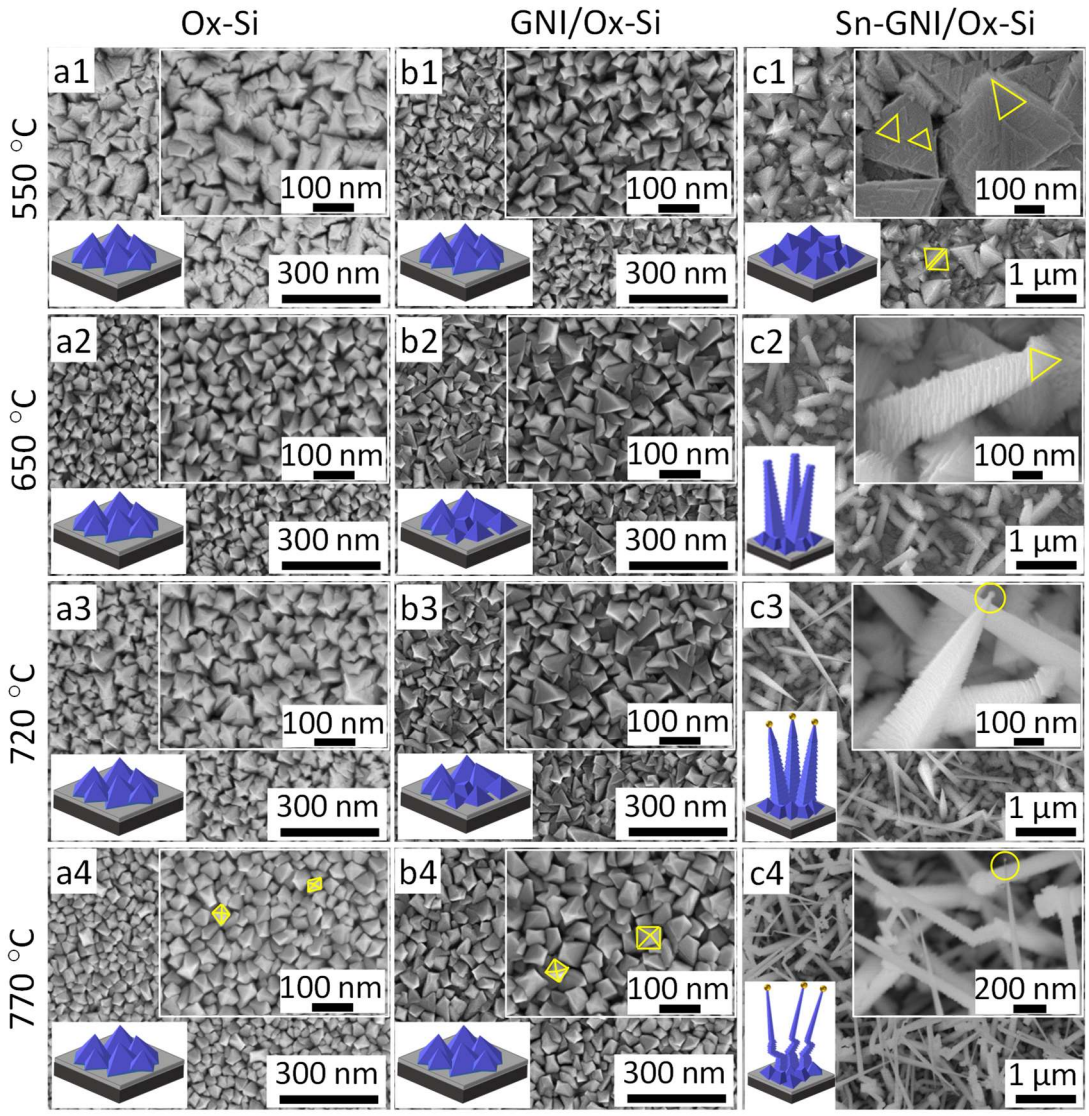

Figure 2-1. SEM images of (a1-a4) HfO_2 nano square pyramids on Ox-Si (without any catalyst), (b1-b4) HfO_2 nano square pyramids and nano triangular pyramids on GNI/Ox-Si, and (c1) nano-tetrahedrons, (c2) nano-columns (with triangular base), (c3) nanospikes, and (c4) nanowires, all on Sn-GNI/Ox-Si, PLD-grown at (a1, b1, c1) 550 °C, (a2, b2, c2) 650 °C, (a3, b3, c3) 720 °C, and (a4, b4, c4, d4) 770 °C. The upper right insets show expanded views, while the lower left insets show pictorial models of the respective as-grown nanostructures.

The dramatic change in the morphology of the nanostructures from 3D nanocrystals to 1D nanospikes and nanowires (Figure 2-1c1-c4) suggests that the VLS mechanism is enhanced by increasing the growth temperature on the Sn-GNI/Ox-Si substrates. By contrast, this trend is not observed for the nanostructures grown on GNI/Ox-Si substrates (Figure 2-1b1-b4). As we introduce Sn into the system by thermal evaporation from the surface of a Sn-coated sample holder, more Sn is therefore expected to be evaporated at a higher temperature. Since VLS growth does not occur with GNIs without Sn at any temperature while it is enhanced when the amount of Sn in the system is increased, Sn appears therefore to be the crucial determinant of promoting VLS growth in our system. In section 2.3.4, we will discuss the possible role of Sn in enhancing the VLS growth mechanism in more detail.

The corresponding glancing-incidence XRD (GIXRD) patterns of the nanostructures obtained under different growth conditions are shown in Figure 2-2. Since the GIXRD patterns of the HfO_2 nanopyramids grown on Ox-Si and GNI/Ox-Si templates at lower temperatures (Figure 2-1a1-a3 and Figure 2-1b1-b3) are similar to the ones grown at 770 ℃ on the respective templates, we only show the GIXRD patterns of the HfO_2 nanopyramids grown on GNI/Ox-Si and Ox-Si templates at 770℃ here. The GIXRD patterns reveal that all the nanostructures predominantly exhibit the monoclinic phase with no sign of tetragonal or cubic phase. Moreover, despite the nanometer size of the synthesized nanostructures, they all show very sharp peaks with small peak widths, which is indicative of a high level of crystallinity in these nanostructures. Previous studies have shown that the presence of oxygen vacancies could stabilize the tetragonal or cubic phase in HfO_2.[190–192] The absence of any secondary phase therefore indicates minimal oxygen deficiency in the bulk structures, or alternatively that accumulation of the oxygen vacancies occurs mostly in the surface region.

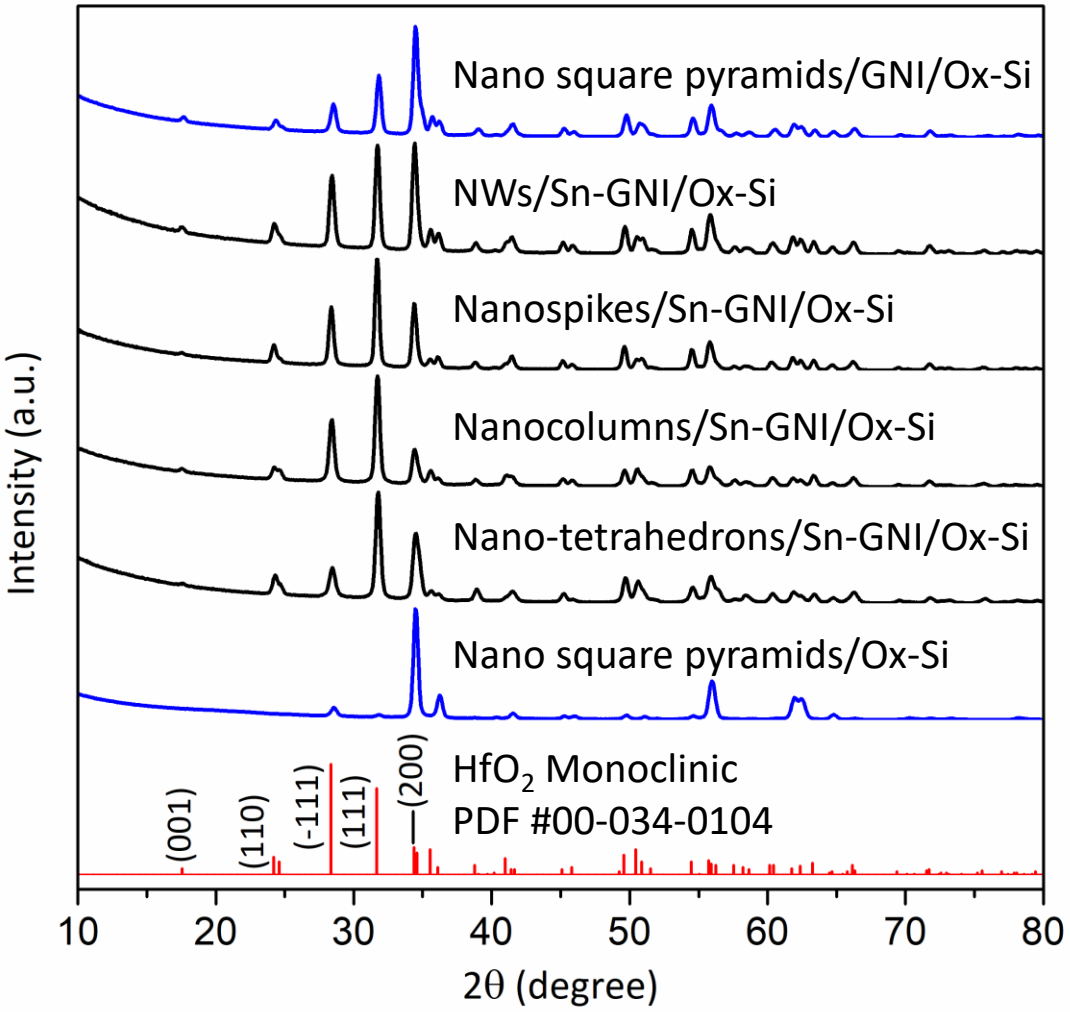

Figure 2-2. Glancing incidence XRD patterns of different HfO_2 nanostructures grown under the following conditions: nano square pyramids on Ox-Si (bottom) and GNI/Ox-Si templates (top) both at 770 ℃, and (from top to bottom) nanowires (NWs) at 770 ℃, nanospikes at 720 ℃, nanocolumns at 650 ℃, and nano-tetrahedrons at 550 ℃ all on Sn-GNI/Ox-Si templates. The reference pattern of the monoclinic phase of HfO_2 powder (PDF #00-034-0104) is shown as the bottom bar graph.

Interestingly, the relative peak intensities for these nanostructures are found to be markedly different from those of the reference pattern (PDF #00-034-0104). The intensities of the (111), (200) and (-111) peaks and the peak intensity ratios of (111) and (200) planes to (-111) plane (the most intense peak in the reference pattern) are summarized in Table 2-1. Since the X-ray strikes the sample

at a fixed incidence angle in GIXRD, the predominant relative intensities of the (111) and (200) peaks in the GIXRD pattern of the HfO_2 nanopyramid film do not correspond to solely the relative contributions of the predominant growth orientations of the nanopyramids. Additional material characterizations such as HRTEM images are required to determine the preferential growth orientation of these nanostructures. However, in 1D HfO_2 nanostructures grown on top of the substate plane (Figure 2-1c2-c4), the stronger relative intensities of the (–111), (111) and (200) peaks considered here suggest that these planes mainly form the cross-sectional planes or the lateral facets in the crystal structure of the nanocolumns, nanospikes and nanowires. Since (200) is the strongest peak of the HfO_2 nanopyramids grown on GNI/Ox-Si at the same growth temperature as the NWs, the strong (200) peak in the XRD pattern of NWs could also be partly attributed to the presence of VS-grown nanopyramids grown concurrently with the NWs. This matter will be discussed in more detail in the next section.

Table 2-1. Relative peak intensities of the (111), (200) and (-111) planes and the respective intensity ratios of (111) and (200) planes to (-111) plane for HfO_2 nanostructures grown under different conditions.

HfO_2 Nanostructures	Relative peak intensity (%)			Peak intensity ratio	
	(-111)	(111)	(200)	I(111)/I(-111)	I(200)/I(-111)
Monoclinic phase (PDF Ref. # 00-034-0104)	100	78	25	0.78	0.25
Nano square pyramids on Ox-Si	8	2	100	0.25	12.5
Nano square pyramids on GNI/Ox-Si	26	54	100	2.08	3.85
Nanowires on Sn-GNI/Ox-Si	67	97	100	1.45	1.49

A closer examination of the GIXRD patterns of these nanostructures reveals notable position shifts from their respective peaks in the reference pattern. Table 2-2 provides the 2θ positions of the three most intense peaks, i.e. (-111), (111) and (200), along with their position shifts relative to their corresponding 2θ positions in the reference pattern. Remarkably, while the relative position shifts for the strongest features all appear rather small for NWs (less than 0.09°), those for the nanopyramids are discernibly larger (0.1°-0.2°). This peak shift toward a larger 2θ angle could be due to the compressive stress in the nanopyramids. The smaller volume of the unit cell calculated for the nanopyramids on GNI/Ox-Si (135.82 $Å^3$) compared to those for NWs on Sn-GNI/Ox-Si (137.97 $Å^3$) and the reference (138.28 $Å^3$) also confirms the larger residual compressive stress in the

nanopyramids. Moreover, the notably smaller position shift found for the NWs suggests that incorporation of Sn into the HfO_2 crystal structure is unlikely, and hence no solid solution phase is formed. We will discuss this matter in more detail in the subsequent sections.

Table 2-2. Comparing shifts of the three most dominant peaks relative to those of the reference for HfO_2 nanostructures grown under different conditions.

Plane Index	PDF Ref. # 00-034-0104 2θ (°)	HfO_2 nano square pyramids on Ox-Si		HfO_2 nano square pyramids on GNI/Ox-Si		HfO_2 Nanowires on Sn-GNI/Ox-Si	
		2θ (°)	Shift (°)	2θ (°)	Shift (°)	Pos (°)	Shift (°)
(-1 1 1)	28.336	28.581	0.245	28.539	0.203	28.425	0.089
(1 1 1)	31.665	31.777	0.112	31.841	0.176	31.730	0.065
(2 0 0)	34.358	34.495	0.137	34.474	0.116	34.410	0.052

2.3.2 TEM Studies

TEM analysis has been performed for all the nanostructures grown in the presence of Sn-GNI catalysts on Ox-Si substrates at different temperatures (770 °C, 720 °C, 650 °C and 550 °C). Evidently, the NWs exhibit growth in two main growth directions, which occur concurrently at the same growth temperature. Figure 2-3.a1 displays a typical low-magnification TEM image of a NW grown at 770 °C. A selected area electron diffraction (SAED) pattern obtained for this NW is shown in Figure 2-3.a3. The classic spot pattern reveals the single-crystalline nature of the NW, and it shows that the NW has grown perpendicular to the (010) plane, i.e., the length of the NW is along the [010] direction. The measured lattice spacings in the corresponding high-resolution TEM image (Figure 2-3.a2) are b=5.19 Å and c=5.08 Å and they further confirm the b axis as the growth direction. It is important to note that although the unit cell in the monoclinic system is skewed compared to the cubic system, the angles between axes b and c and between axes a and b are both equal to 90° ($\alpha=\gamma=90°$). Therefore, the [010] crystallographic direction in the monoclinic system is still perpendicular to the (010) plane. The reciprocal lattice pattern obtained by performing fast Fourier transform (FFT) on the high-resolution TEM image of the nanowire (Figure 2-3.b1 inset) is in excellent agreement with our measured SAED pattern (Figure 3-3a3). Moreover, it can be inferred from the HRTEM image (Figure 2-3.a2) and the SAED pattern (Figure 2-3.a3) that the (100) plane corresponds to the top-side facet of the nanowire perpendicular to the zone axis (-100) while the (001) plane is parallel to the zone axis.

This finding is consistent with the dominant peak intensity of the (200) plane observed in the GIXRD profile of the NWs grown at 770 °C in Figure 2-2.

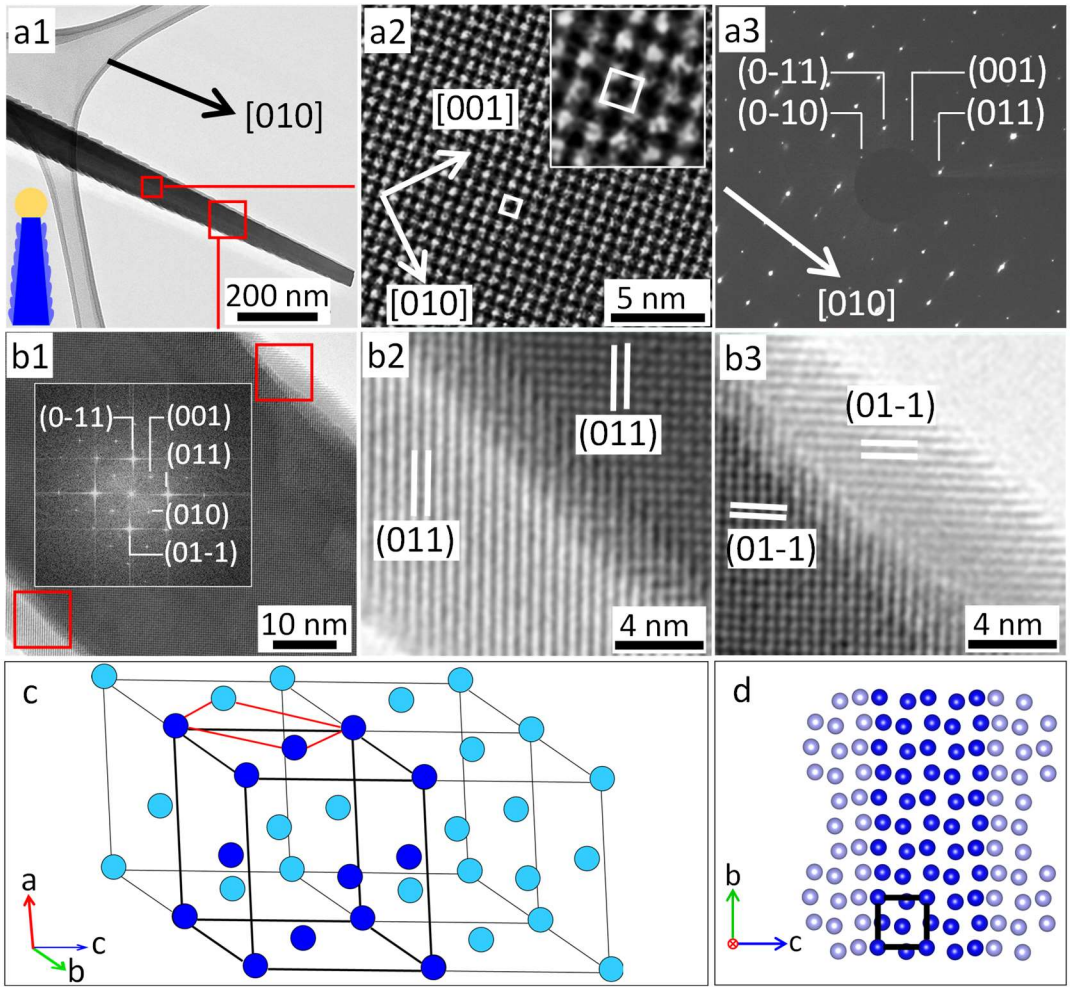

Figure 2-3. (a1) Low-magnification TEM image of a HfO_2 NW grown on Sn-GNI/Ox-Si at 770 °C with (a2) the HRTEM image and (a3) the corresponding SAED pattern depicting the growth direction of the trunk of the NW. The lower left inset in (a1) shows a pictorial model of the NW. (b1) Higher magnification TEM image of the marked area in (a1) depicting the perimeters of the NW. HRTEM images of the (b2) left and (b3) right areas marked in (b1) revealing homoepitaxial secondary growth on the surface (perimeter) of the NW. (c) Schematic model of four adjacent unit cells of the NW with atom positions in the unit cell optimized by DFT calculation. (d) Schematic cross-sectional model of the trunk of a NW (composed of ten unit cells).

The SEM images of the nanostructures (Figure 2-1c1-c4) suggest that the VLS growth and VS growth are two competing growth mechanisms occurring in our system concurrently. In accord with these SEM results, the HRTEM image (Figure 2-3b1) confirms the presence of a thin layer (5-10 nm) on the perimeter of the NW. A closer examination of the interface between the outer layer and the trunk of the NW in the perimeter region marked by the red squares in Figure 2-3b1 reveals a perfect crystal lattice match between the outer layers and the core body of the NW (Figure 2-3b2 and 2-3b3). This high level of crystal lattice match suggests that the lateral growth of the NWs occurs homoepitaxially on the surface of the NWs, likely by direct deposition of HfO_2 from the gas phase, whereas the VLS growth is responsible for the growth along the length of the nanowires.

Using the lattice parameters reported for the monoclinic phase in the reference XRD profile (PDF #00-0340-0104) for our DFT calculations, we obtain the optimized unit cell for the as-grown nanowires shown in the HRTEM image (Figure 2-3a2). Figure 2-3c shows a perspective view of a supercell consisting of four unit cells. Here, the red square marked on the top face of the supercell in the model in Figure 2-3c corresponds to the white square marked in the HRTEM image in Figure 2-3a2 and Figure 2-3a2 inset. We also utilize the DFT optimized unit cell to create an atomic model for the nanowire, a cross section of which is shown in Figure 2-3d. The trunk of the NW in this model is created by repeating five unit cells along the b-axis direction and two unit cells along the c-axis direction. The perimeter of the NW is formed by adding five unit cells along the b-axis direction at both sides of the cross section of the trunk and by arbitrarily removing some atoms to simulate the surface feature of the NW. This atomic model could be useful to provide a better understanding and visualization of the crystal planes and their growth direction in the crystal structures of these NWs.

The epitaxial growth rates on the facets of the NWs are found not to be the same for all NWs grown at 770 °C on Sn-GNI/Ox-Si, which gives rise to NWs with different surface morphologies. Figure 2-4a1 shows a low-magnification TEM image of a typical NW (with the main trunk) grown along the [010] direction, the same growth direction as the NW shown in Figure 2-3. However, an evidently higher VS growth rate has led to some coarse crystallites on the facet of this NW, forming a perule-like pattern on the surface (Figure 2-4a2). The HRTEM image (Figure 2-4a3) shows the perule surface structures grown along the same [010] direction with the (001) planes parallel to the zone axis. The corresponding cross-sectional model of this NW is shown in Figure 2-4a3 inset. The atomic model is constructed using six unit cells along the b-axis direction and two unit cells along the c-axis direction. The perule surface structure is generated by adding five unit cells along the b-axis direction each at both sides of the cross section of the trunk and arbitrarily removing some atoms.

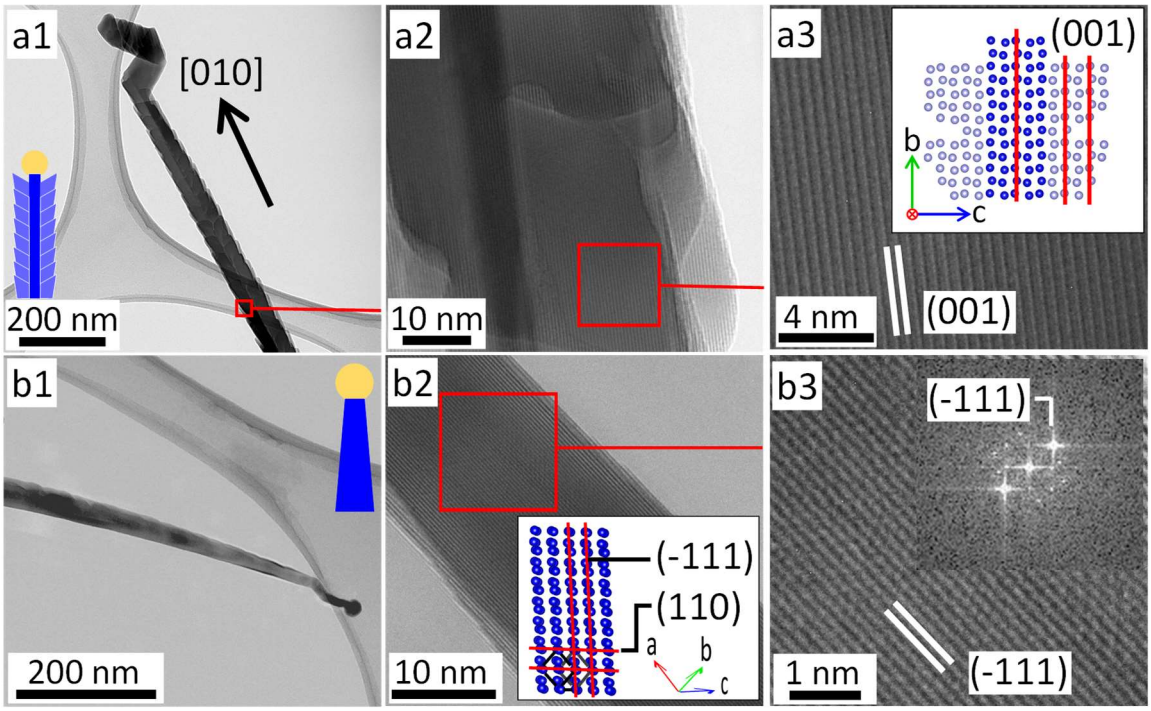

Figure 2-4. (a1) Low-magnification TEM Image and (a2) HRTEM image of a HfO_2 NW grown at 770 °C on Sn-GNI/Ox-Si with perule-like surface structures. (a3) Magnified image of the marked area in (a2) depicting the (001) planes with the corresponding cross-sectional atomic model shown in the inset. (b1) Low-magnification TEM image and (b2) HRTEM image of a smooth HfO_2 NW (i.e. without any perule-like structures) with (110) planes perpendicular to the growth direction with the corresponding perspective atomic model shown in the inset. (b3) Magnified image of the marked area in (b2) illustrating the (-111) planes parallel to the zone axis with the corresponding FFT image shown in the inset. Insets of (a1) and (b1) give the respective pictorial models of the NWs with and without perule-like surface structures.

In addition to the perulated NWs, Figure 2-4b1 and Figure 2-4b2 and Figure 2-4b3 show the low-magnification TEM and HRTEM images of a smooth NW (i.e. without any perule-like structures) grown with (-111) planes parallel to the zone axis. Our atomic model (Figure 2-4b2, inset) shows that the growth direction of this type of non-perulated NWs is perpendicular to the (110) planes. The observed (-111) side planes in the crystal structure of these NWs are consistent with the corresponding GIXRD pattern (Figure 2-2), and their presence could account for the higher intensity of the (-111) XRD peak of the NWs compared to that of the nano square pyramids. It should be noted that the [110] direction in these HfO_2 NWs is not exactly perpendicular to the (110) planes due to the

monoclinic structure of the NWs, despite the rather similar lattice parameters (a=5.28 Å and b=5.18 Å). The atomic model in Figure 2-5 illustrates the orientation of the (110) planes with respect to the [110] direction. The small difference between the [110] direction and the normal vector of the (110) plane can be calculated as $\cos\theta=3.68/[(\sqrt{(5.28^2+5.18^2)}/2]=5.7°$.

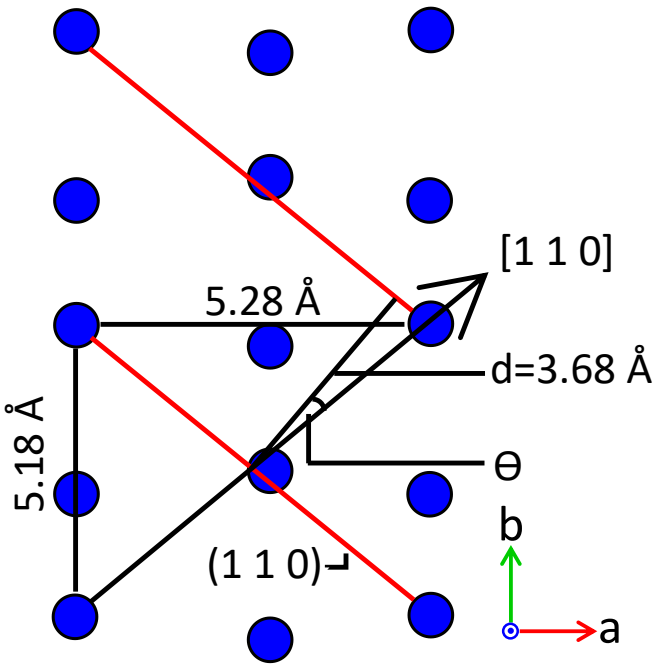

Figure 2-5. Atomic model depicting the minor orientation difference in the [110] direction from the (110) plane in the smooth HfO_2 NWs with monoclinic structure.

Our TEM analysis of the nanospikes grown at 720 °C on Sn-GNI/Ox-Si is shown in Figure 2-6. At this growth temperature, nanospikes are found to grow perpendicular to the (110) planes (Figure 2-6a2 and Figure 2-6a3). In addition to the (110) plane perpendicular to the growth direction, our atomic model (Figure 2-6a3 inset) shows that these nanospikes have the (200) plane oriented 45° from the growth direction and the (001) plane as the top-side facet perpendicular to the zone axis (00-1). From their SEM image (Figure 2-1c3), the nanospikes appear to have a triangular cross section. The (-111) and (1-11) planes should therefore correspond to the side facets of the nanospike, which accounts for the strong (-111) peak in the GIXRD pattern of the nanospikes (Figure 2-2). Similar to the NWs grown at 770 °C, nanospikes with perule-like structures on their surface are also observed (Figure 2-6b1). HRTEM images of the edge area (perimeter) of these nanospikes

(Figure 2-6b2 and Figure 2-6b3) show that the lattice spacing of these nanoscale features at the nanospike surface precisely matches that of the nanospike trunk (Figure 2-6a2). This perfect lattice match suggests that the secondary epitaxial growth on the nanospike surface arises from direct deposition of atoms on the surface through the VS mechanism similar to that observed for the NWs grown at 770 °C.

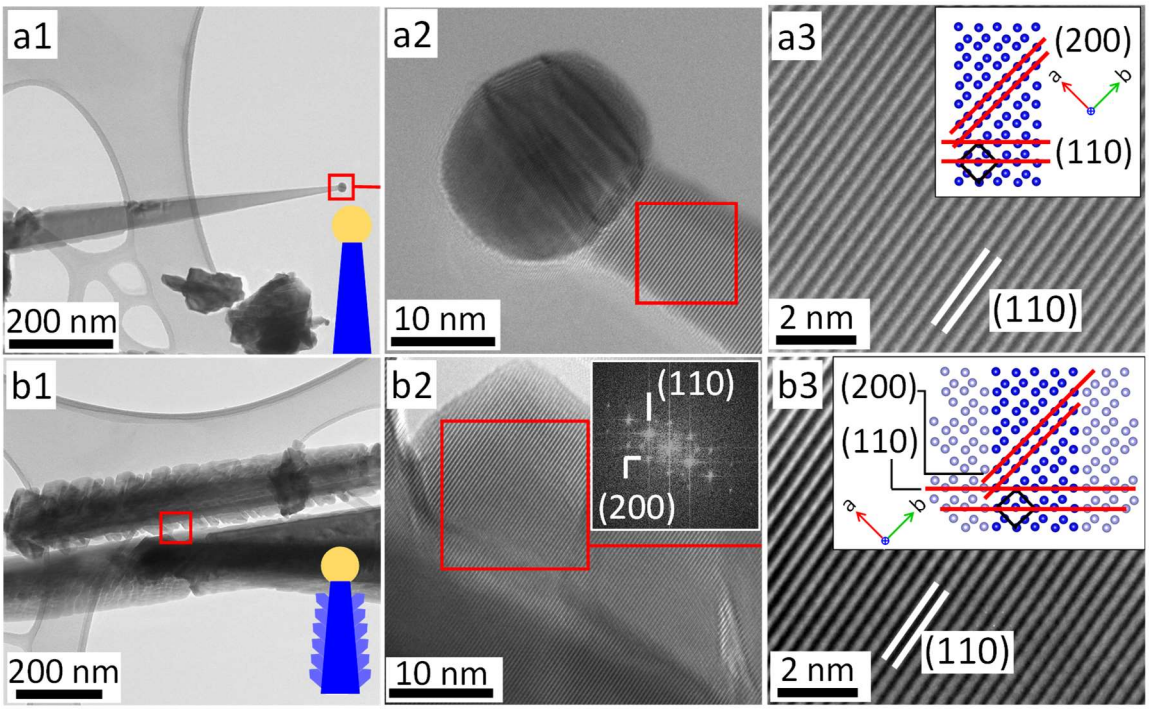

Figure 2-6. (a1) Low-magnification TEM image of a HfO_2 nanospike grown at 720 °C on Sn-GNI/Ox-Si. (a2) Corresponding HRTEM image of the tip area, illustrating (a3) the (110) planes (with interplanar spacing of 3.5 Å) perpendicular to the growth direction with the corresponding cross-sectional atomic model shown in the inset. (b1) Low-magnification TEM image of a HfO_2 nanospike with perule-like surface structure grown at 720 °C. (b2) HRTEM image of the perule-like features on the surface of the as-grown HfO_2 nanospike, illustrating (b3) their growth direction perpendicular to the (110) planes with the corresponding cross-sectional atomic model presented in the inset. The atomic model of the smooth nanospike in (a3) inset is constructed of four unit cells along the [110] direction and two unit cells along the [-110] direction, while the atomic model of the perulated nanospike in (b3) inset is formed by adding six unit cells along the [-110] direction and arbitrarily removing some atoms to simulate the surface features. Pictorial models of the nanospikes without and with perule-like surface structures are shown in lower right insets in (a1) and (b1).

As the growth temperature is decreased to 650 °C, the morphology of the nanostructures on Sn-GNI/Ox-Si changes into nanocolumns with a triangular base (Figure 2-7a1). At the same time, growth of some nanospikes with perule-like surface structures can also be observed at this temperature (Figure 2-7b1). Similar to that observed for the smooth NWs and perulated NWs at 770 °C (Figure 2-4a1 and Figure 2-4b1), the corresponding HRTEM images (Figure 2-7a2,a3 and Figure 2-7b2-b5) show two different growth directions for these nanocolumn and perulated nanospike structures formed at 650 °C. The nanocolumns are found to grow in the [010] direction (Figure 2-7a2,a3) while the growth direction of the perulated nanospikes is perpendicular to the (110) planes (Figure 2-7b5). According to the first-principle calculations,[193] the surface energy γ for low Miller index planes in monoclinic HfO_2 follows the increasing trend: $\gamma_{(-111)}<\gamma_{(111)}<\gamma_{(110)}<\gamma_{(100)}$. As the (–111) planes are thermodynamically most stable, the (–111) face is expected to become a facet common to all these one-dimensional nanostructures. On the other hand, for those one-dimensional nanostructures grown in the [010] direction, the (100) face, as the least stable surface with the highest energy, forms one of the side facets. The presence of thermodynamically less stable planes in the co-existing nanostructures can be attributed to the nature of the PLD method. In contrast to conventional methods of growing nanostructures such as CVD and solution-based methods, PLD is not an equilibrium process. In other words, the kinetics of the growth is a more effective controlling factor than the thermodynamics of the process, which facilitates the emergence of metastable planes during the growth process.

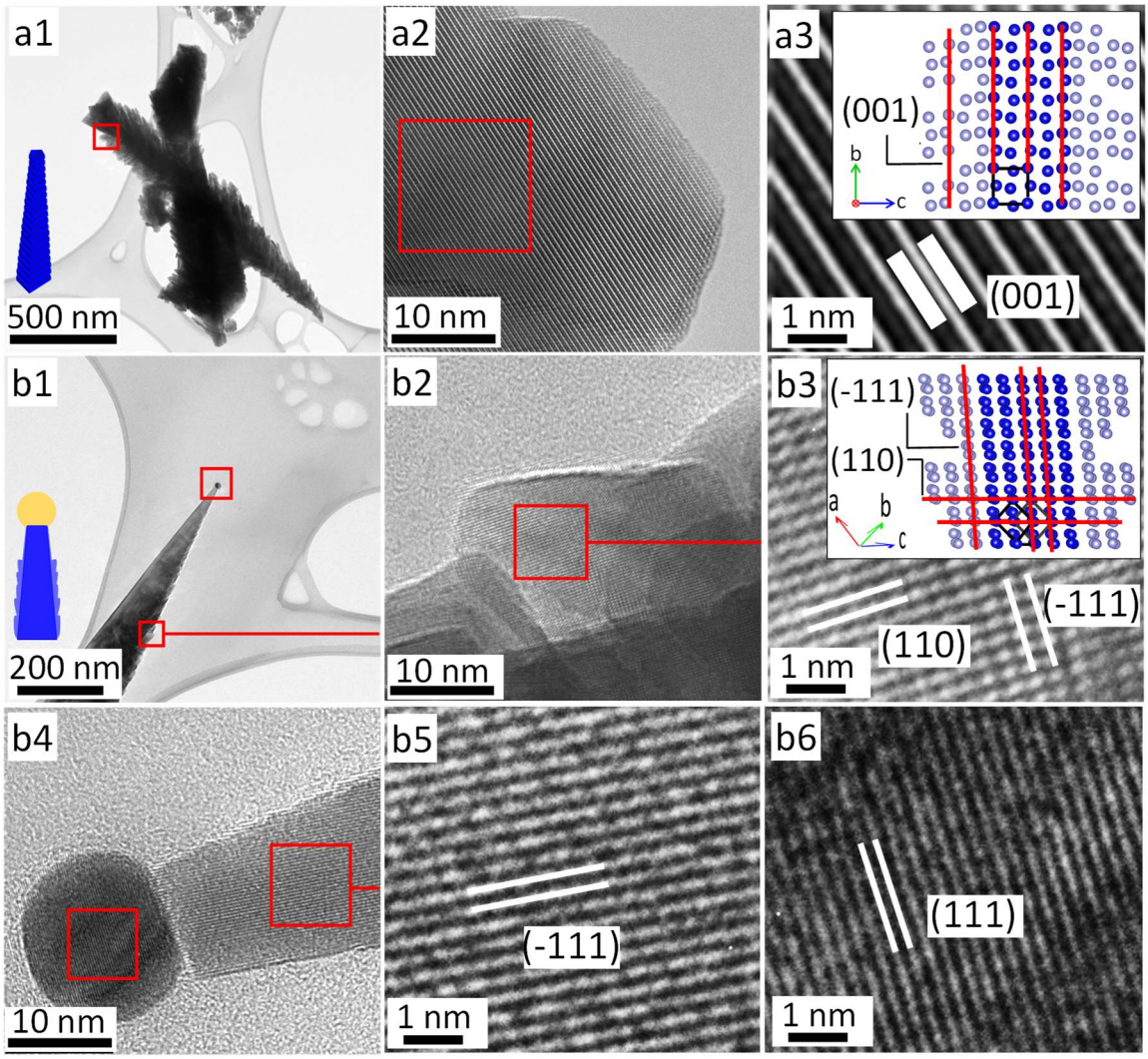

Figure 2-7. (a1) Low-magnification TEM image and (a2, a3) HRTEM images of the perimeter region of a HfO_2 nanocolumn grown in the [010] direction on Sn-GNI/Ox-Si at 650 °C. (b1) Low-magnification TEM image and HRTEM images of (b2, b3) the perimeter, (b4, b6) tip, and (b5) trunk regions of a HfO_2 nanospike grown perpendicular to the (110) planes on Sn-GNI/Ox-Si at 650 °C. Insets in (a1) and (b1) show the respective pictorial models of the nanocolumn and nanospike. Insets in (a3) and (b3) show the corresponding cross-sectional and respective atomic models of the nanocolumn and nanospike, depicting their respective growth directions.

The HRTEM images in Figure 2-7b2,b3 confirm the similar epitaxial growth of surface features to those observed for NWs and nanospikes grown at higher temperatures. Moreover, the nanocatalyst at the tip of the nanospike (Figure 2-7b1), which is also observed for the NWs and nanospikes grown at higher temperatures (Figure 2-4b1 and Figure 2-6a2), exhibits an interplanar spacing in agreement with that of the (111) planes of FCC gold nanoparticle reported in previous studies (Figure 2-7b6).[194,195] This is clear evidence that VLS growth has indeed occurred in our system, which is responsible for the observed catalyst-assisted single-crystalline growth of HfO_2 1D nanostructures.

As shown in our morphology studies in the previous section, the VLS growth of 1D nanostructures is accompanied by the VS growth of tetrahedral-shaped and pyramidal-shaped nanocrystals at all growth temperatures. HRTEM images of typical agglomerates of nano-tetrahedrons and nanopyramids grown at 770 °C, 650 °C and 550 °C are shown in Figure 2-8. Evidently, the VS-grown nanocrystals are found to contain all the atomic planes that are also observed in the crystal structures of the 1D nanostructures. The corresponding diffraction features for the (–111) and (200) planes in the GIXRD pattern (Figure 2-2) can therefore be attributed to both the VLS-grown 1D nanostructures and the VS-grown nanocrystals. According to the GIXRD pattern, these nanostructures should also contain the (111) planes. However, the (111) planes do not appear in the HRTEM images because the electron beam direction happens not to be parallel to the zone axis of the (111) planes. Furthermore, as indicated in our discussion about the morphology of nano-pyramids on Ox-Si templates and nano-tetrahedrons on Sn-GNI/Ox-Si, the larger size of the nano-tetrahedrons is attributed to the initial nucleation and growth occurring on the Sn-GNI catalyst. The emergence of the same lattice planes in both VLS-grown and VS-grown nanostructures on the Sn-GNI/Ox-Si templates could further support that the nucleation of nano-tetrahedrons indeed initiates on the Sn-GNI catalyst. These initial nuclei then start to grow through the VS mechanism creating the nano-tetrahedrons. However, at higher temperature that the VLS mechanism is dominant, the growth process leads to the formation of both 1D nanostructures and nanocrystals together.

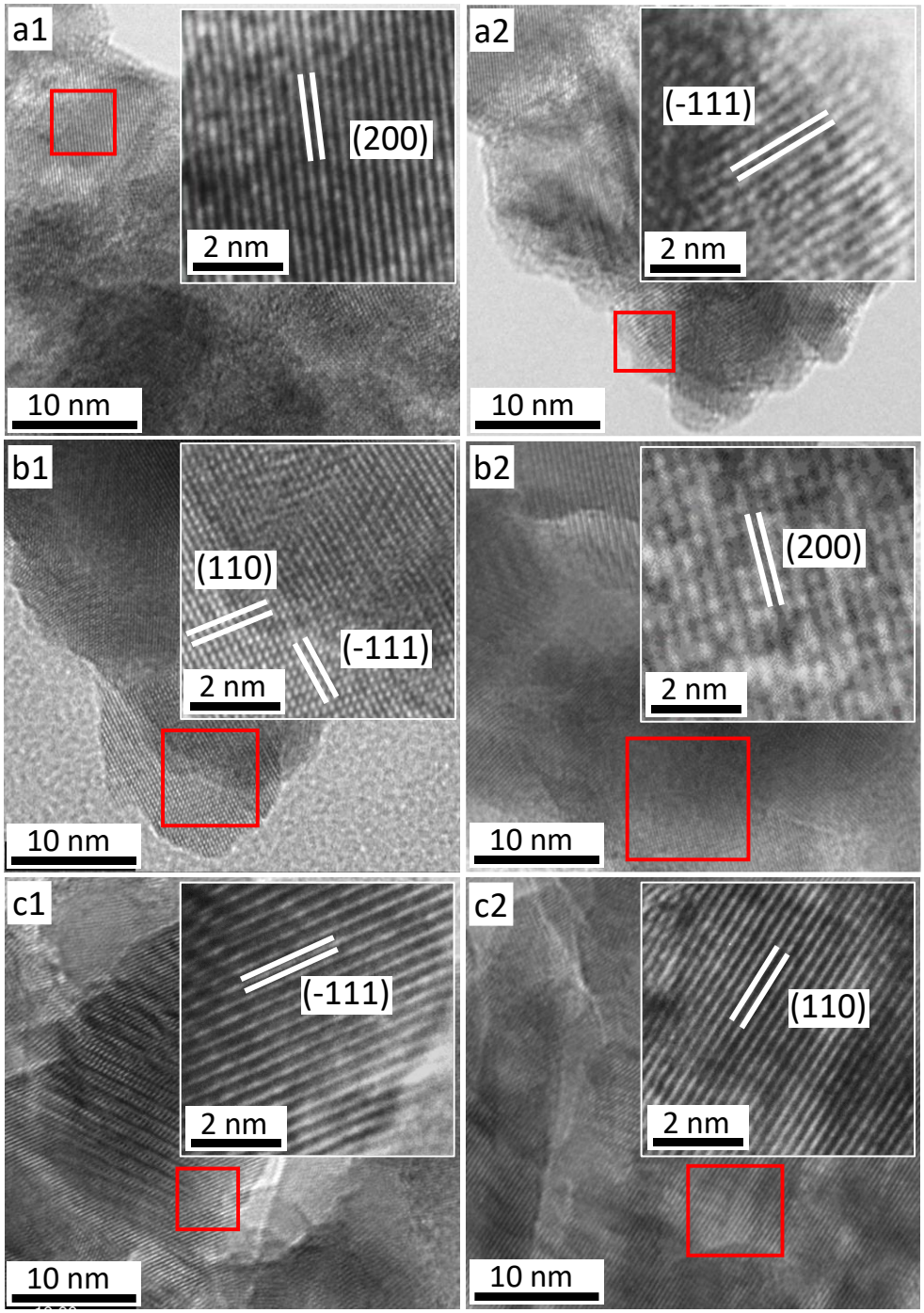

Figure 2-8. HRTEM images of typical agglomerates of nano square pyramids and nano triangular pyramids obtained on Sn-GNI/Ox-Si at (a1, a2) 770 °C (b1, b2) 650 °C and (c1, c2) 550 °C.

The observation that VLS growth could only occur when Sn is present in the system suggests that Sn plays a crucial role in promoting VLS growth. To further investigate the role of Sn in the growth process, we determine how Sn is distributed within the structure of the NWs by using TEM-EDS elemental analysis. Elemental maps of Hf, O, Au and Sn (Figure 2-9a1-a5) are obtained from the EDS analysis on the NW shown in the Scanning TEM image in Figure 2-9b (the corresponding EDS spectrum is provided in Figure A1, Appendix A). The elemental maps confirm the presence of Hf and O along the length of the NW and of Au as the catalyst at the tip of the NW. However, no reliable signal for Sn can be detected.

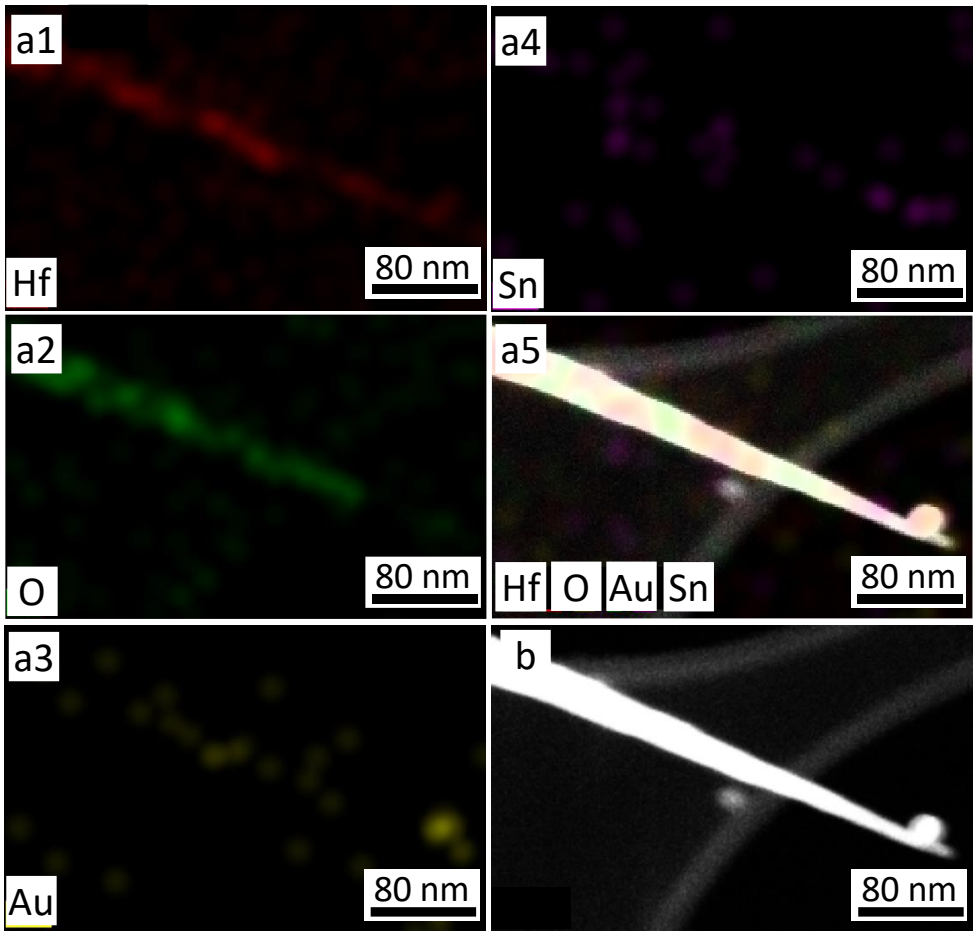

Figure 2-9. (a) STEM-EDS elemental maps for (a1) Hf, (a2) O, (a3) Au, (a4) Sn, and (a5) their overlaps of a NW grown on a Sn-GNI/Ox-Si substrate at 770 °C, along with (b) its STEM Annular Dark Field (STEM-ADF) image.

The elemental profiles (Figure 2-10b) for line-scan across a NW with a perule-like surface structure (Figure 2-10a) also show no detectable Sn signal. Although the TEM-EDS analysis does not detect any Sn signal, we cannot rule out the presence of Sn in our structures. The amount of Sn in our system could be so small that it is beyond the sensitivity range of TEM-EDS analysis. A more surface sensitive analysis technique to determine the distribution of Sn within and particularly in the near-surface region of these NW structures is therefore needed. In the next section, we will discuss our results from the more surface-sensitive techniques, i.e., X-ray Photoelectron Spectroscopy (XPS) and Auger Electron Spectroscopy (AES).

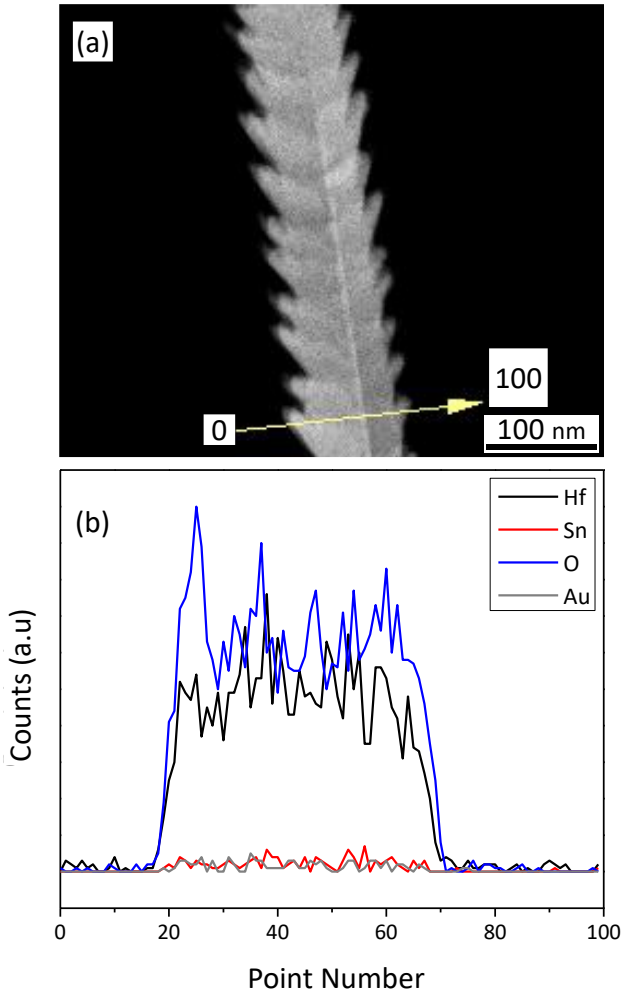

Figure 2-10. (a) STEM Annular Dark Field (STEM-ADF) image of a NW with perule-like surface structure grown on a Sn-GNI/Ox-Si substrate at 770 °C, and (b) the corresponding EDS line scan profiles of Hf, O, Sn and Au along the yellow line across the NW marked in (a).

2.3.3 XPS and AES Studies

XPS analysis has been performed to analyze the chemical-state compositions of HfO_2 nanostructures and particularly to determine how oxygen vacancies and Sn are distributed within these nanostructures. Figure 2-11 compares the XPS survey spectra of HfO_2 NWs grown on Sn-GNI/Ox-Si at 770 °C, HfO_2 nano-tetrahedrons grown on Sn-GNI/Ox-Si at 550 °C and HfO_2 nano square pyramids grown on Ox-Si at 770 °C. While the characteristic peaks of Hf, C and O core-levels are observed in all three samples, the Sn 3d doublet peak (Figure 2-11 insets) is only detectable for the HfO_2 NWs (Figure 2-11a) and not in the HfO_2 nano-tetrahedrons (for which Sn-GNI catalysts are used) nor in the HfO_2 nano square pyramids (for which no catalysts are used). The C 1s peak at 284.5-285.5 eV is attributed to adventitious carbon arising from ambient sample handling, and it can be removed after brief Ar sputtering for 60 s. In this study, the C 1s peak at 284.7 eV is used as the reference for spectral calibration of the binding energy scale.

Figure 2-12 compares the corresponding XPS spectra for the Hf $4d_{5/2}$, Sn 3d, and O 1s spectral regions of the HfO_2 NWs, HfO_2 nano square pyramids and HfO_2 nano-tetrahedrons. To identify the spectral compositions of individual components, we fit individual peaks after appropriately removing a Shirley-type background. In the Hf $4d_{5/2}$ region, the stronger component at 213.7 eV corresponds to Hf^{+4},[196–199] while the weaker lower-binding-energy components at 212.7 eV and 211.7 can be attributed to defect-related peak components with an oxidation number lower than +4. Without a priori knowledge of the number and nature of these defect components, we have categorized them into two general groups: HfO_{x1} ($2>x1>1.5$) and HfO_{x2} ($1.5\geq x2>1$) and fit any excess intensity (from the Hf^{4+} state) with two respective peaks. Evidently, the HfO_2 NWs grown on Sn-GNI/Ox-Si at 770 °C exhibit the strongest suboxide peaks (HfO_{x1}, HfO_{x2}), suggesting that the NWs are the most oxygen deficient. On the other hand, HfO_2 nano square pyramids grown on Ox-Si at 770 °C and HfO_2 nano tetrahedrons grown on Sn-GNI/Ox-Si at 550 °C show discernibly weaker HfO_{x1} and HfO_{x2} peaks indicating that these nanostructures are not as oxygen deficient as the NWs.

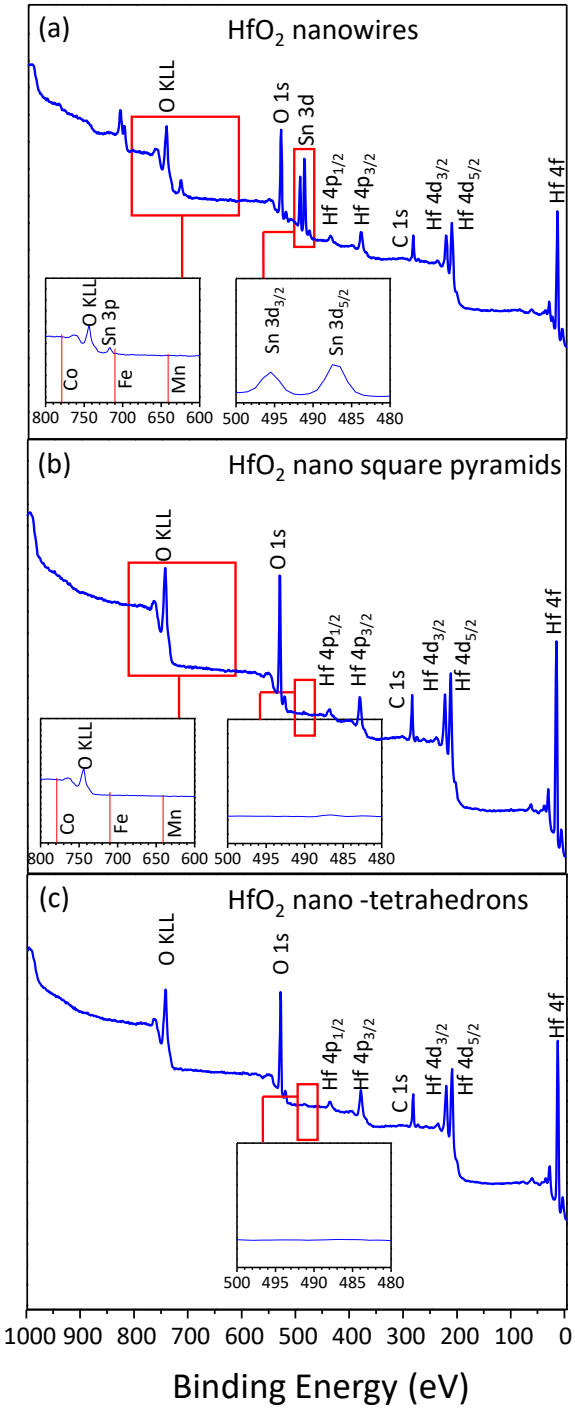

Figure 2-11. XPS survey spectra of (a) HfO_2 NWs grown on Sn-GNI/Ox-Si at 770 °C, (b) HfO_2 nano square pyramids grown on Ox-Si at 770 °C, and (c) HfO_2 nano-tetrahedrons grown on Sn-GNI/Ox-Si at 550 °C. The insets show expanded views of the spectral regions of Sn and of Mn, Fe and Co (with inherent magnetic properties).

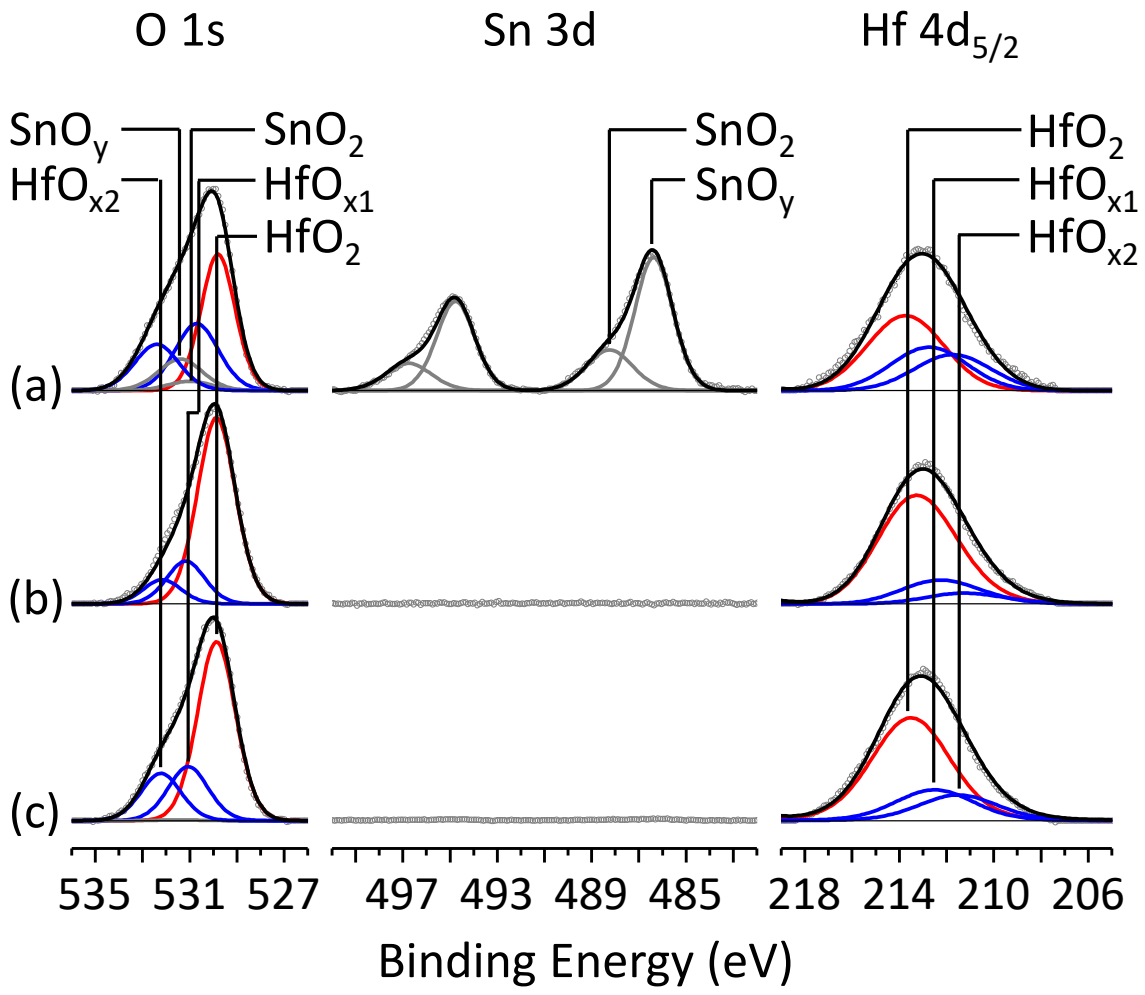

Figure 2-12. XPS spectra of O 1s, Sn 3d and Hf $4d_{5/2}$ regions of (a) HfO_2 NWs grown on Sn-GNI/Ox-Si at 770 °C, (b) HfO_2 nano square pyramids grown on Ox-Si at 770 °C and (c) HfO_2 nano-tetrahedrons grown on Sn-GNI/Ox-Si at 550 °C.

For the Sn 3d region spectra, only the HfO_2 NWs show two strong bands, which can be fitted with two sets of doublet peaks, each with a spin-orbit splitting of 8.4 eV. The stronger lower-binding-energy doublet with Sn $3d_{5/2}$ at 486.4 eV corresponds to Sn atoms in nonstoichiometric SnO_2 (or SnO_y) lattice (Sn^{+y}; $1 \leq y < 2$), while the weaker doublet with Sn $3d_{5/2}$ at 488.3 eV can be attributed to stoichiometric SnO_2 (Sn^{+4}).[200] In the O 1s region, the corresponding oxygen peak component for Hf^{4+} ions is located at 529.8 eV (lattice oxygen),[196,197,201] while the suboxide oxygen components for HfO_{x1} and HfO_{x2} correspond to the weaker higher-bonding-energy peaks at 530.7 eV and 532.4 eV

respectively. For HfO_2 NWs, there are two additional weaker components in the O 1s region located at 531.0 eV and 531.4 eV between the two Hf suboxide peaks. These peaks can be attributed to the oxygen bonds with Sn^{+4} ions and $Sn^{+y,}$ respectively. In agreement with their corresponding spectra of the Hf 4d region, HfO_2 NWs show the strongest suboxide peaks in their O 1s region while the HfO_2 nano square pyramids have the weakest suboxide O 1s peaks, confirming that the NWs grown at 770 ℃ are the most oxygen-deficient structures. The HfO_2 nano pyramids grown at 770 ℃ therefore appear to have a very small amount of oxygen vacancy defects.

Using the peak areas in these XPS spectra and the appropriate relative sensitivity factors for selected transitions, we estimate the relative composition of the defect-related features (HfO_{x1}, HfO_{x2}, and their sum) in the Hf 4d and O 1s regions and the ratio of Sn concentration to Hf concentration for all three nanostructures in Table 2-3. This quantitative analysis also confirms that HfO_2 NWs are the most oxygen-deficient structures with suboxide peaks accounting for over half of the total Hf 4d intensities and total Hf-related O 1s features. The next most oxygen-deficient nanostructures are HfO_2 nano-tetrahedrons grown at 550 ℃ with the suboxide percentage of ~35%, while the least oxygen-deficient nanostructures, HfO_2 nano square pyramids exhibit ~25% of defect-related features. The larger relative amount of defects in the NWs compared to the other nanostructures can be attributed to the higher specific surface area in 1D nanostructures, while the larger relative amount of defects in the nano-tetrahedrons than the square nano pyramids is likely due to the lower growth temperature of the nano-tetrahedrons, which could lead to more defective structures. Furthermore, the ratio of relative atomic concentration of Sn to that of Hf appears considerably higher (0.35) in the HfO_2 NWs sample than those in the other HfO_2 nanostructured films (nano pyramids and nano-tetrahedrons). For the HfO_2 nano-tetrahedrons grown at 550 ℃ on Sn-GNI/Ox-Si, the presence of only a minute amount of Sn (relative to Hf) is consistent with the lower growth temperature of 550 ℃, which appears insufficient to cause evaporation of enough Sn in our system. This composition analysis therefore strongly supports our hypothesis that Sn is indeed a critical component in promoting the VLS growth in this system.

Table 2-3. Area percentages of defect-related features (HfO_{x1}, HfO_{x2} and their sum) in Hf 4d and O 1s regions and the ratio of atomic % of Sn to that of Hf for HfO_2 NWs grown at 770 ℃, HfO_2 nano square pyramids grown at 770 ℃ and HfO_2 nano-tetrahedrons grown at 550 ℃. To calculate the percentage of a defect-related feature, the peak area of that individual component is divided by the total peak area of HfO_2+ HfO_{x1}+HfO_{x2}.

Sample	Percentage of defect-related features (%)						Sn/Hf
	Hf 4d			O 1s			
	HfO_{x1}	HfO_{x2}	HfO_{x1}+ HfO_{x2}	HfO_{x1}	HfO_{x2}	HfO_{x1}+ HfO_{x2}	
HfO_2 NWs grown at 770 ℃ on Sn-GNI/Ox-Si	28.1	23.3	51.4	30.4	21.2	51.7	0.35
HfO_2 nano square pyramids grown at 770 ℃ on Ox-Si	16.7	7.5	24.2	16.9	9.5	26.5	0
HfO_2 nano-tetrahedrons grown at 550 ℃ on Sn-GNI/Ox-Si	19.3	16.1	35.5	19.9	17.4	37.3	0.003

To determine the distribution of oxygen vacancies and Sn within the structure of the NWs, we perform a depth-profiling XPS study by Ar-sputtering the HfO_2 NWs for increasing amounts of time (Figure 2-13). Remarkably, the low-binding energy components at 212.7 eV and 211.7 eV in the Hf $4d_{5/2}$ region representing the oxygen vacancy defects appear to dwindle with increasing sputtering time and they totally disappear after 120 s of sputtering (Figure 2-13c). Their corresponding HfO_{x1} and HfO_{x2} features in the O 1s region at 530.7 eV and 532.4 eV, respectively (Figure 2-13a), also follow the same decreasing trend with increasing sputtering time. This observation indicates that the oxygen vacancies are mostly accumulating on the surface of the nanostructures rather than being incorporated deep into the bulk. This result is also in accord with our earlier XRD finding that the absence of any secondary phase other than monoclinic HfO_2 is indicative of the small amount of oxygen deficiency in the nanostructures and/or accumulation of oxygen vacancies in the surface region. In contrast, the intensity of Sn 3d spectrum (Figure 2-13b) appears to show notably less reduction, by only 28% even after 1020 s of sputtering. The corresponding Sn-related O 1s components [SnO_2 and SnO_y ($1 \leq y < 2$)] in the O 1s region (Figure 2-13a) also show very little change compared to the Hf suboxide features (HfO_{x1} and HfO_{x2}) with increasing sputtering time.

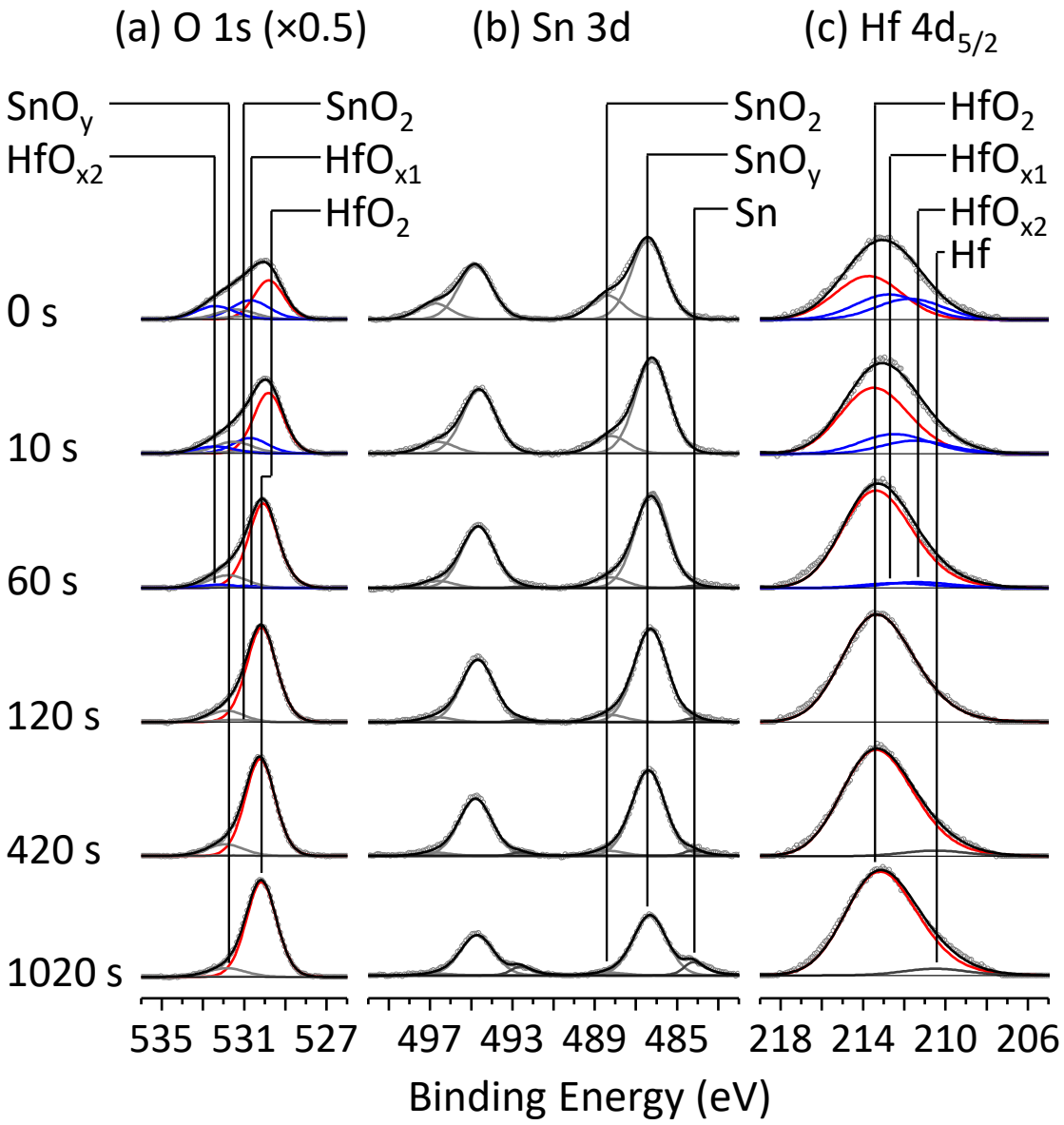

Figure 2-13. Depth-profiling XPS spectra of (a) O 1s, (b) Sn 3d and (c) Hf $4d_{5/2}$ regions for HfO_2 NWs obtained for increasing amounts of Argon sputtering time.

Figure 2-14 summarizes the changes in the peak areas of the Hf suboxide components (HfO_{x1}+HfO_{x2}) relative to the total Hf components (HfO_2+ HfO_{x1}+HfO_{x2}) and of the relative peak area of Sn relative to Hf with increasing sputtering time. Evidently, the relative intensity of defect-related features ($Hf_{suboxides}/Hf_{total}$) decreases sharply to near zero with sputtering for just 120 s, indicating that the defects are mainly located in the surface region. On the other hand, the atomic concentration of Sn relative to Hf does not show any significant change in the near-surface region and throughout the sputtering. This depth profiling results suggest that Sn is incorporated into the structure of the HfO_2 NWs, likely in the form of a solid solution phase or a secondary SnO_2 phase inside the structure. However, this hypothesis appears not to be supported by our XRD (Figure 2-2) and TEM results (Figure 2-3a1-b3, Figure 2-4a1-b4, Figure 2-9 and Figure 2-10). The sputtering rate of HfO_2 has been reported to be about half of that of SiO_2,[202] i.e., 3.3 nm/min of SiO_2 for sputtering by a 3.5 keV Ar^+ beam.[203] We can therefore estimate that the top 20-30 nm of the HfO_2 surface region is removed after 17 minutes (1020 s) of sputtering. Yet even at this sputtering depth, a strong Sn peak can be seen in the XPS spectrum (Figure 2-13). If such a deep Sn-containing region (as a solid solution or a separate SnO_2 phase) were to have formed during the NW growth process, it should be observable in XRD and/or TEM. A more likely explanation is that SnO_2 is mostly concentrated on the coexisting VS-grown HfO_2 nanocrystallite film instead of the NWs. In other words, this film with a layer of SnO_2 on top appears to be the primary source of the detected Sn 3d signal. As the NWs would partially shield the underlying HfO_2 film on the substrate, the Ar beam may not reach the film due to absorption or scattering by the NWs, which results in the SnO_2 on the film surface not being sputtered away as effectively.

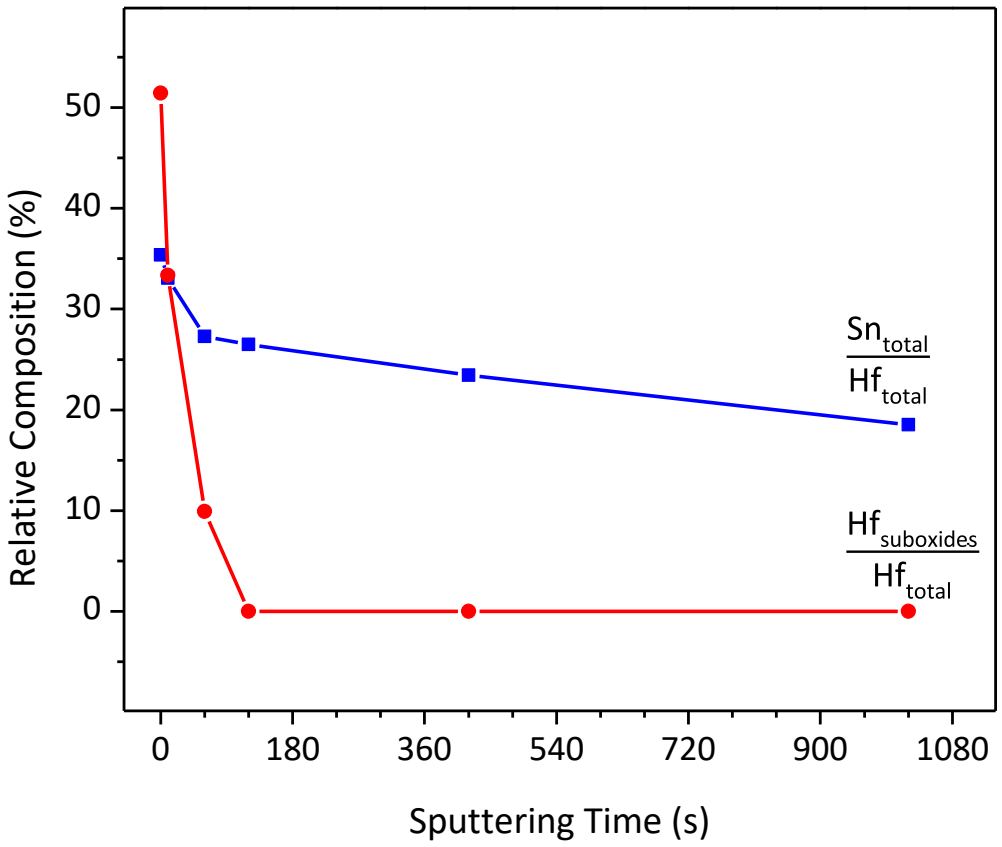

Figure 2-14. Comparison of the change in relative amounts of Hf suboxide features to the total contribution of Hf ($Hf_{suboxides}/Hf_{total}$) and of Sn to Hf ($Sn_{total}/Hf_{total}$) with increasing sputtering time. The $Hf_{suboxides}/Hf_{total}$ ratio is calculated by dividing the sum of peak areas for the suboxide features (HfO_{x1}+HfO_{x2}) in the Hf 4d region by the total area of all the Hf 4d features. Sn_{total}/Hf_{total} ratio is calculated by dividing the total area of Sn 3d by that of Hf 4d after appropriate consideration of their relative sensitivity factors.

Another discernible feature in Figure 2-13b is the emergence of the metallic Sn $3d_{5/2}$ peak at 484.2 eV with increasing sputtering time. The observed Sn^0 state is due to ion-induced reduction of oxide species caused by sputtering.[204,205] Similarly, the small low-binding energy feature in the Hf $4d_{5/2}$ region appearing after 420 s of sputtering could be attributed to sputtering-induced Hf^0 state. While depth-profiling XPS has shown that most of the Sn is deposited likely in the form of SnO_2 or SnO_y ($1 \leq y < 2$) on the surface of the VS-grown film, the distribution of Sn within the structure of individual NWs (grown concurrently on top of the VS-grown film) remains unknown. Laboratory-based

commercial XPS instruments would not be suitable to obtain this specific information due to its relatively large X-ray beam spot (1-2 mm) and low spatial resolution (2-3 μm at best). For the chemical analysis of individual NWs, Auger electron spectroscopy (AES), with a spatial resolution of ~20 nm, is therefore more appropriate. In this technique, it is possible to focus the electron beam generated by a field-emission electron source (with a typical beam spot of less than 5 nm) onto individual nanowires and to detect the electron-induced Auger electron emission.

Figure 2-15a compares the Hf MNN, Sn MNN and O KLL Auger electron emission signals obtained from five different points on the base and center part of selected NWs marked in the corresponding SEM image of HfO_2 NWs grown at 770 °C on Sn-GNI/Ox-Si (Figure 2-15b). The Auger electron spectra of the entire SEM-imaged areas of the HfO_2 NW film and of the HfO_2 nano square pyramid film grown at 770 °C on Ox-Si are also shown as references (Figure 2-15a). Evidently, Sn is found on all the sampling locations (P1-P5) of the surface of the individual HfO_2 NWs. The observed Sn MNN spectra for the NWs (Figure 2-15a) are similar to the reference spectra for the SnO or SnO_2 powder samples but not with the Sn powder reference sample (Figure 3-15b inset). This observation suggests that Sn is sitting on the NWs in the form of SnO_2 or SnO_y ($1 \leq y < 2$), which is consistent with the XPS results (Figure 2-12 and Figure 2-13). Furthermore, the Auger electron spectra obtained from different points on the surface of the NWs (Figure 2-15a, P1-P5) are similar to one another in terms of both kinetic energy position and peak shape, which suggests that the composition of the NWs is relatively uniform across the NW sample.

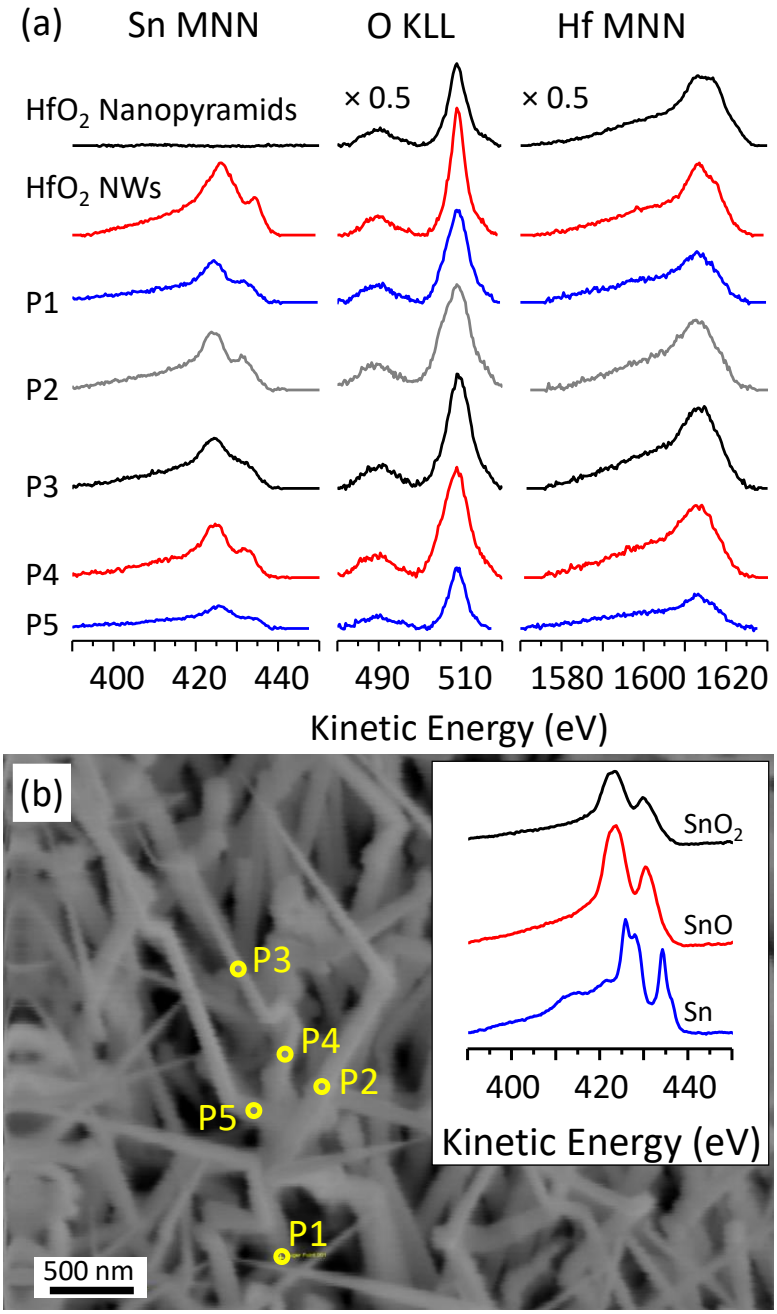

Figure 2-15. Auger electron spectra of Hf MNN, Sn MNN and O KLL regions from (top to bottom) HfO_2 nano square pyramid film grown at 770 °C on Ox-Si, HfO_2 NWs grown at 770 °C on Sn-GNI/Ox-Si collected over the entire area of the SEM image shown in (b) and at five different points (P1-P5) on selected NWs marked by yellow circles in (b). Inset in (b) shows the Sn MNN Auger electron spectra of SnO_2, SnO and Sn powder samples used as references.

To determine whether tin oxide is on the surface of the NWs as a separate phase or incorporated into their structures, we collect depth-profiling AES spectra at two different NW locations (Figure 2-16). As marked in the corresponding SEM image (Figure 2-15b), locations P1 and P2 are selected as P1 and P2 correspond to the base and middle of the NW, respectively. Evidently, while the intensity of the Hf MNN feature appears unchanged with increasing sputtering time, the Sn MNN feature is found to greatly decrease in intensity with sputtering and is almost completely removed after 480 s of sputtering, which further confirms that tin oxide is located mainly on the surface of the NW. Considering the reported sputtering rate of HfO_2 in the literature,[202] we estimate that the top 10-15 nm part of the surface region of the NW contains SnO_2 and/or SnO_y ($1 \leq y < 2$). However, the SnO_2 and/or SnO_y ($1 \leq y < 2$) appear not to form a continuous film over the surface region because no evidence of such film is found in our TEM studies.

Along with the XRD and TEM studies presented in Sections 2.3.1 and 2.3.2, these XPS and AES data provide strong support that Sn is the key factor in promoting VLS growth in the HfO_2 NW system. However, Sn does not appear to mix with HfO_2 during the growth process and it instead settles on the surface of the HfO_2 NWs in the form of SnO_2 and/or SnO_y ($1 \leq y < 2$). Knowing how Sn is contributing on/in the structure of HfO_2 NWs, we will discuss the role of Sn as a VLS growth promoter in more detail and propose a plausible model for the growth mechanism of HfO_2 NWs.

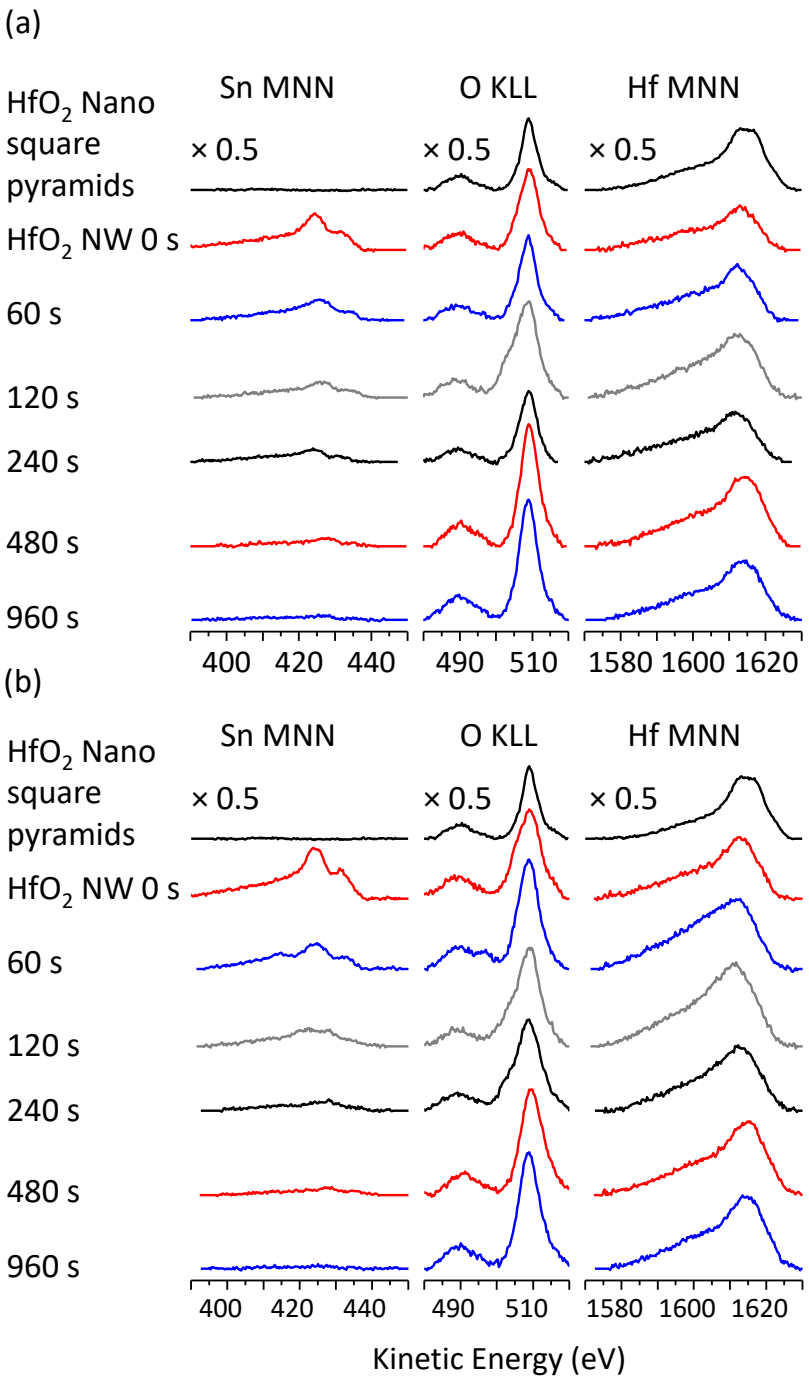

Figure 2-16. Depth-profiling Auger electron spectra of Hf MNN, Sn MNN and O KLL regions from (a) P1 and (b) P2 of the HfO_2 NWs shown in Figure 2-15b. The corresponding Auger electron spectra of a HfO_2 nano square pyramid film are shown as reference.

2.3.4 Growth Mechanism of HfO_2 NWs

Structural and compositional investigations of the HfO_2 nanostructures in the previous sections have shown that Sn is the main determining factor in facilitating the VLS growth of HfO_2 NWs in our material system. In this section, we provide a twofold rationale for the crucial role that Sn plays in promoting the VLS NW growth. First, we focus on the effect of Sn in boosting the VLS nucleation rate. According to the nucleation and growth model introduced by Suzuki et al.,[156] the ratio of the VLS nucleation rate, i.e. the nucleation rate at the LS interface (j_{VLS}), to the VS nucleation rate (j_{VS}) is exponentially proportional to the surface energies of the material species at the LS interface (γ_{LS}) and VS interface (γ_{VS}) weighted by the degree of supersaturation ($\Delta\mu$) and growth temperature (T):

$$\frac{j_{VLS}}{j_{VS}} \propto \exp\left(\frac{\gamma_{VS}^2-\gamma_{LS}^2}{4\Delta\mu T}\right) \qquad \textbf{Eq. 2-1}$$

For VLS growth to occur, Eq. 2-1 must satisfy the condition that the VLS nucleation rate be greater than the VS nucleation rate, i.e., $j_{VLS}/j_{VS}>1$. At a constant degree of supersaturation in the system ($\Delta\mu$), which is controlled by the material flux supply and oxygen partial pressure,[156] the greater is the term ($\gamma_{VS}^2-\gamma_{LS}^2$) the higher is the j_{VLS}/j_{VS} ratio. In other words, a greater difference in the surface energies of the material species at the LS and VS interfaces would give rise to a larger difference in the VLS nucleation rate relative to the VS nucleation rate so that the VLS growth mechanism would become the dominant growth mechanism. Furthermore, when Sn is alloyed with other metals such as Cu, Ag and Zn, the surface energy of the resulting liquid alloy is found to be lower than the pure metals.[182,183] The degree of this reduction in the surface energy depends on the atomic fraction of Sn in the alloy composition. Specifically, the Sn-Au alloys have exhibited significantly lower surface energies than pure liquid gold.[184,185] When Sn is dissolved in gold nanoislands, it could therefore substantially reduce the surface energy of the gold catalysts (γ_{LS}). According to Eq. 2-1, the lower surface energy of the catalyst (γ_{LS}) would lead to a larger numerator ($\gamma_{VS}^2-\gamma_{LS}^2$) in the exponent, which, in turn, increases the VLS nucleation rate over the VS nucleation rate. It is therefore reasonable to hypothesize that Sn is promoting VLS growth in our system by reducing the surface energy at the interface between the gold catalyst and HfO_2 NWs, leading to a higher VLS nucleation rate.

The second part of our rationale is based on the classical theory of diffusion in liquids. It is well known that bimetallic catalysts used in the VLS growth of 1D nanostructure are more efficient due to the improvement in their diffusivity.[177] According to the Stokes-Einstein equation, the diffusion coefficient in liquid (D) is given by:[206]

$$D = \frac{k_B T}{6\pi\eta R_0} \qquad \textbf{Eq. 2-2}$$

where k_B is the Boltzmann constant, T is the absolute temperature, η is the solvent viscosity and R_0 is the solute radius. This equation shows that the diffusivity of a liquid is inversely proportional to its viscosity. In the VLS growth of NWs, the limiting step is the diffusion of the adsorbed atomic species from the surface of the liquid catalyst to the interface between the catalyst and the solid where the VLS growth occurs. Any factor that decreases the viscosity of the liquid catalyst can therefore also cause an increase in the VLS growth rate.

In the binary phase diagram of Au-Sn system (Figure 2-17),[181] there is an eutectic composition at 29 atomic % of Sn. As more Sn is dissolved in the gold-rich alloy, the composition of the alloy moves toward the eutectic composition resulting in a substantial drop in the melting point of the alloy. The viscosity ($\eta_{m.p}$) of the liquid of a metal with a closed pack structure and atomic weight (A) at its melting point ($T_{m.p.}$) can be described by an empirical equation as follows:[207]

$$\eta_{m.p.}(\text{Poise}) = \frac{5.7\times10^{-4}\sqrt{A\,T_{m.p.}}}{V_A^{2/3}} \qquad \textbf{Eq. 2-3}$$

where V_A is the atomic volume of the liquid at the melting point. When Sn is dissolved in liquid gold, the viscosity of gold is therefore reduced due to the lowering of its melting point. Consequently, the diffusion rate of the atomic species across the liquid catalyst would increase, leading to a boost in the VLS growth rate of NWs. It is therefore reasonable to hypothesize that Sn promotes the VLS growth of HfO_2 NWs through these two parallel effects. Not only does Sn enhance the VLS nucleation rate by decreasing the surface energy at the LS interface, but it also increases the VLS growth rate by enhancing the diffusion of atomic species from the surface of the catalyst to the LS interface.

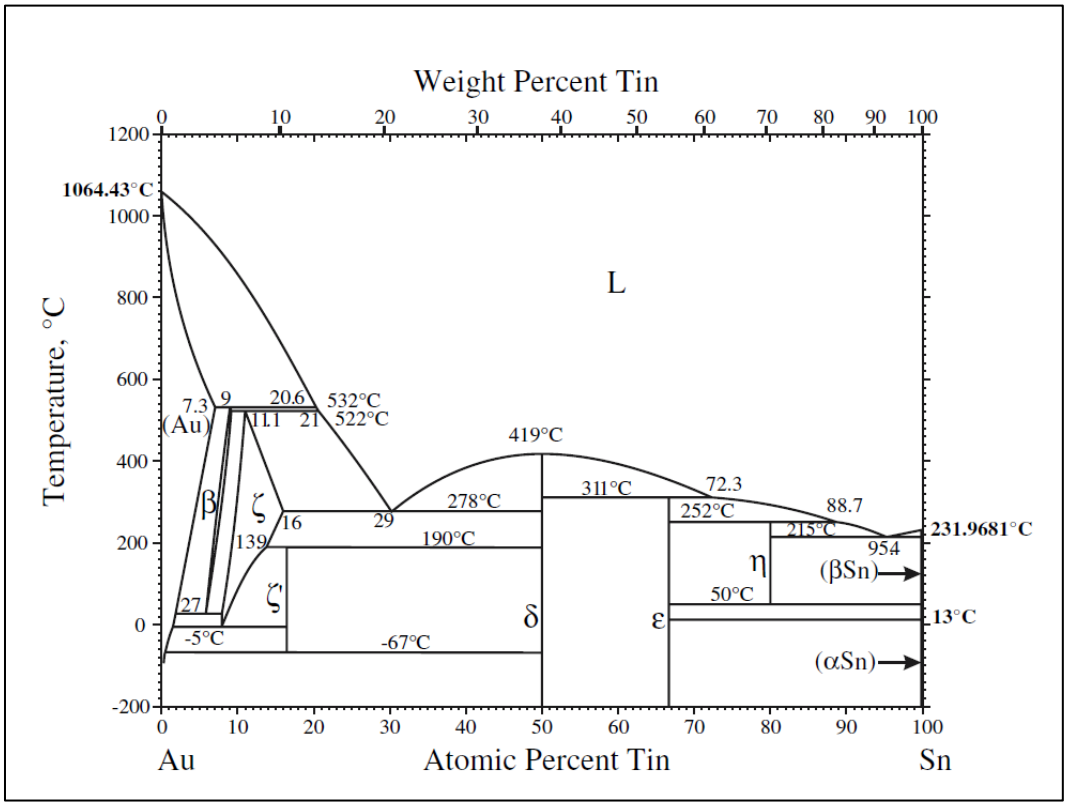

Figure 2-17. Au-Sn binary phase diagram. Reprinted with permission from reference [181]. Copyright (2007) by Springer Nature.

A plausible growth mechanism of HfO_2 NWs can be described as follows. (I) As the temperature of the substrate holder is ramped up to a selected growth temperature, Sn is being evaporated off the substrate holder. (II) Sn then infuses into the GNIs on the substrate and lowers their melting point as a result of an eutectic composition formation. (III) At the interface between the Sn-GNIs and the substrate, a liquid phase of the Au-Sn alloys with lower viscosity and enhanced diffusivity emerges. Meanwhile, Hf species are introduced into the system upon laser ablation off the target and they diffuse into the liquid catalyst. (IV) When the catalyst is supersaturated by the Hf species, HfO_2 NWs start to grow out of the catalyst. Concurrently, HfO_2 deposited on the bare areas of the substrate where there is no catalyst begins to form pyramidal and tetrahedral shaped nanocrystals following the VS growth mechanism. The VLS growth mechanism of the NWs is dominant due to the enhanced nucleation rate and growth rate at the LS interface. (V) Epitaxial growth of the surface (perule-like) nanofeatures on the facets of the VLS-grown HfO_2 NWs occurs due to the continued parallel VS growth in the system. (VI) After the deposition is complete, any excess Sn in the system oxidizes to

SnO_2 and/or SnO_y ($1 \leq y < 2$) and settles on the surface of the HfO_2 NWs and VS-grown nanocrystals. Figure 2-18 illustrates a pictorial summary of different HfO_2 nanostructures grown under different growth conditions. The proposed mechanism is consistent with the formation of these HfO_2 nanostructures.

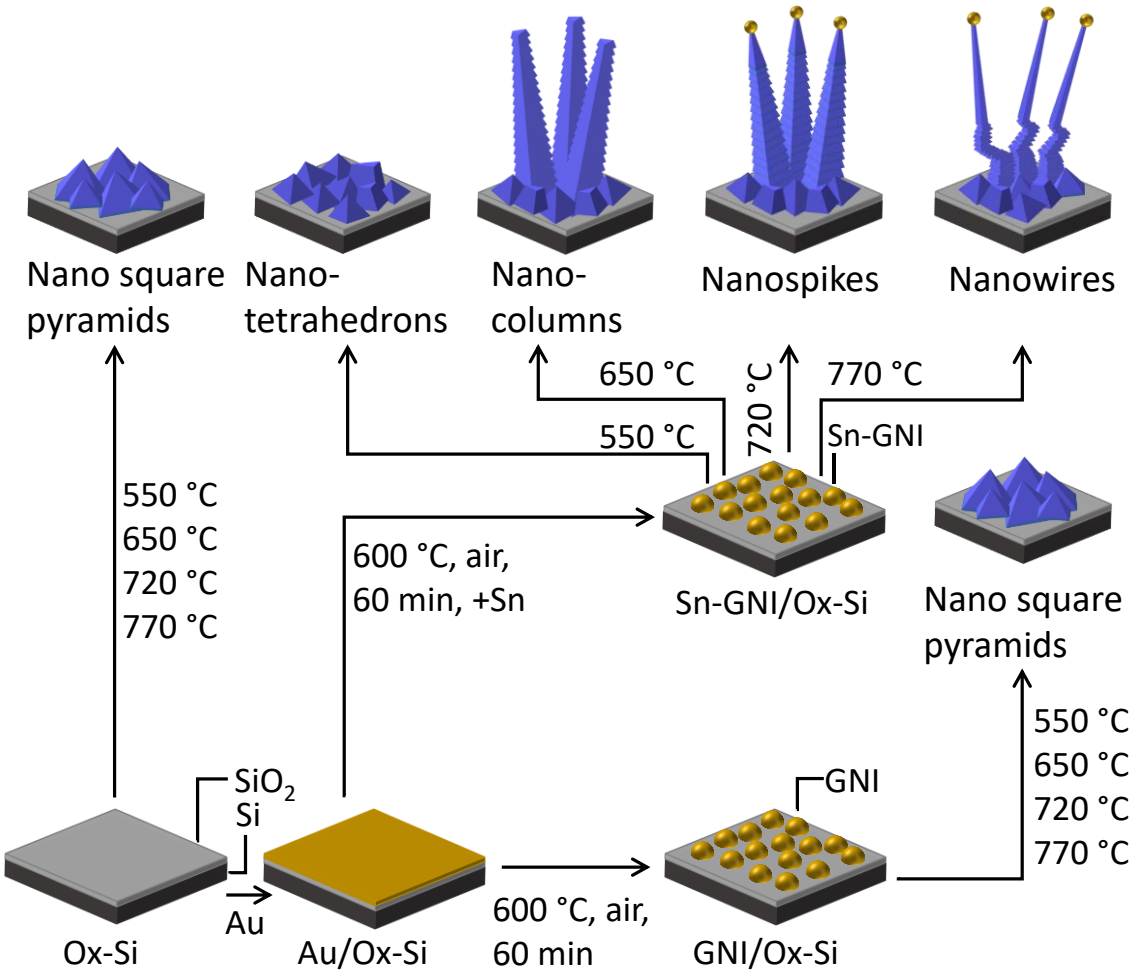

Figure 2-18. Pictorial models of HfO_2 nanostructures grown on Ox-Si, GNI/Ox-Si and Sn-GNI/Ox-Si templates at 550 °C, 650 °C, 720 °C and 770 °C.

2.3.5 Magnetic Properties of Single-Crystalline HfO_2 NWs

It has been more than a decade since unexpected ferromagnetism has been observed in oxygen-deficient HfO_2 thin films.[96,98] Considering that the application of HfO_2 as a high-κ dielectric material is well established in CMOS technology, the observation of ferromagnetism in HfO_2 is an important discovery that could extend its application to the field of spintronics. In this section, we report for the first time the magnetic properties of PLD-grown single-crystalline HfO_2 NWs, and compare them with those of HfO_2 nanostructured film (HfO_2 nano square pyramids). Due to the significantly higher mass of the substrate and the quartz paddle than that of the HfO_2 nanostructures, any weak magnetic signal could be masked by the enormous diamagnetic signal of the substrate. The diamagnetic contribution is therefore removed from the measured signal. In order to extract the magnetization parameters quantitatively, we perform curve-fitting on the HfO_2 NW data by using a combination of hyperbolic and sigmoid functions based on the correction methods of Jackson et al. and Paterson et al.[167,168] with the Hystlab v1.0.9 software. For the HfO_2 nanostructured film, we use a Langevin function to fit the paramagnetic contribution to the data (after the diamagnetic background signal from the substrate and quartz paddle has also been appropriately subtracted from the measured signal).

Figure 2-19 shows the magnetization of HfO_2 NWs grown at 770 ℃ on Sn-GNI/Si and of HfO_2 nanostructured film (nano square pyramids) grown at 770 ℃ on Ox-Si as functions of the applied magnetic field at three different temperatures. As the corresponding XPS survey spectra (Figure 2-11 a and b) show no detectable signals from magnetic ions (Co, Fe, and Mn), the measured magnetic moment therefore corresponds to those of the HfO_2 nanostructures and not to any magnetic contamination. Evidently, the HfO_2 NWs (Figure 2-19a) exhibit ferromagnetic hysteresis at all three sampling temperatures, from 2 K to 70 K to room temperature, while the HfO_2 nano pyramids show a significantly weaker magnetic response to the applied field with no hysteresis (Figure 2-19b). The magnetic saturation (M_s), magnetic remanence (M_r) and coercivity (H_c) of the nanostructures obtained from the respective magnetization curves are summarized in Table 2-4. The saturated magnetization (M_s) of HfO_2 NWs is found to be about an order of magnitude higher than that of HfO_2 nanostructured film. Moreover, all magnetization parameters of the NWs (M_s, M_r, H_c) exhibit higher values at lower measurement temperatures except for M_s, with the same values for 300 K and 70 K. To provide a plausible explanation of these observations, we consider the possible origin of room-temperature ferromagnetism in undoped semiconductors and insulators. Notwithstanding some conflicting reports in the literature,[208] oxygen vacancies are believed to be the primary underlying

source of unexpected room-temperature ferromagnetism in undoped metal oxides such as ZrO_2 and HfO_2 (d^0 ferromagnetism).[63,64,96,98,152,174,175] According to the model that has been recently proposed for ZrO_2 nanostructures,[63,64] singly charged and doubly charged oxygen vacancies serve as charge reservoirs in the structure by donating one or two electrons to the surrounding Zr^{4+} ions, thus reducing them to $Zr^{3+}(4d^1)$ or Zr^{2+} $(4d^2)$ ions. The unpaired electrons in the 4d orbitals of Zr ions can have a ferromagnetic exchange interaction with each other or/and with the single electrons on the singly charged oxygen vacancies creating bound magnetic polarons (BMPs). If the number of the oxygen vacancies is large enough, these BMPs could undergo ferromagnetic exchange with one another, thus generating a long-range ferromagnetic interaction throughout the material. The presence of oxygen vacancies in the structure also creates an impurity band near the bottom of the conduction band. When the ferromagnetic exchange interaction occurs between the unpaired electrons in the d orbitals and the electrons on the oxygen vacancies to create the BMPs, the impurity band hybridizes with the conduction band, which gives rise to spin-up and spin-down band splitting. This band splitting phenomenon is similar to the band splitting that develops at the fermi level of typical ferromagnets like iron and can account for the high-temperature ferromagnetism of dopant-free dilute magnetic semiconductor materials.

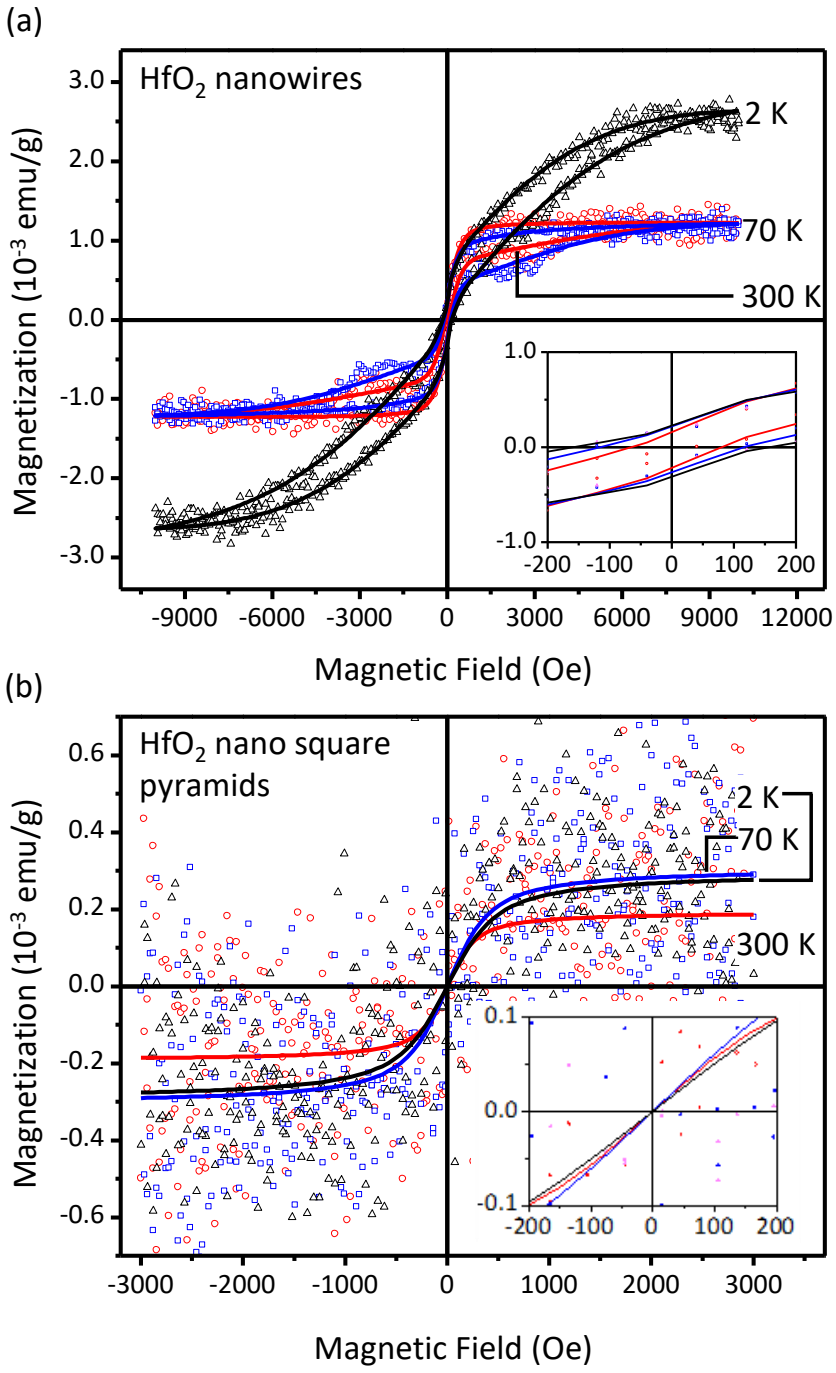

Figure 2-19. Magnetization vs. applied magnetic field (raw data points) and their corresponding fitted hysteresis loops (lines) of (a) HfO_2 NWs grown on Sn-GNI/Ox-Si at 770 °C and (b) HfO_2 nano square pyramids (nanostructured film) grown on Ox-Si at 770 °C.

Table 2-4. Magnetic saturation (M_s), magnetic remanence (M_r) and coercivity (H_c) of the HfO_2 NWs, and magnetic saturation of HfO_2 nano square pyramids.

Temperature (K)	HfO_2 NWs			HfO_2 nano square pyramids
	M_s (emu/g) $\times 10^{-3}$	M_r (emu/g) $\times 10^{-4}$	H_c (Oe)	M_s (emu/g)$\times 10^{-4}$
300	1.2	0.8	28.6	1.9
70	1.2	1.9	111.8	3.0
2	2.5	2	159.8	2.9

The same mechanism that drives ferromagnetism in ZrO_2 nanostructures could also apply to the HfO_2 nanostructures. Figure 2-20. gives a schematic representation of the proposed magnetization mechanism in HfO_2 NWs and HfO_2 nano square pyramids. The Hf 4d and O 1s XPS spectra (Figure 2-12a) confirm the presence of oxygen vacancies in the structure of HfO_2 NWs. According to our peak area calculations (Table 2-3), defect-related features associated with oxygen vacancies account for ~50% of the total peak area in the Hf 4d or O 1s XPS spectrum of HfO_2 NWs, while the contribution of these defect-related components in the Hf 4d or O 1s XPS spectrum of HfO_2 nano square pyramids is about half of the NWs (~25%). The number of oxygen vacancies in HfO_2 NWs could be sufficient to create overlapping BMPs due to the exchange interaction of charged oxygen vacancies with $Hf^{3+}(5d^1)$ and $Hf^{2+}(5d^2)$ ions. This interaction leads to band splitting in the hybridized conduction-impurity band and, consequently, room-temperature ferromagnetism in the HfO_2 NWs. When the measurement is carried out at a lower temperature, it is expected that M_s, M_r, and H_c of the NWs all increase due to the lower thermal energy (vibration) of the atoms. In contrast, for the HfO_2 nano square pyramids (nanostructured film), the concentration of the defects is found to be quite small. If the amount of defects in the structures is less than the percolation threshold, they are insufficient to generate overlapping BMPs,[68,209] and the resulting BMPs behave like isolated magnetic ions giving rise to paramagnetic behavior rather than ferromagnetism. Furthermore, the degree of band hybridization between the donor-derived impurity band and the unoccupied states in d orbitals depends on the concentration of the defects.[63] With an insufficient amount of defects in the structure, an effective band hybridization cannot be realized, and thus band splitting and high-temperature ferromagnetism do not occur.

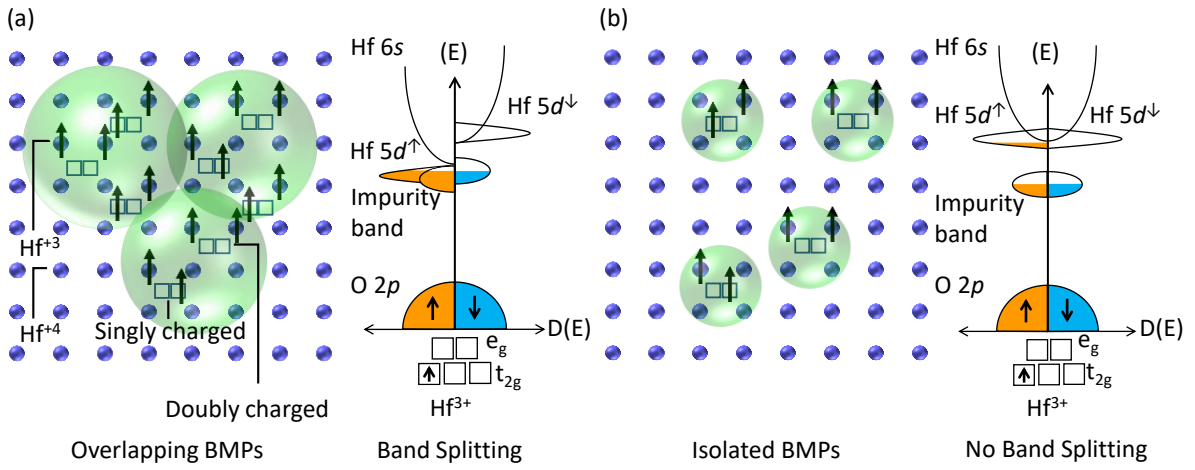

Figure 2-20. Representation of the Bound Magnetic Polaron (BMP)-band ferromagnetism hybrid model and the respective band structures for (a) HfO_2 NWs and (b) HfO_2 nano square pyramid film. The number of oxygen vacancies in the NWs is sufficient to generate overlapping BMPs leading to spin band splitting, in contrast to the limited number of vacancies in the HfO_2 nano square pyramids, in which isolated BMPs with no spin band splitting leading to paramagnetic behavior found similarly in isolated ions.

One noteworthy observation is that despite exhibiting comparable values of coercivity (H_c), the magnetic saturation of our HfO_2 NWs is one to three orders of magnitude lower than those of ZrO_2 nanostructures,[63,64] HfO_2 colloidal nanorods,[175] and HfO_2 thin films.[98,152,174] The ZrO_2 nanostructures with large magnetic moments are crystalized fully or partially in the tetragonal phase. The monoclinic phase is the stable phase of both ZrO_2 and HfO_2 at room temperature. However, some studies have found that a large amount of oxygen vacancies can stabilize the tetragonal phase at room temperature.[101,190–192,210] Considering only monoclinic phase and no tetragonal phase is found in our X-ray diffraction studies of HfO_2 NWs (Figure 2-2), the observed lower magnetic saturation of HfO_2 NWs could be due to the presence of an inherently smaller amount of oxygen vacancies obtained in our HfO_2 NWs. Nonetheless, the large amount of defects is not always associated with the tetragonal phase. For HfO_2 colloidal nanorods[175] and thin films[98,152,174] with monoclinic phase, structural defects (oxygen vacancies, cation vacancies and the defects at the film-substrate interface) are also proposed to be the source of magnetization. However, unlike the present work, no study to determine the exact nature of these defects (e.g. by XPS) is provided by these authors. For the HfO_2 colloidal nanorods,[175] their higher surface area could be the source of their higher amount of oxygen vacancy, while for the HfO_2 films[174] fabricated by magnetron sputtering, deposition in an oxygen-deficient atmosphere using

a metallic target could be the reason for generation of more oxygen vacancies. On the other hand, for the HfO_2 thin films grown by PLD from a metal oxide target in a similar oxygen pressure to that of our growth system, the defects at the film-substrate interface could be the reason for their higher magnetic saturation since different substrates such as Al_2O_3 and yttria-stabilized zirconia (YSZ) are mainly used in those studies. [21,23] The lower total amount of oxygen vacancies in our HfO_2 NWs is also consistent with our observation that most of these vacancies are accumulated in the surface region. The ferromagnetic exchange interaction between Hf^{X+} (x=2,3) and oxygen vacancies in HfO_2 NWs is therefore likely limited to the surface region that limits the number of oxygen vacancies. This surface-limited ferromagnetic coupling results in a smaller total magnetic moment compared to the defect-rich structures reported in the literature.

In summary, magnetic analysis of single-crystalline HfO_2 NWs reveals that these nanostructures exhibit room-temperature ferromagnetism with higher magnetic saturation than the HfO_2 nano square pyramid film, which shows predominantly paramagnetic behavior. According to the impurity band hybridization and BMPs model, the ferromagnetic property of the HfO_2 NWs can be attributed to oxygen vacancies accumulated on the surface of the nanowires. This is consistent with our XPS results that also confirm that HfO_2 NWs are indeed more oxygen-deficient than HfO_2 nano square pyramids.

2.4 Conclusion

In the present work, we report the growth of single-crystalline HfO_2 nanowires for the first time by using the alloy-catalyst assisted pulsed laser deposition technique. The alloy-catalysts provided by Sn-GNIs are found to be remarkably effective in controlling both the morphology and crystal structure of the final nanostructures. The glancing-incidence XRD study shows that HfO_2 NWs grown on Sn-GNI/Ox-Si templates (i.e., oxidized Si substrates with Sn alloyed gold nanoisland catalysts) and VS-grown nanocrystals grown on templates of Ox-Si (i.e., oxidized Si substrates with no catalyst) and GNI/Ox-Si (i.e., oxidized Si substrates seeded with gold nanoisland catalysts) all exhibit the monoclinic phase. However, the HfO_2 nanocrystals on Ox-Si mainly consist of the high-surface-energy (200) planes, while the HfO_2 nanocrystals on GNI/Ox-Si and HfO_2 nanowires on Sn-GNI/Ox-Si tend to form low-surface-energy planes of (111) and (–111) in addition to the (200) and (110) planes. The presence of these high-surface-energy (200) and (110) planes is attributed to the provision of non-equilibrium growth conditions inherent in the PLD technique.

Most importantly, Sn is found to be present in the form of Sn-Au alloy catalysts on the Ox-Si substrate and Sn is demonstrated to be the critical component in the growth of 1D nanostructures of HfO_2. The HRTEM images of these NWs and their corresponding crystal models show that some NWs have grown along the [010] direction with the (100) planes as their top facet, while others have grown along the [110] direction with the (001) plane as their top facet and the (–111) plane as their side facet. Since the growth of NWs is accompanied by the growth of HfO_2 nanocrystals on the Ox-Si surface along with the epitaxial growth of secondary perule-like features on the surface of the NWs, the VLS growth mechanism appears to be occurring concurrently with the VS nucleation and growth mechanism, and the final morphology is the result of competition between these two mechanisms. Moreover, our glancing-incidence XRD, XPS and AES results show that excess Sn is oxidized to SnO_2 and/or SnO_y ($1 \leq y < 2$) on the surface of the VS-grown film and the VLS-grown NWs. Having realized the crucial role of Sn in promoting the VLS growth mechanism, we propose a dual role for Sn in this growth system. First, Au-Sn alloys have a higher VLS nucleation rate likely due to a reduced activation energy for VLS nucleation resulting from a lower surface energy at the LS interface. Second, Sn could enhance the kinetics of the VLS growth by increasing the diffusivity of the catalyst and consequently fostering the diffusion of atomic species from the surface of the catalyst to the LS interface.

These insights gained from the present study could pave the way for growing other novel metal oxide NWs. For example, due to the provision of better control on the stoichiometry of the products, researchers commonly use metal oxide targets for the VLS growth of different types of metal oxide NWs by PLD. The amount of oxygen produced by laser ablation of these targets significantly suppresses VLS growth by increasing the VS nucleation rate.[156–158] Application of an alloy catalyst could therefore offer a remedy to counterbalance the undesirable effect of oxygen and a new approach in the synthesis of novel metal oxide NWs that have not been possible before.

Finally, the magnetic properties of HfO_2 NWs are characterized and compared with those of a HfO_2 nanostructured film of square pyramid shaped nanocrystals. Magnetization measurement at different temperatures reveals that HfO_2 NWs show room-temperature ferromagnetism with a coercivity comparable to other reported undoped metal oxide nanostructures.[63,64,152] In contrast, the HfO_2 nanostructured film sample exhibits just a subtle paramagnetic behavior. Since the XPS study shows no trace of magnetic contamination and confirms the presence of oxygen vacancies in the HfO_2 NWs, the observed room-temperature ferromagnetism of HfO_2 NWs is attributed to the presence of these defects. It is found that the magnetic moment of these HfO_2 NWs is weaker than that of defect-rich

undoped ZrO_2 nanostructures,[63,64] HfO_2 colloidal nanoparticles[175] and HfO_2 thin films[98,152,174] reported in the literature. This notable difference in the observed magnetic moments is due to the smaller amount of oxygen vacancies in HfO_2 NWs that are predominantly present in the surface region of the NWs when compared to the aforementioned nanostructures (with defects reported additionally in the bulk). Further investigations with more precise control on the oxygen vacancies could provide enhancement in the magnetization of these HfO_2 NWs. Indeed, the synthesis of HfO_2 NWs for the first time and the observation of room-temperature ferromagnetism on HfO_2 NWs promise the application of these novel HfO_2 nanostructures in the field of spintronics. More importantly, considering the high dielectric coefficient of HfO_2, the combination of dielectric property and room temperature ferromagnetic response in these HfO_2 NWs present a viable opportunity for integration of complementary metal oxide semiconductor (CMOS) technology with spintronic technology.[15,27,97,174] By exploiting the advantages of the PLD technique in preserving the stoichiometry of the targets, we can synthesize even more exotic NWs doped with various elements to advance not just their magnetic properties, but indeed other properties such as catalytic and high-dielectric electronic properties.

Chapter 3
Novel Ti-doped and Fe-doped HfO_2 Nanostructures: Structural and Magnetic Properties

3.1 Introduction

Electron spin has often been overlooked in conventional charge-based electronics before the discovery of the giant magnetoresistance (GMR) effect in 1988 by Albert Fert and Peter Grünberg,[1,2] who were later awarded the Nobel Prize in physics in 2007. Although Mott[6] was the first to discover spin-dependent electric conduction in ferromagnetic metals in 1936, the importance of this discovery has not been fully recognized before the introduction of GMR. The GMR effect shows that the mobility of the electrons and, therefore, the resistivity in a ferromagnetic metal could be effectively controlled by manipulating the spin of the electrons through the orientation of the magnetization in the ferromagnetic metal.[1,2] The discovery of the GMR effect, along with the subsequent development of the closely related phenomena of tunneling magnetoresistance (TMR) and magnetic tunnel junctions (MTJs), broke new ground in science and technology, and created a new field known today as spin-based electronics or spintronics.[3] Over the last thirty years, intense research in this field has led to the invention of many novel metallic spintronic devices such as hard disc read heads and magnetic random access memories (MRAM) that revolutionize the microelectronics and data storage industry.[3,20,22]

Exploiting the spin of the electron to control the electrical current can provide an extra degree of freedom in conventional charge-based semiconductor devices. The integration of spintronics into semiconductor-based electronics could, therefore, provide an excellent opportunity to produce novel devices with nonvolatility, higher data processing speed, lower electric power consumption and more compact design compared to conventional semiconductor devices in mainstream microelectronics.[21] Invention of a material that has both semiconducting and ferromagnetic properties could be an important milestone in realizing the integration of spintronics and semiconductor electronics. For example, one of the biggest advantages of such material would be the easier injection of spin-polarized electrons between a ferromagnetic semiconductor and a nonmagnetic semiconductor compared to a ferromagnetic metal and a nonmagnetic semiconductor due to the absence of a Schottky barrier.[7] The introduction of dilute magnetic semiconductors (DMS) was a significant breakthrough in the search for ferromagnetic semiconductors.[26] DMSs are a recent class of advanced materials that is produced by dilute doping of a nonmagnetic semiconductor with magnetic ions to incorporate spin functionality in the host material while preserving its semiconductor properties.[26]

Among all DMS materials, III-V dilute magnetic semiconductors such as Mn-doped GaAs ($Ga_{1-x}Mn_xAs$) have attracted the most attention due to their promising ferromagnetic and electron transfer properties.[30,115] However, the low Curie temperature of these DMSs (T_c<200 K)[68] is a major drawback for practical device applications. In the search for DMSs with a higher Curie temperature and better compatibility with the complementary metal oxide semiconductor (CMOS) technology, the first reports on the magnetic properties of Mn-doped ZnO in 1999[41] and Co-doped TiO_2 in 2000[42] have triggered a new round of research in this field. These studies have mainly focused on the magnetic metal oxide semiconductors generally categorized as dilute magnetic semiconducting oxides (DMSOs).[26] DMSO systems have several important advantages over DMS systems, such as much higher Curie temperatures (e.g., up to 850-930 K for Cr-doped indium oxide thin film[44]) and enhanced flexibility in controlling their properties using oxygen non-stoichiometry. However, achieving a homogeneously doped material without any magnetic ion clustering throughout the host lattice in DMSOs has always been a great challenge, which appears to be closely related to the material growth conditions and could potentially be resolved with an appropriate technique.[26]

HfO_2 is a metal oxide with Hf^{4+} ions, with a closed shell $[Xe]4f^{14}$ configuration and no unpaired electron. Diamagnetism is, therefore, expected for HfO_2. In 2004, the observation of unexpected ferromagnetism with a Curie temperature above 500 K in undoped HfO_2 thin films[96] drew renewed interest to this field. Before this discovery, there was no consensus in the scientific community on the origin of the magnetic moment in DMSOs.[211] However, the ferromagnetic behavior of undoped HfO_2 has significantly strengthened the position of those who believe that oxygen vacancies and defects are the main sources of magnetism in DMSOs. Moreover, HfO_2 is a technologically important material with superior electrical and optical properties such as a large dielectric constant ($\kappa \cong 25$), wide bandgap (~5.7 eV), and high refractive index (2.9).[70–75] Due to its large dielectric constant, HfO_2 is the most promising material used as gate dielectric in metal-oxide-semiconductor field-effect transistors (MOSFETs).[1] The successful fabrication of ferromagnetic HfO_2, which is already an excellent CMOS compatible material, is therefore a significant step forward in realizing the idea of integrating spin-based electronics into the semiconductor-based electronics and CMOS technology.[97]

The origin of ferromagnetism in DMSOs remains controversial, and it has continued to be a subject of intense debate.[26] In non-oxide DMSs such as Mn-doped GaAs ($Ga_{1-x}Mn_xAs$), the Ruderman–Kittel–Kasuya–Yosida (RKKY) interaction between the magnetic dopants and the itinerant electrons in the host lattice is believed to be responsible for their ferromagnetic property.[55,212,213] However, since dilute magnetic metal oxides are wide-bandgap semiconductors or insulators with few itinerant

electrons, the RKKY interaction mechanism cannot explain the ferromagnetism in DMSO materials.[61] To date, many attempts have been made to account for the origin of ferromagnetism in DMSOs. While structural defects are generally believed to play a crucial role in the ferromagnetism in these materials,[26,45,69,98] not enough studies have been carried out to determine the exact nature of these defects.[26,69] Although some studies have attributed the observed magnetic moment to cation vacancies,[99,100] there is more solid evidence that support oxygen vacancies as the main source of ferromagnetism in both undoped and doped metal oxides.[62–64,97,98,101–103] Based on the role of defects (including oxygen vacancies) in generating ferromagnetism in metal oxides, models involving bound magnetic polarons (BMPs)[57] and charge transfer mechanism[66] have been proposed to explain the ferromagnetic behavior of DMSOs. None of these models could, however, provide a complete and accurate picture. In particular, while the BMP model can successfully explain the long-range ferromagnetic ordering in DMSOs, it cannot explain the high Curie temperature (T_c) of these materials. On the other hand, despite providing a reasonable account of the high Curie temperature of DMSOs, the charge transfer mechanism can only be applied to oxides doped with multivalent transition metal ions. A significant breakthrough in this matter was made by the model introduced by Coey et al. in 2005.[68] This model combines the Heisenberg approach, in which ferromagnetism occurs due to the exchange interaction of individual magnetic moments (here, BMPs), with the band ferromagnetism approach, in which magnetization occurs due to the spontaneous spin splitting of the bands. This model can explain not only the long-range ferromagnetic ordering in DMSOs using the concept of overlapping BMPs, but also the high Curie temperature of these materials based on spin splitting of impurity bands hybridized with the d-state bands.[66] A modified version of this model has been used to explain ferromagnetism in ZrO_2 nanostructures[63] and nanocrystals,[64] and also in our previous work to explain the ferromagnetic behavior of single-crystalline HfO_2 nanowires made for the first time (Chapter 2). According to this model, the total number of BMPs throughout the crystal lattice and the degree of band hybridization are closely linked to the number of oxygen vacancy defects.[63,68] DMSOs with a large amount of vacancies are therefore expected to exhibit ferromagnetic behavior with high magnetic saturation values and high T_c.

One strategy to increase the amount of oxygen vacancies in DMSOs is to fabricate DMSO nanostructures with high surface area-to-volume ratios (i.e. specific surface areas). For example, undoped ZrO_2 nanostructures and TiO_2 nanostructures exhibit enhanced ferromagnetic properties with very high values of magnetic saturation and T_c due to their large surface area-to-volume ratios.[63,64] In our previous work (Chapter 2), we also show that HfO_2 nanowires exhibit ferromagnetic behavior due to the oxygen vacancies accumulated in their surface region, while HfO_2 nanostructured films (HfO_2

nanopyramids) with lower specific surface areas do not show any ferromagnetic behavior. Another effective strategy is to engineer the formation of oxygen vacancies by incorporating dopant materials into the crystal lattices of metal oxides. Both nonmagnetic and magnetic dopants can serve this purpose. Theoretical studies show that doping of HfO_2 with such non-magnetic ions as Ti, Si, La and Al could reduce the formation energy of oxygen vacancies.[169,170] Moreover, even in the case of metal oxide thin films doped with magnetic ions, dopant-driven oxygen vacancies in the host lattice are believed to be the main source of intrinsic ferromagnetism in these materials.[68,102,103,214]

In this study, we adopt the approach of combining both of the aforementioned ideas to achieve enhanced ferromagnetism in HfO_2. Considering the favorable effect of doping HfO_2 with such ions as Ti, Si, La and Al in reducing the formation energy of oxygen vacancies,[169,170] and given the high solubility of Ti in Hf,[215] we investigate, in the first part of the present study, the effect of Ti doping on the morphological, structural, and magnetic properties of HfO_2 1D nanostructures. Grown by catalyst-assisted PLD technique, the nanostructures reported here for the first time include Ti-doped HfO_2 ($Hf_{1-x}Ti_xO_2$) 1D nanostructures with various Ti atomic concentrations (x=0.01, 0.10, 0.25, 0.50). We recognize that at 50 at. % Ti ($Hf_{0.50}Ti_{0.50}O_2$) the nanostructures are indeed binary oxide alloys and not doped nanostructures. However, to simplify the nomenclature in this work we refer them as nanostructures doped with 50 at. % Ti. The morphologies of the Ti-doped HfO_2 nanostructures are found to change discernibly with Ti doping, with shorter 1D nanostructures with increasing amount of Ti. We also show that the magnetic properties of $Hf_{1-x}Ti_xO_2$ ($0.01 \leq x \leq 0.50$) nanostructures are enhanced with Ti atomic concentration up to 10 at. % (x=0.10), with the magnetic saturation reaching almost twice that of the undoped HfO_2 nanowires. Further Ti doping appears to cause the magnetic properties to weaken. In the second part of this study, we investigate the morphological, structural, and magnetic properties of novel Fe-doped HfO_2 nanostructures ($Hf_{1-x}Fe_xO_2$; x=0.01, 0.05, 0.10 and 0.20) fabricated by catalyst-assisted PLD technique. Our results show that the Fe dopant concentration has a significant effect on the morphology of the $Hf_{1-x}Fe_xO_2$ nanostructures, producing nanocubes with stacked crystal flake composite architecture structure, instead of 1D nanostructures, when the Fe dopant concentration exceeds 1 at. % (x=0.01). Our magnetic property analyses show a remarkable increase in the magnetic saturation with increasing Fe dopant concentration, with two orders of magnitude larger than the undoped HfO_2 NWs for the x=0.10 dopant concentration and no trace of any Fe clustering or secondary phase segregation (within the sensitivity range of X-ray diffraction). To explain the observed magnetic behavior of the $Hf_{1-x}Ti_xO_2$ and $Hf_{1-x}Fe_xO_2$ nanostructures, we propose a modified hybrid model based on defect-induced BMPs and defect-band splitting. With their high magnetic saturation and T_c (above room temperature), along with their

inherently high dielectric constant, these novel Ti-doped and Fe-doped HfO_2 nanostructures promise new applications in integrated spintronics and CMOS-based electronics.

3.2 Experimental Details

The undoped (pristine) HfO_2, Ti-doped and Fe-doped HfO_2, and TiO_2 1D nanostructures are all grown by catalyst-assisted pulsed laser deposition in a NanoPLD system (PVD Products) with a base pressure of 1×10^{-6} Torr. The system is equipped with an excimer KrF laser (248 nm wavelength) operated with a laser fluence of 350 mJ/pulse at a repetition rate of 5 Hz to ablate the HfO_2, Ti-doped HfO_2 and Fe-doped HfO_2 and TiO_2 targets. The HfO_2 target is prepared by cold pressing of HfO_2 powder (Alfa Aesar, 99.9% purity) with a pressure of 30 MPa followed by sintering at 1150 ℃ for 48 h, and the TiO_2 target is prepared by cold pressing of rutile TiO_2 powder (Aldrich, 99.99% purity) with a pressure of 25 MPa followed by sintering at 900 ℃ for 12 h. To prepare Ti-doped HfO_2 target, HfO_2 powder (Alfa Aesar, 99.9% purity) is thoroughly ground and mixed with TiO_2 powder (Aldrich, 99.99% purity) with the Hf:Ti proportions of 0.99:0.01, 0.90:0.10, 0.75:0.25 and 0.50:0.50 to obtain the $Hf_{1-x}Ti_xO_2$ (x=0.01, 0.10, 0.25 and 0.50) targets. The resulting powder mixtures are cold pressed at 30 MPa and sintered at 1150 ℃ for 48 h. The Fe-doped HfO_2 targets are also prepared in a similar way by grinding and mixing HfO_2 powder (Alfa Aesar, 99.9% purity) with Fe nanopowder (Aldrich, 60-80 nm particle size, ≥99% purity). The resulting powder mixtures with the Hf:Fe proportions of 0.99:0.01, 0.95:0.05, 0.90:0.10 and 0.80:0.20 are cold pressed at 30 MPa and sintered at 1150 ℃ for 48 h to make the $Hf_{1-x}Fe_xO_2$ (x=0.01, 0.05, 0.10 and 0.20) targets. TiO_2 1D nanostructures are grown on oxidized Si(100) substrates (Ox-Si) coated with gold nanoislands (GNIs), denoted here as GNI/Ox-Si, while the other nanostructures are grown on Ox-Si coated with Sn-alloyed GNIs, denoted here as Sn-GNI/Ox-Si. To prepare the Ox-Si substrates, precut Si(100) chips (10×10 mm^2 and 5×5 mm^2, 525 μm thick, p-type, B-doped, with the resistivity of 1-5 Ω cm, Siegert Wafer GmbH) are chemically oxidized by following the RCA cleaning procedure.[159] The HF treatment step in the RCA cleaning procedure is not performed in order to obtain a buffer oxygen layer on the Si surface. GNIs are obtained by depositing a thin film of gold (<10 nm thick) on Ox-Si by magnetron sputtering followed by annealing in oxygen at 600 ℃ for 1 h. The resulting GNIs exhibit a Gaussian size distribution of 4-10 nm. To obtain the Sn-GNI/Ox-Si templates, we sputter-coat the substrate holder with Sn (99.9% purity, Fisher Scientific) prior to mounting inside the deposition chamber. When the substrate holder is brought up to the preselected growth temperature, Sn evaporates and mixes with GNIs on Ox-Si to create Sn-GNI alloy catalysts. For the growth process, the substrates are mounted in the PLD chamber perpendicular to the direction of the laser plume using a windowed substrate

holder. The substrate-to-target distance is kept at 25 mm, where the substrate is in close proximity to the top region of the laser plume. The growth temperature can be controlled from room temperature to 900 ℃ by using infrared heating lamps located at the backside of the substate holder to enable radiative heating. TiO_2 1D nanostructures are grown on GNI/Ox-Si templates at 750 ℃ for 90 min in 200 mTorr of Ar with a flow of 10 sccm, while pristine and Ti-doped and Fe-doped HfO_2 1D nanostructures are grown on Sn-GNI/Ox-Si templates at 770 ℃ for 60 min under the same Ar pressure and flow conditions.

The morphology of the nanostructures is examined by field-emission scanning electron microscopy (SEM) in a Zeiss Ultra-plus microscope and by helium ion microscopy (HIM) in a Zeiss ORION Plus microscope. The corresponding crystal structures of the as-grown nanostructures are determined by using glancing-incidence X-ray diffraction (GIXRD) at an incidence angle of ω=0.4° over the selected 2θ range in a PANalytical MRD X'pert Pro diffractometer equipped with a Cu Kα source (1.54 Å). For magnetic property measurements, the nanostructures grown on the 5×5 mm^2 substrates are mounted on clean quartz paddles. Extreme care is taken to eliminate any magnetic contamination from external sources by using only plastic tweezers and sample handling tools. Measurements are performed at different temperatures in a superconducting quantum interference device (SQUID) magnetometer (Quantum Design MPMS SQUID-VSM). The magnetic data is corrected by subtracting the diamagnetic contribution from the bare substrate and quartz paddle, and the magnetic moments of the nanostructured films so obtained are normalized by their masses. To estimate the mass of the nanostructured film, we assume that the film is densely packed within the measuring volume with the bulk densities of 9.68 g/cm^3 for undoped HfO_2,[189] $Hf_{1-x}Fe_xO_2$ (x=0.01, 0.05, 0.10 and 0.20), and $Hf_{1-x}Ti_xO_2$ (x=0.01, 0.10, 0.25); 7.28 g/cm^3 for $Hf_{0.50}Ti_{0.50}O_2$,[216] and 4.23 g/cm^3 for TiO_2[189] nanostructured films. Finally, the resulting data points are fitted to the ferromagnetic curves using sigmoid basis functions and hyperbolic functions in Hystlab version 1.0.9 software, which is a MATLAB-based software for processing magnetic data based on the correction methods of Jackson et al. and Paterson et al.[167,168]

3.3 Results and Discussion

3.3.1 SEM and XRD Studies

Figure 3-1 shows the SEM images of Ti-doped $Hf_{1-x}Ti_xO_2$ nanostructures with different dopant concentrations (x=0.01, 0.10, 0.25 and 0.50) and of TiO_2 nanobelts and undoped HfO_2 nanowires provided as reference. TiO_2 nanobelts are PLD-grown on GNI/Ox-Si in 200 mTorr of Ar at 750 ℃

for 90 min while the HfO_2 nanowires and $Hf_{1-x}Ti_xO_2$ nanostructures are grown on Sn-GNI/Ox-Si at 770°C. Evidently, the TiO_2 nanobelts so produced are typically 40-70 nm wide, 12-20 nm thick and several hundreds of nanometers long (Figure 3-1a2). With a pointy tip and sawtooth facets along the growth direction, the TiO_2 nanobelts grown here are found to have very similar morphology to those reported in an earlier study.[141] The periodic sawtooth sidewalls in these nanobelts indicate a periodic faceting along the growth direction, which is also observed in other VLS-grown NWs.[217,218] On the other hand, the HfO_2 NWs PLD-grown on Sn-GNI/Ox-Si templates at 770°C for 60 min (Figure 3-1b1) are more than 2 μm long and they appear to be tapered with a triangular cross section of side-length 100-150 nm near the base and 20 nm near the tip (Figure 3-1b2). The Ti-doped $Hf_{1-x}Ti_xO_2$ (x=0.01, 0.10, 0.25 and 0.50) nanostructures are grown under the same condition as the HfO_2 NWs. The nanostructures with 50 at. % Ti (x=0.50) correspond technically to a binary oxide alloy ($Hf_{0.50}Ti_{0.50}O_2$), but in the interest of simpler nonmenclature we refer to them as 50 at. % Ti-doped nanostructures in the present work. Evidently, as the concentration of Ti dopant increases, the morphology of the nanostructures changes from long and intertwined undoped HfO_2 NWs (Figure 3-1b1, b2) to 1-1.5 μm long nanospikes with 1 at.% and 10 at. % Ti doping (Figure 3-1c1,c2 and Figure 3-1d1, d2), and to several hundred nm long nanospikes with 25 at. % and 50 at. % Ti doping (Figure 3-1e1, e2 and Figure 3-1f1, f2). While the $Hf_{0.99}Ti_{0.01}O_2$ (1 at. % Ti-doped) and $Hf_{0.90}Ti_{0.10}O_2$ (10 at. % Ti-doped) nanospikes appear to have triangular cross sections similar to those found for the pristine HfO_2 NWs, the $Hf_{0.75}Ti_{0.25}O_2$ (25 at. % Ti-doped) and $Hf_{0.50}Ti_{0.50}O_2$ (50 at. % Ti-doped) nanospikes are shorter with hexagonal cross sections, with a side-length of 100-150 nm near the base and ~40 nm near the tip. Furthermore, the backscattered electron images (Figure 3-1 insets) depict the gold nanoislands at the tips of the nanostructures, confirming that VLS growth is the dominant growth mechanism of these nanostructures. However, the tapering of the nanostructures suggests that VS growth could still occur in the system, which could be responsible for the concurrent lateral growth of the nanostructures and the apparent tapering of the NWs and the nanospikes.[140,141] In addition, notable nanocrystals can be observed among the base of the NWs and nanospikes, which further supports a concurrent VS growth mode in this system.

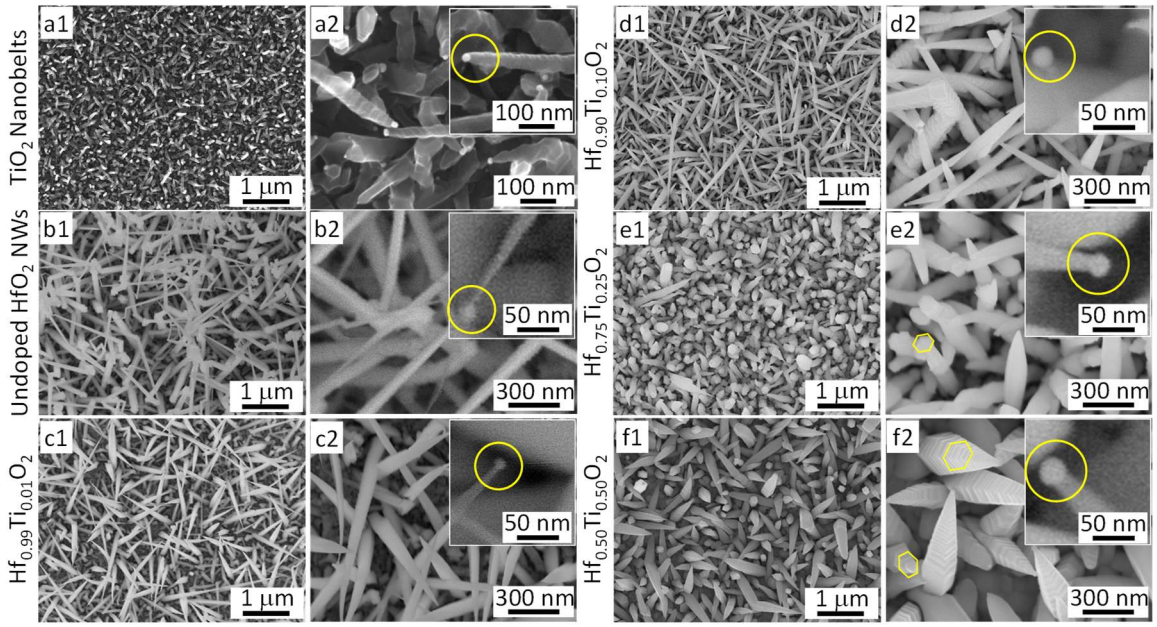

Figure 3-1. SEM images of (a1, a2) TiO_2 nanobelts grown on GNI/Ox-Si in 200 mTorr Ar for 90 min at 750 °C, (b1, b2) undoped HfO_2 NWs, (c1, c2) $Hf_{0.99}Ti_{0.01}O_2$ nanospikes, (d1, d2) $Hf_{0.90}Ti_{0.10}O_2$ nanospikes, (e1, e2) $Hf_{0.75}Ti_{0.25}O_2$ nanospikes, and (f1, f2) $Hf_{0.50}Ti_{0.50}O_2$ nanospikes, all grown on Sn-GNI/Ox-Si in 200 mTorr Ar for 60 min at 770 °C. The insets in (a2-f2) show backscattered electron images revealing the gold nano catalysts at the tip of the nanostructures.

A closer examination of the sidewalls of the nanostructures reveals that their surfaces are not smooth, and they have an oscillatory character that resembles the sawtooth-shaped sidewalls observed in TiO_2 nanobelts. The oscillatory character of the sidewall surface become more evident as the Ti content increases to 50 at. % (Figure 3-1f1, f2), which could similarly indicate an oscillatory growth process.[141,217] To achieve a more detailed view of the $Hf_{1-x}Ti_xO_2$ nanostructure surfaces, we employ helium ion microscopy with a greater depth of field and surface sensitivity than SEM to reveal more details of the nanostructure surfaces. Evidently, the HIM images shown in Figure 3-2 also confirm the increasingly more prominent oscillatory surface character of the nanostructures with increasing Ti content to 25 at. % and 50 at. % (Figure 3-2c and Figure 3-2d).

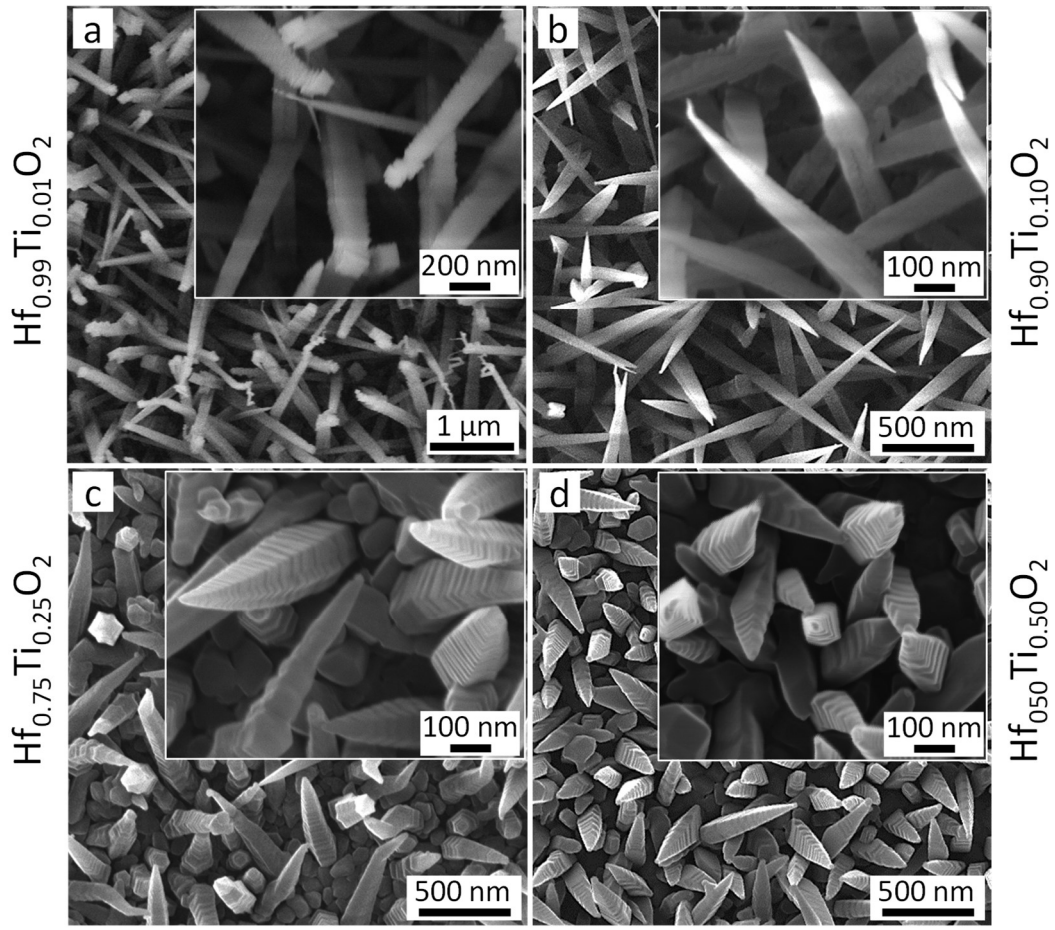

Figure 3-2. HIM images of (a) $Hf_{0.99}Ti_{0.01}O_2$, (b) $Hf_{0.90}Ti_{0.10}O_2$, (c) $Hf_{0.75}Ti_{0.25}O_2$ and (d) $Hf_{0.50}Ti_{0.50}O_2$ nanospikes all grown on Sn-GNI/Ox-Si templates at 770 °C. The high depth of field and surface sensitivity in HIM clearly reveals the oscillatory sidewall surface character of the nanostructures with higher concentrations of Ti shown in (c and d).

Figure 3-1 also shows that the TiO_2 nanobelts are considerably shorter than the HfO_2 NWs despite a longer deposition time (90 min vs. 60 min). Similarly, the Ti-doped nanospikes become shorter with increasing Ti dopant content. These observations suggest the VLS growth rate that determines the length of the nanowires becomes smaller as the Ti dopant content increases in the $Hf_{1-x}Ti_xO_2$ nanospikes and it reaches the lowest rate in the TiO_2 nanobelts. The sawtooth-like faceting of the sidewalls reflects the formation of high-surface-energy planes along the growth direction.[217,219] The formation of these higher-surface-energy planes along the axial growth direction could also explain the lower growth rate and, therefore, shorter length of the TiO_2 nanobelts and Ti-doped nanospikes with a higher Ti dopant content.

The corresponding glancing-incidence XRD (GIXRD) patterns of the undoped HfO_2 NWs and $Hf_{1-x}Ti_xO_2$ nanospikes (x=0.01, 0.10, 0.25 and 0.50) are shown in Figure 3-3. The diffraction peaks of HfO_2 NWs and $Hf_{1-x}Ti_xO_2$ nanospikes with Ti dopant content up to 25 at. % are in excellent accord with the monoclinic HfO_2 reference pattern (PDF #00-034-0104). Nonetheless, in the XRD pattern of the $Hf_{0.75}Ti_{0.25}O_2$ nanospikes, minor contribution (~15%) from the orthorhombic $HfTiO_4$ phase (PDF #00-040-0794) is also observed. On the other hand, the XRD pattern of the $Hf_{0.50}Ti_{0.50}O_2$ nanospikes show predominant orthorhombic $HfTiO_4$ contribution with very little contribution from the HfO_2 monoclinic phase. The GIXRD pattern of the TiO_2 nanobelts (shown in Figure A2, Appendix A) is also obtained, which confirms the as-grown TiO_2 nanobelts predominantly have a rutile crystal structure. Moreover, the diffraction peaks of these nanostructures all show sharp peaks with small widths, indicating their high level of crystallinity despite their nanometer size. It is important to note that no trace of tetragonal or cubic phase is observed in the XRD patterns of these nanostructures. Considering that oxygen vacancies could stabilize the tetragonal and cubic phases in HfO_2,[190–192] the absence of these phases suggests that the amount of vacancies in these nanostructures is not high or/and that these oxygen vacancies are mostly accumulated in the surface regions of the nanostructures. Interestingly, the relative intensities of the (200) peak in HfO_2 NWs and $Hf_{1-x}Ti_xO_2$ nanospikes (x=0.01, 0.10, 0.25) and the (020) peak in $Hf_{0.50}Ti_{0.50}O_2$ nanospikes are discernibly different from those of their corresponding reference patterns (PDF #00-034-0104 and PDF #00-040-0794). As the SEM images (Figure 3-1b1-f2) show that these nanostructures grow out of the substrate plane in a near-vertical fashion, the stronger relative intensities of the (200) and (020) peaks suggest that the (200) planes in HfO_2 NWs and $Hf_{1-x}Ti_xO_2$ nanospikes (x=0.01, 0.10, 0.25) and the (020) planes in $Hf_{0.50}Ti_{0.50}O_2$ nanospikes could correspond to one of the cross-sectional or lateral facet planes of these nanostructures. Further analysis such as HRTEM studies is required here to provide a more accurate assessment of the predominant growth direction of these nanostructures.

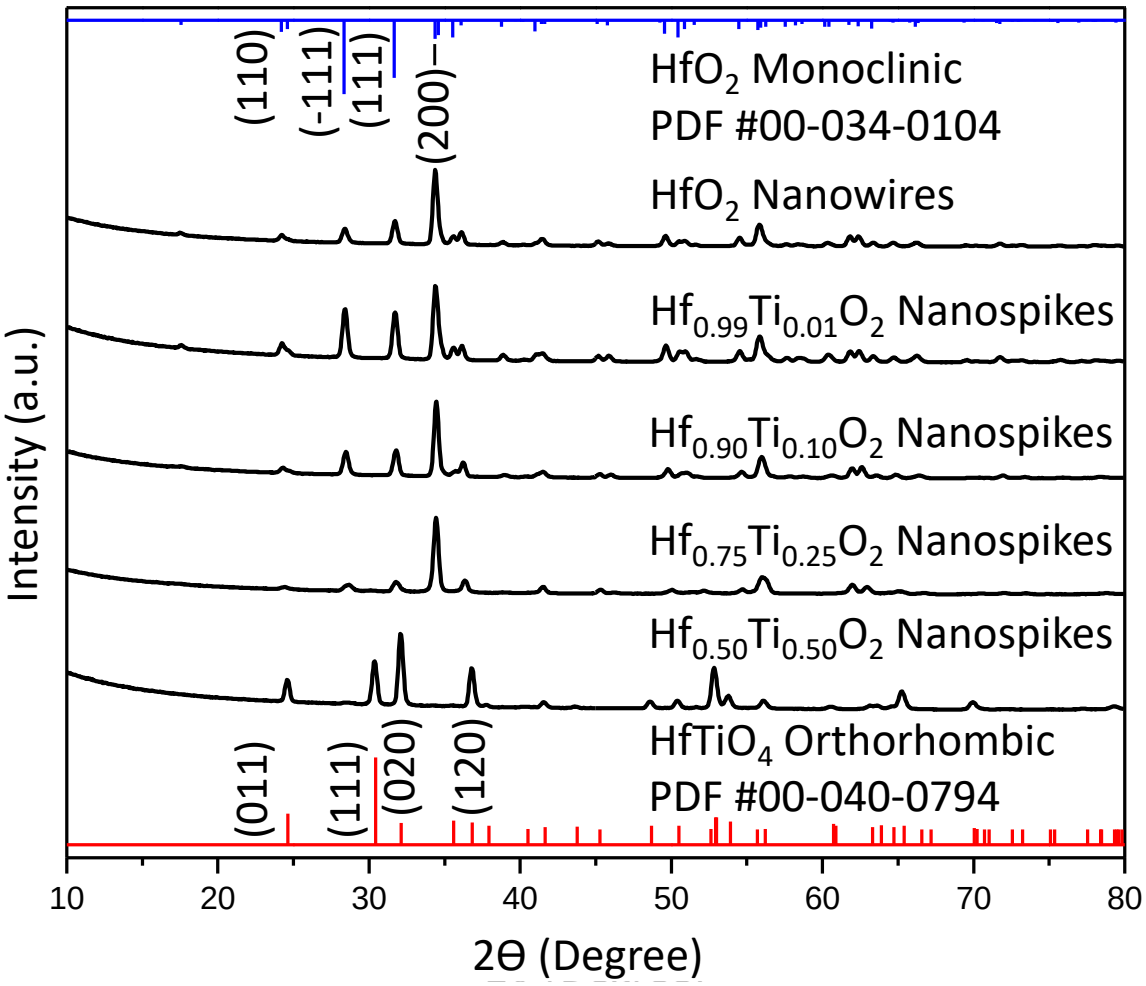

Figure 3-3. Glancing incidence XRD patterns of HfO_2 NWs and $Hf_{1-x}Ti_xO_2$ nanospikes (x=0.01, 0.10, 0.25 and 0.50) obtained at an incident angle of 0.4°. All nanostructures are grown on Sn-GNI/Ox-Si templates at 770°C in 200 mTorr of Ar for 60 min. The HfO_2 monoclinic (PDF #00-034-0104) and $HfTiO_4$ orthorhombic (PDF #00-040-0794) reference profiles are shown as the top and bottom bar graphs, respectively.

A closer examination of the GIXRD patterns of these nanostructures reveals minor position shifts of the diffraction peaks in Ti-doped nanostructures ($Hf_{1-x}Ti_xO_2$ nanospikes; x=0.01, 0.10, 0.25) relative to their respective peaks in undoped HfO_2 NWs. Table 3-1 provides the 2θ positions of the two prominent (111) and (200) peaks in Ti-doped $Hf_{1-x}Ti_xO_2$ nanopikes and their position shifts relative to their respective peaks in the undoped HfO_2 NWs. A 0.02° to 0.09° shift is observed when the structures are doped with Ti, indicating the substitution of larger Hf^{4+} ions with smaller Ti^{4+} in the

lattice. This is consistent with the smaller unit cell volume calculated for the doped nanostructures (from 138.2 $Å^3$ for 1 at. % Ti doping to 135.7 $Å^3$ for 25 at. % Ti doping) compared to that of the undoped HfO_2 NWs (138.6 $Å^3$), and with the probable formation of substitutional solid solution of Ti in HfO_2 lattice.

Table 3-1. Comparison of the position shifts of the two prominent (111) and (200) peaks in Ti-doped $Hf_{1-x}Ti_xO_2$ nanospikes relative to their respective peaks in the undoped HfO_2 NWs.

Plane Index	HfO_2 Nanowires 2θ (°)	$Hf_{0.99}Ti_{0.01}O_2$ Nanopikes		$Hf_{0.90}Ti_{0.10}O_2$ Nanopikes		$Hf_{0.75}Ti_{0.25}O_2$ Nanopikes	
		2θ (°)	Shift (°)	2θ (°)	Shift (°)	2θ (°)	Shift (°)
(1 1 1)	31.71	31.73	0.02	31.80	0.09	31.75	0.04
(2 0 0)	34.37	34.38	0.01	34.44	0.07	34.44	0.07

Figure 3-4 shows the SEM images of Fe-doped $Hf_{1-x}Fe_xO_2$ nanostructures with different dopant content (x=0.01, 0.05, 0.10 and 0.20). All the nanostructures are grown on chemically oxidized Si substrates (Ox-Si) seeded with Sn-alloyed gold nanoislands (Sn-GNI/Ox-Si templates) at 770 ℃ in 200 mTorr of Ar. PLD of 1 at. % Fe-doped HfO_2 target ($Hf_{0.99}Fe_{0.01}O_2$) on Sn-GNI/Ox-Si templates produces nanospikes similar to $Hf_{0.99}Ti_{0.01}O_2$ nanospikes (Figure 3-1c1, c2), typically ~20 nm wide near the tip, 100-150 nm wide near the base and ~1 μm long (Figure 3-4a1, a2). The corresponding backscattered electron image of a $Hf_{0.99}Fe_{0.01}O_2$ nanospike shown in Figure 3-4a1 inset confirms the presence of the gold nanocatalyst at the tip of the nanospike and that the catalyst-assisted VLS growth is also the dominant growth mechanism for these nanospikes. Moreover, a closer examination of these sidewall surfaces of the nanospikes (Figure 3-4a2 inset) reveals that they also have facets with periodic oscillatory features similar to those found on Ti-doped $Hf_{1-x}Ti_xO_2$ nanospikes, indicating the oscillatory nature of their growth process. Interestingly, the morphologies of the Fe-doped HfO_2 ($Hf_{1-x}Fe_xO_2$) nanostructures change dramatically to distorted nanocubes with a typical 300-500 nm edge length and a stacked crystal flake composite architecture as the dopant concentration (x) is increased to 5 at. %, 10 at. % and 20 at. % (Figure 3-4b1-d2). The crystal flakes that are stacked irregularly on top of one another to form the distorted nanocubes appear to have a broad size distribution of 20-100 nm. For simplicity, we refer to 5 at. %, 10 at. % and 20 at. % Fe-doped HfO_2 nanocubes (NCs) hereafter as NC5, NC10 and NC20, respectively. It is important to note that for the Fe dopant concentration exceeding 1 at. %, no 1D nanostructure is produced, which indicates that the

VLS growth is significantly suppressed by the increased concentration of Fe. As discussed in our previous work, when Sn is alloyed with GNIs, the surface energy of the resultant Sn-GNIs at the liquid-solid interface (γ_{LS}) is reduced. Since the VLS nucleation rate (j_{VLS}) is inversely proportional to $\exp(\gamma_{LS})$, the VLS nucleation rate is enhanced, which results in the VLS growth outpacing the competing VS growth. As Fe has a higher surface energy than many other metals such as Au, Sn, Ni and Cu, Fe is expected to increase the surface energy upon alloying with other metals, which is already shown for Ni-Fe and Cu-Fe alloys.[214,215] Increasing the Fe dopant concentration could therefore increase the surface energy of the GNIs at the liquid-solid interface and consequently lead to the reduction of VLS nucleation rate. As a result, the VLS growth of 1D nanostructures such as nanospikes (Figure 3-4a1, a2) is significantly suppressed and VS-grown distorted nanocubes (Figure 3-4b1-d2) are produced.

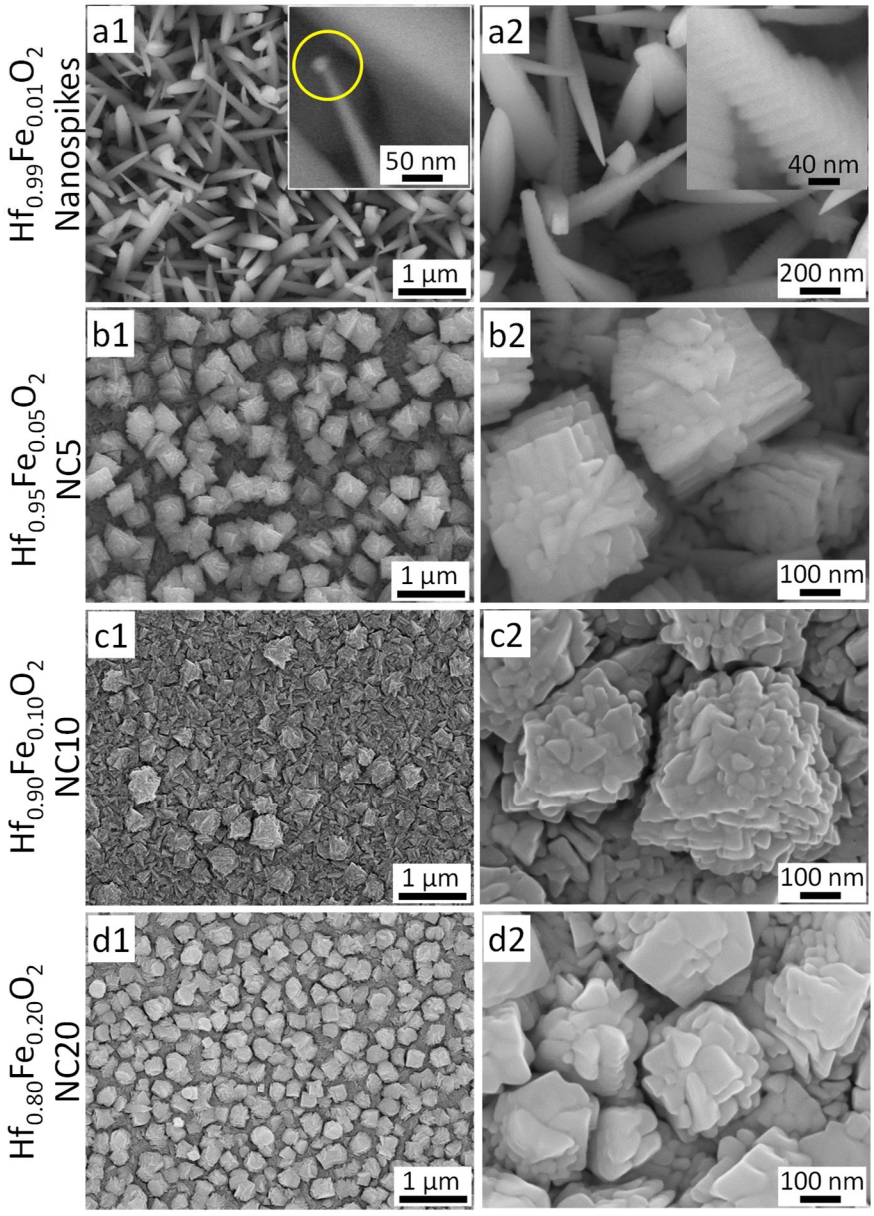

Figure 3-4. SEM images of (a1, a2) $Hf_{0.99}Fe_{0.01}O_2$ nanospikes, distorted nanocubes with a stacked flake composite architecture of (b1, b2) $Hf_{0.95}Fe_{0.05}O_2$, (c1, c2) $Hf_{0.90}Fe_{0.10}O_2$, and (d1, d2) $Hf_{0.80}Fe_{0.20}O_2$, all grown on Sn-GNI/Ox-Si templates at 770 °C.

Figure 3-5 compares the corresponding glancing-incidence XRD patterns of the Fe-doped HfO_2 nanospikes and distorted nanocubes (obtained with different Fe dopant concentrations) and undoped HfO_2 NWs. The diffraction peaks of the as-grown nanostructures are in good accord with the monoclinic HfO_2 reference pattern (PDF #00-034-0104). The nanostructures all show sharp

diffraction peaks with small peak widths indicating their high crystalline quality. More importantly, no diffraction peaks attributable to Fe metal or Fe oxides are observed for any of the Fe-doped HfO_2 nanostructures. The absence of any Fe-related secondary phase suggests that dopant segregation resulting in magnetic clustering is not likely in our nanostructures (or/and that the amount of the magnetic clustering in the host lattices is lower than the typical detection limit of our XRD system).

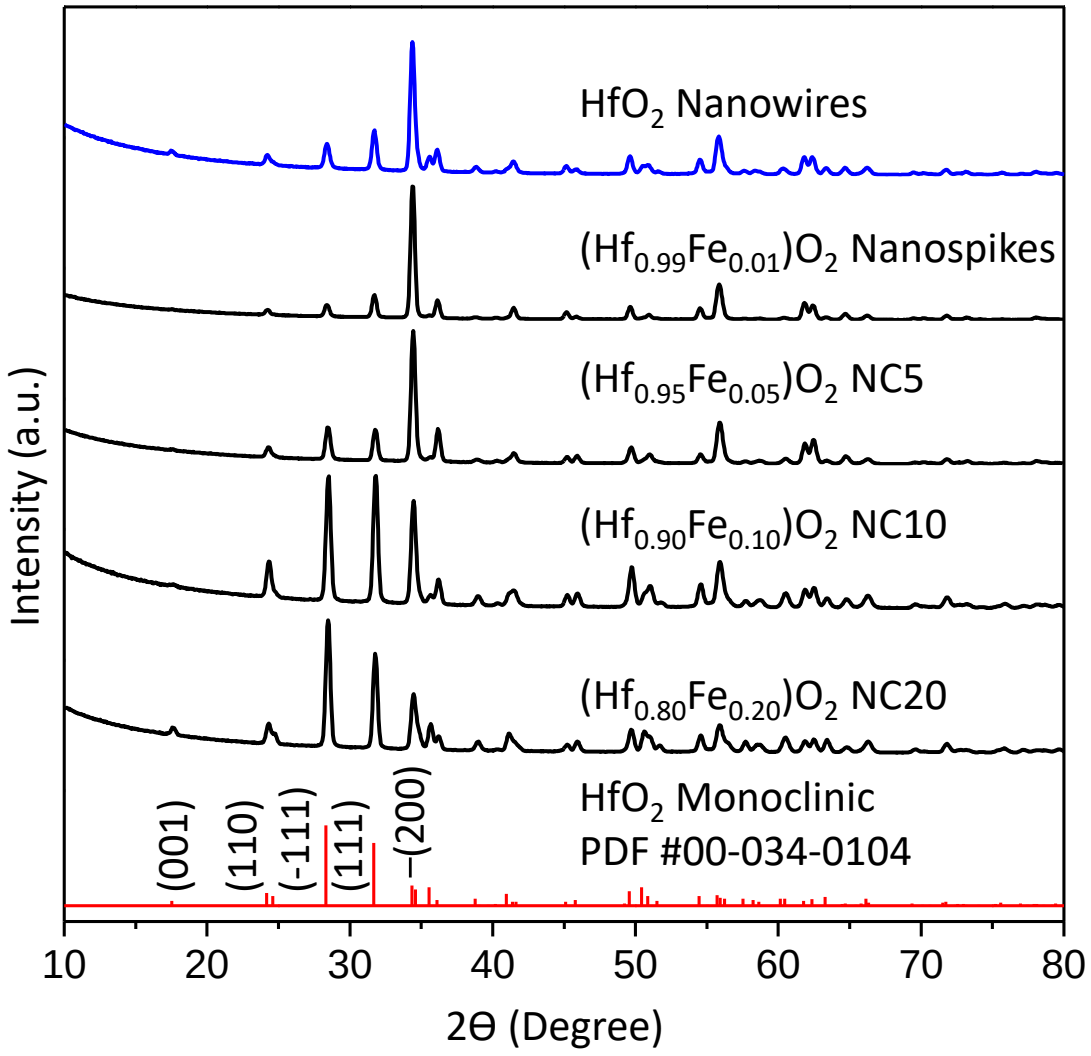

Figure 3-5. Glancing incidence XRD patterns of HfO_2 NWs and $Hf_{1-x}Fe_xO_2$ nanostructures (x=0.01, 0.05, 0.10 and 0.20) obtained at an incident angle of 0.4°. All nanostructures are grown on Sn-GNI/Ox-Si templates at 770°C in 200 mTorr of Ar for 60 min. The HfO_2 monoclinic (PDF #00-034-0104) reference pattern is represented as the bottom bar graph.

A closer examination of the XRD patterns reveals that the positions of the diffraction peaks in the Fe-doped nanostructures appear to shift to a higher 2θ angle, relative to those of the undoped HfO_2 NWs, with increasing Fe dopant concentration. The peak positions of the prominent (111) and (200) peaks in the Fe-doped nanostructures and their peak shifts relative to their respective peaks in undoped HfO_2 NWs are summarized in Table 3-2. When the HfO_2 lattice is doped with Fe, the larger Hf^{4+} ions with an ionic radius of 0.84 Å[222] can be substituted with the smaller Fe^{3+} and/or Fe^{2+} ions with ionic radii of 0.49 Å and 0.64 Å, respectively.[223] The peak shifts of the Fe-doped $Hf_{1-x}Fe_xO_2$ nanostructures toward higher 2θ values, therefore, indicate substitutional incorporation of Fe into the HfO_2 lattice. Moreover, the reduction of calculated unit cell volumes with doping from 138.65 $Å^3$ of undoped HfO_2 NWs to 138.17 $Å^3$, 137.64 $Å^3$, 136.45 $Å^3$, and 137.00 $Å^3$ of $Hf_{0.99}Fe_{0.01}O_2$ nanospikes, $Hf_{0.95}Fe_{0.05}O_2$ NC5, $Hf_{0.90}Fe_{0.10}O_2$ NC10 and $Hf_{0.80}Fe_{0.20}O_2$ NC20, respectively, also confirms the substitutional incorporation of Fe into the host lattice. It is important to note that the unit cell volume of $Hf_{0.80}Fe_{0.20}O_2$ NC20 (137.00 $Å^3$) is slightly larger than that of $Hf_{0.90}Fe_{0.10}O_2$ NC10 (136.45 $Å^3$) and their peak position shifts are found to be smaller than $Hf_{0.90}Fe_{0.10}O_2$ NC10 (Table 3-2). The slight expansion of the lattice in $Hf_{0.80}Fe_{0.20}O_2$ NC20 relative to $Hf_{0.90}Fe_{0.10}O_2$ NC10 suggests some Fe ions are likely interstitially incorporated into the lattice, which could lead to the potential formation of magnetic clusters in the lattice. Although the amount of such clustering could be too small to be detected by XRD, they could significantly influence the magnetic behavior of the nanostructures and give rise to the extrinsic magnetic properties. This matter will be discussed in more detail in the next section.

Table 3-2. Comparison of the position shifts of the prominent (111) and (200) peaks in Fe-doped $Hf_{1-x}Fe_xO_2$ nanostructures relative to their respective peaks in the undoped HfO_2 NWs

Plane Index	HfO_2 Nanowires 2θ (°)	Nanospikes (1 at. % Fe)		NC5 (5 at. % Fe)		NC10 (10 at. % Fe)		NC20 (20 at. % Fe)	
		2θ (°)	Shift (°)	2θ (°)	Shift (°)	Pos (°)	Shift (°)	Pos (°)	Shift (°)
(1 1 1)	31.71	31.73	0.02	31.79	0.08	31.81	0.10	31.77	0.06
(2 0 0)	34.37	34.40	0.03	34.43	0.06	34.46	0.09	34.44	0.07

3.3.2 Magnetic Properties

In the previous chapter, we report the remarkable room-temperature ferromagnetism found for PLD-grown HfO_2 NWs while the nanostructured HfO_2 films show very weak paramagnetic behavior. Although the high crystal quality of our single-crystalline HfO_2 NWs enables us to perform a detailed study on the exact nature of defects in our HfO_2 NWs and to obtain direct evidence for oxygen vacancy-induced ferromagnetism in these nanostructures, the total magnetic saturation of these nanostructures needs to be improved.

An effective strategy to create ferromagnetism or to improve ferromagnetic properties in semiconducting or insulating oxides is dilute doping of these materials with transition-metal ions, which creates a novel class of advanced materials generally known as Dilute magnetic Semiconducting Oxides (DMSO).[26,45] Indeed, this doping method has been widely used particularly to make ferromagnetic ZnO and TiO_2, despite the major challenge in producing a homogeneous distribution of magnetic ions within the host lattice.[26,45] Although the origin of ferromagnetism in DMSOs is still a matter of controversy, the general belief is that the magnetic properties of DMSOs with intrinsic magnetic properties do not originate directly from the magnetic dopants but originates from the structural defects and the oxygen vacancies likely induced by the magnetic dopants in the lattice.[62,68,102,103,214] The hypothesis that the defects and oxygen vacancies are the primary contributor to the ferromagnetism in these materials is supported by the observation of ferromagnetism in undoped metal oxides such as HfO_2 films,[96,98,152] In_2O_3 film,[152] TiO_2 films,[152,224] and ZrO_2 nanostructures.[63,64] Since theoretical calculations have shown that the formation energy of oxygen vacancies in different polymorphs of HfO_2 can be modified by the non-magnetic dopants such as Ti, Si, La and Al,[169,170] doping HfO_2 nanostructures with Ti dopants is also expected to affect their ferromagnetic properties. In this section, we first discuss the effect of doping of Ti as a nonmagnetic ion on the magnetic behavior of HfO_2 nanostructures followed by that of a magnetic ion such as Fe. Magnetization curves of the samples are obtained after the diamagnetic contribution of the substrate and the quartz paddle is removed from the signal, The resulting data is then fitted with a combination of hyperbolic and sigmoid functions based on the correction methods of Jackson et al. and Paterson et al.[167,168] using the Hystlab v1.0.9 software.

Figure 3-6 shows the magnetization of $Hf_{1-x}Ti_xO_2$ (x=0.01, 0.10, 0.25) nanospikes and TiO_2 nanobelts as a function of the applied magnetic field measured at 2 K and room temperature. The magnetization curve of $Hf_{0.50}Ti_{0.50}O_2$ nanospikes at room temperature is also measured, but it is not shown here due to its very similar hysteresis loop to that of $Hf_{0.75}Ti_{0.25}O_2$ nanospikes. The low

temperature (2 K) magnetization of $Hf_{0.50}Ti_{0.50}O_2$ nanospikes is not shown because of their similar magnetic property to that of $Hf_{0.75}Ti_{0.25}O_2$ nanospikes. Evidently, all nanostructures exhibit a ferromagnetic hysteresis loop both at 2 K and room temperature. However, the magnetic saturation of the TiO_2 nanobelts measured at 7000 Oe at 300 K (3.9×10^{-3} emu/g) and at 2 K (2.1×10^{-2} emu/g) are respectively 2-3 times and 4-5 times higher than the corresponding values of the $Hf_{1-x}Ti_xO_2$ nanospikes (1.4- 2.3×10^{-3} emu/g at 300 K and 4.2- 4.8×10^{-3} emu/g at 2 K). Moreover, the magnetic saturation (M_s) and the magnetic remanence (M_r) (Figure 3-6a-c insets) of all nanostructures show a higher value when the measurement is performed at a lower temperature. The temperature dependence of the M_s and M_r suggest that the magnetization behavior of these nanostructures may not be purely ferromagnetic and a weak superparamagnetic component could also contribute to the total magnetization.[225]

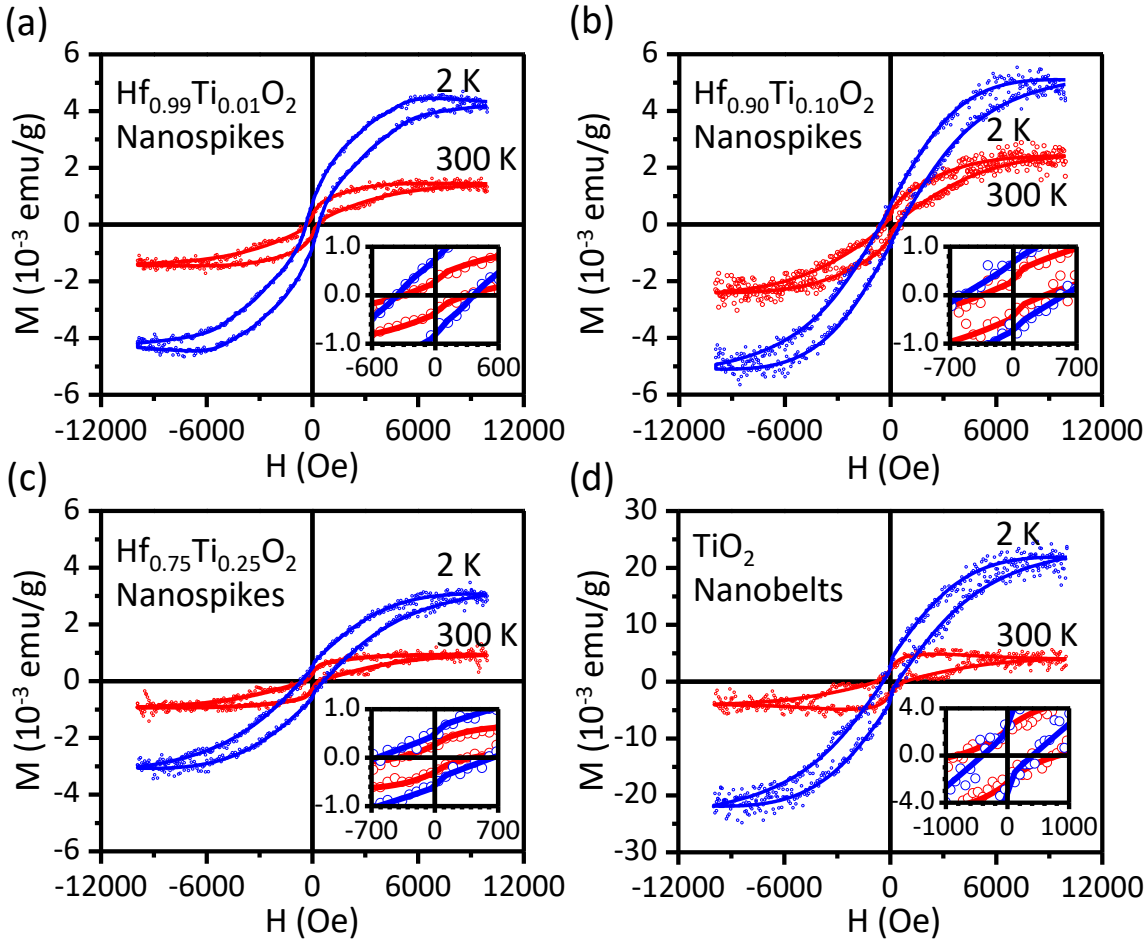

Figure 3-6. Magnetization M as a function of applied magnetic field (raw data points) and their corresponding fitted hysteresis loops (solid lines) of (a) $Hf_{0.99}Ti_{0.01}O_2$ nanospikes, (b) $Hf_{0.90}Ti_{0.10}O_2$ nanospikes, (c) $Hf_{0.75}Ti_{0.25}O_2$ nanospikes, and (d) TiO_2 nanobelts measured at 2 K and 300 K.

Figure 3-7a compares the magnetization curves of the $Hf_{1-x}Ti_xO_2$ (x=0.01, 0.10, 0.25) nanospikes and HfO_2 nanowires measured at room temperature. The magnetization curve of the HfO_2 NWs has been reported in our previous work (Chapter 2). Evidently, all nanostructures reach magnetization saturation at about 7000 Oe and the M_s value appears to depend on the concentration of Ti dopants. Characteristic magnetization parameters: M_s, M_r and coercivity (H_c) of the $Hf_{1-x}Ti_xO_2$ (x=0.01, 0.10, 0.25, 0.50) nanospikes, HfO_2 NWs and TiO_2 nanobelts are summarized in Table 3-3. At 300 K, the M_s value of the HfO_2 NWs (1.2×10^{-3} emu/g) is found to increase slightly when doped with 1 at. % Ti in $Hf_{0.99}Ti_{0.01}O_2$ nanospikes (1.4×10^{-3} emu/g), and nearly doubles with 10 at. % Ti doping in the

$Hf_{0.90}Ti_{0.10}O_2$ nanospikes (2.3×10^3 emu/g). The increasing trend of M_s, however, does not continue, and it drops to 0.9-1×10^{-3} emu/g when the nanostructures are doped with 25 at. % and 50 at. % of Ti in $Hf_{0.75}Ti_{0.25}O_2$ nanospikes and $Hf_{0.50}Ti_{0.50}O_2$ nanospikes, respectively. For TiO_2 nanobelts (x=1), its M_s reaches the highest saturation value of 3.9×10^{-3} emu/g among all the nanostructures. The described trend of M_s in $Hf_{1-x}Ti_xO_2$ ($0\leq x\leq1$) nanostructures with increasing Ti dopant concentration at room temperature is illustrated in Figure 3-7b. The M_s of the nanostructures at 2 K also exhibit a similar trend increasing from 2.5×10^{-3} emu/g in pristine HfO_2 NWs to 4.8×10^{-3} emu/g in $Hf_{0.90}Ti_{0.10}O_2$ nanospikes followed by a decrease to 3×10^{-3} emu/g in $Hf_{0.75}Ti_{0.25}O_2$ nanospikes. Similarly, TiO_2 nanobelts exhibit the highest M_s at 2 K (21.1×10^{-3} emu/g).

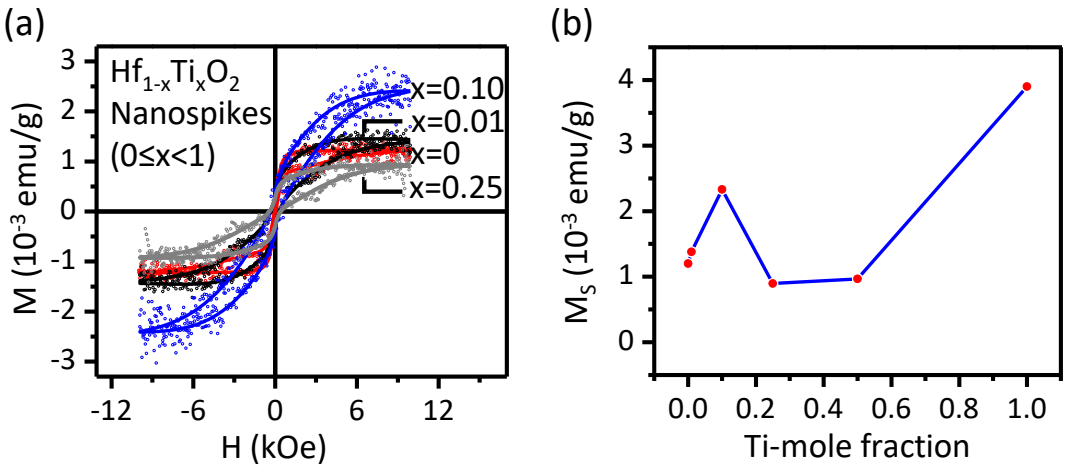

Figure 3-7. (a) Magnetization as a function of applied magnetic field (M-H curves) of $Hf_{1-x}Ti_xO_2$ nanospikes (x=0.01, 0.10, 0.25) and HfO_2 NWs (x=0). (b). The variation of the magnetic saturation (M_s) at 300 K in the $Hf_{1-x}Ti_xO_2$ nanostructures along with TiO_2 nanobelts with the Ti dopant concentration ($0\leq x\leq1$).

Table 3-3. Magnetic saturation (M_s), magnetic remanence (M_r) and coercivity (H_c) of the $Hf_{1-x}Ti_xO_2$ nanospikes, HfO_2 NWs and TiO_2 nanobelts obtained at 2 K and 300 K.

Sample	Measurement Temperature (K)	M_s (emu/g) $\times 10^{-3}$	M_r (emu/g) $\times 10^{-4}$	H_c (Oe)
HfO_2 NWs[a]	300	1.2	0.8	29
	2	2.5	2.0	160
$Hf_{0.99}Ti_{0.01}O_2$ Nanospikes	300	1.4	3.2	312
	2	4.2	7.3	362
$Hf_{0.90}Ti_{0.10}O_2$ Nanospikes	300	2.3	3.2	431
	2	4.8	7	547
$Hf_{0.75}Ti_{0.25}O_2$ Nanospikes	300	0.9	2.6	417
	2	3.0	5.2	663
$Hf_{0.50}Ti_{0.50}O_2$ Nanospikes[b]	300	1.0	3.3	219
TiO_2 Nanobelts	300	3.9	17.5	702
	2	21.1	25.0	597

[a]The magnetic characteristics of HfO_2 NWs are reported from our previous work. [b]The magnetic measurement of $Hf_{0.50}Ti_{0.50}O_2$ Nanospikes at 2 K is not performed due to their similar properties to $Hf_{0.75}Ti_{0.25}O_2$ Nanospikes.

It is generally believed that oxygen vacancies are the original source of room-temperature ferromagnetism in dilute magnetic semiconducting and/or insulating metal oxides.[26,68] Using the BMP-hybridized impurity band structure model, we have explained the origin of room-temperature magnetization in HfO_2 NWs observed in our previous work (Chapter 2). In the BMP model, the oxygen vacancies act as a charge reservoir, transferring one or two of their electrons to the surrounding $Hf^{4+}(5d^0)$ ions and reducing them to $Hf^{3+}(5d^1)$ ions. The zero-spin Hf^{4+} ions become non-zero spin Hf^{3+} ions and serve as F-centers (ferromagnetic-centers). The magnetic exchange coupling of these F-centers with one another and with the remaining electrons on the oxygen vacancies leads to the formation of BMPs. When the amount of oxygen vacancies is sufficient, the concentration of the BMPs surpasses the polaron percolation threshold, creating long-range ferromagnetic order throughout the material due to the substantial overlap among the BMPs. Although the BMP model can explain the long-range ferromagnetic ordering in HfO_2 nanostructures, it cannot explain their high Curie temperature. A hybridized band structure model is therefore

employed to explain the high Curie temperature of dilute magnetic metal oxides, including ZrO_2 and HfO_2.[63,68] In this model, the oxygen vacancies create an impurity band close to the bottom of the conduction band. For a high enough amount of oxygen vacancies, the impurity band hybridizes with the unoccupied Hf 5d states. When an electron is transferred from the oxygen vacancies to the unoccupied Hf 5d states at the Fermi level to create BMPs, the hybridized impurity band undergoes a spin-up and spin-down band splitting, which leads to high Curie temperature ferromagnetism in HfO_2 nanostructures.

In the case of Ti-doped HfO_2 nanospikes ($Hf_{1-x}Ti_xO_2$ nanospikes) and TiO_2 nanobelts, theoretical calculations show that the formation energy of oxygen vacancy in TiO_2 is lower than HfO_2.[226] More oxygen vacancies are therefore expected to form in the TiO_2 nanobelts, which results in the formation of more BMPs. The larger number of BMPs in TiO_2 nanobelts could explain their highest magnetic saturation among all the nanostructures studied in the present work. Similarly, according to theoretical calculations,[169,170] the formation energy of oxygen vacancy in HfO_2 nanostructures is reduced when doped with Ti ions. The amount of oxygen vacancies could therefore increase with Ti doping, which creates more overlapping BMPs and consequently higher magnetic saturation values in Ti-doped HfO_2 nanospikes. This explanation is consistent with our observation of the higher M_s value found for the $Hf_{0.99}Ti_{0.01}O_2$ nanospikes (1 at. % Ti doping) and $Hf_{0.90}Ti_{0.10}O_2$ (10 at. % Ti doping) than that for the HfO_2 NWs. However, to provide a possible explanation for the lower M_s values for the $Hf_{0.75}Ti_{0.25}O_2$ (25 at. % Ti doping) and $Hf_{0.50}Ti_{0.50}O_2$ (50 at. % Ti doping) nanospikes, we need to consider the effective parameters on the oxygen vacancy formation energy in the lattice. The required energy for oxygen vacancy formation depends on many parameters such as bandgap energy (E_g), atomic coordination, the strengths of metal-oxygen bonds relative to the bond strength in pure elements, bond lengths[226] and even bond angles.[227] The XRD patterns of the PLD-grown nanostructures (Figure 3-3) show that the $Hf_{1-x}Ti_xO_2$ (x=0.01, 0.10) nanospikes crystalize in the monoclinic phase (space group P21/a) similar to the HfO_2 NWs, while the $Hf_{0.50}Ti_{0.50}O_2$ nanospikes (50 at. % Ti doping) consist mainly of orthorhombic $HfTiO_4$ phase (space group: Pnab) and the $Hf_{0.75}Ti_{0.25}O_2$ nanospikes (25 at. % Ti doping) consist of ~15% orthorhombic $HfTiO_4$ phase. The oxygen atoms in monoclinic HfO_2 are located in four-fold or three-fold coordinated sites[170,228,229] (Figure 3-8a), while in orthorhombic $HfTiO_4$, they are located in three-fold sites with different bond angles (Figure 3-8b). Though the oxygen vacancy formation energy in orthorhombic $HfTiO_4$ has not been reported in the literature, it is expected to be higher than the oxygen vacancy formation energy in monoclinic HfO_2 due to the different configuration of surrounding cations. The observed lower M_s

values in $Hf_{0.50}Ti_{0.50}O_2$ and $Hf_{0.75}Ti_{0.25}O_2$ nanospikes could therefore be attributed to their different crystal structures that increase the oxygen vacancy formation energies in these nanostructures.

It is noteworthy that, despite the improvement in the magnetic saturation of the HfO_2 NWs with Ti doping, M_s is still one to three orders of magnitude smaller than those of undoped HfO_2 thin films and nanoparticles or ZrO_2 nanostructures reported in the literature.[63,64,98,152,174,175] In our previous work, we attribute the smaller magnetic saturation in HfO_2 NWs to the presence of oxygen vacancies in the surface region (and not throughout the bulk), which limits the long-range ferromagnetic ordering only to the surface region. This hypothesis is supported by our depth-profiling XPS studies that confirm the location of oxygen vacancies mainly in the near-surface region of the HfO_2 NWs. In contrast, the other nanostructures reported in the literature could additionally have oxygen vacancies distributed inside the bulk of their respective nanostructures, thus producing BMPs that percolate throughout the entire material. One collaborating observation for this hypothesis is the tetragonal phase found in the ZrO_2 nanostructures with high magnetic saturation.[63,64] The tetragonal phase is believed to become stabilized at room temperature due to the presence of structural defects, including oxygen vacancies.[190–192] Like HfO_2 NWs, the low magnetic saturation of the $Hf_{1-x}Ti_xO_2$ nanospikes in the present study also suggests that the oxygen vacancies are mainly located and therefore generate ferromagnetic ordering in the surface region. Doping HfO_2 nanostructures with Ti, despite increasing the amount of oxygen vacancies in the surface region, appears inadequate to create sufficient oxygen vacancies inside the bulk of nanostructures necessary to attain high magnetic saturation values.

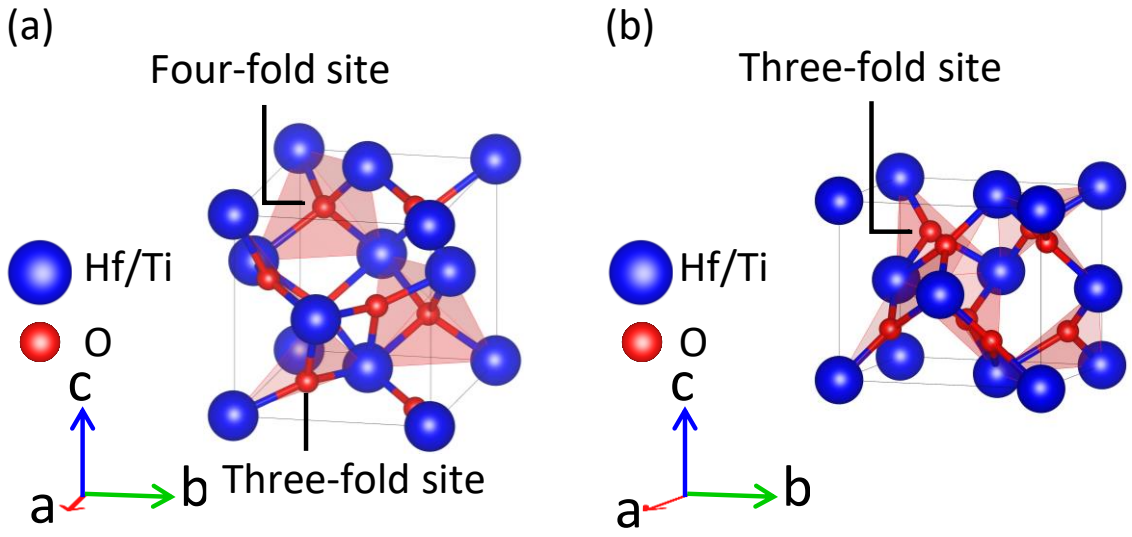

Figure 3-8. Unit cells of (a) monoclinic Ti-doped HfO_2 nanospikes ($Hf_{1-x}Ti_xO_2$; x=0.01, 0.10) and (b) orthorhombic $Hf_{0.50}Ti_{0.50}O_2$ nanospikes, depicting both three-fold and four-fold coordinated oxygen sites in (a) and only three-fold coordinated oxygen sites in (b).

Figure 3-9 shows the room-temperature magnetization curves (the M-H curves) of $Hf_{0.99}Fe_{0.01}O_2$ nanospikes, $Hf_{0.95}Fe_{0.05}O_2$ NC5, $Hf_{0.90}Fe_{0.10}O_2$ NC10 and $Hf_{0.80}Fe_{0.20}O_2$ NC20. Evidently, the $Hf_{1-x}Fe_xO_2$ nanostructures with x=0.01, 0.05 and 0.10 (Figure 3-9a-c) exhibit well-defined ferromagnetic hystereses at room temperature while $Hf_{0.80}Fe_{0.20}O_2$ NC20 (Figure 3-9d) shows a superparamagnetic characteristic. The magnetization parameters (M_s, M_r, and H_c) as well as M_r/M_s of these Fe-doped nanostructures are summarized in Table 3-4. Interestingly, the minimally Fe-doped $Hf_{0.99}Fe_{0.01}O_2$ nanospikes are found to exhibit the lowest magnetic saturation (8.6×10^{-4} emu/g), which is even lower than that found for the undoped HfO_2 nanowires (1.2×10^{-3} emu/g), indicating that doping of the HfO_2 nanostructure up to 1 at. % is not promoting any additional ferromagnetic ordering but instead may activate more antiferromagnetic interactions in the lattice. However, with the dopant concentration increased to 5 at. %, $Hf_{0.95}Fe_{0.05}O_2$ NC5 exhibits a magnetic saturation as large as 0.05 emu/g, i.e., more than one order of magnitude larger than that of $Hf_{0.99}Fe_{0.01}O_2$ nanospikes. The M_s in Fe-doped HfO_2 nanostructures becomes even higher with Fe doping, reaching 0.5 emu/g for $Hf_{0.90}Fe_{0.10}O_2$ NC10 (two orders of magnitude larger than the 1 at. % Fe-doped nanospikes) and 2.64 emu/g for $Hf_{0.80}Fe_{0.20}O_2$ NC20 (three orders of magnitude larger than the 1 at. % Fe-doped nanospikes).

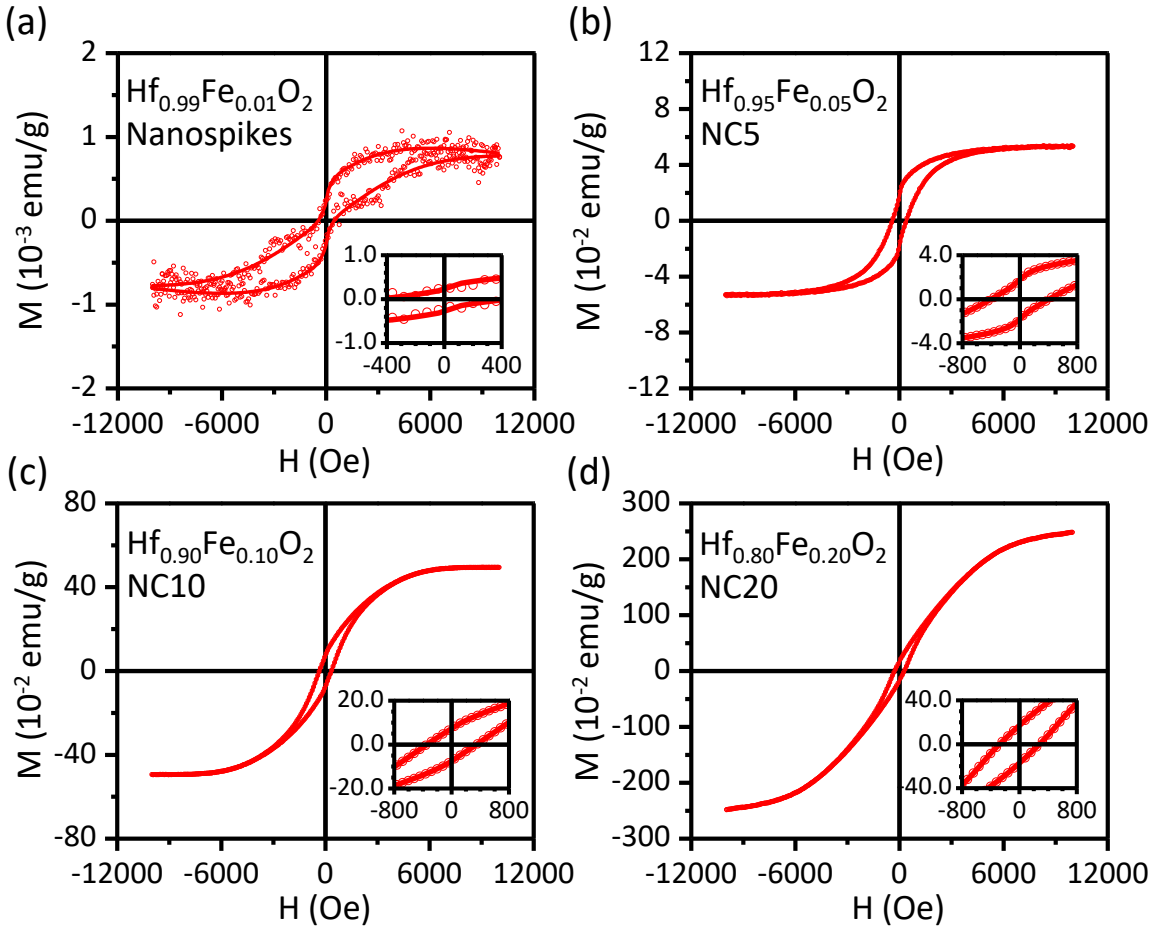

Figure 3-9. Room-temperature magnetization curves (M-H curves) of (a) $Hf_{0.99}Fe_{0.01}O_2$ nanospikes (b) $Hf_{0.95}Fe_{0.05}O_2$ NC5 (c) $Hf_{0.90}Fe_{0.10}O_2$ NC10 and (d) $Hf_{0.80}Fe_{0.20}O_2$ NC20.

Table 3-4. Magnetic saturation (M_s), magnetic remanence (M_r), coercivity (H_c) and magnetic remanence to magnetic saturation ratio (M_r/M_s) of $Hf_{0.99}Fe_{0.01}O_2$ nanospikes, $Hf_{0.95}Fe_{0.05}O_2$ NC5, $Hf_{0.90}Fe_{0.10}O_2$ NC10 and $Hf_{0.80}Fe_{0.20}O_2$ NC20 measured at 300 K and 2 K

Sample	Measurement Temperature (K)	M_s (emu/g)	M_r (emu/g)	H_c (Oe)	M_r/M_s
$Hf_{0.99}Fe_{0.01}O_2$ Nanospikes*	300	8.6×10^{-4}	2.5×10^{-4}	461	0.29
$Hf_{0.95}Fe_{0.05}O_2$ NC5	300	0.05	0.02	403	0.33
	2	0.08	0.03	1000	0.37
$Hf_{0.90}Fe_{0.10}O_2$ NC10	300	0.49	0.07	346	0.15
	2	0.53	0.10	590	0.20
$Hf_{0.80}Fe_{0.20}O_2$ NC20	300	2.64	0.17	278	0.06
	2	2.63	0.22	384	0.08

*As no improvement in room-temperature magnetic properties are found for 1 at. % Fe doping when compared to pristine NWs without any doping, the low temperature magnetic properties of $Hf_{0.99}Fe_{0.01}O_2$ Nanospikes are not of particular interest for the present purpose.

We have also obtained the magnetization curves for the $Hf_{1-x}Fe_xO_2$ nanostructures (x=0.05, 0.10, 0.20) at 2 K. Figure 3-10a-c compares the measured magnetization curves of the nanostructures at 2 K with the ones at room temperature. The M_s and H_c values at 2 K for the 5 at. %, 10 at. % and 20 at. % Fe-doped nanostructures follow the same M_s trend observed at room temperature with respect to the dopant content, with the highest M_s for $Hf_{0.80}Fe_{0.20}O_2$ NC20 (2.63 emu/g) and the highest H_c for $Hf0_{0.95}Fe_{0.05}O_2$ NC5 (1000 Oe). Furthermore, the M_s is found to increase slightly to 0.08 emu/g (0.53 emu/g) at 2 K from 0.05 emu/g (0.49 emu/g) at 300 K for $Hf_{0.95}Fe_{0.05}O_2$ NC5 ($Hf_{0.90}Fe_{0.10}O_2$ NC10) and remains almost unchanged for $Hf_{0.80}Fe_{0.20}O_2$ NC20 over the entire temperature range from 2 K (2.63 emu/g) to 300 K (2.64 emu/g), which suggests no magnetic phase change over this temperature range. In addition, the coercivity (H_c) and the ratio of the magnetic remanence to magnetic saturation (M_r/M_s) are found to decrease with increasing Fe dopant concentration (Figure 3-10d). This indicates that the hysteresis loops start to "shrink", and the magnetic behavior of the Fe-dopped HfO_2 nanostructures shifts from ferromagnetic to superparamagnetic with increasing Fe dopant concentration.

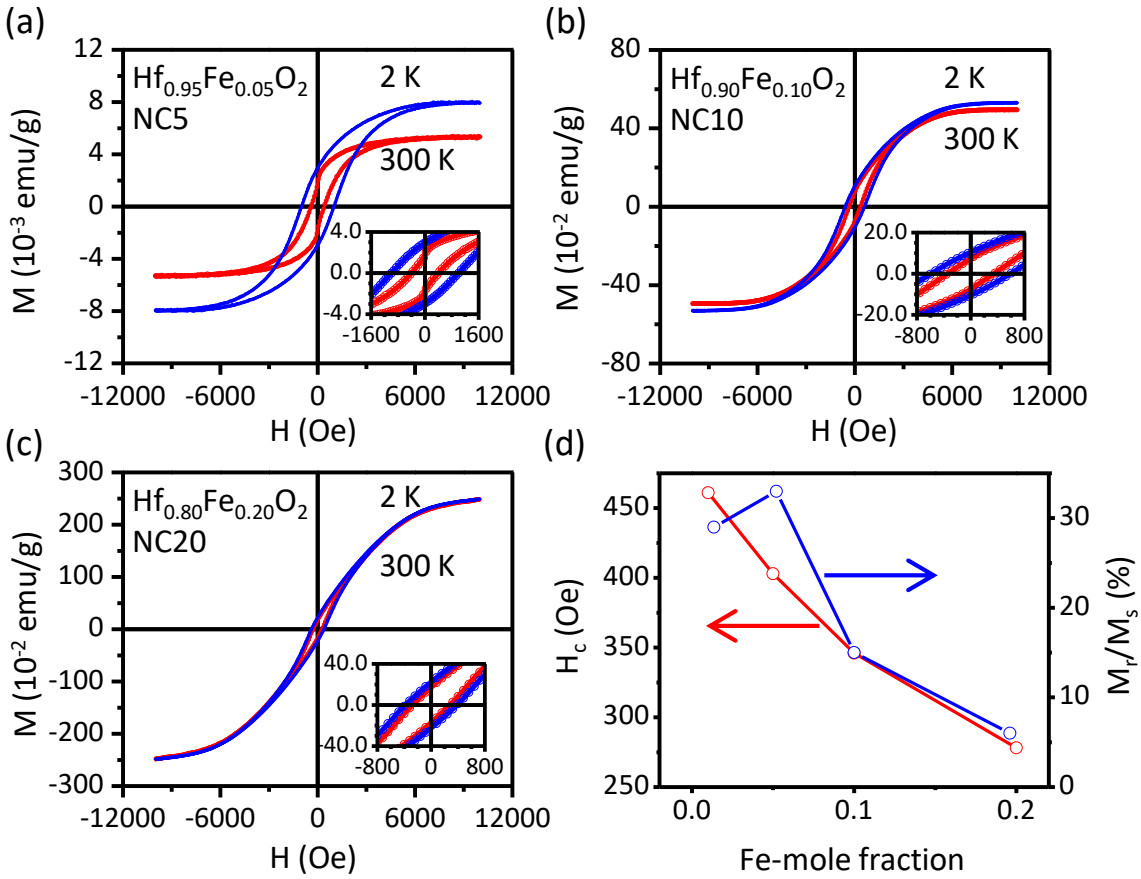

Figure 3-10. Magnetization (M-H curves) (a) $Hf_{0.95}Fe_{0.05}O_2$ NC5, (b) $Hf_{0.90}Fe_{0.10}O_2$ NC10 and (c) $Hf_{0.80}Fe_{0.20}O_2$ NC20 obtained at 2 K and room temperature. (d) Coercivity (H_c) and the ratio of magnetic remanence to magnetic saturation (M_r/M_s) for the Fe-doped HfO_2 nanostructures as functions of the Fe dopant concentration.

A closer look at the high-field portion of the magnetization curves of the nanostructures reveals that while $Hf_{0.95}Fe_{0.05}O_2$ NC5 (Figure 3-11a) and $Hf_{0.90}Fe_{0.10}O_2$ NC10 (Figure 3-11b) have already reached saturation, the $Hf_{0.80}Fe_{0.20}O_2$ NC20 (Figure 3-11c) is still far from saturation at 10 kOe, resembling a typical paramagnetic behavior. Since magnetic clustering in DMSO materials can sometimes create a superparamagnetic contribution to their magnetization signals,[26] the prominence of the superparamagnetic component in the magnetization profile of $Hf_{0.80}Fe_{0.20}O_2$ NC20 could indicate that its magnetic behavior is extrinsic, i.e., it originates from magnetic clusters. Although the XRD pattern (Figure 3-5) of $Hf_{0.80}Fe_{0.20}O_2$ NC20 does not show any evidence of a secondary phase or Fe clusters in the sample, the magnetic inhomogeneity leading to extrinsic magnetization behavior could occur at atomic-scale below the detection limit of XRD[214] or form an amorphous phase without

any XRD peak. On the other hand, the presence of well-defined ferromagnetic hystereses in $Hf_{0.95}Fe_{0.05}O_2$ NC5 and $Hf_{0.90}Fe_{0.10}O_2$ NC10 at both room temperature and 2 K (Figure 3-10a and Figure 3-10b) confirms that their ferromagnetic behavior is likely intrinsic with origin from the doped host lattice rather than the clustered magnetic ions. Among these "intrinsic" Fe-doped nanostructures, $Hf_{0.90}Fe_{0.10}O_2$ NC10 appears to show the most promising magnetic properties with a relatively large magnetic saturation at room temperature (0.5 emu/g), which is more than two orders of magnitude larger than those of undoped HfO_2 NWs (1.2×10^{-3} emu/g) and TiO_2 nanobelts (3.9×10^{-3} emu/g), and yet with a reasonable hysteresis characteristic at both 2 K and 300 K. In addition, we have also obtained the Arrot plots for $Hf_{0.90}Fe_{0.10}O_2$ NC10 (Figure 3-11d), in order to qualitatively estimate the Curie temperature (T_c) of a ferromagnet.[230] Near the phase transition temperature, the magnetization of a ferromagnet (M) is generally small, and M^2 is related to H/M from Landau's expression of free energy by the following:[46,63,230]

$$M^2=(1/b)\,(H/M)-(a/b)\,[(T-T_c)/T_c] \qquad \textbf{Eq. 3-1}$$

where M is the magnetization, H is the applied magnetic field, T is the temperature, and a and b are arbitrary constants. According to this equation, the Arrot plot of M^2 vs. H/M at the Curie temperature T_c should be linear with an intercept at zero. As can be seen from Figure 3-11d, the linear parts of the M^2 vs. H/M plots for $Hf_{0.90}Fe_{0.10}O_2$ NC10 within the temperature range from 2 K to 70 K to 300 K all have non-zero intercepts confirming that the Curie temperature of these nanostructures is still far from reach. Decisively well above the room temperature, their high Curie temperature makes these nanostructures a promising candidate for practical spintronic applications.

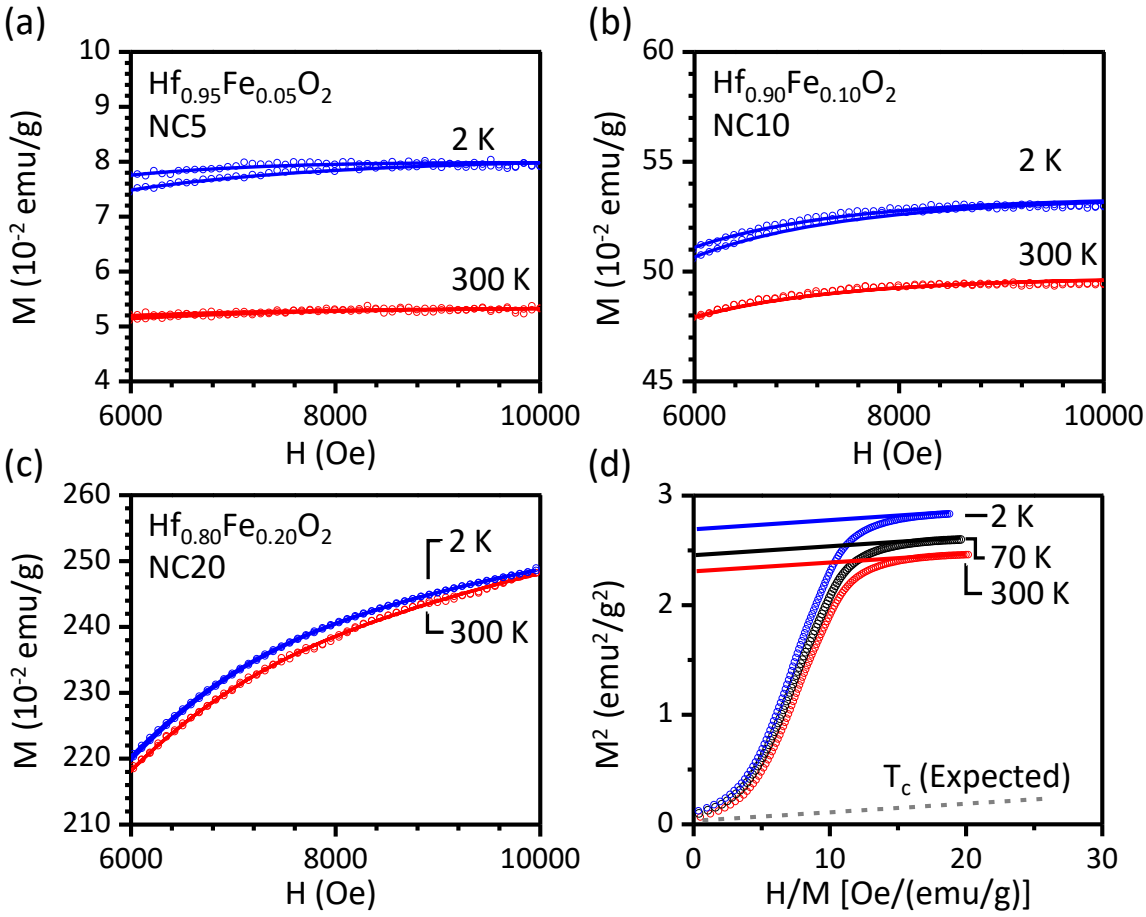

Figure 3-11. High field portions of the magnetization curves of (a) $Hf_{0.95}Fe_{0.05}O_2$ NC5, (b) $Hf_{0.90}Fe_{0.10}O_2$ NC10, and (c) $Hf_{0.80}Fe_{0.20}O_2$ NC20 collected at 2 K and 300 K. (d) Arrot plots for $Hf_{0.90}Fe_{0.10}O_2$ NC10 at 2 K, 70 K and 300 K.

To explain the mechanism behind the magnetic behavior of the $Hf_{1-x}Fe_xO_2$ nanostructures, we employ the same combined BMP and band hybridization model that we used earlier for the Ti-doped HfO_2 nanostructures. For the Fe-doped nanostructures, however, we consider Fe^{3+} as magnetic ions, which require some modifications to this model. When Hf^{4+} are substituted with Fe^{3+} ions, we could envisage two possible scenarios that the host lattice could maintain charge neutrality. In the first scenario, when Fe^{3+} substitutes Hf^{4+} in the lattice, a hole is created in the oxygen orbital.[214] To reduce the total energy of the system, electrons tend to hop between the overlapping orbitals.[46] Electrons from the neighboring Fe^{3+} 3d orbitals hop into the empty state of the oxygen orbital and the other electron in the oxygen orbital would transfer into the unoccupied states of the neighboring Fe^{3+} 3d orbitals (Figure 3-12a). Since the 3d orbitals are half-full, the electrons hopping from the oxygen

orbital to the available empty 3d orbitals have to have antiparallel spins with respect to the electrons occupying the full state. As it is less energetically favorable for the system if the electron undergoes a spin flip when hopping between the neighboring orbitals, the total energy of the system would be lower if the two Fe^{3+} ions around the bridging oxygen have antiparallel spin alignment (Figure 3-12a).[214] This type of oxygen-mediated interaction between Fe^{3+} ions is called superexchange interaction, which is antiferromagnetic and it does not create any additional magnetization in the lattice and could even reduce the total magnetic saturation. The second possible way to ensure charge neutrality is to create oxygen vacancies with a trapped electron ($V^{\bullet}_{O}$) near the Fe^{3+} sites in the lattice.[214] The Kröger-Vink notation for this type of defect reaction can be written as $O^{x}_{O} + Hf^{x}_{Hf} + Fe \rightarrow Fe'_{Hf} + V^{\bullet}_{O} + 1/2O_2$ where O^{x}_{O}, Hf^{x}_{Hf}, Fe'_{Hf} and $V^{\bullet}_{O}$, respectively, denote neutral oxygen site, neutral Hf site, Fe ion substituting Hf with an -1 effective charge, and singly charged oxygen vacancy with an +1 effective charge. Since the Fe^{3+} $3d^5$ orbitals are half-full, the trapped electron in the oxygen vacancy would interact with the electrons in the 3d orbitals antiferromagnetically, inducing a ferromagnetic interaction between the Fe^{3+} ions. The oxygen vacancy in this mechanism is called a ferromagnetic center (F-center), and the resulting direct ferromagnetic coupling is known as F-center exchange (FCE) interaction that leads to formation of magnetic polarons (Figure 3-12b).[214] In this mechanism, the substitutional Fe^{3+} ions could create enough oxygen vacancies so that the number of the BMPs exceeds the polaron percolation threshold and a long-range ferromagnetic ordering can therefore be generated throughout the doped lattice. From the band structure viewpoint, similar to the native oxygen vacancies of the lattice, those oxygen vacancies created by the substitutional Fe^{3+} ions can also form an impurity band close to the bottom of the conduction band. The resultant impurity band hybridizes with the empty states of the Fe $3d^5$ orbitals if there is a sufficient number of oxygen vacancies in the host lattice. When BMPs are formed in the lattice, electrons are transferred from the impurity band to the 3d orbital empty states at the Fermi level, which leads to spin-up and spin-down splitting of the impurity band (Figure 3-12c). The impurity band splitting occurring here can explain the high Curie temperature of these Fe-doped HfO_2 nanostructures similar to the undoped HfO_2 nanostructure.

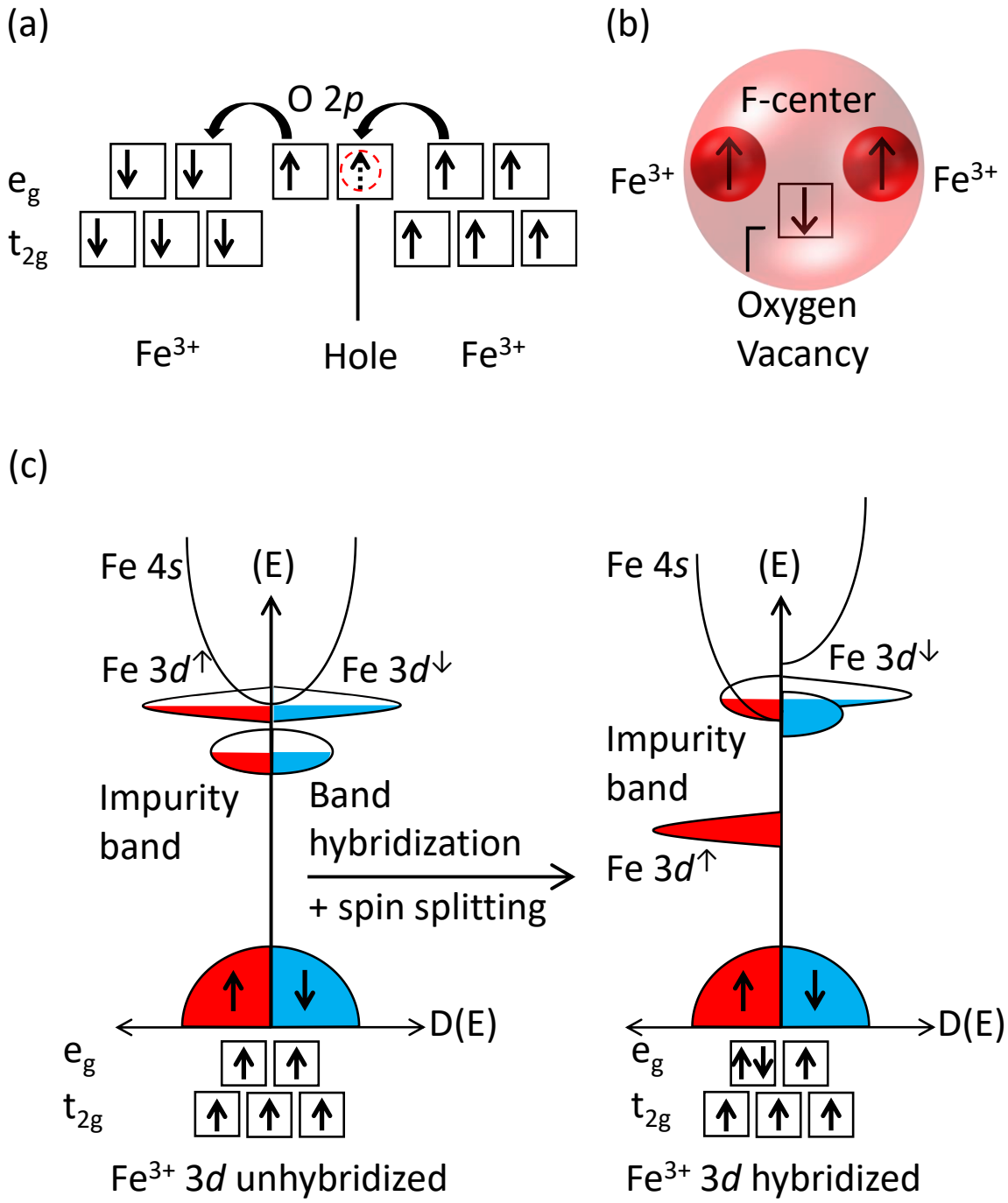

Figure 3-12. Schematic illustrations of (a) antiferromagnetic superexchange interaction between two neighboring Fe^{3+} ions substituting Hf^{4+} in the lattice, (b) oxygen vacancy-induced F-center exchange interaction, and (c) impurity band and 3d band hybridization leading to spin-up spin-down band splitting.

In the $Hf_{0.99}Fe_{0.01}O_2$ nanospikes that show a discernibly lower M_s value (8.6×10^{-4} emu/g) than that of the undoped HfO_2 NWs (1.2×10^{-3} emu/g), the antiferromagnetic superexchange interaction (Figure 3-12a) appears to occur between the Fe dopants. Consequently, similar to the undoped HfO_2 NWs, the magnetization comes primarily from those native oxygen vacancies in the (near-)surface region. These surface oxygen vacancies create enough polarons to generate long-range ferromagnetic ordering in the surface region, and also induce band hybridization, which leads to spin splitting in the impurity band (Figure 3-13a). However, the overall number of the BMPs is not large enough to produce a large M_s value. On the other hand, in $Hf_{0.95}Fe_{0.05}O_2$ NC5 and $Hf_{0.90}Fe_{0.10}O_2$ NC10, FCE appears to be the predominant interaction, creating many additional BMPs in the crystal lattice of the nanostructures. The larger number of the overlapping BMPs produces stronger ferromagnetic ordering throughout the lattice and a higher degree of spin band splitting of the impurity band derived from oxygen vacancies (Figure 3-13b). Consequently, the M_s values for $Hf_{0.95}Fe_{0.05}O_2$ NC5 and $Hf_{0.90}Fe_{0.10}O_2$ NC10 are significantly higher, by one order and two orders of magnitude (0.05 emu/g and 0.5 emu/g), respectively. For $Hf_{0.80}Fe_{0.20}O_2$ NC20, which exhibits a hybrid ferromagnetic and superparamagnetic behavior (Figure 3-10c), the concentration of the Fe dopants appears to be so high that the Fe ions are not distributed homogeneously throughout the nanostructure, leading to the formation of magnetic clusters (Figure 3-13c). Although there may still be BMPs that create small coercivity (H_c) and M_r/M_s, the contribution from the magnetic clusters appears to be dominant. These magnetic clusters behave like isolated superparamagnetic clusters and produce a large M_s (in response to the magnetic field) with no hysteresis. Moreover, the observed ferromagnetic component contributing to the magnetic behavior of $Hf_{0.80}Fe_{0.20}O_2$ NC20 may also originate from the ferromagnetic clusters that are created in the lattice but are too small to be detectable by XRD and EDS.

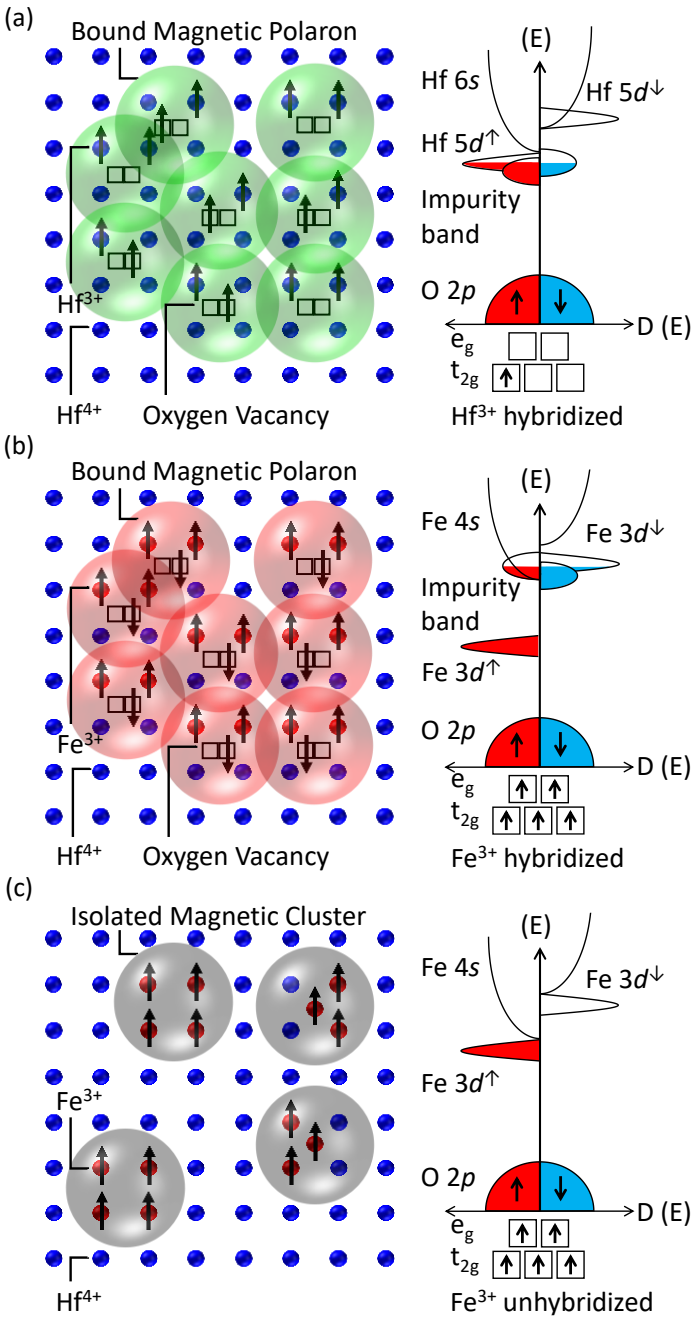

Figure 3-13. Schematic representations of the proposed magnetization mechanisms in (a) $Hf_{0.99}Fe_{0.01}O_2$ nanospikes with native oxygen vacancy-induced polarons leading to long-range magnetic ordering and impurity band spin splitting, (b) $Hf_{0.95}Fe_{0.05}O_2$ NC5 and $Hf_{0.90}Fe_{0.10}O_2$ NC10 with Fe^{3+} F-center exchange mechanism leading to long-range magnetic ordering and impurity band spin splitting, and (c) $Hf_{0.80}Fe_{0.20}O_2$ NC20 with magnetic clusters leading to predominant superparamagnetic behavior.

In summary, our study on the magnetic properties of Ti-doped nanostructures ($Hf_{1-x}Ti_xO_2$; $0 \leq x \leq 1$) shows that doping HfO_2 nanostructures with Ti can improve their magnetic properties. The magnetic saturation of the undoped HfO_2 NWs is doubled with 10 at. % Ti doping reaching 2.3×10^{-3} emu/g. According to the proposed models for the ferromagnetic ordering in doped and undoped DMSO materials, oxygen vacancy defects are the main contributor to ferromagnetism in these materials.[26,63,64,68] The lower oxygen vacancy formation energy for Ti compared to Hf,[169,170,226] which leads to the formation of more oxygen vacancy-induced BMPs in the lattice, is suggested to be responsible for such increase in M_s. Interestingly, the observed increase in M_s of the Ti-doped nanostructures is found to stop at 25 at. % and 50 at. % Ti, with smaller M_s values found for $Hf_{0.75}Ti_{0.25}O_2$ and $Hf_{0.50}Ti_{0.50}O_2$ nanospikes. This observation is attributed to the formation of orthorhombic $HfTiO_4$ phase in $Hf_{0.75}Ti_{0.25}O_2$ and $Hf_{0.50}Ti_{0.50}O_2$ nanospikes. The $HfTiO_4$ may have a larger oxygen vacancy formation energy due to having a different oxygen coordination number and bond angles that can consequently affect the number of resulting BMPs. For the Fe- doped HfO_2 nanostructures ($Hf_{1-x}Fe_xO_2$; $0.01 \leq x \leq 0.20$), 1 at. % Fe doping (in $Hf_{0.99}Fe_{0.01}O_2$ nanospikes) is found to produce no enhancement in the magnetization in the host lattice since the antiferromagnetic superexchange interaction between substitutional Fe ions would be the main contributor. At the other extreme, $Hf_{0.80}Fe_{0.20}O_2$ NC20 (20 at. % Fe doping) is found to be magnetically inhomogeneous, exhibiting a hybrid superparamagnetic-ferromagnetic magnetization curve with a dominant superparamagnetic characteristic. The magnetization behavior of these nanostructures is attributed to the nanoscale magnetic clusters that behave similarly to superparamagnetic nanoparticles. However, for those nanostructures doped with 5 at. % Fe ($Hf_{0.95}Fe_{0.05}O_2$ NC5) and 10 at. % Fe ($Hf_{0.90}Fe_{0.10}O_2$ NC10), their magnetic properties appear to be intrinsic and originate from the doped lattice rather than the magnetic ions. The magnetic saturation of these nanostructures is improved by one to two orders of magnitude (to 0.05 emu/g and 0.5 emu/g) compared to the undoped HfO_2 nanostructures (1.2×10^{-3} emu/g). The ferromagnetic center exchange (FCE) mechanism activated by the substitutional Fe^{3+}-induced oxygen vacancies is proposed to be the mechanism behind such strong ferromagnetic coupling throughout the host lattice.

These results provide further insights into the role of oxygen vacancies in the activation of ferromagnetic mechanisms in undoped and doped DMSO materials. More importantly, our $Hf_{0.90}Fe_{0.10}O_2$ NC10 is a promising DMSO candidate since these distorted nanocubes exhibit a relatively large magnetic saturation (0.5 emu/g) over a wide range of temperatures with a Curie temperature well above room temperature. The magnetic saturation of these nanostructures at room temperature is comparable with defect-rich ZrO_2 nanostructures such as ZrO_2 nanobricks

(0.6 emu/g)[63] and 5-nm ZrO_2 nanoclusters[64] (0.46 emu/g) and it is much higher than most of the magnetic metal oxides materials, including undoped colloidal HfO_2 nanorods (0.02 emu/g),[175] undoped ZrO_2 thin films (0.18 emu/g),[101] Mn-doped ZrO_2 thin films (0.02 emu/g),[231] Mn-doped ZnO thin films (0.05 emu/g),[151] undoped ZnO nanoparticles (0.003 emu/g),[232] Cu-doped ZnO nanowire arrays (0.2 emu/g),[233] undoped TiO_2 nanoribbons (0.2 emu/g),[234] Fe + N codoped TiO_2 nanorods (0.06 emu/g),[235] Cr-doped TiO_2 nanorods (0.07 emu/g),[62] V-doped TiO_2 nanotubes (0.008 emu/g),[236] and (Fe,Co,Mn)-doped mesoporous In_2O_{3-y} (0.03 emu/g).[237] Since HfO_2 is an advanced material compatible with and widely used in CMOS-based technologies, our Fe-doped HfO_2 nanostructured film with such a high magnetic response promises new opportunity for integrated CMOS and spintronic applications.

3.4 Conclusion

Ti-doped $Hf_{1-x}Ti_xO_2$ (x=0.01, 0.10, 0.25, 0.50) 1D nanostructures and Fe-doped $Hf_{1-x}Fe_xO_2$ (x=0.01, 0.05, 0.10, 0.20) nanostructures consisting of nanospikes and distorted nanocubes with stacked crystal flakes have been synthesized for the first time by using the catalyst-assisted PLD method on GNI/Ox-Si and Sn-GNI/Ox-Si templates. The morphological, structural, and magnetic properties of Ti-doped $Hf_{1-x}Ti_xO_2$ and Fe-doped $Hf_{1-x}Fe_xO_2$ are studied in detail and compared with those of undoped HfO_2 NWs and TiO_2 nanobelts grown under similar growth conditions. SEM and HIM images show that Ti doping does not inhibit the VLS growth mechanism, producing $Hf_{1-x}Ti_xO_2$ nanospikes even with the Ti concentration as high as 50 at. % ($Hf_{0.50}Ti_{0.50}O_2$ nanospikes). Nonetheless, VLS growth has been found to decrease with increasing Ti dopant concentration in the nanostructures, yielding shorter nanospikes with an oscillatory sidewall surface character. The origin of this oscillatory character is attributed to the formation of high surface energy planes along the growth direction.[217,219] The GIXRD patterns of these Ti-doped $Hf_{1-x}Ti_xO_2$ nanostructures and their peak position shifts confirm the substitutional incorporation of Ti into the host lattice. On the other hand, Fe is found to significantly suppress the VLS growth, producing Fe-doped nanospikes for 1 at. % Fe doping ($Hf_{0.99}Fe_{0.01}O_2$ nanospikes) while Fe-doped HfO_2 distorted nanocubes with stacked flake structures for 5 at. %, 10 at. % and 20 at. % Fe doping ($Hf_{0.95}Fe_{0.05}O_2$ NC5, $Hf_{0.90}Fe_{0.10}O_2$ NC10, $Hf_{0.80}Fe_{0.20}O_2$ NC20). The dramatic decrease of VLS growth with Fe doping is attributed to the effect of Fe in reducing the VLS nucleation rate at the liquid-solid interface by increasing the surface energy of the catalyst, which inhibits the effect of Sn in promoting VLS growth. Similar to $Hf_{1-x}Ti_xO_2$ nanostructures, the GIXRD patterns of the $Hf_{1-x}Fe_xO_2$ nanostructures also show the contraction of the host lattice, indicating the substitution of Hf^{4+} with Fe ions in the host lattice with no evidence of

secondary magnetic phase (within the sensitivity of XRD). The expansion of the $Hf_{0.80}Fe_{0.20}O_2$ NC20 lattice relative to the $Hf_{0.90}Fe_{0.10}O_2$ NC10, nevertheless, suggests some interstitial incorporation of Fe ions into the host lattice at higher dopant concentrations which could lead to the formation of magnetic clusters in the lattice.

In our previous work (Chapter 2), undoped HfO_2 NWs have been found to exhibit room-temperature ferromagnetic behavior, despite their low magnetic saturation due to the presence of oxygen vacancy defects limited to the (near-)surface region. In the present work, HfO_2 nanostructures are doped with Ti and Fe to enhance their magnetic properties. Since the oxygen vacancy defects are believed to be responsible for the magnetic properties of DMSO materials[26,63,64,68] and their formation energy in Ti-doped HfO_2 have been reported to be lower,[169,170,226] Ti-doping is therefore expected to improve the saturated magnetization of HfO_2 nanostructures. Indeed, Ti doping up to 10 at. % has been found to double the magnetic saturation in $Hf_{0.90}Ti_{0.10}O_2$ nanospikes when compared to the undoped HfO_2 NWs. However, doping the HfO_2 nanostructures with a higher concentration of Ti (25 at. % and 50 at. % in $Hf_{0.75}Ti_{0.25}O_2$ and $Hf_{0.50}Ti_{0.50}O_2$ nanospikes, respectively) provides no improvement in their magnetic saturation (Table 3-3). The increase in M_s of Ti-doped HfO_2 nanospikes up to 10 at. % doping is associated with the larger number of oxygen-vacancy induced BMPs in the lattice, while the lower magnetic saturation of 25 at. % and 50 at. % Ti-doped HfO_2 nanostructures is attributed to the presence of $HfTiO_4$ phase as confirmed by the XRD analysis. We hypothesize that the possible higher oxygen vacancy formation energy in the $HfTiO_4$ phase due to the different configuration of surrounding cations in this phase, such as different coordination number and bond angles, could contribute to their lower magnetic saturation. In general, the enhancement of the magnetic saturation in Ti-doped HfO_2 nanostructures is not profound, indicating that there is a small number of BMPs contributing to the magnetization of the sample, likely due to their presence being limited to the surface region.

On the other hand, our investigation on Fe-doped HfO_2 nanostructures shows that Fe doping has a more significant impact on the magnetic properties of HfO_2 nanostructures. However, having a homogenous distribution of Fe dopant in the lattice becomes challenging when the dopant content exceeds a certain concentration. Although GIXRD analysis shows no evidence of secondary phase formation, $Hf_{0.80}Fe_{0.20}O_2$ NC20 appears to have an extrinsic magnetic behavior originating from nano-scale magnetic clusters not detectable by XRD. In contrast, 1 at. % doping ($Hf_{0.99}Fe_{0.01}O_2$ nanospikes), 5 at. % doping ($Hf_{0.95}Fe_{0.05}O_2$ NC5) and 10% doping ($Hf_{0.90}Fe_{0.10}O_2$ NC10) appear to produce intrinsic ferromagnetic metal oxides with well-defined hystereses from 2 K to 300 K.

$Hf_{0.99}Fe_{0.01}O_2$ nanospikes with 1 at. % Fe doping do not show any improvement in magnetic saturation due to the antiferromagnetic coupling of substitutional Fe^{3+} ions through superexchange interaction in the lattice. On the other hand, $Hf_{0.95}Fe_{0.05}O_2$ NC5 and $Hf_{0.90}Fe_{0.10}O_2$ NC10 exhibit a significant enhancement in magnetic saturation values reaching up to two orders of magnitude larger than the undoped HfO_2 nanostructures. We propose oxygen-vacancy induced F-center exchange interaction[214] as the predominant mechanism responsible for such large magnetic saturation values in these nanostructures. These high magnetic saturation values qualify $Hf_{0.95}Fe_{0.05}O_2$ NC5 and $Hf_{0.90}Fe_{0.10}O_2$ NC10 introduced in this work as viable candidates for spintronic applications such as spin transistors[238] and spin-based logic circuits.[239] Moreover, their high Curie temperatures could facilitate the operation of these devices well above room temperature. In addition, the compatibility of HfO_2 with CMOS technology provides an excellent opportunity for the application of these nanostructures in integrated CMOS and spintronic technology.

Chapter 4
Concluding Remarks and Future Work

4.1 Summary of the Results and Contributions

Dilute magnetic semiconducting oxides (DMSOs) are believed to be the most promising materials for integrated spintronics and semiconductor-based electronic applications due to their superior ferromagnetic properties and high Curie temperatures well above room temperature. Among all DMSOs, HfO_2 is known to be the most CMOS-technology-compatible oxide material[70] and is therefore considered to be a very promising candidate for realizing the integration of CMOS and spintronic technologies. Despite several reports on fabrication and magnetic characterization of HfO_2 thin films,[96–98,102,152,153] the nature of their structural defects in effecting ferromagnetism is still not fully understood. Nanostructured materials with high specific surface areas have been reported to have enhanced ferromagnetic properties. [63,64] Inspired by the great potential of nanostructured material with high crystal quality for fundamental studies on these defects and their role in enhancing ferromagnetism, our objective in the present work is to fabricate doped/undoped single-crystalline HfO_2 low-dimensional nanostructures and to investigate the role of oxygen vacancy defects in facilitating -ferromagnetism. Using catalyst-assisted PLD, we develop a wide range of fascinating HfO_2 low-dimensional nanomaterials for the first time. These include doped/undoped HfO_2 nano square pyramids, nano triangular pyramids, and nano-tetrahedrons; undoped HfO_2 nanowires, nanospikes, and nano-columns; Ti-doped HfO_2 nanospikes, Fe-doped HfO_2 nanospikes, and Fe-doped HfO_2 distorted nanocubes with stacked flake structures. Indeed, the 1D HfO_2, $Hf_{1-x}Ti_xO_2$ (x=0.01, 0.10, 0.25, 0.50) and $Hf_{0.99}Fe_{0.01}O_2$ nanostructures grown in this work are the first single-crystalline doped/undoped HfO_2 1D nanostructures, particularly nanowires, ever reported.

In the first study of this work, we investigate the effect of growth temperature and growth templates on the morphological and structural properties of HfO_2 nanostructures grown by a catalyst-assisted PLD method. We grow HfO_2 nanostructures on Ox-Si (chemically oxidized Si), GNI/Ox-Si (chemically oxidized Si seeded with gold nanoislands) and Sn-GNI/Ox-Si (chemically oxidized Si seeded with Sn-alloyed gold nanoislands) growth templates at different temperatures (550 ℃, 650 ℃, 720 ℃ and 770 ℃), while precisely controlling other growth parameters such as vacuum pressure, processing gas (Ar) flow and pressure and the gold nanoisland (GNI) size. The SEM studies (Figure 2-1) reveal that only nano square pyramids (on Ox-Si) and a mixture of nano square pyramids and triangular pyramids (on GNI/Ox-Si) grow in the absence of Sn at all selected temperatures,

suggesting that the VS growth is the predominant growth mechanism in such conditions. On the other hand, in the presence of Sn (i.e., on Sn-GNI/Ox-Si), 1D HfO_2 nanostructures including nano-columns (with triangular base), nanospikes and nanowires grow, respectively, at 650 ℃, 720 ℃ and 770 ℃, indicating the crucial role of Sn in promoting VLS growth. Since Sn is introduced into the system by evaporation from the Sn-coated substrate holder, the growth of VS-grown nano-tetrahedrons on Sn-GNI/Ox-Si at 550 ℃ is attributed to the low temperature of the substrate holder, which is not high enough to introduce a sufficient amount of Sn into the system. Another important observation here is the simultaneous growth of nanocrystals on the substrate and among the 1D nanostructures, which is indicative of concurrent VS growth competing with the VLS growth in this system. The GIXRD analysis (Figure 2-2) confirms a HfO_2 monoclinic phase for all VS-grown nanostructures on Ox-Si and GNI/Ox-Si and VLS-grown 1D nanostructures on Sn-GNI/Ox-Si, with no indication of any Sn/SnO_2 secondary phase or Sn being incorporated into the HfO_2 lattice. In addition, the absence of any tetragonal or cubic phases in the GIXRD patterns suggests small amount of oxygen vacancies in the bulk of these nanostructures, because large amount of oxygen vacancies have been shown to stabilize tetragonal and cubic phases in HfO_2.[190–192]

More detailed studies on the structural properties of the nanostructures are performed by TEM. HRTEM images and simulated atomic models reveal that some HfO_2 NWs and nanospikes have grown along the [010] direction with the (100) plane as their top facet while others have grown along the normal vector of (110) plane with (001) plane as their top facet and the (-111) plane as their side facet. It is important to note that, due to the monoclinic phase of the nanostructures, the (110) normal vector and the [110] direction are not exactly parallel and are separated by 5.7 ° (Figure 2-5). More importantly, the TEM images show perule-like surface features that appear to be formed because of a secondary epitaxial growth occurring on the surface of the NWs. These epitaxially grown surface features further support that VS growth is competing with the VLS growth in this system and the final morphology indeed results from the interplay between these two growth mechanisms. To further investigate the role of Sn in promoting the VLS growth, XPS and AES analysis are performed, confirming the presence of Sn in all 1D nanostructures with the excess Sn oxidized to SnO_2 and/or SnO_y ($1 \leq y, 2$) on the surface of the VS-grown film and the VLS-grown NWs. Having realized the pivotal role of Sn in encouraging the VLS growth, we propose a dual role for Sn in this process. First, since the VLS nucleation rate is exponentially related to the surface energy at LS interface by an Arrhenius-type equation[156] and Au-Sn liquid alloy has lower surface energy than pure liquid gold,[184,185] Sn can enhance the VLS nucleation rate by alloying with gold (Sn-GNIs) and therefore decreasing the surface energy at the growth interface (LS interface). Secondly, Sn can assist with the

kinetics of the VLS growth by increasing the diffusivity of the catalyst and hence promoting the diffusion of the material species from the surface of the catalyst to the growth interface. For these reasons, in the presence of Sn, the VLS growth outruns the VS growth resulting in the growth of 1D nanostructures.

Single-crystalline 1D HfO_2 nanostructures obtained in the present work provide a great opportunity to study oxygen vacancy-induced ferromagnetism due to the high crystal quality and minimal effects arising from other structural defects. For this purpose, we compare the magnetic properties of HfO_2 NWs with those of the nanostructured film of HfO_2 nano square pyramids. The magnetization measurement reveals that HfO_2 NWs exhibit room-temperature ferromagnetism with a coercivity comparable to other reported undoped metal oxides nanostructures,[63,64,152] while HfO_2 nano square pyramids only exhibit a weak paramagnetic behavior. Since XPS analysis shows stronger defect-related features for HfO_2 NWs compared to the HfO_2 nano square pyramids without any trace of magnetic contamination, the ferromagnetic behavior of HfO_2 NWs is attributed to their higher amount of oxygen vacancies. To understand these results, we employ a modified BMP-band ferromagnetism model that has been previously used for explaining ferromagnetism in defect-rich ZrO_2 nanostructures.[63,64] Based on this model, long-range ferromagnetic ordering in HfO_2 NWs is caused by the ferromagnetic exchange interaction of bound magnetic polarons (BMPs) formed due to interaction between charged oxygen vacancies and reduced Hf ions (Hf^{3+}/Hf^{2+}). Their high Curie temperature, however, is due to the spin splitting of the oxygen-vacancy-driven impurity band resulting from its hybridization with the Hf 5d band. On the other hand, the weak paramagnetic behavior of the HfO_2 nano square pyramids is attributed to their small amount of oxygen vacancies, which generate isolated BMPs behaving like isolated magnetic ions with paramagnetic interactions. Another important observation is the low magnetic saturation (M_s) of the as-grown HfO_2 NWs (1.2×10^{-3}), despite their room temperature ferromagnetism. Our depth-profiling XPS studies reveal that the oxygen vacancies are mainly accumulated in the surface region of HfO_2 NWs and only a small amount of vacancies may exist in the bulk of the material. The amount of surface-limited oxygen vacancies could be high enough to produce overlapping BMPs within the surface region, but the total amount of oxygen vacancies within the entire material is apparently not high enough to produce large magnetic saturation.

By taking advantage of the lower oxygen vacancy formation energy in Ti-doped HfO_2 nanostructures,[169,170] we also investigate the morphological, structural and magnetic properties of Ti-doped $Hf_{1-x}Ti_xO_2$ (x=0.01, 0.10, 0.25, 0.50) 1D nanostructures reported for the first time in this work.

$Hf_{1-x}Ti_xO_2$ 1D nanostructures are grown on Sn-GNI/Ox-Si templates using a similar catalyst-assisted PLD method used for undoped HfO_2 nanostructures in the previous study. We also obtain TiO_2 1D nanostructures (nanobelts) on GNI/Ox-Si as the control sample so that we have a better understanding of the Ti-doping effect on the observed properties. The SEM and HIM images (Figure 3-1 and Figure 3-2) show Ti doping has a minor effect on the VLS growth of the nanostructures, producing 1D nanostructures for all doping concentrations ranging from 1 at. % ($Hf_{0.99}Ti_{0.01}O_2$ nanospikes) up to 50 at. % ($Hf_{0.50}Ti_{0.50}O_2$, bimetallic oxide nanospikes). Nonetheless, these 1D nanostructures appear to become shorter with increasing Ti content, changing from 2-2.5 μm long for intertwined undoped HfO_2 NWs to several hundred nm long for $Hf_{0.50}Ti_{0.50}O_2$ bimetallic oxide nanospikes, which suggests a lower VLS growth rate in nanostructures with higher Ti content. In addition, a closer examination of the sidewall surface with HIM reveals a sawtooth faceting on the surface along the growth direction, which becomes more obvious for nanostructures with higher Ti concentrations ($Hf_{0.75}Ti_{0.25}O_2$ and $Hf_{0.50}Ti_{0.50}O_2$). This kind of saw-tooth faceting is also observed for pure TiO_2 nanobelts and is attributed to the oscillatory growth process of the 1D nanostructures that could occur due to the formation of high surface energy planes during growth.[217,219] The GIXRD patterns of the as-grown nanostructures (Figure 3-3) show only a monoclinic HfO_2 phase for $Hf_{1-x}Ti_xO_2$ (x=0.01, 0.10) nanospikes, with ~15% additional orthorhombic $HfTiO_4$ phase for $Hf_{0.75}Ti_{0.25}O_2$ nanospikes and mainly orthorhombic $HfTiO_4$ phase for $Hf_{0.50}Ti_{0.50}O_2$ bimetallic oxide nanospikes. More importantly, the GIXRD pattern exhibit an upward position shift for the monoclinic HfO_2 phase relative to the reference peak position confirming the substitution of larger Hf^{+4} ions in the lattice with smaller Ti^{+4} ions.

We further demonstrate that these Ti-doped HfO_2 nanostructures all exhibit room-temperature ferromagnetism with increased magnetic saturation up to twice the M_s of undoped HfO_2 NWs for $Hf_{0.99}Ti_{0.01}O_2$ nanospikes. The increased magnetic saturation values here are attributed to the higher amount of oxygen vacancies in Ti-doped HfO_2 nanostructures due to their lower oxygen vacancy formation energy as previously confirmed by theoretical calculations.[169,170] The magnetic saturation of $Hf_{0.75}Ti_{0.25}O_2$ and $Hf_{0.50}Ti_{0.50}O_2$ nanospikes, however, drops to the same order of magnitude as that of undoped HfO_2 NWs. In addition to the monoclinic HfO_2 phase, an orthorhombic $HfTiO_4$ phase is found in $Hf_{0.75}Ti_{0.25}O_2$ and $Hf_{0.50}Ti_{0.50}O_2$ nanospikes, which leads us to hypothesize that their lower magnetic saturation is likely due to lower amount of oxygen vacancies caused by higher oxygen vacancy formation energy in the orthorhombic $HfTiO_4$ phase.

In the last phase of this work, we synthesize and study the properties of Fe-doped HfO_2 nanostructures so that we can compare the effect of Fe doping, as a ferromagnetic dopant, on the properties of HfO_2 nanostructures with the effect of doping a nonmagnetic dopant like Ti. $Hf_{1-x}Fe_xO_2$ (x=0.01, 0.05, 0.10, 0.20) nanostructures are grown on Sn-GNI/Ox-Si using catalyst-assisted PLD with growth conditions similar to those used for undoped and Ti-doped HfO_2 nanostructures. Unlike Ti doping, Fe doping is found to significantly restrict the VLS growth, producing $Hf_{0.99}Fe_{0.01}O_2$ nanospikes for 1 at. % Fe doping, and distorted nanocubes with stacked crystal flakes for Fe doping of 5 at. % ($Hf_{0.95}Fe_{0.05}O_2$ NC5), 10 at. % ($Hf_{0.90}Fe_{0.10}O_2$ NC10) and 20 at. % ($Hf_{0.80}Fe_{0.20}O_2$ NC20) (Figure 3-4). The disruption in the VLS growth observed here is attributed to the unfavorable effect of Fe in reducing the VLS growth nucleation rate by increasing the surface energy at the interface between the catalyst and the emerging solid. This negative effect on the VLS growth counterbalances the positive effect of Sn in promoting VLS growth so that the VS growth becomes the dominant mechanism producing distorted nanocubes as the final products (and not 1D nanostructures). The GIXRD analysis of these nanostructures (Figure 3-5) shows only a monoclinic HfO_2 phase with an upward position shift indicating the substitution of larger Hf^{+4} ions with smaller Fe^{+3}/Fe^{+2} ions in the lattice. More importantly, no trace of any secondary phase of Fe or iron oxides is found in the XRD pattern suggesting that no magnetic ion clustering occurs in the host lattice (within the sensitivity range of XRD analysis).

Finally, the magnetic characterization of Fe-doped nanostructures demonstrates intrinsic ferromagnetism with high Curie temperature (well above room temperature) for Fe doping up to 10 at. %. It is found that the nanostructures doped with 1 at. % Fe ($Hf_{0.99}Fe_{0.01}O_2$ nanospikes) do not show a larger magnetic saturation that is of almost the same order as that of undoped HfO_2 NWs. On the other hand, nanostructures doped with 5 at. % Fe ($Hf_{0.95}Fe_{0.05}O_2$ NC5) and 10 at. % Fe ($Hf_{0.90}Fe_{0.10}O_2$ NC10) exhibit significantly larger M_s values, up to 2 orders of magnitude larger than $Hf_{0.99}Fe_{0.01}O_2$ nanospikes. The small M_s of $Hf_{0.99}Fe_{0.01}O_2$ nanospikes is attributed to the dominant antiferromagnetic interaction of Fe ions in the lattice, which does not generate any extra magnetic moment, while the high magnetic saturations of $Hf_{0.95}Fe_{0.05}O_2$ NC5 and $Hf_{0.90}Fe_{0.10}O_2$ NC10 appear to be the result of ferromagnetic center exchange (FCE) mechanism activated by additional oxygen vacancies induced by the magnetic ions in the host lattice. The other important observation here is the extrinsic magnetic property of nanostructures with 20 at. % Fe concentration ($Hf_{0.80}Fe_{0.20}O_2$ NC20), which exhibit a hybrid ferromagnetic-superparamagnetic behavior dominated by the contribution from the superparamagnetic component. The superparamagnetic characteristic of $Hf_{0.80}Fe_{0.20}O_2$ NC20

suggests an atomic-scale magnetic inhomogeneity in the lattice (despite not being detected by the XRD analysis).

In general, the present work offers valuable insights into the synthesis of semiconductor NWs, especially complex oxide NWs. For example, in those cases that precise control of stoichiometry requires the use of an oxide target for PLD, the application of an alloy catalyst like Sn-GNIs can facilitate fabrication of oxide NWs by minimizing the unfavorable effect of oxygen in enhancing the VS growth. In addition, the near single-crystalline nature of nanostructures obtained in this work has allowed us to significantly improve our understanding of oxygen vacancy-driven ferromagnetism mechanisms in DMSO materials. Moreover, HfO_2 nanostructures with high Curie temperature introduced in the present work could be promising DMSOs for spintronic applications such as magnetic tunneling junctions (MTJs),[14] spin transistors,[238] and spin-based logic circuits.[239] In particular, the $Hf_{0.90}Fe_{0.10}O_2$ NC10 nanostructures exhibit a relatively high magnetic saturation (0.5 emu/g) at room temperature which is comparable with defect-rich ZrO_2 nanostructures such as ZrO_2 nanobricks (0.6 emu/g)[63] and 5-nm ZrO_2 nanoclusters (0.46 emu/g)[64] and it is much higher than most of the magnetic metal oxides materials, including undoped colloidal HfO_2 nanorods (0.02 emu/g),[175]undoped ZrO_2 thin films (0.18 emu/g),[101] Mn-doped ZrO_2 thin films (0.02 emu/g),[231] Mn-doped ZnO thin films (0.05 emu/g),[151] undoped ZnO nanoparticles (0.003 emu/g),[232] Cu-doped ZnO nanowire arrays (0.2 emu/g),[233] undoped TiO_2 nanoribbons (0.2 emu/g),[234] Fe + N codoped TiO_2 nanorods (0.06 emu/g),[235] Cr-doped TiO_2 nanorods (0.07 emu/g),[62] V-doped TiO_2 nanotubes (0.008 emu/g),[236] and (Fe,Co,Mn)-doped mesoporous In_2O_{3-y} (0.03 emu/g).[237] Their high magnetic saturation, along with Curie temperature well above room temperature, promise real-life spintronic device applications. More importantly, considering the high compatibility of HfO_2 with CMOS technology, the spintronic application of the nanostructures synthesized in the present work offers a viable opportunity for realizing the idea of integration between semiconductor-based electronics and spintronics to fabricate high-performance devices.

4.2 Future Work

The present work demonstrates the crucial role of oxygen vacancies in inducing ferromagnetism in HfO_2 nanostructures. One strategy to further improve the magnetic properties of the HfO_2 nanostructures is to introduce more oxygen vacancies into their structure. This could be done by using a metallic Hf target instead of an oxide target for the laser ablation. This would allow the amount of oxygen vacancies in the final structures to be precisely controlled by manipulating the O_2 to Ar ratio in the processing gas mixture to provide different ambient environments during deposition. Using a metallic target for the PLD synthesis could also facilitate growing HfO_2 1D nanostructures due to the elimination of the excess oxygen from the target.

Our present results show that the observed defects are mainly accumulated on the surface of the nanostructures. Some earlier studies[98,152] on the magnetic properties of HfO_2 thin films have proposed that additional defects, including oxygen vacancies, could also accumulate at the interface between the deposited film and the substrate. The substrates used in those studies (sapphire and yttria-stabilized zirconium or YSZ) are different from the SiO_2 surface used in the present work. As they have reported higher magnetic saturation on these substrates, an interesting future study could be investigating the magnetic properties of the HfO_2 single-crystalline 1D nanostructures grown on other substrates including sapphire and YSZ substrates. Such a study can significantly improve our understanding of defect-induced ferromagnetism in DMSOs and could be used as another strategy to enhance the magnetic saturation of HfO_2 1D nanostructures.

Another important subject that requires more investigation is the homogenous doping of the host lattice, particularly for magnetic dopants. Generally, magnetic homogeneity of DMSOs is a controversial issue in this field, raising some questions about the intrinsic nature of the ferromagnetism observed in DMSOs. Fe-doped HfO_2 nanostructures produced in this work apparently exhibit intrinsic ferromagnetism up to 10 at. % Fe doping with GIXRD patterns showing no evidence of magnetic ion clustering in the lattice. Other helpful probes that can shed some more light on the intrinsic nature of the ferromagnetism in doped HfO_2 nanostructures are depth profiling by secondary ion mass spectroscopy (SIMS) and by XPS. These advanced surface analysis techniques are particularly surface sensitive that they could detect any minor magnetic clustering near the surface of the nanostructures that may be beyond the detection limit of XRD. Testing samples for anisotropic magnetization, where the magnetization of the samples under parallel and vertical external fields are compared, could also help recognize these intrinsic properties. The anisotropy of magnetic saturation can rule out any extrinsic magnetic source such as segregated ferromagnetic impurities below the

XRD sensitivity range.[98] Another way to minimize the possibility of extrinsic ferromagnetism is to use antiferromagnetic metal ions such as Mn and Cr for doping the HfO_2 lattice. While substitution of these antiferromagnetic ions in the lattice can create defect-induced ferromagnetism, their clustering within the lattice, even if it occurs, does not generate any additional extrinsic ferromagnetism.

The high Curie temperature of the doped/undoped HfO_2 nanostructures found in this work makes these HfO_2 nanostructures very promising DMSOs for the fabrication of practical spintronic devices that could operate above room temperature. $Hf_{0.95}Fe_{0.05}O_2$ NC5 and $Hf_{0.90}Fe_{0.10}O_2$ NC10 nanostructures with relatively high magnetic saturation are of particular interest for this purpose. Therefore, another important future project could be magneto-transport characterization (magnetoresistance and Hall effect measurements) of these materials for MTJ[14] and spin transistor[238] applications. Furthermore, as HfO_2 is a wide-bandgap oxide, it could accommodate a large number of defect states within its bandgap leading to super-efficient light absorption in the visible range of the solar spectrum. If defect-rich HfO_2 nanostructures could be achieved by using laser ablation of a metal target, exploring the application of such nanostructures for photocatalytic water splitting and hydrogen production systems could be a very intriguing study.

Finally, the advantage of PLD synthesis in precisely controlling the composition of the final products opens up a great opportunity to fabricate nanostructures of other complex oxide systems with interesting properties. Of particular interest are solid solutions of hematite (α-Fe_2O_3) and ilmenite ($FeTiO_3$). Although α-Fe_2O_3 and $FeTiO_3$ are both antiferromagnetic insulators, their solid solutions with intermediate compositions interestingly exhibit strong ferrimagnetism with semiconducting property. The unique advantage of this system is the capability of switching between p-type and n-type semiconducting properties by simply adjusting the concentration of α-Fe_2O_3 in $FeTiO_3$.[240,241] An exciting future project could be the synthesis of defect-rich nanostructures of α-Fe_2O_3-$FeTiO_3$ solid solutions with novel magnetic and optical properties for spintronics and photocatalytic applications.

Bibliography

(1) Baibich, M. N.; Broto, J. M.; Fert, A.; Van Dau, F. N.; Petroff, F.; Eitenne, P.; Creuzet, G.; Friederich, A.; Chazelas, J. Giant Magnetoresistance of (001)Fe/(001)Cr Magnetic Superlattices. *Phys. Rev. Lett.* **1988**, *61* (21), 2472–2475.

(2) Binasch, G.; Grünberg, P.; Saurenbach, F.; Zinn, W. Enhanced Magnetoresistance in Layered Magnetic Structures with Antiferromagnetic Interlayer Exchange. *Phys. Rev. B* **1989**, *39* (7), 4828–4830.

(3) Fert, A. Origin, Development, and Future of Spintronics (Nobel Lecture). *Angew. Chemie - Int. Ed.* **2008**, *47* (32), 5956–5967.

(4) Grünberg, P.; Bürgler, D. E. Metallic Multilayers: Discovery of Interlayer Exchange Coupling and GMR. In *Handbook of Spintronics*; Xu, Y., Awschalom, D. D., Nitta, J., Eds.; Springer Netherlands: Dordrecht, 2014; pp 1–16.

(5) Hirohata, A.; Takanashi, K. Future Perspectives for Spintronic Devices. *J. Phys. D. Appl. Phys.* **2014**, *47* (19), 193001.

(6) Mott, N. F.; Fowler, R. H. The Electrical Conductivity of Transition Metals. *Proc. R. Soc. London. Ser. A - Math. Phys. Sci.* **1936**, *153* (880), 699–717.

(7) Felser, C.; Fecher, G. H.; Balke, B. Spintronics: A Challenge for Materials Science and Solid-State Chemistry. *Angew. Chemie - Int. Ed.* **2007**, *46* (5), 668–699.

(8) Coughlin, T. 80 TB Hard Disk Drives https://www.forbes.com/sites/tomcoughlin/2020/02/12/80-tb-hard-disk-drives/?sh=40be2a6048f7.

(9) Thomas Alsop. Hard disk drive (HDD) unit shipments worldwide from 1976 to 2020 https://www.statista.com/statistics/398951/global-shipment-figures-for-hard-disk-drives/.

(10) What's the outlook for enterprise hard disk drives (HDD) in the data center? https://horizontechnology.com/news/hdd-remains-dominant-storage-technology-1219/.

(11) Allen, L. Toshiba Nearline HDD Shipment & Capacity Sets New Company Record In 2CQ21 https://www.businesswire.com/news/home/20210809005605/en/Toshiba-Nearline-HDD-Shipment-Capacity-Sets-New-Company-Record-In-2CQ21.

(12) Coughlin, T. In 2020 HDD Companies Shipped Over 1ZB Of Storage Capacity

https://www.forbes.com/sites/tomcoughlin/2021/02/07/in-2020-hdd-companies-shipped-over-1zb-of-storage-capacity/?sh=5cd4c0f14894.

(13) Edward Burns. IDC Forecasts Solid Growth for the Hard Disk Drive and Solid State Drive Markets to Meet Increasing Demand for Data Storage Capacity https://www.idc.com/getdoc.jsp?containerId=prUS47975921.

(14) Peng, S. Z.; Zhang, Y.; Wang, M. X.; Zhang, Y. G.; Zhao, W. Magnetic Tunnel Junctions for Spintronics: Principles and Applications. *Wiley Encycl. Electr. Electron. Eng.* **2014**, *1936* (12), 1–16.

(15) Igor Žutić, Jaroslav Fabian, and S. D. S. Spintronics: Fundamentals and Applications. *Rev. Mod. Phys.* **2004**, *76* (2), 323–410.

(16) Julliere, M. Tunneling between Ferromagnetic Films. *Phys. Lett. A* **1975**, *54* (3), 225–226.

(17) Moodera, J. S.; Kinder, L. R.; Wong, T. M.; Meservey, R. Large Magnetoresistance at Room Temperature in Ferromagnetic Thin Film Tunnel Junctions. *Phys. Rev. Lett.* **1995**, *74* (16), 3273–3276.

(18) Miyazaki, T.; Tezuka, N. Giant Magnetic Tunneling Effect in Fe/Al_2O_3/Fe Junction. *J. Magn. Magn. Mater.* **1995**, *139* (3), 94–97.

(19) Ikeda, S.; Hayakawa, J.; Ashizawa, Y.; Lee, Y. M.; Miura, K.; Hasegawa, H.; Tsunoda, M.; Matsukura, F.; Ohno, H. Tunnel Magnetoresistance of 604% at 300 K by Suppression of Ta Diffusion in CoFeBMgOCoFeB Pseudo-Spin-Valves Annealed at High Temperature. *Appl. Phys. Lett.* **2008**, *93* (8), 082508.

(20) Hirohata, A.; Yamada, K.; Nakatani, Y.; Prejbeanu, I.-L.; Diény, B.; Pirro, P.; Hillebrands, B.; Prejbeanu, L.; Diény, B.; Pirro, P.; Hillebrands, B. Review on Spintronics: Principles and Device Applications. *J. Magn. Magn. Mater.* **2020**, *509* (January), 166711.

(21) Wolf, S. A.; Awschalom, D. D.; Buhrman, R. A.; Daughton, J. M.; Von Molnár, S.; Roukes, M. L.; Chtchelkanova, A. Y.; Treger, D. M. Spintronics: A Spin-Based Electronics Vision for the Future. *Science* **2001**, *294* (5546), 1488–1495.

(22) Awschalom, D. D.; Flatté, M. E. Challenges for Semiconductor Spintronics. *Nat. Phys.* **2007**, *3* (3), 153–159.

(23) Mauger, A.; Godart, C. The Magnetic, Optical, and Transport Properties of Representatives of a Class of Magnetic Semiconductors: The Europium Chalcogenides. *Phys. Rep.* **1986**, *141* (2–

3), 51–176.

(24) Steigmeier, E. F.; Harbeke, G. Phonons and Magnetic Order in Ferromagnetic CdCr2Se4 and CdCr2S4. *Phys. der Kondens. Mater.* **1970**, *12* (1), 1–15.

(25) Treitinger, L.; Göbel, H.; Pink, H. Magnetic Semiconducting Spinels in the Mixed System $Co_{1-x}Fe_xCr_2S_4$. *Mater. Res. Bull.* **1976**, *11* (11), 1375–1379.

(26) Ogale, S. B. Dilute Doping, Defects, and Ferromagnetism in Metal Oxide Systems. *Adv. Mater.* **2010**, *22* (29), 3125–3155.

(27) Furdyna, J. K. Diluted Magnetic Semiconductors. *J. Appl. Phys.* **1988**, *64* (4), R29–R64.

(28) Ohno, H. Making Nonmagnetic Semiconductors Ferromagnetic. *Science* **1998**, *281* (5379), 951–956.

(29) Janisch, R.; Gopal, P.; Spaldin, N. A. Transition Metal-Doped TiO_2 and ZnO - Present Status of the Field. *J. Phys. Condens. Matter* **2005**, *17* (27), R657–R689.

(30) Munekata, H.; Ohno, H.; Von Molnar, S.; Segmüller, A.; Chang, L. L.; Esaki, L. Diluted Magnetic III-V Semiconductors. *Phys. Rev. Lett.* **1989**, *63* (17), 1849–1852.

(31) Ohno, H.; Munekata, H.; Penney, T.; Von Molnar, S.; Chang, L. L. Magnetotransport Properties of P-Type (In,Mn)As Diluted Magnetic III-V Semiconductors. *Phys. Rev. Lett.* **1992**, *68* (17), 2664–2667.

(32) Munekata, H.; Zaslavsky, A.; Fumagalli, P.; Gambino, R. J. Preparation of (In,Mn)As/(Ga,Al)Sb Magnetic Semiconductor Heterostructures and Their Ferromagnetic Characteristics. *Appl. Phys. Lett.* **1993**, *63* (21), 2929–2931.

(33) Ohno, H.; Shen, A.; Matsukura, F.; Oiwa, A.; Endo, A.; Katsumoto, S.; Iye, Y. (Ga,Mn)As: A New Diluted Magnetic Semiconductor Based on GaAs. *Appl. Phys. Lett.* **1996**, *69* (3), 363–365.

(34) Chiba, D.; Takamura, K.; Matsukura, F.; Ohno, H. Effect of Low-Temperature Annealing on (Ga,Mn)As Trilayer Structures. *Appl. Phys. Lett.* **2003**, *82* (18), 3020–3022.

(35) Ohno, H. Properties of Ferromagnetic III–V Semiconductors. *J. Magn. Magn. Mater.* **1999**, *200* (1–3), 110–129.

(36) Lee, S.; Chung, J. H.; Liu, X.; Furdyna, J. K.; Kirby, B. J. Ferromagnetic Semiconductor GaMnAs. *Mater. Today* **2009**, *12* (4), 14–21.

(37) Edmonds, K. W.; Wang, K. Y.; Campion, R. P.; Neumann, A. C.; Farley, N. R. S.; Gallagher, B. L.; Foxon, C. T. High-Curie-Temperature Ga1-XMnxAs Obtained by Resistance-Monitored Annealing. *Appl. Phys. Lett.* **2002**, *81* (26), 4991–4993.

(38) Wang, K. Y.; Campion, R. P.; Edmonds, K. W.; Sawicki, M.; Dietl, T.; Foxon, C. T.; Gallagher, B. L. Magnetism in (Ga,Mn)As Thin Films With TC Up To 173K. *AIP Conf. Proc.* **2005**, *772* (1), 333–334.

(39) Chen, L.; Yan, S.; Xu, P. F.; Lu, J.; Wang, W. Z.; Deng, J. J.; Qian, X.; Ji, Y.; Zhao, J. H. Low-Temperature Magnetotransport Behaviors of Heavily Mn-Doped (Ga,Mn)As Films with High Ferromagnetic Transition Temperature. *Appl. Phys. Lett.* **2009**, *95* (18), 18–20.

(40) Chen, L.; Yang, X.; Yang, F.; Zhao, J.; Misuraca, J.; Xiong, P.; Von Molnár, S. Enhancing the Curie Temperature of Ferromagnetic Semiconductor (Ga,Mn)As to 200 K via Nanostructure Engineering. *Nano Lett.* **2011**, *11* (7), 2584–2589.

(41) Fukumura, T.; Jin, Z.; Ohtomo, A.; Koinuma, H.; Kawasaki, M. An Oxide-Diluted Magnetic Semiconductor: Mn-Doped ZnO. *Appl. Phys. Lett.* **1999**, *75* (21), 3366–3368.

(42) Matsumoto, Y.; Murakami, M.; Shono, T.; Hasegawa, T.; Fukumura, T.; Kawasaki, M.; Ahmet, P.; Chikyow, T.; Koshihara, S. Y.; Koinuma, H. Room-Temperature Ferromagnetism in Transparent Transition Metal-Doped Titanium Dioxide. *Science* **2001**, *291* (5505), 854–856.

(43) Matsumoto, Y.; Takahashi, R.; Murakami, M.; Koida, T.; Fan, X. J.; Hasegawa, T.; Fukumura, T.; Kawasaki, M.; Koshihara, S. Y.; Koinuma, H. Ferromagnetism in Co-Doped TiO_2 Rutile Thin Films Grown by Laser Molecular Beam Epitaxy. *Japanese J. Appl. Physics, Part 2 Lett.* **2001**, *40* (11 B), L1204–L1206.

(44) Philip, J.; Punnoose, A.; Kim, B. I.; Reddy, K. M.; Layne, S.; Holmes, J. O.; Satpati, B.; Leclair, P. R.; Santos, T. S.; Moodera, J. S. Carrier-Controlled Ferromagnetism in Transparent Oxide Semiconductors. *Nat. Mater.* **2006**, *5* (4), 298–304.

(45) Coey, J. M. D. Dilute Magnetic Oxides. *Curr. Opin. Solid State Mater. Sci.* **2006**, *10* (2), 83–92.

(46) Blundell, S. *Magnetism in Condensed Matter*; Oxford University Press Inc: New York, 2001.

(47) Goodenough, J. B. An Interpretation of the Magnetic Properties of the Perovskite-Type Mixed Crystals $La_{1-x}Sr_xCoO_{3-\lambda}$. *J. Phys. Chem. Solids* **1958**, *6* (2–3), 287–297.

(48) Goodenough, J. B. Theory of the Role of Covalence in the Perovskite-Type Manganites [La,M(II)]MnO_3. *Phys. Rev.* **1955**, *100* (2), 564–573.

(49) Kanamori, J. Superexchange Interaction and Symmetry Properties of Electron Orbitals. *J. Phys. Chem. Solids* **1959**, *10* (2–3), 87–98.

(50) Anderson, P. W. Antiferromagnetism. Theory of Suyerexchange. *Phys. Rev.* **1950**, *79* (2), 350–356.

(51) Zener, C. Interaction between the D-Shells in the Transition Metals. II. Ferromagnetic Compounds of Manganese with Perovskite Structure. *Phys. Rev.* **1951**, *82* (3), 403–405.

(52) Zener, C. Interaction between the d Shells in the Transition Metals. *Phys. Rev.* **1951**, *81* (3), 440–444.

(53) Dietl, T.; Ohno, H.; Matsukura, F.; Cibert, J.; Ferrand, D. Zener Model Description of Ferromagnetism in Zinc-Blende Magnetic Semiconductors. *Science (80-.).* **2000**, *287* (5455), 1019–1022.

(54) Jungwirth, T.; Sinova, J.; Mašek, J.; Kučera, J.; MacDonald, A. H. Theory of Ferromagnetic (III,Mn)V Semiconductors. *Rev. Mod. Phys.* **2006**, *78* (3), 809–864.

(55) Matsukura, F.; Ohno, H.; Shen, A.; Sugawara, Y. Transport Properties and Origin of Ferromagnetism in (Ga,Mn)As. *Phys. Rev. B* **1998**, *57* (4), R2037–R2040.

(56) Torrance, J. B.; Shafer, M. W.; McGuire, T. R. Bound Magnetic Polarons and the Insulator-Metal Transition in EuO. *Phys. Rev. Lett.* **1972**, *29* (17), 1168–1171.

(57) Durst, A. C.; Durst, A. C.; Bhatt, R. N.; Wolff, P. A. Bound Magnetic Polaron Interactions in Insulating Doped Diluted Magnetic Semiconductors. *Phys. Rev. B - Condens. Matter Mater. Phys.* **2002**, *65* (23), 2352051–23520510.

(58) Angelescu, D. E.; Bhatt, R. N. Effective Interaction Hamiltonian of Polaron Pairs in Diluted Magnetic Semiconductors. *Phys. Rev. B - Condens. Matter Mater. Phys.* **2002**, *65* (7), 75211.

(59) Das Sarma, S.; Hwang, E. H.; Kaminski, A. Temperature-Dependent Magnetization in Diluted Magnetic Semiconductors. *Phys. Rev. B - Condens. Matter Mater. Phys.* **2003**, *67* (15), 155201.

(60) Liu, C.; Yun, F.; Morkoç, H. Ferromagnetism of ZnO and GaN: A Review. *J. Mater. Sci. Mater. Electron.* **2005**, *16*, 555–597.

(61) Zhao, T.; Shinde, S. R.; Ogale, S. B.; Zheng, H.; Venkatesan, T.; Ramesh, R.; Sarma, S. Das. Electric Field Effect in Diluted Magnetic Insulator Anatase Co: TiO_2. *Phys. Rev. Lett.* **2005**, *94* (12), 126601.

(62) Patel, S. K. S.; Gajbhiye, N. S. Oxygen Deficiency Induced Ferromagnetism in Cr-Doped TiO_2 Nanorods. *J. Magn. Magn. Mater.* **2013**, *330*, 21–24.

(63) Rahman, M. A.; Rout, S.; Thomas, J. P.; McGillivray, D.; Leung, K. T. Defect-Rich Dopant-Free ZrO_2 Nanostructures with Superior Dilute Ferromagnetic Semiconductor Properties. *J. Am. Chem. Soc.* **2016**, *138* (36), 11896–11906.

(64) Guan, X.; Srivastava, S.; Thomas, J. P.; Heinig, N. F.; Kang, J. S.; Rahman, M. A.; Leung, K. T. Defect-Rich Dopant-Free ZrO_2 Nanoclusters and Their Size-Dependent Ferromagnetism. *ACS Appl. Mater. Interfaces* **2020**, *12* (43), 48998–49005.

(65) Yang, D.; An, Y.; Wang, S.; Wu, Z.; Liu, J. Evidence of the Oxygen Vacancies-Induced Room-Temperature Ferromagnetism in the $(In_{0.97-x}Fe_xSn_{0.03})_2O_3$ Films. *RSC Adv.* **2014**, *4* (64), 33680–33686.

(66) Coey, J. M. D.; Wongsaprom, K.; Alaria, J.; Venkatesan, M. Charge-Transfer Ferromagnetism in Oxide Nanoparticles. *J. Phys. D. Appl. Phys.* **2008**, *41* (13), 134012.

(67) Farvid, S. S.; Sabergharesou, T.; Hutfluss, L. N.; Hegde, M.; Prouzet, E.; Radovanovic, P. V. Evidence of Charge-Transfer Ferromagnetism in Transparent Diluted Magnetic Oxide Nanocrystals: Switching the Mechanism of Magnetic Interactions. *J. Am. Chem. Soc.* **2014**, *136* (21), 7669–7679.

(68) Coey, J. M. D.; Venkatesan, M.; Fitzgerald, C. B. Donor Impurity Band Exchange in Dilute Ferromagnetic Oxides. *Nat. Mater.* | **2005**, *4*, 173–179.

(69) Coey, J. M. D. D0 Ferromagnetism. *Solid State Sci.* **2005**, *7* (6), 660–667.

(70) Choi, J. H.; Mao, Y.; Chang, J. P. Development of Hafnium Based High-k Materials - A Review. *Mater. Sci. Eng. R Reports* **2011**, *72* (6), 97–136.

(71) Ramadoss, A.; Krishnamoorthy, K.; Kim, S. J. Novel Synthesis of Hafnium Oxide Nanoparticles by Precipitation Method and Its Characterization. *Mater. Res. Bull.* **2012**, *47* (9), 2680–2684.

(72) Sahraneshin, A.; Takami, S.; Hojo, D.; Minami, K.; Arita, T.; Adschiri, T. Synthesis of Shape-Controlled and Organic-Hybridized Hafnium Oxide Nanoparticles under Sub- and

Supercritical Hydrothermal Conditions. *J. Supercrit. Fluids* **2012**, *62*, 190–196.

(73) Sahraneshin, A.; Asahina, S.; Togashi, T.; Singh, V.; Takami, S.; Hojo, D.; Arita, T.; Minami, K.; Adschiri, T. Surfactant-Assisted Hydrothermal Synthesis of Water-Dispersible Hafnium Oxide Nanoparticles in Highly Alkaline Media. *Cryst. Growth Des.* **2012**, *12* (11), 5219–5226.

(74) Kumar, G. M.; Ilanchezhiyan, P.; Xiao, F.; Siva, C.; Kumar, A. M.; Yalishev, V.; Yuldashev, S. U.; Kang, T. W. Blue Luminescence and Schottky Diode Applications of Monoclinic HfO_2 Nanostructures. *RSC Adv.* **2016**, *6* (63), 57941–57947.

(75) Donmez, I.; Kayaci, F.; Ozgit-Akgun, C.; Uyar, T.; Biyikli, N. Fabrication of Hafnia Hollow Nanofibers by Atomic Layer Deposition Using Electrospun Nanofiber Templates. *J. Alloys Compd.* **2013**, *559*, 146–151.

(76) Jaffe, J. E.; Bachorz, R. A.; Gutowski, M. Low-Temperature Polymorphs of ZrO_2 and HfO_2: A Density-Functional Theory Study. *Phys. Rev. B - Condens. Matter Mater. Phys.* **2005**, *72* (14), 144107.

(77) Desgreniers, S.; Lagarec, K. High-Density ZrO_2 and HfO_2 : Crystalline Structures and Equations of State. **1999**, *59* (13), 8467–8472.

(78) Jayaraman, A.; Wang, S. Y.; Sharma, S. K.; Ming, L. C. Pressure-Induced Phase Transformations in HfO_2 to 50 GPa Studied by Raman Spectroscopy. *Phys. Rev. B* **1993**, *48* (13), 9205–9211.

(79) Caravaca, M. A.; Casali, R. A. Ab Initio Localized Basis Set Study of Structural Parameters and Elastic Properties of HfO_2 Polymorphs. *J. Phys. Condens. Matter* **2005**, *17* (37), 5795–5811.

(80) Lowther, J. E.; Dewhurst, J. K.; Leger, J. M.; Haines, J. Relative Stability of ZrO_2 and HfO_2 Structural Phases . *Phys. Rev. B* **1999**, *60* (21), 14485–14488.

(81) J.E.Lowther. Superhard Ceramic Oxides. *MRS Bull.* **2003**, *28* (March), 189–193.

(82) Böscke, T. S.; Müller, J.; Bräuhaus, D.; Schröder, U.; Böttger, U. Ferroelectricity in Hafnium Oxide Thin Films. *Appl. Phys. Lett.* **2011**, *99* (10), 102903.

(83) Polakowski, P.; Müller, J. Ferroelectricity in Undoped Hafnium Oxide. *Appl. Phys. Lett.* **2015**, *106* (23), 232905.

(84) Schroeder, U.; Mueller, S.; Mueller, J.; Yurchuk, E.; Martin, D.; Adelmann, C.; Schloesser,

T.; van Bentum, R.; Mikolajick, T. Hafnium Oxide Based CMOS Compatible Ferroelectric Materials. *ECS J. Solid State Sci. Technol.* **2013**, *2* (4), N69–N72.

(85) Mulaos, H.; Ker, J. O.; Mulle, S.; Schroeder, U.; Müller, J.; Polakowski, P.; Flachowsky, S.; Van Bentum, R.; Mikolajick, T.; Slesazeck, S. Switching Kinetics in Nanoscale Hafnium Oxide Based Ferroelectric Field-Effect Transistors. *ACS Appl. Mater. Interfaces* **2017**, *9* (4), 3792–3798.

(86) Muller, J.; Boscke, T. S.; Muller, S.; Yurchuk, E.; Polakowski, P.; Paul, J.; Martin, D.; Schenk, T.; Khullar, K.; Kersch, A.; Weinreich, W.; Riedel, S.; Seidel, K.; Kumar, A.; Arruda, T. M.; Kalinin, S. V.; Schlosser, T.; Boschke, R.; Van Bentum, R.; Schroder, U.; Mikolajick, T. Ferroelectric Hafnium Oxide: A CMOS-Compatible and Highly Scalable Approach to Future Ferroelectric Memories. *Tech. Dig. - Int. Electron Devices Meet. IEDM* **2013**, 10.8.1-10.8.4.

(87) Ni, J.; Zhu, Y.; Wang, S.; Li, Z.; Zhang, Z.; Wei, B. Nanostructuring HfO_2 Thin Films as Antireflection Coatings. *J. Am. Ceram. Soc.* **2009**, *92* (12), 3077–3080.

(88) Waldorf, A. J.; Dobrowolski, J. A.; Sullivan, B. T.; Plante, L. M. Optical Coatings Deposited by Reactive Ion Plating. *Appl. Opt.* **1993**, *32* (28), 5583.

(89) Chow, R.; Falabella, S.; Loomis, G. E.; Rainer, F.; Stolz, C. J.; Kozlowski, M. R. Reactive Evaporation of Low-Defect Density Hafnia. *Appl. Opt.* **1993**, *32* (28), 5567.

(90) Khoshman, J. M.; Kordesch, M. E. Optical Properties of a-HfO_2 Thin Films. *Surf. Coatings Technol.* **2006**, *201* (6), 3530–3535.

(91) Tran, X. A.; Yu, H. Y.; Yeo, Y. C.; Wu, L.; Liu, W. J.; Wang, Z. R.; Fang, Z.; Pey, K. L.; Sun, X. W.; Du, A. Y.; Nguyen, B. Y.; Li, M. F. A High-Yield HfO_x-Based Unipolar Resistive Ram Employing Ni Electrode Compatible with Si-Diode Selector for Crossbar Integration. *IEEE Electron Device Lett.* **2011**, *32* (3), 396–398.

(92) Govoreanu, B.; Kar, G. S.; Chen, Y. Y.; Paraschiv, V.; Kubicek, S.; Fantini, A.; Radu, I. P.; Goux, L.; Clima, S.; Degraeve, R.; Jossart, N.; Richard, O.; Vandeweyer, T.; Seo, K.; Hendrickx, P.; Pourtois, G.; Bender, H.; Altimime, L.; Wouters, D. J.; Kittl, J. A.; Jurczak, M. 10×10nm 2 Hf/HfO_x Crossbar Resistive RAM with Excellent Performance, Reliability and Low-Energy Operation. *Tech. Dig. - Int. Electron Devices Meet. IEDM* **2011**, 31.6.1-31.6.4.

(93) Abunahla, H.; Mohammad, B.; Jaoude, M. A.; Al-Qutayri, M. Novel Hafnium Oxide

Memristor Device: Switching Behaviour and Size Effect. *Proc. - IEEE Int. Symp. Circuits Syst.* **2017**, 7–10.

(94) He, W.; Sun, H.; Zhou, Y.; Lu, K.; Xue, K.; Miao, X. Customized Binary and Multi-Level HfO_{2-x}-Based Memristors Tuned by Oxidation Conditions. *Sci. Rep.* **2017**, *7* (1), 10070.

(95) Capone, S.; Leo, G.; Rella, R.; Siciliano, P.; Vasanelli, L.; Alvisi, M.; Mirenghi, L.; Rizzo, A. Physical Characterization of Hafnium Oxide Thin Films and Their Application as Gas Sensing Devices. *J. Vac. Sci. Technol. A Vacuum, Surfaces, Film.* **1998**, *16* (6), 3564–3568.

(96) Venkatesan, M.; Fitzgerald, C. B.; Coey, J. M. D.; M., V.; C.B., F.; J.M.D., C. Unexpected Magnetism in a Dielectric Oxide. *Nature* **2004**, *430*, 630.

(97) Rao, M. S. R.; Kundaliya, D. C.; Ogale, S. B.; Fu, L. F.; Welz, S. J.; Browning, N. D.; Zaitsev, V.; Varughese, B.; Cardoso, C. A.; Curtin, A.; Dhar, S.; Shinde, S. R.; Venkatesan, T.; Lofland, S. E.; Schwarz, S. A. Search for Ferromagnetism in Undoped and Cobalt-Doped Hf O 2-δ. *Appl. Phys. Lett.* **2006**, *88* (14), 142505.

(98) Coey, J. M. D.; Venkatesan, M.; Stamenov, P.; Fitzgerald, C. B.; Dorneles, L. S. Magnetism in Hafnium Dioxide. *Phys. Rev. B - Condens. Matter Mater. Phys.* **2005**, *72* (2), 024450.

(99) Zhang, S.; Ogale, S. B.; Yu, W.; Cao, X.; Liu, T.; Ghosh, S.; Das, G. P.; Wee, A. T. S.; Greene, R. L.; Venkatesan, T. Electronic Manifestation of Cation-Vacancy-Induced Magnetic Moments in a Transparent Oxide Semiconductor: Anatase $Nb:TiO_2$. *Adv. Mater.* **2009**, *21* (22), 2282–2287.

(100) Ali, N.; Singh, B.; A R, V.; Lal, S.; Yadav, C. S.; Tarafder, K.; Ghosh, S. Ferromagnetism in Mn-Doped ZnO: A Joint Theoretical and Experimental Study. *J. Phys. Chem. C* **2021**, *125* (14), 7734–7745.

(101) Ning, S.; Zhang, Z. Phase-Dependent and Defect-Driven D0 Ferromagnetism in Undoped ZrO_2 Thin Films. *RSC Adv.* **2015**, *5* (5), 3636–3641.

(102) Hong, N. H.; Poirot, N.; Sakai, J. Evidence for Magnetism Due to Oxygen Vacancies in Fe-Doped HfO_2 Thin Films. *Appl. Phys. Lett.* **2006**, *89* (4), 87–90.

(103) Saadaoui, H.; Luo, X.; Salman, Z.; Cui, X. Y.; Bao, N. N.; Bao, P.; Zheng, R. K.; Tseng, L. T.; Du, Y. H.; Prokscha, T.; Suter, A.; Liu, T.; Wang, Y. R.; Li, S.; Ding, J.; Ringer, S. P.; Morenzoni, E.; Yi, J. B. Intrinsic Ferromagnetism in the Diluted Magnetic Semiconductor $Co:TiO_2$. *Phys. Rev. Lett.* **2016**, *117* (22), 227202.

(104) Lu, W.; Lieber, C. M. Semiconductor Nanowires. *J. Phys. D. Appl. Phys.* **2006**, *39* (21).

(105) Léonard, F.; Talin, A. A.; Katzenmeyer, A.; Swartzentruber, B. S.; Picraux, S. T.; Toimil-Molares, E.; Cederberg, J. G.; Wang, X.; Hersee, S. D.; Rishinaramangalum, A. Electronic Transport in Nanowires: From Injection-Limited to Space-Charge-Limited Behavior. In *Nanoepitaxy: Homo- and Heterogeneous Synthesis, Characterization, and Device Integration of Nanomaterials*; Islam, M. S., Talin, A. A., Hersee, S. D., Eds.; SPIE, 2009; Vol. 7406, pp 66–78.

(106) Berengue, O. M.; Simon, R. A.; Leite, E. R.; Chiquito, A. J. The Study of Electron Scattering Mechanisms in Single Crystal Oxide Nanowires. *J. Phys. D. Appl. Phys.* **2011**, *44* (21), 215405.

(107) Zhang, D.; Liu, Z.; Han, S.; Li, C.; Lei, B.; Stewart, M. P.; Tour, J. M.; Zhou, C. Magnetite (Fe_3O_4) Core − Shell Nanowires : Synthesis and Magnetoresistance. *Nano Lett.* **2004**, *4* (11), 2151–2155.

(108) Ramadoss, A.; Kim, S. J. Synthesis and Characterization of HfO_2 Nanoparticles by Sonochemical Approach. *J. Alloys Compd.* **2012**, *544*, 115–119.

(109) Ramadoss, A.; Krishnamoorthy, K.; Kim, S. J. Novel Synthesis of Hafnium Oxide Nanoparticles by Precipitation Method and Its Characterization. *Mater. Res. Bull.* **2012**, *47* (9), 2680–2684.

(110) Meskin, P. E.; Sharikov, F. Y.; Ivanov, V. K.; Churagulov, B. R.; Tretyakov, Y. D. Rapid Formation of Nanocrystalline HfO_2 Powders from Amorphous Hafnium Hydroxide under Ultrasonically Assisted Hydrothermal Treatment. *Mater. Chem. Phys.* **2007**, *104* (2–3), 439–443.

(111) Meskin, P. E.; Gavrilov, A. I.; Maksimov, V. D.; Ivanov, V. K.; Churagulov, B. P. Hydrothermal/Microwave and Hydrothermal/Ultrasonic Synthesis of Nanocrystalline Titania, Zirconia, and Hafnia. *Russ. J. Inorg. Chem.* **2007**, *52* (11), 1648–1656.

(112) Buha, J.; Arčon, D.; Niederberger, M.; Djerdj, I. Solvothermal and Surfactant-Free Synthesis of Crystalline Nb_2O_5, Ta_2O_5, HfO_2, and Co-Doped HfO_2 Nanoparticles. *Phys. Chem. Chem. Phys.* **2010**, *12* (47), 15537–15543.

(113) Pinna, N.; Garnweitner, G.; Antonietti, M.; Niederberger, M. Non-Aqueous Synthesis of High-Purity Metal Oxide Nanopowders Using an Ether Elimination Process. *Adv. Mater.*

2004, *16* (23–24), 2196–2200.

(114) Semaltianos, N. G.; Friedt, J. M.; Chassagnon, R.; Moutarlier, V.; Blondeau-Patissier, V.; Combe, G.; Assoul, M.; Monteil, G. Oxide or Carbide Nanoparticles Synthesized by Laser Ablation of a Bulk Hf Target in Liquids and Their Structural, Optical, and Dielectric Properties. *J. Appl. Phys.* **2016**, *119* (20), 204903.

(115) Dhanunjaya, M.; Byram, C.; Vendamani, V. S.; Rao, S. V.; Pathak, A. P.; Rao, S. V. S. N. Hafnium Oxide Nanoparticles Fabricated by Femtosecond Laser Ablation in Water. *Appl. Phys. A Mater. Sci. Process.* **2019**, *125* (1), 74.

(116) Pugachevskii, M. A.; Panfilov, V. I. Optical Properties of HfO_2 Nanoparticles Produced by Laser Ablation. *J. Appl. Spectrosc.* **2014**, *81* (4), 640–643.

(117) Zeng, H.; Du, X. W.; Singh, S. C.; Kulinich, S. A.; Yang, S.; He, J.; Cai, W. Nanomaterials via Laser Ablation/Irradiation in Liquid: A Review. *Adv. Funct. Mater.* **2012**, *22* (7), 1333–1353.

(118) Tsuchiya, H.; Schmuki, P. Self-Organized High Aspect Ratio Porous Hafnium Oxide Prepared by Electrochemical Anodization. *Electrochem. commun.* **2005**, *7* (1), 49–52.

(119) Qiu, X.; Howe, J. Y.; Cardoso, M. B.; Polat, O.; Heller, W. T.; Parans Paranthaman, M. Size Control of Highly Ordered HfO_2 Nanotube Arrays and a Possible Growth Mechanism. *Nanotechnology* **2009**, *20* (45), 455601.

(120) Berger, S.; Jakubka, F.; Schmuki, P. Self-Ordered Hexagonal Nanoporous Hafnium Oxide and Transition to Aligned HfO_2 Nanotube Layers. *Electrochem. Solid-State Lett.* **2009**, *12* (7), K45–K48.

(121) Apolinário, A.; Sousa, C. T.; Oliveira, G. N. P.; Lopes, A. M. L.; Ventura, J.; Andrade, L.; Mendes, A.; Araújo, J. P. Tailoring the Anodic Hafnium Oxide Morphology Using Different Organic Solvent Electrolytes. *Nanomaterials* **2020**, *10* (2), 382.

(122) Perez, I.; Robertson, E.; Banerjee, P.; Henn-Lecordier, L.; Son, S. J.; Lee, S. B.; Rubloff, G. W. TEM-Based Metrology for HfO_2 Layers and Nanotubes Formed in Anodic Aluminum Oxide Nanopore Structures. *Small* **2008**, *4* (8), 1223–1232.

(123) Su, Y.; Lu, B.; Xie, Y.; Ma, Z.; Liu, L.; Zhao, H.; Zhang, J.; Duan, H.; Zhang, H.; Li, J.; Xiong, Y.; Xie, E. Temperature Effect on Electrospinning of Nanobelts: The Case of Hafnium Oxide. *Nanotechnology* **2011**, *22* (28), 285609.

(124) Jung, J. W.; Kim, G. Y.; Lee, N. W.; Ryu, W. H. Low-Temperature Synthesis of Tetragonal Phase of Hafnium Oxide Using Polymer-Blended Nanofiber Precursor. *Appl. Surf. Sci.* **2020**, *533* (May), 147496.

(125) Wu, Y.; Yan, H.; Huang, M.; Messer, B.; Song, J. H.; Yang, P. Inorganic Semiconductor Nanowires: Rational Growth, Assembly, and Novel Properties. *Chem. - A Eur. J.* **2002**, *8* (6), 1260–1268.

(126) Güniat, L.; Caroff, P.; Fontcuberta I Morral, A. Vapor Phase Growth of Semiconductor Nanowires: Key Developments and Open Questions. *Chem. Rev.* **2019**, *119* (15), 8958–8971.

(127) Chen, L.; Lu, W.; Lieber, C. M. Chapter 1 Semiconductor Nanowire Growth and Integration. In *Semiconductor Nanowires: From Next-Generation Electronics to Sustainable Energy*; The Royal Society of Chemistry, 2015; pp 1–53.

(128) Hochbaum, A. I.; Fan, R.; He, R.; Yang, P. Controlled Growth of Si Nanowire Arrays for Device Integration. *Nano Lett.* **2005**, *5* (3), 457–460.

(129) Fontcuberta I Morral, A.; Arbiol, J.; Prades, J. D.; Cirera, A.; Morante, J. R. Synthesis of Silicon Nanowires with Wurtzite Crystalline Structure by Using Standard Chemical Vapor Deposition. *Adv. Mater.* **2007**, *19* (10), 1347–1351.

(130) Khanlary, M. R.; alijarahi, S.; Reyhani, A. Growth Temperature Dependence of VLS-Grown Ultra-Long ZnS Nanowires Prepared by CVD Method. *J. Theor. Appl. Phys.* **2018**, *12* (2), 121–126.

(131) Puglisi, R. A.; Bongiorno, C.; Caccamo, S.; Fazio, E.; Mannino, G.; Neri, F.; Scalese, S.; Spucches, D.; La Magna, A. Chemical Vapor Deposition Growth of Silicon Nanowires with Diameter Smaller Than 5 Nm. *ACS Omega* **2019**, *4* (19), 17967–17971.

(132) Haraguchi, K.; Katsuyama, T.; Hiruma, K.; Ogawa, K. GaAs P-n Junction Formed in Quantum Wire Crystals. *Appl. Phys. Lett.* **1992**, *60* (6), 745–747.

(133) Dai, Z. R.; Gole, J. L.; Stout, J. D.; Wang, Z. L. Tin Oxide Nanowires, Nanoribbons, and Nanotubes. *J. Phys. Chem. B* **2002**, *106* (6), 1274–1279.

(134) Dai, Z. R.; Pan, Z. W.; Wang, Z. L. Novel Nanostructures of Functional Oxides Synthesized by Thermal Evaporation. *Adv. Funct. Mater.* **2003**, *13* (1), 9–24.

(135) Sivakov, V.; Andrä, G.; Himcinschi, C.; Gösele, U.; Zahn, D. R. T.; Christiansen, S. Growth Peculiarities during Vapor-Liquid-Solid Growth of Silicon Nanowhiskers by Electron-Beam

Evaporation. *Appl. Phys. A Mater. Sci. Process.* **2006**, *85* (3), 311–315.

(136) Liu, J. L.; Cai, S. J.; Jin, G. L.; Thomas, S. G.; Wang, K. L. Growth of Si Whiskers on Au/Si(1 1 1) Substrate by Gas Source Molecular Beam Epitaxy (MBE). *J. Cryst. Growth* **1999**, *200* (1–2), 106–111.

(137) Kanungo, P. Das; Zakharov, N.; Bauer, J.; Breitenstein, O.; Werner, P.; Goesele, U. Controlled in Situ Boron Doping of Short Silicon Nanowires Grown by Molecular Beam Epitaxy. *Appl. Phys. Lett.* **2008**, *92* (26), 263107.

(138) Tchernycheva, M.; Harmand, J. C.; Patriarche, G.; Travers, L.; Cirlin, G. E. Temperature Conditions for GaAs Nanowire Formation by Au-Assisted Molecular Beam Epitaxy. *Nanotechnology* **2006**, *17* (16), 4025–4030.

(139) Morales, A. M.; Lieber, C. M. A Laser Ablation Method for the Synthesis of Crystalline Semiconductor Nanowires. *Science (80-.).* **1998**, *279* (5348), 208–211.

(140) Bazargan, S.; Leung, K. T. Catalyst-Assisted Pulsed Laser Deposition of One-Dimensional Single-Crystalline Nanostructures of Tin(IV) Oxide: Interplay of VS and VLS Growth Mechanisms at Low Temperature. *J. Phys. Chem. C* **2012**, *116* (9), 5427–5434.

(141) Rahman, M. A.; Bazargan, S.; Srivastava, S.; Wang, X.; Abd-Ellah, M.; Thomas, J. P.; Heinig, N. F.; Pradhan, D.; Leung, K. T. Defect-Rich Decorated TiO_2 Nanowires for Super-Efficient Photoelectrochemical Water Splitting Driven by Visible Light. *Energy Environ. Sci.* **2015**, *8* (11), 3363–3373.

(142) *Pulsed Laser Deposition of Thin Films*; Chrisey, D. B., Hulber, G. K., Eds.; John Wiley & Sons, Inc.: New York, 1994.

(143) Smith, H. M.; Turner, A. F. Vacuum Deposited Thin Films Using a Ruby Laser. *Appl. Opt.* **1965**, *4* (1), 147–148.

(144) Dijkkamp, D.; Venkatesan, T.; Wu, X. D.; Shaheen, S. A.; Jisrawi, N.; Min-Lee, Y. H.; McLean, W. L.; Croft, M. Preparation of Y-Ba-Cu Oxide Superconductor Thin Films Using Pulsed Laser Evaporation from High Tc Bulk Material. *Appl. Phys. Lett.* **1987**, *51* (8), 619–621.

(145) Schneider, C.; Lippert, T. Laser Ablation and Thin Film Deposition. In *Laser Processing of Materials, Fundamentals, Applications and Developments*; Schaaf, P., Ed.; Springe-Verlag Berlin Heidelberg, 2010; pp 89–91.

(146) Willmott, P. R.; Huber, J. R. Pulsed Laser Vaporization and Deposition. *Rev. Mod. Phys.* **2000**, *72* (1), 315–328.

(147) Yang, Z.; Hao, J. Progress in Pulsed Laser Deposited Two-Dimensional Layered Materials for Device Applications. *J. Mater. Chem. C* **2016**, *4* (38), 8859–8878.

(148) Pervolaraki, M.; Mihailescu, C. N.; Luculescu, C. R.; Ionescu, P.; Dracea, M. D.; Pantelica, D.; Giapintzakis, J. Picosecond Ultrafast Pulsed Laser Deposition of $SrTiO_3$. *Appl. Surf. Sci.* **2015**, *336*, 278–282.

(149) Amoruso, S.; Ausanio, G.; De Lisio, C.; Iannotti, V.; Vitiello, M.; Wang, X.; Lanotte, L. Synthesis of Nickel Nanoparticles and Nanoparticles Magnetic Films by Femtosecond Laser Ablation in Vacuum. *Appl. Surf. Sci.* **2005**, *247* (1–4), 71–75.

(150) Christen, H. M.; Eres, G. Recent Advances in Pulsed-Laser Deposition of Complex Oxides. *J. Phys. Condens. Matter* **2008**, *20* (26), 264005.

(151) Sharma, P.; Gupta, A.; Rao, K. V.; Owens, F. J.; Sharma, R.; Ahuja, R.; Guillen, J. M. O.; Johansson, B.; Gehring, G. A. Ferromagnetism above Room Temperature in Bulk and Transparent Thin Films of Mn-Doped ZnO. *Nat. Mater.* **2003**, *2* (10), 673–677.

(152) Hong, N. H.; Sakai, J.; Poirot, N.; Brizé, V. Room-Temperature Ferromagnetism Observed in Undoped Semiconducting and Insulating Oxide Thin Films. *Phys. Rev. B - Condens. Matter Mater. Phys.* **2006**, *73* (13), 132404.

(153) Hong, N. H.; Sakai, J.; Poirot, N.; Ruyter, A. Laser Ablated Ni-Doped HfO_2 Thin Films: Room Temperature Ferromagnets. *Appl. Phys. Lett.* **2005**, *86* (24), 242505.

(154) Marcu, A.; Trupina, L.; Zamani, R.; Arbiol, J.; Grigoriu, C.; Morante, J. R. Catalyst Size Limitation in Vapor-Liquid-Solid ZnO Nanowire Growth Using Pulsed Laser Deposition. *Thin Solid Films* **2012**, *520* (14), 4626–4631.

(155) Nagashima, K.; Yanagida, T.; Tanaka, H.; Kawai, T. Epitaxial Growth of MgO Nanowires by Pulsed Laser Deposition. *J. Appl. Phys.* **2007**, *101* (12), 124304.

(156) Suzuki, M.; Hidaka, Y.; Yanagida, T.; Klamchuen, A.; Kanai, M.; Kawai, T.; Kai, S. Essential Role of Catalyst in Vapor-Liquid-Solid Growth of Compounds. *Phys. Rev. E - Stat. Nonlinear, Soft Matter Phys.* **2011**, *83* (6), 61606.

(157) Klamchuen, A.; Suzuki, M.; Nagashima, K.; Yoshida, H.; Kanai, M.; Zhuge, F.; He, Y.; Meng, G.; Kai, S.; Takeda, S.; Kawai, T.; Yanagida, T. Rational Concept for Designing

Vapor-Liquid-Solid Growth of Single Crystalline Metal Oxide Nanowires. *Nano Lett.* **2015**, *15* (10), 6406–6412.

(158) Zhu, Z.; Suzuki, M.; Nagashima, K.; Yoshida, H.; Kanai, M.; Meng, G.; Anzai, H.; Zhuge, F.; He, Y.; Boudot, M.; Takeda, S.; Yanagida, T. Rational Confcept for Reducing Growth Temperature in Vapor-Liquid-Solid Process of Metal Oxide Nanowires. *Nano Lett.* **2016**, *16* (12), 7495–7502.

(159) Werner Kern. *Handbook of Semiconductor Wafer Cleaning Technology: Science, Technology, and Applications*; Noyes Publications, 1993.

(160) Qiu, Z. Q.; Bader, S. D. Surface Magneto-Optic Kerr Effect. *Rev. Sci. Instrum.* **2000**, *71* (3), 1243–1255.

(161) Felcher, G. P. Neutron Reflectometry as a Tool to Study Magnetism (Invited). *J. Appl. Phys.* **2000**, *87* (9 II), 5431–5436.

(162) Dürr, H. A.; Eimüller, T.; Elmers, H. J.; Eisebitt, S.; Farle, M.; Kuch, W.; Matthes, F.; Martins, M.; Mertins, H. C.; Oppeneer, P. M.; Plucinski, L.; Schneider, C. M.; Wende, H.; Wurth, W.; Zabel, H. A Closer Look into Magnetism: Opportunities with Synchrotron Radiation. *IEEE Trans. Magn.* **2009**, *45* (1), 15–57.

(163) Fagaly, R. L. Superconducting Quantum Interference Device Instruments and Applications. *Rev. Sci. Instrum.* **2006**, *77* (10), 101101.

(164) Buchner, M.; Höfler, K.; Henne, B.; Ney, V.; Ney, A. Tutorial: Basic Principles, Limits of Detection, and Pitfalls of Highly Sensitive SQUID Magnetometry for Nanomagnetism and Spintronics. *J. Appl. Phys.* **2018**, *124* (16), 161101.

(165) Clarke, J. SQUIDs. *Sci. Am.* **1994**, *271* (2), 46–53.

(166) Quantum Design, Inc., 10307 Pacific Center Court, San Diego, CA 92121, USA, See www.Qdusa.Com.

(167) Jackson, M.; Solheid, P. On the Quantitative Analysis and Evaluation of Magnetic Hysteresis Data. *Geochemistry, Geophys. Geosystems* **2010**, *11* (4).

(168) Paterson, G. A.; Zhao, X.; Jackson, M.; Heslop, D. Measuring, Processing, and Analyzing Hysteresis Data. *Geochemistry, Geophys. Geosystems* **2018**, *19* (7), 1925–1945.

(169) Zhao, L.; Clima, S.; Magyari-Köpe, B.; Jurczak, M.; Nishi, Y. Ab Initio Modeling of Oxygen-

Vacancy Formation in Doped-HfO_x RRAM: Effects of Oxide Phases, Stoichiometry, and Dopant Concentrations. *Appl. Phys. Lett.* **2015**, *107* (1), 013504.

(170) Zhang, H.; Gao, B.; Yu, S.; Lai, L.; Zeng, L.; Sun, B.; Liu, L.; Liu, X.; Lu, J.; Han, R.; Kang, J. Effects of Ionic Doping on the Behaviors of Oxygen Vacancies in HfO_2 and ZrO_2: A First Principles Study. In *International Conference on Simulation of Semiconductor Processes and Devices, SISPAD*; IEEE, 2009; pp 1–4.

(171) Lee, B. H.; Kang, L.; Qi, W. J.; Nieh, R.; Jeon, Y.; Onishi, K.; Lee, J. C. Ultrathin Hafnium Oxide with Low Leakage and Excellent Reliability for Alternative Gate Dielectric Application. In *Technical Digest - International Electron Devices Meeting*; 1999; pp 133–136.

(172) Kang, L.; Lee, B. H.; Qi, W. J.; Jeon, Y.; Nieh, R.; Gopalan, S.; Onishi, K.; Lee, J. C. Electrical Characteristics of Highly Reliable Ultrathin Hafnium Oxide Gate Dielectric. *IEEE Electron Device Lett.* **2000**, *21* (4), 181–183.

(173) Maiti, C. K.; Maikap, S.; Chatterjee, S.; Nandi, S. K.; Samanta, S. K. Hafnium Oxide Gate Dielectric for Strained-Si1-XGex. *Solid. State. Electron.* **2003**, *47* (11), 1995–2000.

(174) Bharathi, K. K.; Venkatesh, S.; Prathiba, G.; Kumar, N. H.; Ramana, C. V. Room Temperature Ferromagnetism in HfO_2 Films. *J. Appl. Phys.* **2011**, *109* (7), 07C318.

(175) Tirosh, E.; Markovich, G. Control of Defects and Magnetic Properties in Colloidal HfO_2 Nanorods. *Adv. Mater.* **2007**, *19* (18), 2608–2612.

(176) Rahman, M. A.; Thomas, J. P.; Leung, K. T. A Delaminated Defect-Rich ZrO_2 Hierarchical Nanowire Photocathode for Efficient Photoelectrochemical Hydrogen Evolution. *Adv. Energy Mater.* **2018**, *8* (4), 1701234.

(177) Mohammad, S. N. Bimetallic-Catalyst-Mediated Syntheses of Nanomaterials (Nanowires, Nanotubes, Nanofibers, Nanodots, Etc) by the VQS (Vapor-Quasiliquid-Solid, Vapor-Quasisolid-Solid) Growth Mechanism. *J. Phys. D. Appl. Phys.* **2016**, *49* (49), 495304.

(178) Chou, Y.-C.; Wen, C.-Y.; Reuter, M. C.; Su, D.; Stach, E. A.; Ross, F. M. Controlling the Growth of Si/Ge Nanowires and Heterojunctions Using SilverÀGold Alloy Catalysts. *ACS Nano* **2012**, *6* (7), 6407–6415.

(179) Felizco, J. C.; Uenuma, M.; Senaha, D.; Ishikawa, Y.; Uraoka, Y. Growth of InGaZnO Nanowires via a Mo/Au Catalyst from Amorphous Thin Film. *Appl. Phys. Lett.* **2017**, *111* (3), 33104.

(180) Cargnello, M.; Agarwal, R.; Klein, D. R.; Diroll, B. T.; Agarwal, R.; Murray, C. B. Uniform Bimetallic Nanocrystals by High-Temperature Seed-Mediated Colloidal Synthesis and Their Catalytic Properties for Semiconducting Nanowire Growth. *Chem. Mater.* **2015**, *27* (16), 5833–5838.

(181) Okamoto, H. Au-Sn (Gold-Tin). *J. Phase Equilibria Diffus.* **2007**, *28* (5), 490.

(182) Lee, J.; Shimoda, W.; Tanaka, T. Surface Tension and Its Temperature Coefficient of Liquid Sn-X (X=Ag, Cu) Alloys. *Mater. Trans.* **2004**, *45* (9), 2864–2870.

(183) Pstruś, J.; Moser, Z.; Gąsior, W.; Dębski, A. Surface Tension and Density Measurements of Liquid Sn-Zn Alloys. Experiment vs. Surdat Database of Pb-Free Solders. *Arch. Metall. Mater.* **2006**, *51* (3), 335–343.

(184) R. Novakovic, E. Ricci, F. Gnecco, D. Giuranno, G. B. Surface and Transport Properties of Liquid Au–Sn Alloys. *Surf. Sci.* **2005**, *599* (1–3), 230–247.

(185) S.M Kaufman, T. . W. The Surface Tension of Liquid Gold, Liquid Tin, and Liquid Gold-Tin Binary Solutions. *Acta Metall.* **1965**, *13* (7), 797–805.

(186) Blöchl, P. E.; Jepsen, O.; Andersen, O. K. Improved Tetrahedron. *Phys. Rev. B* **1994**, *49* (23), 16223–16233.

(187) Joubert, D. From Ultrasoft Pseudopotentials to the Projector Augmented-Wave Method. *Phys. Rev. B - Condens. Matter Mater. Phys.* **1999**, *59* (3), 1758–1775.

(188) Perdew, J. P.; Burke, K.; Ernzerhof, M. Generalized Gradient Approximation Made Simple. *Phys. Rev. Lett.* **1996**, *77* (18), 3865–3868.

(189) *"Physical Constants of Inorganic Compounds" in CRC Handbook of Chemistry and Physics*, 102nd Edit.; Rumble, J. R., Ed.; CRC Press/Taylor & Francis: Boca Raton, FL.

(190) Lee, C.-K.; Cho, E.; Lee, H.-S.; Hwang, C. S.; Han, S. First-Principles Study on Doping and Phase Stability of HfO_2. *Phys. Rev. B* **2008**, *78* (1), 12102.

(191) Sharath, S. U.; Bertaud, T.; Kurian, J.; Hildebrandt, E.; Walczyk, C.; Calka, P.; Zaumseil, P.; Sowinska, M.; Walczyk, D.; Gloskovskii, A.; Schroeder, T.; Alff, L. Towards Forming-Free Resistive Switching in Oxygen Engineered HfO_{2-x}. *Appl. Phys. Lett.* **2014**, *104* (6), 63502.

(192) Cho, D. Y.; Jung, H. S.; Yu, I. H.; Yoon, J. H.; Kim, H. K.; Lee, S. Y.; Jeon, S. H.; Han, S.; Kim, J. H.; Park, T. J.; Park, B. G.; Hwang, C. S. Stabilization of Tetragonal HfO_2 under Low

Active Oxygen Source Environment in Atomic Layer Deposition. *Chem. Mater.* **2012**, *24* (18), 3534–3543.

(193) Mukhopadhyay, A. B.; Sanz, J. F.; Musgrave, C. B. First-Principles Calculations of Structural and Electronic Properties of Monoclinic Hafnia Surfaces. *Phys. Rev. B - Condens. Matter Mater. Phys.* **2006**, *73* (11), 115330.

(194) Nakamura, T.; Mochidzuki, Y.; Sato, S. Fabrication of Gold Nanoparticles in Intense Optical Field by Femtosecond Laser Irradiation of Aqueous Solution. *J. Mater. Res.* **2008**, *23* (4), 968–974.

(195) Torres-Mendieta, R.; Ventura-Espinosa, D.; Sabater, S.; Lancis, J.; Mínguez-Vega, G.; Mata, J. A. In Situ Decoration of Graphene Sheets with Gold Nanoparticles Synthetized by Pulsed Laser Ablation in Liquids. *Sci. Rep.* **2016**, *6* (1), 30478.

(196) Barreca, D.; Milanov, A.; Fischer, R. A.; Devi, A.; Tondello, E. Hafnium Oxide Thin Film Grown by ALD: An XPS Study. *Surf. Sci. Spectra* **2007**, *14* (1), 34–40.

(197) Sivaneri, K. V. I.; Ozmen, O.; Aziziha, M.; Sabolsky, E. M.; Evans, T. H.; Devallance, D. B.; Johnson, M. B. Robust Polymer-HfO_2 Thin Film Laminar Composites for Tactile Sensing Applications. *Smart Mater. Struct.* **2019**, *28* (2), 025002.

(198) Moulder, J. F.; Stickle, W. F.; Sobol, P. E.; Bomben, K. D. *Handbook of X-Ray Photoelectron Spectroscopy*; Chastain, J., Ed.; Perkin-Elmer Corporation: Minnesota, 1992.

(199) Liu, Y.; Li, J.; Li, W.; Liu, Q.; Yang, Y.; Li, Y.; Chen, Q. Enhanced Photoelectrochemical Performance of WO_3 Film with HfO_2 Passivation Layer. *Int. J. Hydrogen Energy* **2015**, *40* (29), 8856–8863.

(200) Kumar, M.; Bhatt, V.; Abhyankar, A. C.; Kim, J.; Kumar, A.; Patil, S. H.; Yun, J. H. New Insights towards Strikingly Improved Room Temperature Ethanol Sensing Properties of P-Type Ce-Doped SnO_2 Sensors. *Sci. Rep.* **2018**, *8* (1), 8079.

(201) Sokolov, A. S.; Jeon, Y. R.; Kim, S.; Ku, B.; Lim, D.; Han, H.; Chae, M. G.; Lee, J.; Ha, B. G.; Choi, C. Influence of Oxygen Vacancies in ALD HfO_{2-x} Thin Films on Non-Volatile Resistive Switching Phenomena with a Ti/HfO_{2-x}/Pt Structure. *Appl. Surf. Sci.* **2018**, *434*, 822–830.

(202) Baer, D. R.; Engelhard, M. H.; Lea, A. S.; Nachimuthu, P.; Droubay, T. C.; Kim, J.; Lee, B.; Mathews, C.; Opila, R. L.; Saraf, L. V.; Stickle, W. F.; Wallace, R. M.; Wright, B. S.

Comparison of the Sputter Rates of Oxide Films Relative to the Sputter Rate of SiO_2. *J. Vac. Sci. Technol. A Vacuum, Surfaces, Film.* **2010**, *28* (5), 1060–1072.

(203) Oswald, S.; Lattner, E.; Seifert, M. XPS Chemical State Analysis of Sputter Depth Profiling Measurements for Annealed TiAl-SiO_2 and TiAl-W Layer Stacks. *Surf. Interface Anal.* **2020**, *52* (12), 924–928.

(204) Süzer, Ş. XPS Investigation of X-Ray-Induced Reduction of Metal Ions. *Appl. Spectrosc.* **2000**, *54* (11), 1716–1718.

(205) Mitchell, D. F.; Sproule, G. I.; Graham, M. J. Sputter Reduction of Oxides by Ion Bombardment during Auger Depth Profile Analysis. *Surf. Interface Anal.* **1990**, *15* (8), 487–497.

(206) Fei, W.; Bart, H. J. Prediction of Diffusivities in Liquids. *Chem. Eng. Technol.* **1998**, *21* (8), 659–665.

(207) Grosse, A. V. The Viscosity of Liquid Metals and an Empirical Relationship between Their Activation Energy of Viscosity and Their Melting Points. *J. Inorg. Nucl. Chem.* **1961**, *23* (3–4), 333–339.

(208) Hadacek, N.; Nosov, A.; Ranno, L.; Strobel, P.; Galéra, R. M. Magnetic Properties of HfO_2 Thin Films. *J. Phys. Condens. Matter* **2007**, *19* (48), 486206.

(209) MacDonald, A. H.; Schiffer, P.; Samarth, N. Ferromagnetic Semiconductors: Moving beyond (Ga,Mn)As. *Nat. Mater.* **2005**, *4* (3), 195–202.

(210) Ning, S.; Zhan, P.; Xie, Q.; Li, Z.; Zhang, Z. Room-Temperature Ferromagnetism in Un-Doped ZrO_2 Thin Films. *J. Phys. D. Appl. Phys.* **2013**, *46* (44), 445004.

(211) Prellier, W.; Fouchet, A.; Mercey, B. Oxide-Diluted Magnetic Semiconductors: A Review of the Experimental Status. *J. Phys. Condens. Matter* **2003**, *15* (37), R1583–R1601.

(212) Dietl, T.; Haury, A.; Merle dșAubigné, Y. Free Carrier-Induced Ferromagnetism in Structures of Diluted Magnetic Semiconductors. *Phys. Rev. B - Condens. Matter Mater. Phys.* **1997**, *55* (6), R3347–R3350.

(213) Priour, D. J.; Das Sarma, S. Phase Diagram of the Disordered RKKY Model in Dilute Magnetic Semiconductors. *Phys. Rev. Lett.* **2006**, *97* (12), 127201.

(214) Coey, J. M. D.; Douvalis, A. P.; Fitzgerald, C. B.; Venkatesan, M. Ferromagnetism in Fe-

Doped SnO_2 Thin Films. *Appl. Phys. Lett.* **2004**, *84* (8), 1332–1334.

(215) Murray, J. L. The Hf-Ti (Hafnium-Titanium) System. *Bull. Alloy Phase Diagrams* **1981**, *2* (2), 181–185.

(216) $HfTiO_4$ ($Hf_{0.5}Ti_{0.5}O_2$) Crystal Structure: Datasheet from "PAULING FILE Multinaries Edition – 2012" in SpringerMaterials (Https://Materials.Springer.Com/Isp/Crystallographic/Docs/Sd_0551225). Springer-Verlag Berlin Heidelberg & Material Phases Data System (MPDS), Switzerland & National Institute for Materials Science (NIMS), Japan.

(217) Ross, F. M.; Tersoff, J.; Reuter, M. C. Sawtooth Faceting in Silicon Nanowires. *Phys. Rev. Lett.* **2005**, *95* (14), 146104.

(218) Ma, Z.; McDowell, D.; Panaitescu, E.; Davydov, A. V.; Upmanyu, M.; Menon, L. Vapor-Liquid-Solid Growth of Serrated GaN Nanowires: Shape Selection Driven by Kinetic Frustration. *J. Mater. Chem. C* **2013**, *1* (44), 7294–7302.

(219) McIntyre, P. C.; Fontcuberta i Morral, A. Semiconductor Nanowires: To Grow or Not to Grow? *Mater. Today Nano* **2020**, *9*, 100058.

(220) Brillo, J.; Egry, I. Surface Tension of Nickel, Copper, Iron and Their Binary Alloys. *J. Mater. Sci.* **2005**, *40* (9–10), 2213–2216.

(221) Egry, I.; Ricci, E.; Novakovic, R.; Ozawa, S. Surface Tension of Liquid Metals and Alloys-Recent Developments. *Adv. Colloid Interface Sci.* **2010**, *159* (2), 198–212.

(222) Fischer, D.; Kersch, A. The Effect of Dopants on the Dielectric Constant of HfO_2 and ZrO_2 from First Principles. *Appl. Phys. Lett.* **2008**, *92* (1), 12908.

(223) Minh, N. Van; Long, D. H.; Khoi, N. T.; Jung, Y.; Kim, S.-J.; Yang, I.-S. Raman Studies of $Ti_{1-x}Fe_xO_2$ Noparticles. *IEEE Trans. Nanotechnol.* **2008**, *7* (2), 177–180.

(224) Yoon, S. D.; Chen, Y.; Yang, A.; Goodrich, T. L.; Zuo, X.; Arena, D. A.; Ziemer, K.; Vittoria, C.; Harris, V. G. Oxygen-Defect-Induced Magnetism to 880 K in Semiconducting Anatase TiO_2-δ Films. *J. Phys. Condens. Matter* **2006**, *18* (27), L355–L361.

(225) Maaz, K.; Mumtaz, A.; Hasanain, S. K.; Bertino, M. F. Temperature Dependent Coercivity and Magnetization of Nickel Ferrite Nanoparticles. *J. Magn. Magn. Mater.* **2010**, *322* (15), 2199–2202.

(226) Deml, A. M.; Holder, A. M.; O'Hayre, R. P.; Musgrave, C. B.; Stevanović, V. Intrinsic Material Properties Dictating Oxygen Vacancy Formation Energetics in Metal Oxides. *J. Phys. Chem. Lett.* **2015**, *6* (10), 1948–1953.

(227) Hinuma, Y.; Kamachi, T.; Hamamoto, N.; Takao, M.; Toyao, T.; Shimizu, K. I. Surface Oxygen Vacancy Formation Energy Calculations in 34 Orientations of β-Ga_2O_3 and θ-Al_2O_3. *J. Phys. Chem. C* **2020**, *124* (19), 10509–10522.

(228) Alam, M. N. K.; Clima, S.; O'sullivan, B. J.; Kaczer, B.; Pourtois, G.; Heyns, M.; Van Houdt, J. First Principles Investigation of Charge Transition Levels in Monoclinic, Orthorhombic, Tetragonal, and Cubic Crystallographic Phases of HfO_2. *J. Appl. Phys.* **2021**, *129* (8), 84102.

(229) Bradley, S. R.; Bersuker, G.; Shluger, A. L. Modelling of Oxygen Vacancy Aggregates in Monoclinic HfO_2: Can They Contribute to Conductive Filament Formation? *J. Phys. Condens. Matter* **2015**, *27* (41), 415401.

(230) Arrott, A. Criterion for Ferromagnetism from Observations of Magnetic Isotherms. *Phys. Rev.* **1957**, *108* (6), 1394–1396.

(231) Zippel, J.; Lorenz, M.; Setzer, A.; Wagner, G.; Sobolev, N.; Esquinazi, P.; Grundmann, M. Defect-Induced Ferromagnetism in Undoped and Mn-Doped Zirconia Thin Films. *Phys. Rev. B - Condens. Matter Mater. Phys.* **2010**, *82* (12), 125209.

(232) Xu, X.; Xu, C.; Dai, J.; Hu, J.; Li, F.; Zhang, S. Size Dependence of Defect-Induced Room Temperature Ferromagnetism in Undoped ZnO Nanoparticles. *J. Phys. Chem. C* **2012**, *116* (15), 8813–8818.

(233) Wan, W.; Huang, J.; Zhu, L.; Hu, L.; Wen, Z.; Sun, L.; Ye, Z. Defects Induced Ferromagnetism in ZnO Nanowire Arrays Doped with Copper. *CrystEngComm* **2013**, *15* (39), 7887–7894.

(234) Santara, B.; Giri, P. K.; Imakita, K.; Fujii, M. Evidence of Oxygen Vacancy Induced Room Temperature Ferromagnetism in Solvothermally Synthesized Undoped TiO_2 Nanoribbons. *Nanoscale* **2013**, *5* (12), 5476–5488.

(235) Wang, H.; Wei, J.; Xiong, R.; Shi, J. Enhanced Ferromagnetic Properties of Fe+N Codoped TiO_2 Anatase. *J. Magn. Magn. Mater.* **2012**, *324* (13), 2057–2061.

(236) Patel, S. K. S.; Gajbhiye, N. S. Intrinsic Room-Temperature Ferromagnetism of V-Doped TiO_2 (B) Nanotubes Synthesized by the Hydrothermal Method. *Solid State Commun.* **2011**,

151 (20), 1500–1503.

(237) Pellicer, E.; Cabo, M.; Rossinyol, E.; Solsona, P.; Suriñach, S.; Barõ, M. D.; Sort, J. Nanocasting of Mesoporous In-TM (TM=Co, Fe, Mn) Oxides: Towards 3D Diluted-Oxide Magnetic Semiconductor Architectures. *Adv. Funct. Mater*. **2013**, *23* (7), 900–911.

(238) Chang, L. Te; Wang, C. Y.; Tang, J.; Nie, T.; Jiang, W.; Chu, C. P.; Arafin, S.; He, L.; Afsal, M.; Chen, L. J.; Wang, K. L. Electric-Field Control of Ferromagnetism in Mn-Doped ZnO Nanowires. *Nano Lett.* **2014**, *14* (4), 1823–1829.

(239) Dery, H.; Dalal, P.; Cywiński; Sham, L. J. Spin-Based Logic in Semiconductors for Reconfigurable Large-Scale Circuits. *Nature* **2007**, *447* (7144), 573–576.

(240) Hojo, H.; Fujita, K.; Tanaka, K.; Hirao, K. Epitaxial Growth of Room-Temperature Ferrimagnetic Semiconductor Thin Films Based on the Ilmenite-Hematite Solid Solution. *Appl. Phys. Lett.* **2006**, *89* (8), 82509.

(241) Fujii, T.; Kayano, M.; Takada, Y.; Nakanishi, M.; Takada, J. Ilmenite-Hematite Solid Solution Films for Novel Electronic Devices. *Solid State Ionics* **2004**, *172* (1-4 SPEC. ISS.), 289–292.

Appendix A

Supplementary Information

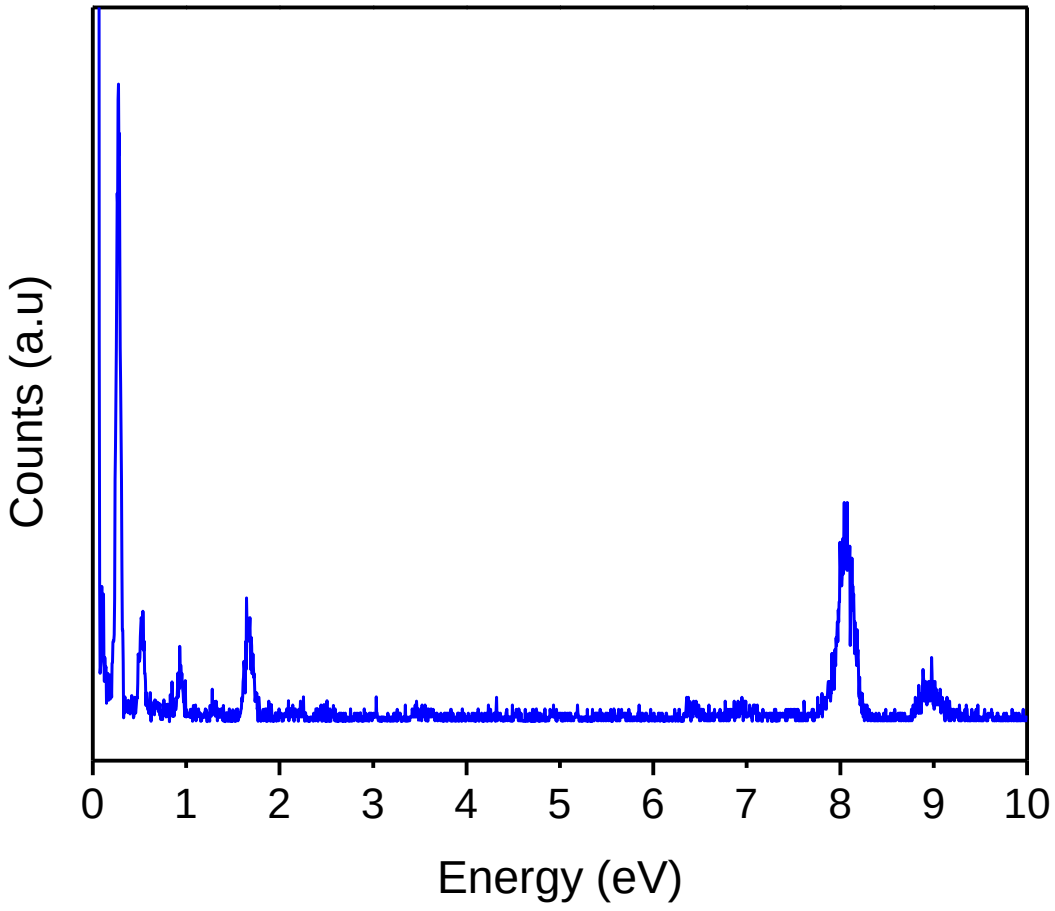

Figure A1. The corresponding EDS spectrum of the NWs Shown in Figure 2-9b.

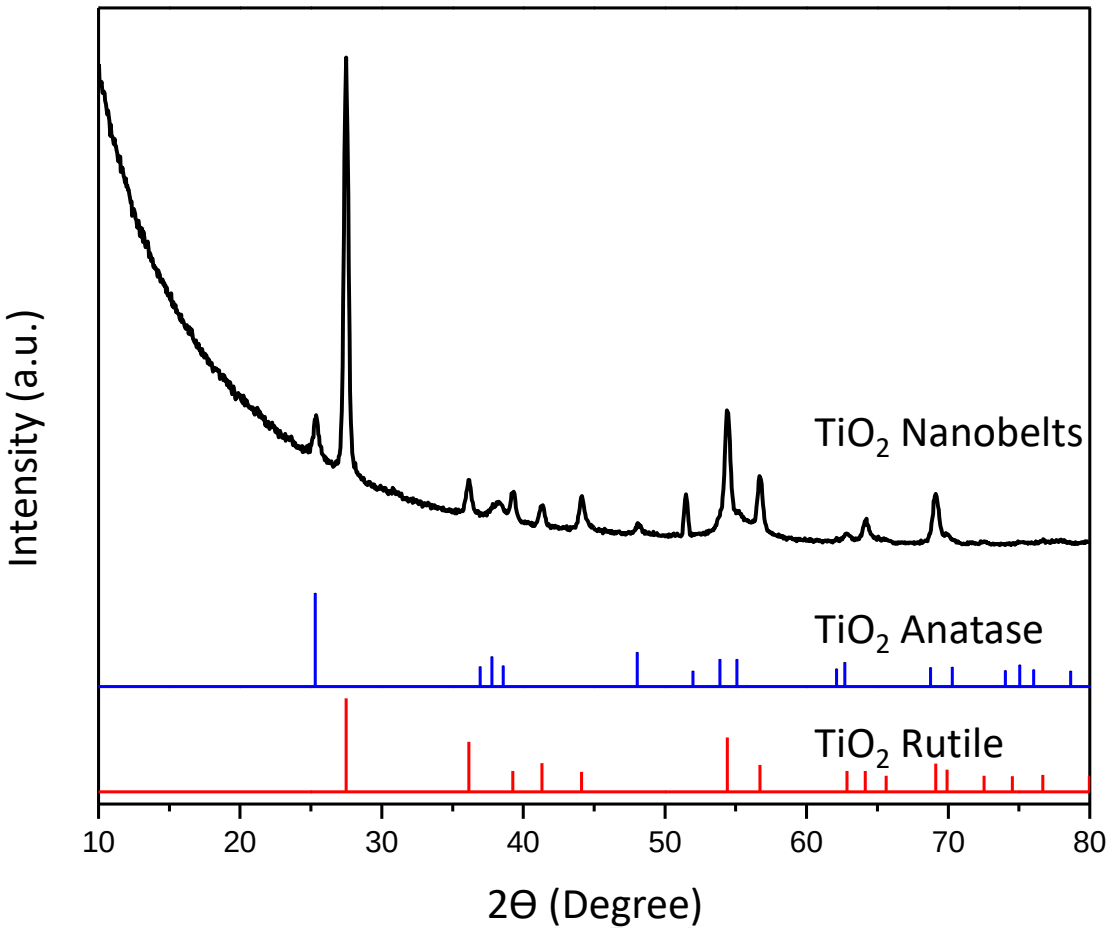

Figure A2. The GIXRD pattern of TiO_2 nanobelt grown by catalyst-assisted PLD.

Appendix B

Permissions

American Physical Society Reuse and Permissions License

24-Oct-2021

This license agreement between the American Physical Society ("APS") and Mahdi Beedel ("You") consists of your license details and the terms and conditions provided by the American Physical Society and SciPris.

Licensed Content Information

License Number:	**RNP/21/OCT/045899**
License date:	24-Oct-2021
DOI:	10.1103/PhysRevB.39.4828
Title:	Enhanced magnetoresistance in layered magnetic structures with antiferromagnetic interlayer exchange
Author:	G. Binasch et al.
Publication:	Physical Review B
Publisher:	American Physical Society
Cost:	USD $ 0.00

Request Details

Does your reuse require significant modifications: No

Specify intended distribution locations:	Worldwide
Reuse Category:	Reuse in a thesis/dissertation
Requestor Type:	Student
Items for Reuse:	Figures/Tables
Number of Figure/Tables:	1
Figure/Tables Details:	Figure 2(d) on page 4829
Format for Reuse:	Print and Electronic
Total number of print copies:	Up to 1000

Information about New Publication:

University/Publisher:	University of Waterloo
Title of dissertation/thesis:	One-dimensional Nanostructures of Hafnium Oxides: Fabrication with and without Ti/Fe Doping, and Magnetic Properties
Author(s):	Mahdi Beedel
Expected completion date:	Dec. 2021

License Requestor Information

Name:	Mahdi Beedel
Affiliation:	Individual
Email Id:	mahdibeedel@gmail.com
Country:	Canada

American Physical Society Reuse and Permissions License

24-Oct-2021

This license agreement between the American Physical Society ("APS") and Mahdi Beedel ("You") consists of your license details and the terms and conditions provided by the American Physical Society and SciPris.

Licensed Content Information

License Number:	**RNP/21/OCT/045901**
License date:	24-Oct-2021
DOI:	10.1103/PhysRevLett.61.2472
Title:	Giant Magnetoresistance of (001)Fe/(001)Cr Magnetic Superlattices
Author:	M. N. Baibich et al.
Publication:	Physical Review Letters
Publisher:	American Physical Society
Cost:	USD $ 0.00

Request Details

Does your reuse require significant modifications: No

Specify intended distribution locations:	Worldwide
Reuse Category:	Reuse in a thesis/dissertation
Requestor Type:	Student
Items for Reuse:	Figures/Tables
Number of Figure/Tables:	1
Figure/Tables Details:	Figure 3 on page 2473
Format for Reuse:	Print and Electronic
Total number of print copies:	Up to 1000

Information about New Publication:

University/Publisher:	University of Waterloo
Title of dissertation/thesis:	One-dimensional Nanostructures of Hafnium Oxides: Fabrication with and without Ti/Fe Doping, and Magnetic Properties
Author(s):	Mahdi Beedel
Expected completion date:	Dec. 2021

License Requestor Information

Name:	Mahdi Beedel
Affiliation:	Individual
Email Id:	mahdibeedel@gmail.com
Country:	Canada

License Details

This Agreement between Mr. Mahdi Beedel ("You") and Springer Nature ("Springer Nature") consists of your license details and the terms and conditions provided by Springer Nature and Copyright Clearance Center.

Print Copy

License Number	5175560450130
License date	Oct 24, 2021
Licensed Content Publisher	Springer Nature
Licensed Content Publication	Springer eBook
Licensed Content Title	Metallic Multilayers: Discovery of Interlayer Exchange Coupling and GMR
Licensed Content Author	Peter Grünberg, Daniel E. Bürgler
Licensed Content Date	Jan 1, 2015
Type of Use	Thesis/Dissertation
Requestor type	non-commercial (non-profit)
Format	print and electronic
Portion	figures/tables/illustrations
Number of figures/tables/illustrations	1
Will you be translating?	no
Circulation/distribution	1 - 29
Author of this Springer Nature content	no
Title	One-dimensional Nanostructures of Hafnium Oxides: Fabrication with and without Ti/Fe Doping, and Magnetic Properties
Institution name	University of Waterloo
Expected presentation date	Dec 2021
Portions	Figure 10 on page 10
Requestor Location	Mr. Mahdi Beedel C2-062, Department of Chemistry, University of Waterloo, 200 University Avenue West Waterloo, ON N2L 3G1 Canada Attn: University of Waterloo-WATLAB
Total	**0.00 CAD**

BACK

CCC | RightsLink®

My Orders My Library My Profile Welcome mbeedel@uwaterloo.ca Log out | Help | FA

My Orders > Orders > All Orders

License Details

This Agreement between Mr. Mahdi Beedel ("You") and John Wiley and Sons ("John Wiley and Sons") consists of your license details and the terms and conditions provided b John Wiley and Sons and Copyright Clearance Center.

Print Copy

License Number	5175960995510
License date	Oct 25, 2021
Licensed Content Publisher	John Wiley and Sons
Licensed Content Publication	Angewandte Chemie International Edition
Licensed Content Title	Spintronics: A Challenge for Materials Science and Solid-State Chemistry
Licensed Content Author	Claudia Felser, Gerhard H. Fecher, Benjamin Balke
Licensed Content Date	Jan 12, 2007
Licensed Content Volume	46
Licensed Content Issue	5
Licensed Content Pages	32
Type of Use	Dissertation/Thesis
Requestor type	University/Academic
Format	Print and electronic
Portion	Figure/table
Number of figures/tables	1
Will you be translating?	No
Title	One-dimensional Nanostructures of Hafnium Oxides: Fabrication with and without Ti/Fe Doping, and Magnetic Properties
Institution name	University of Waterloo
Expected presentation date	Dec 2021
Portions	Figure 5 on page 672
Requestor Location	Mr. Mahdi Beedel C2-062, Department of Chemistry, University of Waterloo, 200 University Avenue West Waterloo, ON N2L 3G1 Canada Attn: University of Waterloo-WATLAB
Publisher Tax ID	EU826007151
Total	**0.00 CAD**

BACK

American Physical Society
Reuse and Permissions License

24-Oct-2021

This license agreement between the American Physical Society ("APS") and Mahdi Beedel ("You") consists of your license details and the terms and conditions provided by the American Physical Society and SciPris.

Licensed Content Information

License Number:	**RNP/21/OCT/045902**
License date:	24-Oct-2021
DOI:	10.1103/RevModPhys.76.323
Title:	Spintronics: Fundamentals and applications
Author:	Igor Žutić, Jaroslav Fabian, and S. Das Sarma
Publication:	Reviews of Modern Physics
Publisher:	American Physical Society
Cost:	USD $ 0.00

Request Details

Does your reuse require significant modifications: No

Specify intended distribution locations:	Worldwide
Reuse Category:	Reuse in a thesis/dissertation
Requestor Type:	Student
Items for Reuse:	Figures/Tables
Number of Figure/Tables:	1
Figure/Tables Details:	Figure 2 on page 326
Format for Reuse:	Print and Electronic
Total number of print copies:	Up to 1000

Information about New Publication:

University/Publisher:	University of Waterloo
Title of dissertation/thesis:	One-dimensional Nanostructures of Hafnium Oxides: Fabrication with and without Ti/Fe Doping, and Magnetic Properties
Author(s):	Mahdi Beedel
Expected completion date:	Dec. 2021

License Requestor Information

Name:	Mahdi Beedel
Affiliation:	Individual
Email Id:	mahdibeedel@gmail.com
Country:	Canada

CCC Marketplace™

Order Date	24-Oct-2021	Type of Use	Republish in a thesis/dissertation
Order License ID	1156607-1		
ISSN	1361-6463	Publisher	IOP Publishing
		Portion	Image/photo/illustration

LICENSED CONTENT

Publication Title	Journal of Physics D : Applied Physics	Country	United Kingdom of Great Britain and Northern Ireland
Author/Editor	Institute of Physics (Great Britain), Institute of Physics and the Physical Society.	Rightsholder	IOP Publishing, Ltd
		Publication Type	e-Journal
Date	01/01/1996	URL	http://iopscience.iop.org/0022-3727/
Language	English		

REQUEST DETAILS

Portion Type	Image/photo/illustration	Distribution	Worldwide
Number of images / photos / illustrations	1	Translation	Original language of publication
Format (select all that apply)	Print, Electronic	Copies for the disabled?	No
		Minor editing privileges?	Yes
Who will republish the content?	Not-for-profit entity	Incidental promotional use?	No
Duration of Use	Life of current and all future editions	Currency	CAD
Lifetime Unit Quantity	Up to 499		
Rights Requested	Main product and any product related to main product		

NEW WORK DETAILS

Title	One-dimensional Nanostructures of Hafnium Oxides: Fabrication with and without Ti/Fe Doping, and Magnetic Properties	Institution name	University of Waterloo
		Expected presentation date	2021-12-13
Instructor name	Mahdi Beedel		

ADDITIONAL DETAILS

Order reference number	N/A	The requesting person / organization to appear on the license	Mahdi Beedel

REUSE CONTENT DETAILS

Title, description or numeric reference of the portion(s)	Figure 41	Title of the article/chapter the portion is from	Future perspectives for spintronic devices
Editor of portion(s)	N/A	Author of portion(s)	Atsufumi Hirohata, Koki Takanashi
Volume of serial or monograph	N/A	Issue, if republishing an article from a serial	N/A
Page or page range of portion	34	Publication date of portion	2014-04-25

CCC Marketplace™

Order Date	24-Oct-2021	Type of Use	Republish in a thesis/dissertation
Order License ID	1156613-1		
ISSN	0953-8984	Publisher	IOP Publishing
		Portion	Chart/graph/table/figure

LICENSED CONTENT

Publication Title	Journal of Physics : Condensed Matter	Country	United Kingdom of Great Britain and Northern Ireland
Author/Editor	Institute of Physics (Great Britain)	Rightsholder	IOP Publishing, Ltd
Date	01/01/1989	Publication Type	Journal
Language	English		

REQUEST DETAILS

Portion Type	Chart/graph/table/figure	Distribution	Worldwide
Number of charts / graphs / tables / figures requested	1	Translation	Original language of publication
		Copies for the disabled?	No
Format (select all that apply)	Print, Electronic	Minor editing privileges?	No
Who will republish the content?	Not-for-profit entity	Incidental promotional use?	No
Duration of Use	Life of current and all future editions	Currency	CAD
Lifetime Unit Quantity	Up to 499		
Rights Requested	Main product and any product related to main product		

NEW WORK DETAILS

Title	One-dimensional Nanostructures of Hafnium Oxides: Fabrication with and without Ti/Fe Doping, and Magnetic Properties	Institution name	University of Waterloo
		Expected presentation date	2021-12-13
Instructor name	Mahdi Beedel		

ADDITIONAL DETAILS

Order reference number	N/A	The requesting person / organization to appear on the license	Mahdi Beedel

REUSE CONTENT DETAILS

Title, description or numeric reference of the portion(s)	Figure 2	Title of the article/chapter the portion is from	Transition metal-doped TiO2 and ZnO—present status of the field
Editor of portion(s)	N/A	Author of portion(s)	Rebecca Janisch, PriyaGopal and Nicola A Spaldin
Volume of serial or monograph	N/A		
		Issue, if republishing an article from a serial	N/A
Page or page range of portion	R661		
		Publication date of portion	2005-06-24

CCC Marketplace™

This is a License Agreement between Mahdi Beedel ("User") and Copyright Clearance Center, Inc. ("CCC") on behalf of the Rightsholder identified in the order details below. The license consists of the order details, the CCC Terms and Conditions below, and any Rightsholder Terms and Conditions which are included below.

All payments must be made in full to CCC in accordance with the CCC Terms and Conditions below.

Order Date	25-Oct-2021	Type of Use	Republish in a thesis/dissertation
Order License ID	1156765-1		
ISSN	0953-8984	Publisher	IOP Publishing
		Portion	Chart/graph/table/figure

LICENSED CONTENT

Publication Title	Journal of Physics : Condensed Matter	Country	United Kingdom of Great Britain and Northern Ireland
Author/Editor	Institute of Physics (Great Britain)	Rightsholder	IOP Publishing, Ltd
Date	01/01/1989	Publication Type	Journal
Language	English		

REQUEST DETAILS

Portion Type	Chart/graph/table/figure	Distribution	Worldwide
Number of charts / graphs / tables / figures requested	1	Translation	Original language of publication
Format (select all that apply)	Print, Electronic	Copies for the disabled?	No
		Minor editing privileges?	Yes
Who will republish the content?	Not-for-profit entity	Incidental promotional use?	No
Duration of Use	Life of current and all future editions	Currency	CAD
Lifetime Unit Quantity	Up to 499		
Rights Requested	Main product and any product related to main product		

NEW WORK DETAILS

Title	One-dimensional Nanostructures of Hafnium Oxides: Fabrication with and without Ti/Fe Doping, and Magnetic Properties	Institution name	University of Waterloo
		Expected presentation date	2021-12-13
Instructor name	Mahdi Beedel		

ADDITIONAL DETAILS

Order reference number	N/A	The requesting person / organization to appear on the license	Mahdi Beedel

REUSE CONTENT DETAILS

Title, description or numeric reference of the portion(s)	Figure 1	Title of the article/chapter the portion is from	Ab initio localized basis set study of structural parameters and elastic properties of HfO2 polymorphs
Editor of portion(s)	N/A		
Volume of serial or monograph	N/A	Author of portion(s)	M A Caravaca, R A Casali
		Issue, if republishing an article from a serial	N/A
Page or page range of portion	5799		
		Publication date of portion	2005-09-02

License Details

This Agreement between Mr. Mahdi Beedel ("You") and Elsevier ("Elsevier") consists of your license details and the terms and conditions provided by Elsevier and Copyright Clearance Center.

License Number	5175970372718
License date	Oct 25, 2021
Licensed Content Publisher	Elsevier
Licensed Content Publication	Materials Science and Engineering: R: Reports
Licensed Content Title	Development of hafnium based high-k materials—A review
Licensed Content Author	J.H. Choi,Y. Mao,J.P. Chang
Licensed Content Date	Jul 22, 2011
Licensed Content Volume	72
Licensed Content Issue	6
Licensed Content Pages	40
Type of Use	reuse in a thesis/dissertation
Portion	figures/tables/illustrations
Number of figures/tables/illustrations	1
Format	both print and electronic
Are you the author of this Elsevier article?	No
Will you be translating?	No
Title	One-dimensional Nanostructures of Hafnium Oxides: Fabrication with and without Ti/Fe Doping, and Magnetic Properties
Institution name	University of Waterloo
Expected presentation date	Dec 2021
Portions	Figure 4 on page 101
Requestor Location	Mr. Mahdi Beedel C2-062, Department of Chemistry, University of Waterloo, 200 University Avenue West Waterloo, ON N2L 3G1 Canada Attn: University of Waterloo-WATLAB
Publisher Tax ID	GB 494 6272 12
Total	**0.00 CAD**

CCC Marketplace™

This is a License Agreement between Mahdi Beedel ("User") and Copyright Clearance Center, Inc. ("CCC") on behalf of the Rightsholder identified in the order details below. The license consists of the order details, the CCC Terms and Conditions below, and any Rightsholder Terms and Conditions which are included below.

All payments must be made in full to CCC in accordance with the CCC Terms and Conditions below.

Order Date	25-Oct-2021	Type of Use	Republish in a thesis/dissertation
Order License ID	1156789-1		
ISSN	1361-6463	Publisher	IOP Publishing
		Portion	Chart/graph/table/figure

LICENSED CONTENT

Publication Title	Journal of Physics D : Applied Physics	Country	United Kingdom of Great Britain and Northern Ireland
Author/Editor	Institute of Physics (Great Britain), Institute of Physics and the Physical Society.	Rightsholder	IOP Publishing, Ltd
		Publication Type	e-Journal
Date	01/01/1996	URL	http://iopscience.iop.org/0022-3727/
Language	English		

REQUEST DETAILS

Portion Type	Chart/graph/table/figure	Distribution	Worldwide
Number of charts / graphs / tables / figures requested	1	Translation	Original language of publication
		Copies for the disabled?	No
Format (select all that apply)	Print, Electronic	Minor editing privileges?	Yes
Who will republish the content?	Not-for-profit entity	Incidental promotional use?	No
Duration of Use	Life of current and all future editions	Currency	CAD
Lifetime Unit Quantity	Up to 499		
Rights Requested	Main product and any product related to main product		

NEW WORK DETAILS

Title	One-dimensional Nanostructures of Hafnium Oxides: Fabrication with and without Ti/Fe Doping, and Magnetic Properties	Institution name	University of Waterloo
		Expected presentation date	2021-12-13
Instructor name	Mahdi Beedel		

ADDITIONAL DETAILS

Order reference number	N/A	The requesting person / organization to appear on the license	Mahdi Beedel

REUSE CONTENT DETAILS

Title, description or numeric reference of the portion(s)	Figure 1	Title of the article/chapter the portion is from	Semiconductor nanowires
Editor of portion(s)	N/A	Author of portion(s)	Wei Lu, and Charles M Lieber
Volume of serial or monograph	N/A	Issue, if republishing an article from a serial	N/A
Page or page range of portion	R388	Publication date of portion	2006-10-20

License Details

This Agreement between Mr. Mahdi Beedel ("You") and AIP Publishing ("AIP Publishing") consists of your license details and the terms and conditions provided by AIP Publishing and Copyright Clearance Center.

License Number	5175980784241
License date	Oct 25, 2021
Licensed Content Publisher	AIP Publishing
Licensed Content Publication	Journal of Applied Physics
Licensed Content Title	Tutorial: Basic principles, limits of detection, and pitfalls of highly sensitive SQUID magnetometry for nanomagnetism and spintronics
Licensed Content Author	M. Buchner, K. Höfler, B. Henne, et al
Licensed Content Date	Oct 28, 2018
Licensed Content Volume	124
Licensed Content Issue	16
Type of Use	Thesis/Dissertation
Requestor type	Student
Format	Print and electronic
Portion	Photograph/Image
Number of Photographs/Images	1
Will you be translating?	No
Title	One-dimensional Nanostructures of Hafnium Oxides: Fabrication with and without Ti/Fe Doping, and Magnetic Properties
Institution name	University of Waterloo
Expected presentation date	Dec 2021
Portions	Figure 1 on page 161101-2
Requestor Location	Mr. Mahdi Beedel C2-062, Department of Chemistry, University of Waterloo, 200 University Avenue West Waterloo, ON N2L 3G1 Canada Attn: University of Waterloo-WATLAB
Total	**0.00 CAD**

CCC | RightsLink®

My Orders My Library My Profile Welcome mbeedel@uwaterloo.ca Log out | Help | FA

My Orders > Orders > All Orders

License Details

This Agreement between Mr. Mahdi Beedel ("You") and Springer Nature ("Springer Nature") consists of your license details and the terms and conditions provided by Springer Nature and Copyright Clearance Center.

Print Copy

License Number	5176000064814
License date	Oct 25, 2021
Licensed Content Publisher	Springer Nature
Licensed Content Publication	Journal of Phase Equilibria (and diffusion)
Licensed Content Title	Au-Sn (Gold-Tin)
Licensed Content Author	H. Okamoto
Licensed Content Date	Jul 12, 2007
Type of Use	Thesis/Dissertation
Requestor type	non-commercial (non-profit)
Format	print and electronic
Portion	figures/tables/illustrations
Number of figures/tables/illustrations	1
Will you be translating?	no
Circulation/distribution	1 - 29
Author of this Springer Nature content	no
Title	One-dimensional Nanostructures of Hafnium Oxides: Fabrication with and without Ti/Fe Doping, and Magnetic Properties
Institution name	University of Waterloo
Expected presentation date	Dec 2021
Portions	Figure 1
Requestor Location	Mr. Mahdi Beedel C2-062, Department of Chemistry, University of Waterloo, 200 University Avenue West Waterloo, ON N2L 3G1 Canada Attn: University of Waterloo-WATLAB
Total	**0.00 CAD**

BACK